Ultracold and quantum degenerate mixtures of Cs and Yb

JACK DANIEL SEGAL

Ultracold and quantum degenerate mixtures of Cs and Yb

Jack Daniel Segal

A thesis submitted in partial fulfilment
of the requirements for the degree of
Doctor of Philosophy

Department of Physics
Durham University

2022

Ultracold and quantum degenerate mixtures of Cs and Yb

Jack Daniel Segal

Abstract

The study of ultracold mixtures of neutral atoms builds on the techniques of trapping and cooling single species of atoms to access more complex physical systems, and provides a route towards formation of ultracold molecules. In this thesis, we experimentally produce and study ultracold mixtures of Cs and Yb. This choice of Cs and Yb gives a versatile experimental system, with high tuneability of reduced mass, intraspecies and interspecies scattering properties, and the ability to study Bose-Bose and Bose-Fermi atomic mixtures. A long-term goal of working with the mixture is production of ultracold CsYb molecules. The CsYb molecule has a $^2\Sigma$ symmetry ground state, and both magnetic and electric dipole moments. An array of such CsYb molecules would therefore be a versatile experimental platform for applications such as quantum simulation of physical systems, quantum computation and ultracold quantum chemistry.

In this thesis, we report on experimental observations within the Cs-Yb mixture, made possible by the implementation of a bichromatic optical dipole trap consisting of individual dipole trapping beams of 532 nm and 1070 nm. This trap has been designed to overcome the problems of mismatched trap depths and in-trap losses previously encountered in a single-wavelength optical dipole trap. This allowed us for the first time to produce dual quantum degenerate mixtures. We report production of pure dual Bose-Einstein condensates (BECs) of Cs+^{174}Yb with $N_{\mathrm{Cs}} \sim 5 \times 10^3$ and $N_{\mathrm{Yb}} \sim 7 \times 10^4$. We also report production of pure dual BECs of Cs+^{170}Yb with $N_{\mathrm{Cs}} \sim 1 \times 10^4$ and $N_{\mathrm{Yb}} \sim 4 \times 10^4$. We further study these quantum degenerate mixtures, observing their lifetimes, dynamics, and properties such as mixture immiscibility and dual-species collapse.

We further improve the versatility of our experimental apparatus by implementing an optical lattice with tuneable wavelength. The lattice can operate at two Cs 'tune-out' wavelengths in the region of 460 nm. This allows a species-specific lattice potential which traps only Yb. Alternatively, it can be operated at wavelengths where either the trapping potential or the trap frequency is balanced for Cs and Yb. We measure the polarizability of Cs with Kapitza-Dirac diffraction of a Cs BEC using the tuneable lattice. This helps us obtain a more precise measurement of the Cs tune-out wavelengths.

Finally, we investigate a potential route to formation of CsYb molecules by performing Feshbach spectroscopy on an ultracold mixture of Cs+^{173}Yb. Using predictions supported by previous experimental and theoretical work, we report the first experimental observations of interspecies magnetic Cs-Yb Feshbach resonances. We observe two sets of resonances, at magnetic bias fields around 622 G and 702 G. These observations motivate further discussion on the utilisation of the resonances for magnetoassociation, as well as experimental techniques to detect and manipulate the nuclear spin substate composition of Fermionic Yb.

Declaration

I confirm that no part of the material offered has previously been submitted by myself for a degree in this or any other university. Where material has been generated through joint work, the work of others has been indicated.

Jack Daniel Segal

Durham, 09 September, 2022

Acknowledgements

The process of studying for a PhD is not a simple or straightforward one. In my case, and that of many others, this was further complicated by the Covid-19 pandemic – and the long periods of lockdown and no lab access that came with it. I would not have got very far through these "interesting times" without the help and guidance of a large group of people, to whom I give acknowledgments below.

I start by thanking my PhD supervisor, Professor Simon Cornish. Simon has been a constant and invaluable source of guidance, knowledge and expertise throughout my PhD. Under his supervision, I have become a far better and much more confident researcher than I was at the start. Simon has also instilled in me a better and smarter approach to solving the problems which near-constantly bombard you in a cold atom lab. All of Simon's students are familiar with his 'five steps to a successful measurement' and I am no exception. In particular I learnt from Simon the valuable importance of checking that what is going on in the lab matches your expectations – and indeed knowing what your expectations are in the first place! The lessons and skills I have learned while working in Simon's group will stay with me throughout the rest of my career.

I also thank my co-supervisor, Professor Ifan Hughes. Our regular co-supervisory meetings (typically Fridays after 6pm, in one of Durham's many excellent public houses) have been of great benefit to me throughout! Ifan has a limitless and infectious enthusiasm for all of the research in the QLM section, and has always provided me with fresh and insightful perspectives on the progress of my research. His excellent book 'Measurements and their Uncertainties' is a must-have for any science student and I have kept my copy close to hand throughout my PhD.

Most PhD students are lucky if they get to work with one brilliant postdoc; I have had the good fortune to work with three. Firstly, I thank Alex Guttridge, a dedicated and highly knowledgeable researcher who, at the beginning of my PhD, was the person who showed me the ropes and taught me the intricacies of the CsYb experiment. I thank him for both his patience and all his thorough explan-

ations. Secondly, I thank Kali Wilson for her support, guidance and expertise, for everything from aligning optics to making data presentable for a poster or a paper, to improving the efficiency of our measurement 'campaigns' - I might still be in the lab if it wasn't for Kali! Finally, I thank Tobias Franzen, who always takes an optimistic yet thorough approach to both data taking, and fixing and improving anything in the lab – truly a safe pair of hands to take the CsYb experiment forward into the next phase of exciting measurements.

I thank all Postdocs and PhD students, past and present, in the other labs of the Cornish group, for imparting with me useful knowledge and expertise over the years, and for making the group a vibrant and stimulating place to do research. I thank the members of Jeremy Hutson's group in the Chemistry department, whose theoretical work has enabled us to obtain some of the experimental results within this thesis. I thank all the technicians in the mechanical and electrical workshops as well as the other technical support staff in the Physics department, for their support and tireless work dealing with our many requests.

The QLM research section in Durham is an amazing, ever-welcoming community of intelligent and dedicated researchers. I simply could not have chosen a better environment in which to do a PhD. I have countless fond memories of group activities both in and out of the department, including cake club on Wednesdays and the aforementioned pub trips on Fridays. I thank all QLM students and staff members for their friendship and support.

I have forged many great and lasting friendships over my time in Durham. From the Physics department, I give particular thanks to fellow PhD candidates Atreya, Callum, Liam, Tom, and Vincent, all companions on many days out to Newcastle, York and beyond. I thank all the friends I have met through Van Mildert college MCR, particularly my fellow 'life society' members Daniel, Simos and Taha. I also thank Pertev, my housemate of over three years, for his companionship and the countless hours of conversations we have had discussing everything and anything, from archaeology to armoured vehicles.

Finally, I give thanks to the unwavering love and support of my family; to my mother Helen; to my sister Rose and brother-in-law David; and to my two young nephews (who have been born during the course of this PhD!). I appreciate you listening to each and every lecture and rant about my PhD, and how you have helped me during the more stressful moments. I wouldn't have been able to do it without you!

Contents

List of Figures

List of Tables

Chapter 1

Introduction

1.1 Introduction to quantum degenerate mixtures

The study of ultracold and quantum degenerate mixtures of atomic gases is a broad and rich area of research, which has built upon the well-established techniques of trapping a single atomic species and cooling to quantum degeneracy. The applications of such mixtures are numerous. Novel quantum phases have been realised in Bose-Fermi mixtures with tuneable interspecies interactions [1; 2; 3; 4; 5; 6; 7]. Self-bound droplets of quantum gases have been created by tuning the interactions of a Bose-Bose mixture around the region of dual-species collapse [8; 9; 10]. Formation of solitons has been observed in both Bose-Bose and Bose-Fermi mixtures [11; 12]. Dual-species mixtures of superfluids have been shown to have coupled and collective dynamics mediated by the interspecies interaction [13; 14; 15]. Three-body Efimov resonances have also been observed in two-species mixtures [16; 17; 18; 19].

Experiments using two alkali atom species were initially used to provide sympathetic cooling between species [20; 21]. A degenerate Bose-Fermi mixture of Li and Na was reported in 2002 [22]. Other examples of degenerate mixtures of alkali atoms include Li-K [23], Rb-Cs [24; 25], K-Rb[26], and K-Cs [27]. In recent years, there has been growing interest in extending these techniques to mixtures of alkali and alkaline-earth-like atoms with a closed valence shell (see section 1.3.1). Dual

degeneracy was reported in a Rb-Sr mixture in 2013 [28], with other examples of dual-degenerate mixtures including Rb-Yb [29] and Sr-Li [30]. Mixtures involving the highly magnetic lanthanide atoms Er and Dy have also been proposed and realised [31; 32; 33].

1.2 Introduction to ultracold molecules

The study of ultracold polar molecules is a broad and active field of research, with numerous applications in both physics and chemistry [34; 35; 36; 37]. The internal energy structure of a diatomic molecule is significantly more complex than the structure found in single neutral atoms. Each electronic state supports vibrational and rotational degrees of freedom relative to the interatomic axis. Molecules may also possess hyperfine structure due to the nuclear spin of constituent atoms. This internal structure can be utilised for numerous applications.

Ultracold molecules may also possess permanent dipole moments. Experimentally, electric and magnetic fields can be utilised to manipulate the orientation of the dipole moments. By experimentally realising molecules confined in a lattice with one molecule per site, the interactions between dipoles on neighbouring sites can be tuned. An array of ultracold molecules could in this way be used for quantum computation and quantum information applications [38]. The dipole-dipole interaction, through which the molecules can interact, can be switched 'on' and 'off' through selective excitation to different rotational states, using using transitions in the microwave frequency range [39].

The internal structure of molecules makes them sensitive to tests of fundamental physics. Molecular dipole moments are utilised in precision measurements making such tests [35; 40], the most prominent among which are experiments aiming to search for an electron electric dipole moment [41; 42; 43]. Polar molecules trapped in optical lattices can also be used to realise and simulate strongly correlated many-body systems [37], including numerous spin-lattice models [44].

Ultracold molecules also have applications in the field of ultracold chemistry [45; 46]. The low collision energy of ultracold molecules allows better understanding and control of collisions. Chemical reactions can be observed on energy scales where quantum effects determine the product particles of collisions [47; 48; 49].

1.2.1 Routes to formation of ultracold molecules

Gases of ultracold molecules can generally be formed by two contrasting experimental methods. Firstly, there are a number of diatomic molecules for which laser cooling is experimentally feasible. In recent years, this direct cooling approach has been successfully applied to generate ultracold samples of these molecules. The main challenge in the direct cooling method is the application of the various cooling methods. Typically, precooling methods such as buffer gas cooling [50; 51; 52] are required to create a cold molecular beam. The beam is then slowed, using techniques such as Stark deceleration [53; 54; 55; 56; 57], laser slowing [58], or Zeeman-Sisyphus slowing [59]. Laser cooling can then be applied in a magneto-optical trap (MOT). However, molecular laser cooling schemes are further complicated by the complex internal structure. In typical laser-cooling schemes for such molecules, there are more dark states which the molecules can decay into and fall out of the cooling cycle. Additional laser light sources are therefore required to maintain an effective closed cooling cycle. Nevertheless, three-dimensional molecular MOTs of SrF [60; 61], CaF [52; 62], and YO[63] have been achieved.

The alternative method is an indirect cooling method, an example of which may in future be used for formation of CsYb molecules. This method makes use of the advanced techniques developed in the field of neutral atom trapping, and in particular those of ultracold mixtures. Ultracold heteronuclear molecules may be formed by creation of an ultracold dual-species mixture, and subsequently utilising a molecular association process. Similarly, homonuclear molecules may be formed by associating atoms in an ultracold single-species gas. The molecules produced

are ultracold, inheriting the high phase-space density of the initial atomic mixture and with little heating from the association process.

The first method that was used to produce ultracold molecules was photoassociation [64], where a colliding atom pair is optically excited to a bound molecular state by absorption of a resonant photon. The molecules produced by photoassociation are typically in a high-lying vibrational level near threshold of an excited electronic state. In some cases, the molecules then decay to a deeply-bound level within the electronic ground state. This technique has been used to produce molecules in the rovibrational ground state [65; 66; 67]. However, this is dependent on the molecular structure and the wave-function overlap (Franck-Condon overlap) between electronic states. This generally dictates whether the photoassociation method is effective for producing molecules in the ground state. However, Franck-Condon overlap can be enhanced using a Feshbach resonance, as has been demonstrated for LiCs molecules [68].

The alternative indirect process is magnetoassociation, where the mixture is adiabatically ramped across an avoided crossing of energy levels at a broad Feshbach resonance. Several examples of homonuclear and heteronuclear bialkali atoms have been created using the method of magnetoassociation [69]. Following magnetoassociation, the molecules can then be transferred to the rovibrational ground state, which is the required state for many of the proposed applications previously discussed. The efficacy of any transfer process relies on favourable wavefunction overlap between the excited state the molecule is formed in, the molecular ground state, and any intermediate states in the transfer. One method commonly used for this is stimulated Raman adiabatic passage (STIRAP) [70; 71]. The advantage of the magnetoassociation+STIRAP schemes is that both techniques are coherent and reversible. This means that after formation of, and experiments with, ultracold molecules, reverse STIRAP and reverse magnetoassiciation can be used dissociate the molecules into their constituent atoms. Important experimental quantities can then be measured using well-established atom imaging techniques. The combined

technique of magnetoassociation and STIRAP has been used to produce numerous examples of both homonuclear [72; 73] and heteronuclear [74; 75; 76; 77; 78; 79] bialkali dimer molecules in the rovibrational ground state.

1.3 Making ultracold molecules from Alkali+alkaline-earth-like mixtures

The physical properties of diatomic molecules formed from an alkali atom and an alkaline-earth-like atom have motivated much experimental and theoretical research towards formation of such molecules. As the outer shells of these constituent atoms contain one and two electrons respectively, the resultant molecule possesses one unpaired electron. As a result, the ground state of the molecule has a $^2\Sigma$ symmetry. This is in contrast to bialkali molecules, whose ground states are $^1\Sigma$. Molecules with a $^2\Sigma$ ground state are paramagnetic, possessing a magnetic dipole moment as well as an electric dipole moment. This additional dipole, and the resulting dipole-dipole interactions, can be manipulated using similar techniques to the electric dipole. An ensemble of $^2\Sigma$ molecules arranged in an optical lattice with one molecule per site is an ideal experimental platform in which to utilise this tuneability. The additional 'handle' of experimental complexity provided by the magnetic dipole moment can, for example, be used to access more complex spin lattice Hamiltonians for quantum simulation [44], and exploration of novel quantum phases [80]. Molecules with a $^2\Sigma$ ground state may have applications in quantum chemistry, with previous studies on their collisional properties in a range of geometries in electric and magnetic fields [81], and prospects of collisional shielding using electric fields [82]. There are also potential applications in quantum computation, with proposals to use an array $^2\Sigma$ polar molecules as qubits [83; 84].

Directly-cooled molecules such as CaF possess ground states with a $^2\Sigma$ symmetry. However, it remains advantageous to pursue formation of $^2\Sigma$ molecules through indirect methods due to the high phase-space density that can be achieved in the

constituent atomic samples, which the molecules subsequently inherit. The formation of such molecules, however, poses many challenges experimentally. The strong couplings which provide the wide Feshbach resonances used for magnetoassociation found in bi-alkali systems are not present in alkali + alkaline-earth-like systems, due to the closed shell structure and lack of electron spin in the alkaline-earth-like atoms. Narrower Feshbach resonances have been predicted for Rb-Sr [85], Li-Yb [86], Rb-Yb, and Cs-Yb [87] mixtures. Furthermore, they have been observed experimentally in Rb-Sr [88] and Li-Yb [89] mixtures. The ability to predict such Feshbach resonances relies on knowledge of the structure and binding energies of the molecular potential, and the atomic interspecies scattering properties. This has been a main focus of our prior work on CsYb [90; 91; 92; 93].

1.3.1 Alkali+alkaline-earth-like mixture experiments elsewhere

The CsYb experment described in this thesis is one of a number of experiments worldwide which study ultracold mixtures of alkali and alkaline-earth-like atoms. Here we give a brief review of other experiments working with such mixtures, and describe their experimental progress and the range of research themes being pursued in this field.

The group of Axel Görlitz in Düsseldorf developed an experiment of ultracold mixtures of Rb and Yb in a hybrid trap, with Yb confined in a bichromatic optical dipole trap and Rb confined in an Ioffe-Pritchard-type magnetic trap [94]. A main focus of their work has been production of RbYb molecules using one- and two-photon spectroscopy [95; 96], which was then used to determine the interspecies scattering lengths of the isotopologs in their system [97]. Further experiments probed the hyperfine splitting of bound molecular states [98] and Autler-Townes spectroscopy using photoassociation of atoms from a dual-species magneto-optical trap [99]. The group has also studied the interactions in thermal mixtures of Rb and Yb [100].

A Rb-Yb mixture experiment has also been developed in the group of Trey Porto at the joint quantum institute in Maryland, with a dual-degenerate mixture reported [29].

The group of Yoshiro Takahashi in Kyoto has extended its considerable experimental experience with ultracold Yb [101; 102; 103; 104; 105; 106] to the development of a ultracold and quantum degenerate Li-Yb mixtures, with a mixed-dimensional system realised by optical lattices [107; 108; 109; 110]. Their research to date has focussed on the collision and interaction properties of the mixture, including its dependence on external magnetic field, and spin state of the atoms [111; 112; 113; 114]. More recently, they have upgraded their experimental apparatus to include Er as a third element, and have observed Feshbach spectroscopy in Er-Li mixtures [115].

The group of Florian Schreck first produced a quantum degenerate mixture of Rb and Sr while located in Innsbruck [28], before relocating to Amsterdam. Here, they have performed both photoassociation spectroscopy to probe the molecular ground state [116], and Feshbach spectroscopy [88]. This latter study reported the first observation of interspecies Feshbach resonances between an alkali atom and an alkaline-earth-like atom. This is an important result, opening up the possibility of creating ultracold molecules from such mixtures by magnetoassociation.

The group of Subhadeep Gupta in Washington have also developed an Li-Yb experiment, with mixtures cooled to quantum degeneracy [117; 118; 119; 120; 15]. Similarly to the Düsseldorf group, they have performed one- and two-photon spectroscopy [121; 122], to probe the LiYb molecular ground state. Recently, they have observed interspecies Feshbach resonances in their system [89], becoming the second group in the alkali+closed-shell field of research to do so.

Other examples of alkali+alkaline-earth-like mixtures include mixtures of Rb and metastable He [123], of Rb and Hg [124], and of Li and Sr [30], with double degeneracy having been reported in the latter. Cold RbSr and RbCa molecules have

Yb Isotope	Abundance [129]	Nuclear spin	a_{Yb} (a_0) [130]	a_{CsYb} (a_0) [92]
^{176}Yb	12.70 %	0	-24	798
^{174}Yb	31.80 %	0	105	-75
^{173}Yb	16.10 %	5/2	199	1.0
^{172}Yb	21.90 %	0	-598	41
^{171}Yb	14.30 %	1/2	-3	70
^{170}Yb	3.05 %	0	64	96
^{168}Yb	0.13 %	0	251	166

Table 1.1: All stable isotopes of Yb with their respective natural abundance, nuclear spin, intraspecies scattering length a_{Yb}, and interspecies scattering length with ^{133}Cs, a_{CsYb}.

also been created by formation on Helium nanodroplets [125; 126]. Heat pipe spectroscopy has also been used to probe the molecular electronic states of LiCa [127] and LiSr [128].

1.4 Why CsYb?

Our choice of studying ultracold Cs-Yb mixtures, and routes towards creation of CsYb ultracold molecules, is due to the atomic properties of each constituent species. Yb is our alkaline-earth-like atom of choice due to the versatility of working with this species. Yb has seven stable isotopes, of which five are Bosons and two are Fermions. The properties of these isotopes are given in table 1.1. All isotopes of Yb, except for ^{172}Yb, have been cooled to quantum degeneracy [101; 102; 103; 104; 105; 106]. This allows us to explore both Bose-Bose and Bose-Fermi mixtures in the quantum degenerate regime, and tune the Yb intraspecies scattering length over a wide range of positive and negative values [130] by switching Yb isotope. The range of Yb isotope masses means the reduced mass of the CsYb molecule is tuneable by $\sim 3\,\%$. As a result, the interspecies scattering properties of the available isotopic combinations of Cs-Yb mixtures are highly tuneable. The interspecies scattering lengths a_{CsYb} are reported in reference [92], and plotted in figure 1.1. It can be seen that across the seven isotopes, there is a wide range of magnitude of scattering

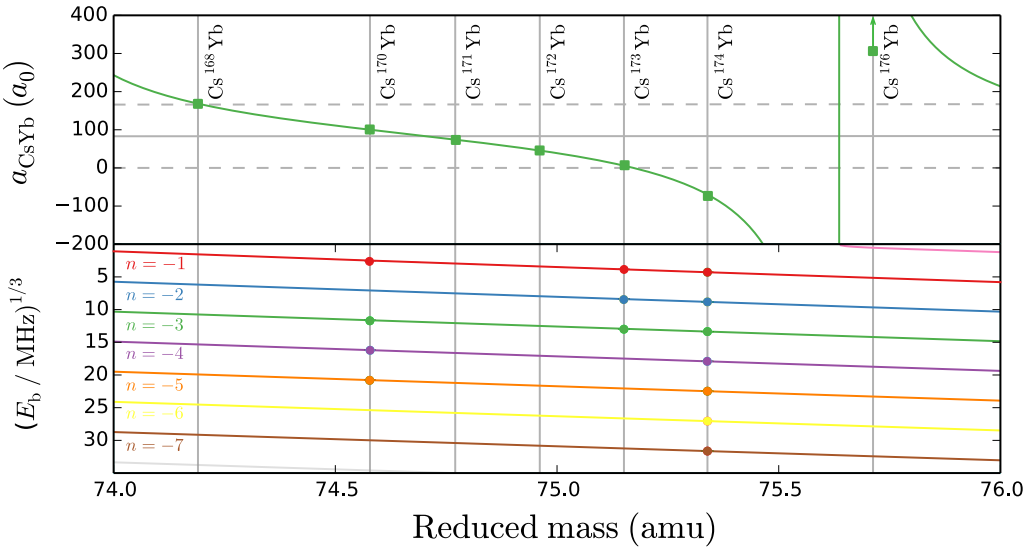

Figure 1.1: **The variation of reduced mass and interspecies scattering length of Cs-Yb mixtures.** Plot from [92] showing interspecies scattering length (upper panel) and binding energy of the Cs-Yb mixture as a function of reduced mass, calculated using the interaction potential fitted to two-photon photoassociation spectroscopy measurements. Points on the lower plot show binding energies measured in the photoassociation experiment. Horizontal lines in the upper plot correspond to $a = 0, \bar{a}$ and $2\bar{a}$, where $\bar{a}$ is the average scattering length of all isotopic combinations.

lengths, as well as one isotope, ^{174}Yb, for which a_{CsYb} is negative. We can thus identify which Cs-Yb mixtures are suitable candidates for sympathetic cooling to dual degeneracy. It also informs us of the strength of the interspecies interactions of the degenerate mixture, and whether they are attractive or repulsive. This gives useful information on how the degenerate mixture can be manipulated and what experiments can potentially be achieved.

The main advantage of working with Cs is its highly tuneable intraspecies scattering properties at low magnetic bias field due to its rich Feshbach structure [131; 132; 133; 134]. The presence of broad, well-understood Feshbach resonances at accessible magnetic fields means that the Cs intraspecies scattering length a_{Cs} can be easily tuned. Of particular experimental interest for fine control of a_{Cs} is the region spanning its zero crossing at 17 G [134]. Here the slope of a_{Cs} with respect to the

magnetic field $\frac{da}{dB}$ is $\sim 65\,a_0\,\mathrm{G}^{-1}$. The $^1S_0$ ground state of Yb has no magnetic moment, and is not affected by tuning a_{Cs} using a magnetic field. The tuneability of a_{Cs}, in combination with the knowledge of the interspecies scattering length a_{CsYb}, can be used to manipulate the balance between intra- and inter-species interactions in degenerate mixtures, and enable a wider range of experiments to be performed.

1.5 Thesis outline

The remainder of this thesis is structured into the following chapters:

- Chapter 2 gives an overview of the experimental apparatus and laser systems used to produce MOTs of Cs and Yb atoms. We also give summaries of the methods which had been used to achieve quantum degeneracy of Cs and Yb in single-species experiments prior to results described in later chapters of the thesis.

- Chapter 3 gives a motivation of using a bichromatic optical dipole trap (BODT) in order to produce dual-degenerate mixtures. We describe a new 532 nm laser setup, and how this is incorporated into the existing dipole trapping apparatus to realise a BODT.

- Chapter 4 describes the experimental routine for producing dual-degenerate mixtures of Cs and Yb using the BODT. We report on the production of dual BECs of both ^{133}Cs+^{174}Yb and ^{133}Cs+^{170}Yb. We describe the initial experiments using these degenerate mixtures, including collective dynamics and dual-species collapse of ^{133}Cs+^{174}Yb, and number-dependent immiscibility of ^{133}Cs+^{170}Yb.

- Chapter 5 describes the setup and characterisation of a tuneable optical lattice, which can be set to 'tune-out' wavelengths where Cs experiences no lattice potential, or wavelengths where Cs and Yb experience the same lattice

potential or trapping frequency. We use the lattice to take preliminary measurements of the polarizability of ground state Cs within the lattice wavelength range around 460 nm.

- Chapter 6 reports on the Feshbach spectroscopy of an ultracold mixture of ^{133}Cs+^{173}Yb, and the observation of two sets of interspecies Feshbach resonances, at 622 G and 702 G, with resolution of the resonances between ^{133}Cs and individual hyperfine sub-states m_F in ^{173}Yb.

- Chapter 7 discusses the possibility of measuring the distribution of m_F states in ultracold gases of the two Fermionic isotopes of Yb by implementation of an optical Stern-Gerlach beam. We also discuss the feasibility of applying optical pumping to these isotopes to modify the spin composition, and the necessary upgrades and alterations to the experimental setup need to implement both experimental techniques.

- Chapter 8 gives a summary of the results reported in the previous chapter of this thesis. We also provide a brief outlook on imminent upgrades to the experimental apparatus and the upcoming research goals we wish to achieve in the experiment.

- There are also four appendices relating to further details on calculations, the apparatus and experimental techniques used in this thesis.

This thesis covers a broad range of topics in atomic and molecular physics. A brief summary of the relevant background theory to each topic is presented at the appropriate points within each chapter. For further details on each topic, the reader is directed to detailed review articles and seminal publications given in reference at the appropriate points within each chapter.

1.6 Contributions of the author

The research presented in this thesis has been made by the author in collaboration with postdoctoral research assistants Alexander Guttridge (AG), Kali Wilson (KEW), and Tobias Franzen (TF), under the supervision of principal investigator Professor Simon Cornish (SLC). The author's contributions to the work in each chapter is as follows:

- In chapter 2, the experimental overview summarises work developed by previous researchers in the laboratory (with relevant references given). The single-species routines as described were developed by AG, KEW, and the author working in collaboration.
- The author designed and implemented the experimental setup described in chapter 3, with the assistance of AG and KEW.
- In chapter 4, the author modelled the evaporative cooling trajectories described, and assisted AG and KEW in taking the experimental data.
- The author designed and implemented the experiment described in chapter 5 with the assistance of KEW. The experimental data was taken and analysed by the author with the assistance of KEW.
- The experiment described in chapter 6 was designed and implemented by KEW, TF, AG, and the author working in collaboration. AG, KEW, TF, and the author have all contributed to taking of the experimental data presented.
- The work presented in chapter 7 is solely that of the author.

1.6.1 Impact of the Covid-19 pandemic

The start of the Covid-19 pandemic occurred within the time period of this PhD. As a result, the author did not have laboratory access between March 2020 and

August 2020 and was unable to conduct experimental research during this time period. Laboratory access was severely restricted due to social distancing measures and restricted work hours for the remainder of the calendar year 2020. The author utilised this time period by performing analysis of the data presented in chapter 5, and by performing the non-experimental research and design work presented in chapter 7.

1.7 Publications

The following publications have resulted from the work presented within this thesis:

- **Quantum degenerate mixtures of Cs and Yb**

  K. E. Wilson, A. Guttridge, J. Segal, and S. L. Cornish

  Phys. Rev. A ***103*** *033306 (2021).*

  The author assisted in designing and implementing the bichromatic trap described, and modelled the evaporative cooling trajectories described. The author assisted in taking the experimental data and helped prepare the manuscript.

- **Dynamics of a degenerate Cs-Yb mixture with attractive interspecies interactions**

  K. E. Wilson, A. Guttridge, I-K. Liu, J. Segal, T. P. Billam, N. G. Parker, N. P. Proukakis, and S. L. Cornish

  Phys. Rev. Research ***3*** *033096 (2021).*

  The author assisted in taking the experimental data and helped prepare the manuscript.

- **Observation of magnetic Feshbach resonances between Cs and ^{173}Yb**

  T. Franzen, A. Guttridge, K. E. Wilson, J. Segal, M. D. Frye, J. M. Hutson, and S. L. Cornish

  Phys. Rev. Research ***4*** *043072 (2022).*

  The author assisted in taking the experimental data and helped prepare the manuscript.

Chapter 2

Experimental setup

The results of this thesis were attained using an experimental setup developed over several years. In this chapter we give a brief summary of the physical apparatus of the experiment, and the laser systems required for initial laser cooling and trapping of Cs and Yb. We also give a summary of the experimental routines previously used to create single-species quantum-degenerate gases. Further detail on the apparatus discussed can be found in previous publications [135; 136; 137] and PhD theses [138; 139; 140] of the experimental group. Further additions and modifications to the setup in order to attain new results will be discussed in later chapters.

2.1 Basic atomic properties

In this section, we introduce the basic properties of the atomic structure of Cs and Yb, relevant to the laser cooling techniques necessary to trap and cool both species in the experiment.

2.1.1 Caesium

Caesium (Cs) is the heaviest stable element of the alkali metals. It has an atomic number of 55 and has a single stable isotope, the bosonic isotope ^{133}Cs. It is solid at

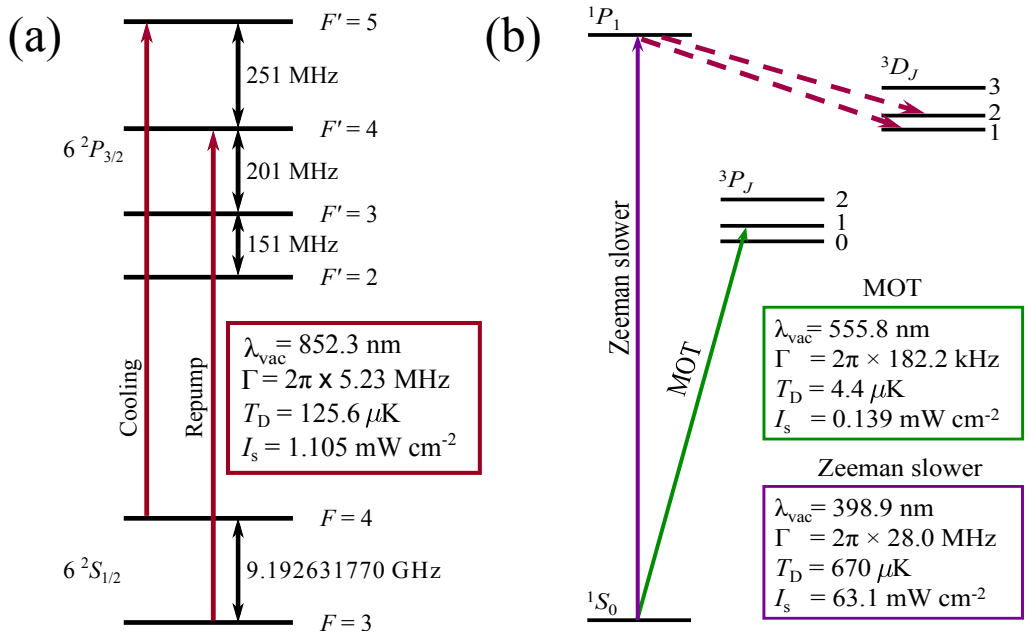

Figure 2.1: **Energy levels used for laser cooling of Cs and Yb.** Figure reproduced from [135]. a) The D2 transition in Cs at 852.3 nm. The hyperfine energy levels of the ground and excited states, F and F', are shown with their relevant splitting values. The main cooling transition is from $F = 4$ to $F' = 5$. The repump transition is from $F = 3$ to $F' = 4$.b) Energy level diagram for Yb. The dominant singlet transition to the $^1P_1$ state is used for the Zeeman slower beam. The narrow intercombination to the $^3P_1$ state is used for the MOT beams.

room temperature, but has a melting point of 28 °C. Its most well-known application in the physical sciences is that of metrology, with the hyperfine splitting of the $6^2S_{1/2}$ ground state of Cs used to define the SI second since 1967 [141]. Similarly to other alkali metal atoms, its atomic structure due to its single valence electron is suitable for laser cooling applications. The first Cs BEC was experimentally realised in 2003 by the group of Rudolf Grimm in Innsbruck [142].

As with the other alkali metals, a characteristic feature of the spectrum of Cs is the D1 and D2 lines from the ground state $ns_{1/2}$ to excited states $np_{1/2}$ and $np_{3/2}$. All of our laser cooling of Cs in the experiment utilises the transition of the D2 line, from $6^2S_{1/2}$ to $6^2P_{3/2}$, at 852.3 nm. The relevant energy levels of this transition are shown in figure 2.1a. The transition has a linewidth of $2\pi \times 5.23$ MHz and a doppler temperature of 125.6 µK. We must also consider the effect of hyperfine structure in

Cs, due to its nuclear spin $I = 7/2$. The coupling of the nuclear spin to the total angular momentum J gives two hyperfine spin states in the ground state manifold, $F = 3$ and $F = 4$, and four in the excited state manifold, $F = 2$, $F = 3$, $F = 4$, and $F = 5$. Section 2.3.1 describes in detail the choice of the available hyperfine transitions which are used for effective cooling and trapping of Cs.

2.1.2 Ytterbium

Ytterbium (Yb) is a rare earth metal and a lanthanide element, with an atomic number of 70. As discussed in chapter 1, there are seven stable isotopes of Yb, including five bosonic isotopes and two fermionic isotopes. It has two valence electrons, and hence a closed outer valence shell. Its atomic structure therefore resembles that of an alkaline-earth atom such as strontium or calcium. All isotopes of Yb, except for ^{172}Yb, which possesses a large negative scattering length, were first cooled to quantum degeneracy by the group of Yoshiro Takahashi in Kyoto [101; 102; 103; 104; 105; 106].

Figure 2.1b shows the relevant energy level structure of Yb. In contrast to Cs, due to its closed-shell structure, the ground state of Yb has electron spin $S = 0$ and hence $J = 0$. There is therefore no hyperfine splitting in the ground state. The two transitions used in our experiment are the singlet transition from $^1S_0$ to $^1P_1$ at 398.9 nm, and the intercombination transition from $^1S_0$ to $^3P_1$ at 555.8 nm. We use the singlet transition for our Zeeman slower due to its linewidth of $2\pi \times 28.0$ MHz, making it suitable for slowing of an atomic beam with an initially wide velocity distribution. However, the doppler temperature of 670 µK limits the transition's efficacy for use in the MOT. We therefore use the intercombination transition for the Yb MOT. This transition has a linewidth of $2\pi \times 182.2$ kHz and a doppler temperature of 4.4 µK. This allows the realisation of Yb MOTs of a low enough temperature to be able to directly load Yb atoms from the MOT to an optical dipole trap.

2.2 Overview of main apparatus

The main apparatus in our lab consists of a vacuum chamber we refer to as the 'science chamber', designed with provision for optical access and generation of magnetic fields. It is in this chamber that Cs and Yb is trapped and cooled to conduct all experiments. Cs and Yb atoms enter the science chamber in atomic beams generated by a dual-species oven. Between the oven and the science chamber, the beam propagates through a spectroscopy section followed by a dual-species Zeeman slower. This slower reduces the atoms' velocity in the beams in order for them to be trapped by a magneto-optical trap (MOT) for each species, upon entering the main chamber. The entire vacuum apparatus is kept under vacuum by three dedicated ion pumps (Agilent, VacIon55), one each for the science chamber and ovens, and a third in the spectroscopy section. Schematic drawings of this full vacuum apparatus is shown in figure 2.2.

2.2.1 Dual-species oven

The high vapour pressure of alkali metals such as Cs often allow experimental groups working with such atomic species to directly load 2- or 3-dimensional MOTs from an atomic vapour. Cs, for example, has a vapour pressure of 7×10^{-7} torr at room temperature [143]. However, the vapour pressure of Yb is 3×10^{-21} torr at room temperature [144]. Creating an Yb MOT therefore requires loading from a Zeeman-slowed atomic beam. We therefore use a dual-species oven as our starting point to generate hot atomic beams of Cs and Yb. The oven is at the opposite end of the vacuum apparatus to the science chamber, and comprises section A of the schematics in figure 2.2. A more detailed view of the oven is shown in figure 2.3.

The oven is under vacuum conditions during running of the experiment, but must be opened up to atmosphere to load samples of Cs and Yb into their respective reservoirs. Replenishment of the reservoirs must be undertaken every 3–5 years of

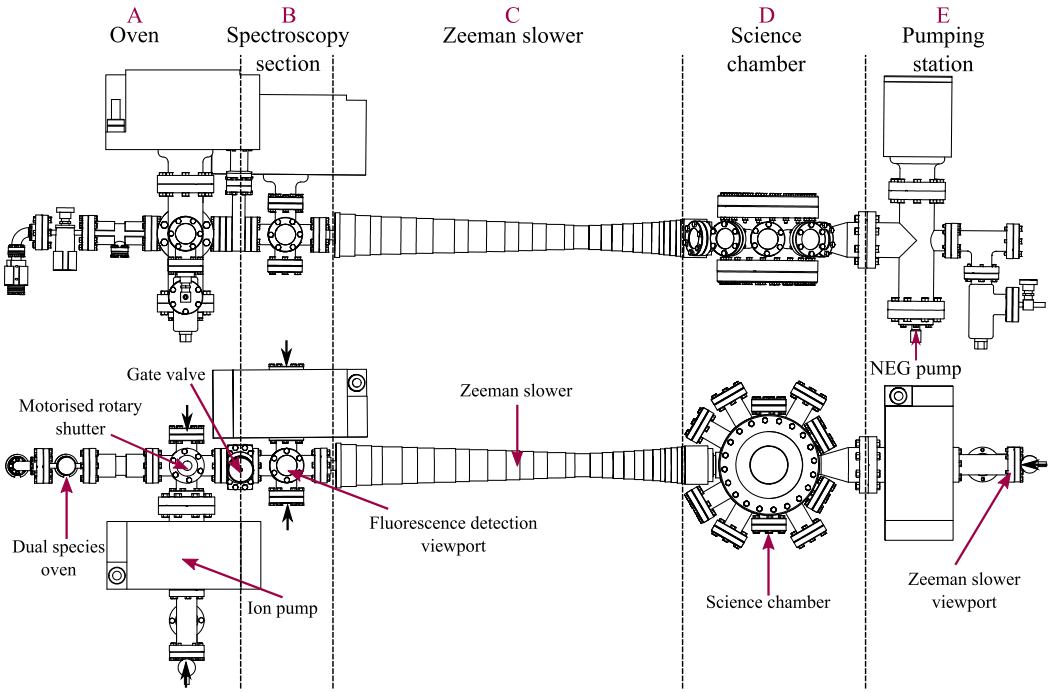

Figure 2.2: **Main vacuum system of the experiment.** Figure reproduced from [135]. Schematic drawings of the vacuum system from a side view (upper) and top-down view (lower). Dashed lines split the apparatus into the regions labelled A–E, as described in the text.

ordinary running of the experiment. A 5 g ingot of Yb is loaded directly into the Yb reservoir, whereas a glass ampoule of Cs is loaded into the Cs reservoir. The flexible bellows of the reservoir allows this ampoule to be broken once the oven apparatus has been pumped back down to vacuum. A Swagelock valve can be used to seal off the Cs reservoir from the rest of the oven when not in use.

Once heated in their respective reservoirs, the hot atoms are directed through two separate semicircular channels, the ends of which are incident on a section of 55 capillary tubes arranged in a triangular array, shown in detail in figure 2.3c. The capillaries ensure the atomic beams are collimated as they are directed through the Zeeman slower to the science chamber. We heat the oven with a series of four band heaters (Watlow, MB1J1JN2-X66). These are configured such that there is a heat gradient through the oven, with the Cs reservoir the coolest section to the hottest section at the capillaries. This ensures that the sources of Cs and Yb

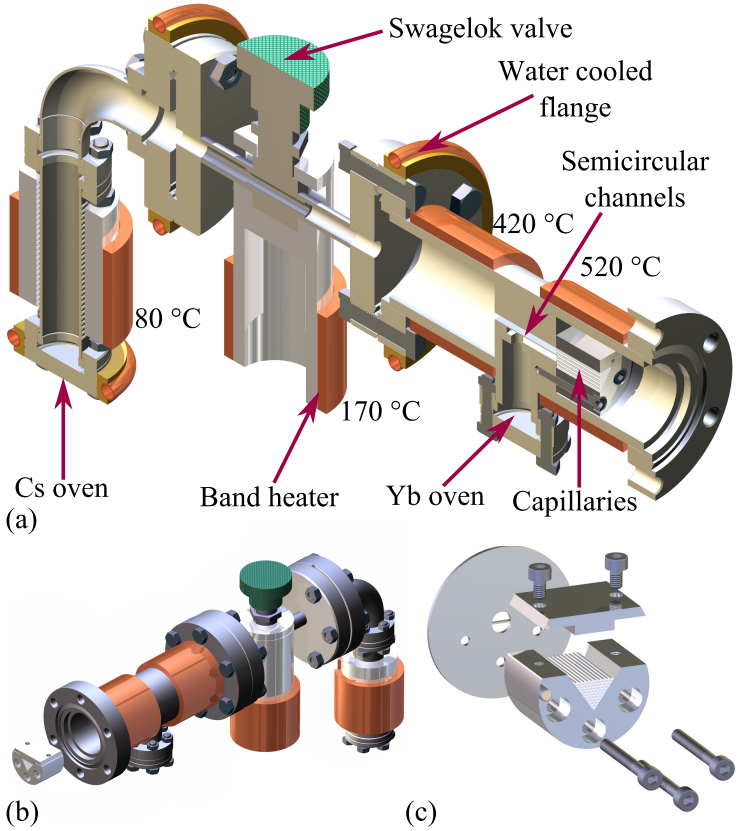

Figure 2.3: **The dual-species oven for Cs and Yb.** Figure reproduced from [135]. a) A cutaway schematic of the oven, showing the paths of the two species through the oven. The temperatures displayed are the band heater set points. b) Rendering of the oven, with the capillary clamp shown outside the oven for detail. c) Exploded view of the capillary array, and the semicircular channels that the array is clamped over within the oven.

do not migrate from their reservoirs, and that atoms do not stick to the interior walls of the capillaries as they travel through them, potentially blocking the atomic beams. We typically run the experiment with the following temperature settings on the band heaters: Cs reservoir 80 °C, Cs valve 170 °C, 'middle' section 420 °C, and 'Yb' section 520 °C. The Yb reservoir is located between the latter of these two, ensuring the highest possible vapour pressure of Yb. With the temperature settings described above, the temperature of the Yb reservoir is typically measured to be $\sim$ 485 °C. To increase the atomic beam signal of Yb isotopes which are less abundant in our Yb sample, these temperature of these heaters can be increased by up to $\sim$ 475 °C and $\sim$ 550 °C respectively. A chilled water supply to water cooled

flanges located near the band heaters prevents thermal damage.

The collimated atomic beams then propagate through a motorised rotary shutter. This intersects the atomic beam with two channels crossed at 90°. From the experimental control, the shutter can be rotated in 45° increments to either allow or block passage of the atomic beam. In a typical experimental sequence, the shutter is opened in this way to allow Zeeman slowing and MOT loading, before being closed once a sufficient atom number has been loaded into the MOT. After this shutter, the beams pass through a gate valve. This can be used to separate the oven from the rest of the vacuum apparatus. It is usually kept closed when the experiment is not in operation.

2.2.2 Zeeman slower

Between the gate valve and the Zeeman slower, a transverse spectroscopy section allows optical access for spectroscopy of the atomic beam. This is shown in section B of figure 2.2. This can provide information on whether the flux of both atoms is sufficient for successful loading of MOTs in the main chamber.

The atoms then propagate through the Zeeman slower, shown in section B of figure 2.2. The Zeeman slower in this experiment [136] has been designed to provide the necessary Zeeman shift for either Cs or Yb. It consists of a 77 cm long DN16 tube. Along the length of tube are wound five sets of coils. The main field profile of the Zeeman slower is generated by two coils, with an increasing field profile from negative fields at the oven end to positive fields at the science chamber end. This allows large detunings to be used for the Zeeman slower beams. This is particularly important in the case of Yb. If low detunings are used, light resonant to the $^1S_0 \rightarrow {}^1P_1$ transition used for the Zeeman slower could cause a pushing force on the Yb MOT. The MOT operates on the comparatively weaker $^1S_0 \rightarrow {}^3P_1$ transition. Two smaller, high-current coils at the science chamber end of the Zeeman slower produce a large end field and a sharp field drop-off before atoms enter the science

chamber. A solenoid coil running the length of the slower provides a field offset to match the Zeeman slower laser detuning. In order to load an Yb MOT on the $^1S_0 \rightarrow {}^3P_1$ transition, atoms must enter the capture region of the MOT with a velocity of less than $7\,\mathrm{ms}^{-1}$. This poses a significant constraint of the Zeeman slower design, as the end of the Zeeman slower must be close enough to the MOT capture region to prevent the slowly-moving atoms from falling too far under gravity to be captured by the MOT. The distance between the exit of the Zeeman slower and the MOT capture region is 7.5 cm. This ensures that both the slowed atoms are able to reach the MOT capture region, and that the field magnitude from the Zeeman slower coils is negligible at the MOT capture region.

2.2.3 Science chamber

The science chamber is shown in section D of figure 2.2. It has five pairs of viewports in the horizontal plane of the atomic beam, as well as a viewport in the Zeeman slower axis and opposite to the Zeeman slower. There are also viewports above and below the centre of the chamber to allow vertical access. The beams which access the science chamber include:

- Cs and Yb Zeeman slower beams
- Cs MOT beams (three beams, each retroreflected)
- Yb MOT beams (three beams, each retroreflected)
- Cs and Yb imaging beams
- Cs degenerate Raman sideband cooling (DRSC) beams (two horizontal, one of which is retroreflected; two vertical)
- Dipole trapping beams (two 1070 nm 'reservoir' beams, two 1070 nm 'dimple' beams, one 532 nm 'dimple' beam)
- Tuneable lattice beam

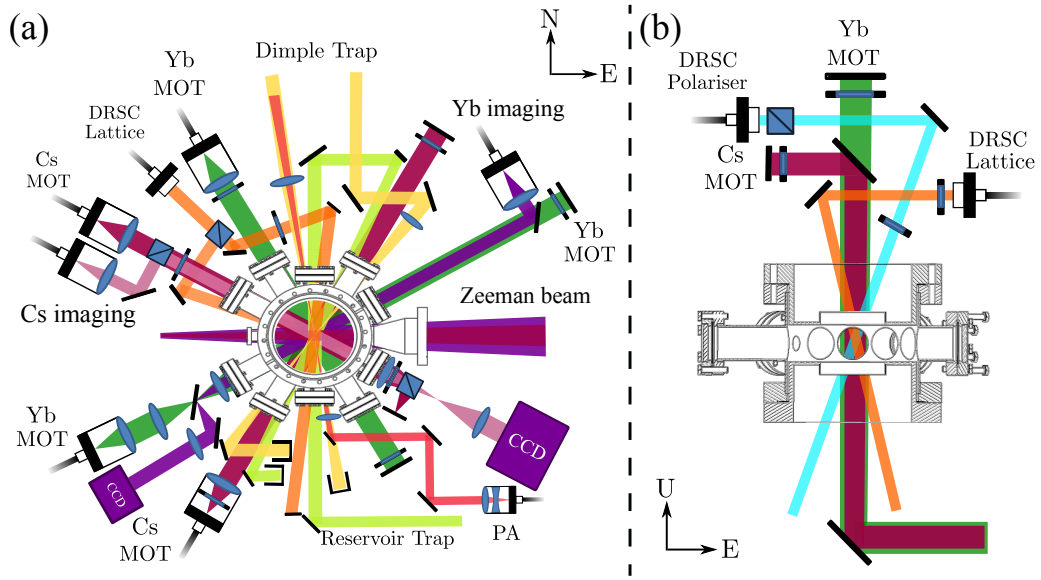

Figure 2.4: **Schematic of beams and optics around the science chamber.** a) Beams and optics in the horizontal plane. b) Beams and optics in the vertical plane. For clarity, the MOT and Bias coils are not shown.

The various viewport pairs have a variety of antireflection coatings, allowing efficient transmission of light of the wide range of wavelengths used in the experiment. A full schematic of the beams and optics surrounding the science chamber is given in figure 2.4. We define a cartesian coordinate system to describe the geometry of the chamber based on its approximate geographical alignment, with the 'East-West' axis in the horizontal plane parallel to the atomic beam and Zeeman slower, the 'North-South' axis in the horizontal plane perpendicular to the East-West axis, and the vertical 'Top-Bottom' axis. The pumping apparatus that maintains the vacuum in the science chamber is at the far end of the vacuum apparatus, and is shown in section E of figure 2.2.

2.2.4 Magnetic field generation coils

A series of coils to generate fields and field gradients within the science chamber are used. Two pairs of coils, the 'MOT' and 'bias coils' are aligned above and below the chamber in the vertical axis. The larger of these two pairs is the MOT

coils, designed to provide field gradients, and quadrupole fields for magneto-optical trapping, and consist of 16 turns of wire per coil. The bias coils provide a constant magnetic bias field, and consist of four turns of wire per coil. These coils are both further discussed in chapter 6. We also use three pairs of 'shim' coils, one each in the East-West, North-South and Top-Bottom axes. These generate small (up to 5 G) field gradients in each experimental axis in order to fine-tune the field minimum of the quadrupole field of the MOT coils. This assists in the MOT loading of each species. The MOT and bias coils, as well as the Zeeman slower coils, are constructed of hollow-core wire. A chilled water supply is pumped through the hollow core of each of these, as well as to a heat sink for the MOSFETs controlling current flow through the coils, to prevent overheating.

2.3 Laser cooling systems

The following section is a brief overview of the laser systems required for trapping, cooling, and absorption imaging of both species. The apparatus described below is situated on our spectroscopy laser table adjacent to the laser table on which the science chamber is located. Light for the various applications described below is transferred from this table to the main table using optical fibers.

2.3.1 Cs laser cooling systems

Our main cooling transition for Cs is the $F = 4 \rightarrow F' = 5$ transition on the D2 line. Our primary laser light source for this transition is a Toptica DL100 Pro diode laser. The laser is operated with a power output of 100 mW. It is stabilised to a detuning of -385.4 MHz from the $F = 4 \rightarrow F' = 5$ transition. The output of the laser is split into three components, for frequency stabilisation, absorption imaging, and a tapered amplifier (TA) seed. The component for frequency stabilisation is double-passed through an acousto-optical modulator (AOM) (AOM 2 in figure 2.5), which generates the required frequency difference to resonance. The beam then passes

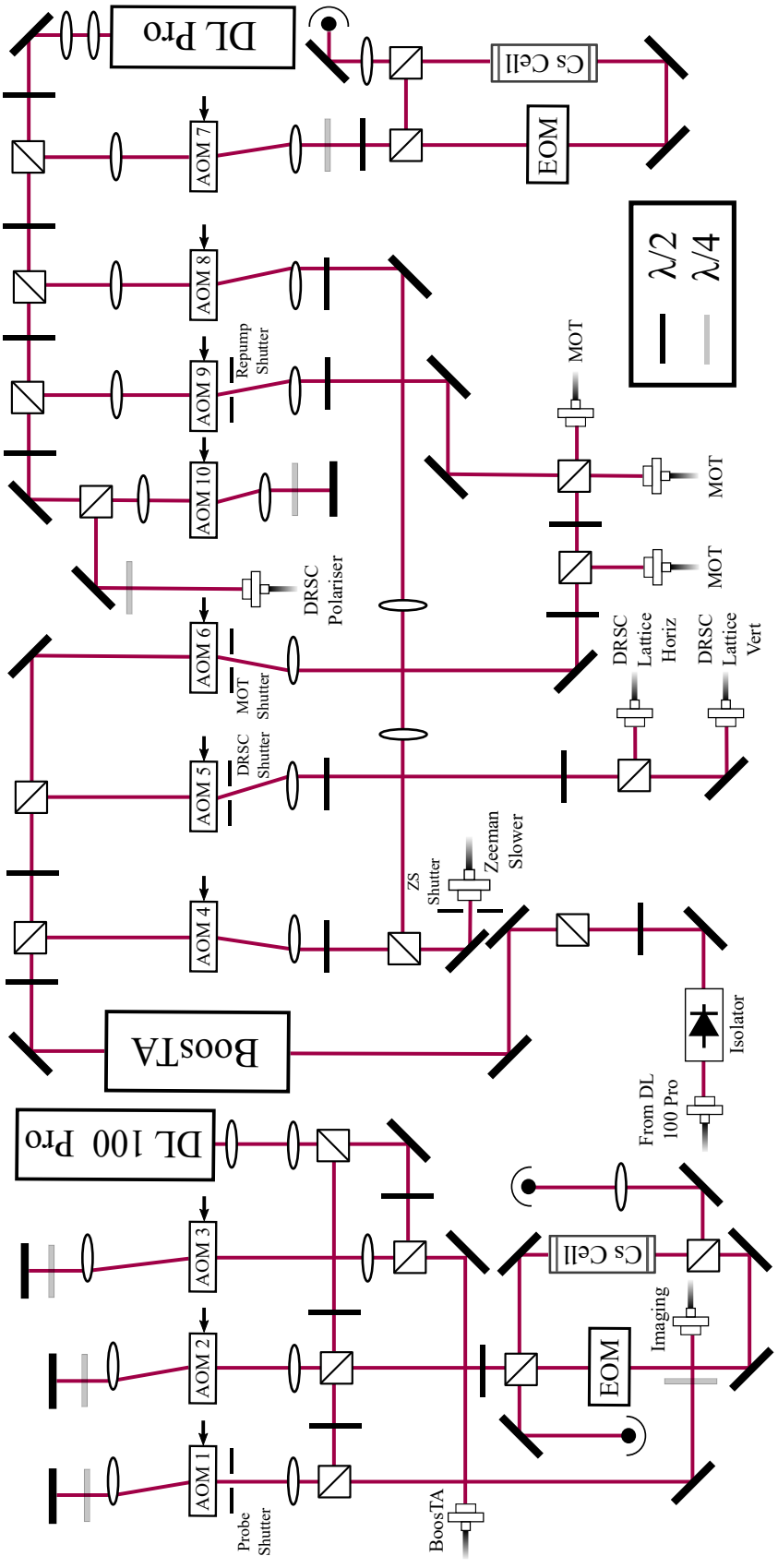

Figure 2.5: **Optical setup for Cs laser cooling systems.** Cooling light close to the $F = 4 \rightarrow F' = 5$ transition is produced by the Toptica DL 100 pro diode laser and amplified by the Toptica BoosTA tapered amplifier, both on the left of the figure. Repump light close to the $F = 4 \rightarrow F' = 4$ transition is produced by the Toptica DL pro diode laser on the right of the figure.

through a Cs vapour cell and an electro-optic modulator (EOM), where modulation transfer spectroscopy [145; 146] is used to generate the error signal for frequency stabilisation. The component for absorption imaging is double-passed through a separate AOM (AOM 1 in figure 2.5) and then coupled into an optical fiber to the main experimental table. The remaining majority of the laser output is double-passed through an AOM (AOM 3 in figure 2.5). It is then fiber coupled to the input of a tapered amplifier (TA) TA (Toptica BOOSTA). The full output power of the TA is 460 mW. This is redistributed to provide power for the three MOT beams, Zeeman slower beam, and DRSC lattice beams (see section 2.4). A series of AOMs provide the frequency shift for each of these applications to provide the correct detuning.

When using this transition, there is a probability of the Cs atom being off-resonantly excited to $F' = 4$ in the excited state manifold. From there it can decay to $F = 3$ in the ground state. This state is not addressed by the main cooling transition and is therefore a dark state. Atoms transferred to this state will not be further cooled by the transition and may be lost from a MOT. In this way the number of atoms in a MOT may be depleted. We therefore use the $F = 3 \rightarrow F' = 4$ transition as a repump transition, cycling atoms back to $F = 4$ in the ground state and hence the main cooling transition.

Our light source for this transition is a diode laser (Toptica DL 100 pro). The laser is operated with a power output of 100 mW. The output is detuned by +80 MHz from the $F = 3 \rightarrow F' = 4$ transition. The frequency output of this laser is stabilised to the $F = 3 \rightarrow F' = 4$ transition using frequency modulation spectroscopy [147; 148], by first single-passing a component of the output through an AOM (AOM 7 in figure 2.5) to make up the difference of frequency detuning, and then by transmission through a Cs vapour cell and an electro-optic modulator (EOM). The remaining laser output power is distributed between beams for the MOT (one of the three MOT axes only), Zeeman slower, and the DRSC polariser beam (see section 2.4). Similarly to the cooling beam, a series of AOMs provide the frequency shift for

Application	Transition	Detuning (MHz)	AOM number
Cooling primary laser output	$F = 4 \rightarrow F' = 5$	-385.4	
Imaging	$F = 4 \rightarrow F' = 5$	+1.2	1
Cooling spectroscopy	$F = 4 \rightarrow F' = 5$	0.0	2
BoosTA input	$F = 4 \rightarrow F' = 5$	-132.0	3
Zeeman slower Cooling	$F = 4 \rightarrow F' = 5$	-49.4	3 + 4
MOT cooling	$F = 4 \rightarrow F' = 5$	-9.0	3 + 6
DRSC lattice	$F = 4 \rightarrow F' = 4$	0.0	3 + 5
Repump laser output	$F = 3 \rightarrow F' = 4$	+80.0	
Repump spectroscopy	$F = 3 \rightarrow F' = 4$	0.0	7
Zeeman slower repump	$F = 3 \rightarrow F' = 4$	-32.5	8
MOT repump	$F = 3 \rightarrow F' = 4$	-5.4	9
DRSC polariser	$F = 3 \rightarrow F' = 2$	+10	10

Table 2.1: The application of each Cs cooling laser beam, with the detuning from the relevant transition, and the AOM or AOMs used to generate the necessary detuning. Beams derived from the primary cooling laser are in the upper section of the table. Beams derived from the repump laser are in the lower section of the table.

each of these applications to provide the correct detuning. The MOT and Zeeman slower repump beams are coupled into the same optical fibers as their counterparts on the cooling transition.

Figure 2.5 shows the full optical layout of both the cooling and repump laser systems. Each AOM controlling light for an application on the main experimental table can be digitally controlled from the experimental control. Beam shutters, also digitally controlled from the experimental control, are also used in these beam paths before the optical fiber inputs. This ensures light for each application only reaches the experiment when required during an experimental routine. Table 2.1 summarises the application of each cooling beam from both laser systems, the detuning from the relevant transition of each application, and the combination of AOMs used to provide the necessary detuning.

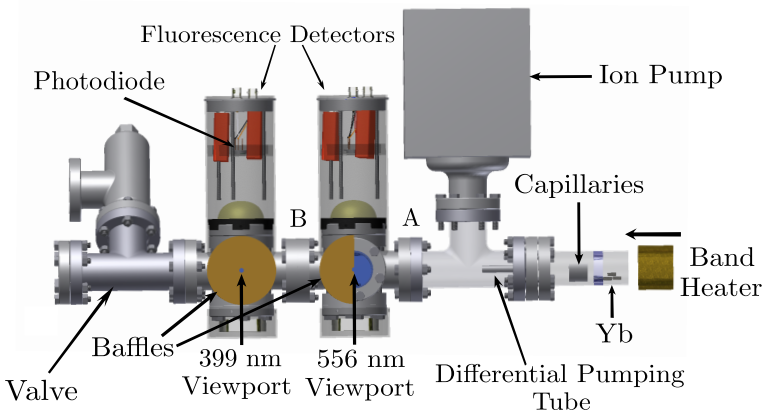

Figure 2.6: **The Yb 'beam machine' atomic beam spectroscopy apparatus.** An Yb oven produces an atomic beam, which travels from right to left. The beam is collimated by an array of capillary tubes and passes through a differential pumping tube and two further circular apertures A and B. Optical access is provided through the horizontal viewports of two six-way crosses. Atomic fluorescence is detected in the vertical direction by two photodiode assemblies.

2.3.2 Yb beam machine

The vapour pressure of Cs at room temperature allows the use of standard vapour cells in the frequency stabilisation systems for both Cs transitions. However, this option is not available for Yb. We instead use an atomic beam of Yb as a frequency reference for the two cooling transitions used for this element. This beam is provided by the 'beam machine' vacuum apparatus, shown in figure 2.6. A reservoir of Yb is heated by a single band heater (Watlow, MB1J1JN2-X73), and collimated into a beam using an identical array of capillary tubes as those used in the main atomic ovens. The heater is normally run at 475°C, although this can be increased to improve the atomic beam flux for less abundant Yb isotopes. A chilled water supply to a water-cooled flange located near the band heater prevents thermal damage. Vacuum is maintained inside the apparatus using an ion pump (Agilent, VacIon55).

Laser light for each transition is stabilised to the atomic beam using fluorescence spectroscopy. Two transverse viewports allow beams of light for each transition

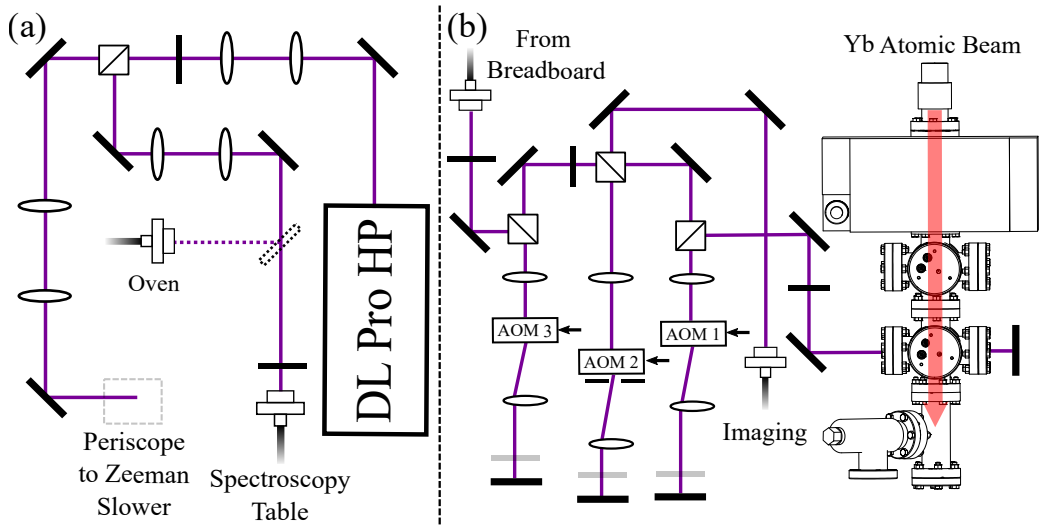

Figure 2.7: **Optical layout of the 399 nm laser system.** a) Optical setup on the breadboard above the Zeeman slower viewport (right-hand end of figure 2.2. The majority of the optical power is directed down the periscope to the Zeeman slower. The input to the fiber to the spectroscopy table can alternatively be used to measure the Yb atomic beam flux from the oven using the transverse spectroscopy section. b) Optical setup on the laser table. The light is double-passed through a series of AOMs to provide the necessary detunings for fluorescence spectroscopy and absorption imaging.

to intersect the beam at a 90° angle. A photodiode in a vertical cylinder is positioned above each crossing point. Resonant light emitted upwards by atoms in the beam are focused by a collection lens onto the photodiode. Light which is re-emitted downwards is reflected by a mirror at the bottom of the cylinder onto the collection lens, improving the photodiode signal. The fluorescence signals for each transition are modulated and fed back into each laser's locking system, where it is demodulated to give a dispersive error signal, to which the frequency of the lasers can be stabilised. The accessible frequency range for both lasers cover the relevant transitions for all Yb isotopes [139].

2.3.3 Yb Zeeman slower laser system

Figure 2.7 shows the optical layout of the laser system for the Zeeman slower beam and for absorption imaging. The 399 nm light source is a diode laser (Toptica DL

pro HP). The power output is 100 mW. Due to the poor fiber coupling efficiency typically found with light in the near-UV frequency range, this is the only cooling laser positioned on the same table as the science chamber. It is positioned on a breadboard above the Zeeman slower viewport, at the opposite end of the vacuum apparatus to the atomic ovens. The majority of the laser output (75 mW) is directed into the Zeeman slower using a periscope to bring the beam down from the breadboard to the horizontal plane of the science chamber. A smaller (25 mW) portion of the light is fiber coupled to the beam machine for frequency stabilisation. Due to the large (~ -600 MHz) detuning required for the Zeeman slower beam, this portion of the beam is double-passed through a 200 MHz AOM (AOM 3 in figure 2.7), before being split into two beams, for fluorescence spectroscopy and imaging. Both of these beams are double-passed through 100 MHz AOMs (AOMs 1 and 2 in figure 2.7), before being directed to the beam machine and optical fiber for the imaging beam respectively. The detuning of the imaging beam is set by the frequency difference between the two 100 MHz AOMs.

2.3.4 Yb MOT laser system

Figure 2.8 shows the optical layout for the 556 nm Yb MOT beam. We use the 450 mW output of an 1111.6 nm fiber laser (Menlo Orange One), fiber coupled to a single harmonic generation (SHG) module from NTT photonics for frequency doubling. This gives a 200 mW output of 556 nm light. This light is split into two beams, one for the three MOT beam axes and one for frequency stabilisation. They are then both single-passed through 200 MHz AOMs (AOMs 1 and 2 in figure 2.8). The frequency stabilisation beam is then directed to the beam machine. The beam for the MOT is distributed into three beams for each axis of the MOT, before being fiber coupled to the main table of the experiment.

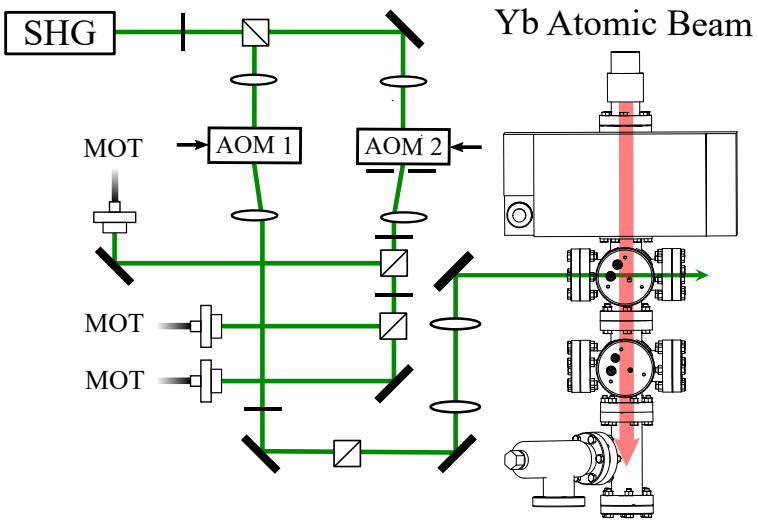

Figure 2.8: **Optical layout of the 556 nm laser system.** The output of the SHG module is split into two branches, one for fluorescence spectroscopy, and one for the MOT beams. Each of these branches is single-passed through an AOM. The MOT beam is then split into three further branches, each of which is fiber coupled to the main experimental table.

2.3.5 Absorption imaging

Following the end of each experimental sequence, we use absorption imaging after time of flight (ToF) to measure the atom number in each atom cloud and determine other physical quantities (for more detail see appendix D). For both Cs and Yb we use a pulse of resonant light to perform absorption imaging. For Cs this is resonant to the main $F = 4 \rightarrow F' = 5$ transition. The imaging beam has a power of 200 µW and is incident on the Cs atoms through one of the horizontal Cs MOT beam axes. Following propagation through the science chamber, the beam is incident on a camera (Andor iXon 885) which takes the absorption images. For Yb this is resonant to the ${}^1S_0 \rightarrow {}^1P_1$ transition. The imaging beam has a power of 25 µW and is incident on the Yb atoms through one of the horizontal Yb MOT beam axes. Following propagation through the science chamber, the beam is incident on a camera (Andor Luca) which takes the absorption images.

2.4 Cooling Cs to quantum degeneracy

The doppler cooling limit of 125 µK in the Cs MOT is insufficient for effectively loading Cs atoms into a dipole trap. We must also carefully manage the temperature and density of the Cs. This is to avoid loss due to inelastic collisions, in particular, due to three-body recombination [149]. The Cs three-body loss rate is $K_3 \sim 1 \times 10^{-27}\,\mathrm{cm}^6/\mathrm{s}$ [150; 90]. (see chapter 4). We therefore employ intermediate cooling methods prior to dipole trapping in order to create ultracold Cs gases. Our approach follows the method developed in the Innsbruck group [142; 151].

Following accumulation of Cs atoms in the MOT, we turn off the Zeeman slower coils and light, and perform a compressed MOT stage by increasing the quadrupole field gradient and the MOT detuning. We then use the shim coils to move the Cs atoms to the correct location for the following cooling stages. We then perform sub-doppler cooling by turning off the quadrupole gradient and increasing the MOT detuning. We then perform 25 ms of cooling in the optical molasses, which cools the Cs atoms to 20 µK.

We then apply the method of degenerate Raman sideband cooling (DRSC). Two horizontal beams (one retroreflected) and one vertical beam of linearly polarised light resonant with the $F = 4 \rightarrow F' = 4$ transition form a Raman lattice. The Cs atoms are initially in the $|F = 3, m_\mathrm{F} = +3\rangle$ state and occupy a high vibrational level ν of this lattice. A small magnetic field is applied which shifts the magnetic sublevels m_F. This makes the states $|F = 3, m_\mathrm{F} = +1, \nu - 2\rangle$,$|F = 3, m_\mathrm{F} = +2, \nu - 1\rangle$ and $|F = 3, m_\mathrm{F} = +3, \nu\rangle$ degenerate. The lattice beams induce coupling between these states via two-photon Raman transitions. A polariser beam blue detuned from the $F = 3 \rightarrow F' = 2$ transition of the Cs cooling transition is also incident on the atoms. This beam is circularly polarised and optically pumps the atoms from $m_\mathrm{F} = 1$ to $m_\mathrm{F} = 3$. The transition, however, conserves the vibrational level ν, so for every cycle of cooling, a Cs atom loses two quanta of vibrational energy. By aligning the polariser beam with a small angle to the magnetic field, it

has a small linearly polarised component. This is used to pump atoms out of the $|F = 3, m_F = +2, \nu = 0\rangle$ state, where atoms cannot access the $m_F = 3$ state and be pumped by the circularly polarised component. This ensures that the Cs atoms are not only cooled to the lowest vibrational level of the Raman lattice, but are also polarised in the $|F = 3, m_F = +3\rangle$ at the end of DRSC. Further detail of the implementation of DRSC in the experiment is given in [140].

After DRSC the Cs atoms are transferred to our 'reservoir' trap. This consists of two 1070 nm beams crossed at an angle of 25 °, with beam waists of 640(20) µm and 440(10) µm respectively. Light for the beams is provided by a 50 W IPG laser. The reservoir is loaded using a power of 20 W in both beams. A magnetic field gradient of 31.3 G cm^{-1} is used to levitate the atoms in this trap. A bias field of 70 G is also applied to counteract the effect of antitrapping in the axial direction of the trap due to the levitation gradient.

2.4.1 Dimple trap

To load Cs atoms into a smaller-volume dipole trap suitable for evaporative cooling, we perform the 'dimple trick' [152; 153; 154; 151] first demonstrated in the Innsbruck experiment. The principle of the dimple trick is shown in figure 2.9. A crossed optical dipole trap is overlaid with the reservoir trap. Prior to the development of the bichromatic trap discussed in chapter 3, this consisted of two 1070 nm beams, referred to as dimple beam 1 (DB1) and dimple beam 2 (DB2), crossed at a 40° angle. Light for the beams is provided by a 100 W IPG laser. In practice, the laser is operated to give the beams a maximum combined power of 55 W in the dimple, distributed between up to 44 W in DB1 and up to 11 W in DB2. Power control and stabilisation for both beams is provided using a pair of AOMs in a feedback loop (see section 3.3.2). DB1 has a beam waist of 29(2) µm in the horizontal axis and 35(3) µm in the vertical axis. We can also modify DB1's horizontal waist by dithering the frequency of DB1's intensity stabilisation AOM, as the optical path between the AOM and the science chamber is in free space.

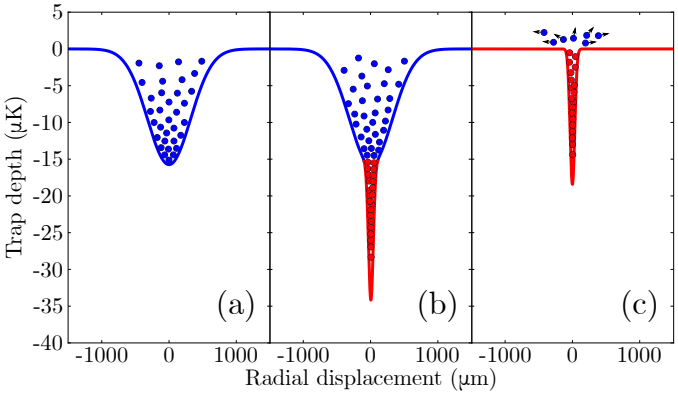

Figure 2.9: **The 'dimple trick' used in creation of ultracold Cs gases.** a) Cs atoms are initially confined in the wide and shallow potential of the reservoir trap (blue). b) The dimple trap (red) is now overlapped with the reservoir. Atoms can be cooled to the deep minimum of the dimple potential through elastic collisions with atoms in the reservoir potential. c) When the reservoir trap is turned off, evaporation of the atoms in the reservoir occurs, leaving a dense sample of atoms confined in the dimple.

This causes atoms in DB1 to experience an approximately Gaussian time averaged potential. This also allows us to modify the trap frequencies in the beam [155]. The technique of a dithered trapping beam has also been used in similar experiments [32; 156; 157; 158]. DB2 has a symmetrical beam waist of 70(4) μm.

During the time period the reservoir and dimple beams are overlapped, Cs atoms in the reservoir are able to access the much tighter and deeper potential of the dimple. However, as they are cooled through collisions with the bath of reservoir atoms, they experience negligible heating despite the increased density in the dimple. The reservoir trap is then turned off by extinguishing the reservoir beams and turning off the magnetic gradient and bias field. This causes loss of the Cs atoms remaining in the reservoir, but a cold gas of Cs atoms remains in the dimple.

2.4.2 Single-species experimental routine

We typically accumulate 3×10^8 Cs atoms in the MOT after a 6 s load. We then use optical molasses followed by DRSC. This further cools approximately 6×10^7 Cs atoms to $T_{\mathrm{Cs}} \sim 2\,\mu\mathrm{K}$. In the process of DRSC, these atoms are optically pumped to

the $|F = 3, m_F = +3\rangle$ hyperfine state. We then load approximately 2.5×10^7 atoms into the reservoir, reducing to 4×10^6 atoms at 1.5 µK after 2 s of plain evaporation. Approximately 10 % of the atoms trapped in the reservoir are then loaded into the dimple. The total initial power in the dimple is 280 mW. The corresponding initial trap depth is 20 µK. We then perform forced evaporation by reducing the dimple beams' power to ~ 20 mW. During the evaporation, Cs crosses the BEC transition at ~ 60 nK. A bias field of 22.3 G is used throughout the evaporation. This ensures the Cs intraspecies scattering length remains close in value to the Efimov minimum in the three-body recombination rate [150]. This optimises the ratio of elastic to inelastic collisions [149]. At the end of evaporation, we typically produce pure Cs BECs of up to 5×10^4 atoms in the $|F = 3, m_F = +3\rangle$ hyperfine state.

2.5 Cooling Yb to quantum degeneracy

In contrast to Cs, the low Doppler cooling limit allows us to directly load Yb from the MOT into a dipole trap without the need for intermediate cooling routines. Here we give a brief summary of the experimental sequence for cooling ^{174}Yb as an example. We load $\sim 2 \times 10^7$ atoms from the MOT a crossed dimple trap. This trap uses the same dimple beams as for cooling of Cs, although DB1 is dithered, resulting in a dimple with a horizontal waist of 72(4) µm and a vertical waist of 35(3) µm. The dimple has an initial total power of 55 W. The corresponding initial trap depth is 950 µK. We then perform forced evaporative cooling to degeneracy by reducing the power in the dimple to ~ 400 mW. An approximately exponential ramp of the beam powers is used in the evaporation. Evaporation of ^{174}Yb is particularly fast and efficient. The three-body loss rate is low due to a favourable scattering length $a_{\mathrm{Yb}} = 105\, a_0$, allowing high density and high collision rates in the dimple throughout evaporation. During evaporation, we cross the BEC phase transition, with the critical temperature in our system approximately 350 nK. At the end of evaporation, we typically produce pure ^{174}Yb BECs of up to 4×10^5

atoms. Beyond the example of ^{174}Yb given here, the experimental setup has also been used to create BECs of ^{170}Yb, and a degenerate Fermi gas of ^{173}Yb. The other isotopes have not to date been cooled to quantum degeneracy in our setup. This is due to either low natural abundance of the isotope causing impractical load times and challenges to transition frequency stabilisation, or due to the intraspecies scattering length being unfavourable for evaporative cooling or creation of a stable condensate.

Chapter 3

Development of a bichromatic optical dipole trap

The experimental setup developed as described in chapter 2 has been successful in conducting single-species experiments of either Cs or Yb, with quantum degeneracy in both species previously reported. Dual-species experiments with thermal samples of both species have also been achieved. However, the apparatus cannot be used to produce dual-species samples with low enough temperatures and high enough phase-space density to reach dual quantum degeneracy. This chapter describes the existing dipole trapping apparatus in the experiment and discusses its limitations in reaching this experimental goal. We discuss how the implementation of a bichromatic optical dipole trap (BODT) can reduce the difference in trapping potential experienced by the two atomic species. We then detail the experimental upgrades involving the addition of a 532 nm dipole trapping beam, allowing us to realise a BODT.

3.1 Introduction to dipole trapping

Optical dipole traps [159] are an essential tool in cold atom experiments, allowing access to lower atom temperatures and tighter spatial confinement than that pos-

sible with laser cooling or magneto-optical techniques alone. In this section, we introduce the basic theory of optical dipole traps and their properties.

3.1.1 Polarizability and dipole trapping potential

When an atom is placed in a electromagnetic field with electric field component **E**, the field induces a dipole moment **p** in the atom which oscillates at the field driving angular frequency ω, with a complex amplitude $\tilde{p}$ given by [159]

$$\tilde{p} = \alpha \tilde{E}, \tag{3.1}$$

where $\tilde{E}$ is the electric field magnitude and α is the complex polarizability, which dependent on ω. The interaction potential the dipole moment U_{Dipole} is given by

$$U_{\text{Dipole}} = -\frac{1}{2} < \mathbf{pE} >, \tag{3.2}$$

where the angled brackets represent the time average of rapidly oscillating terms in **p** and **E**, and the factor of $\frac{1}{2}$ arises from the fact the dipole is induced and not permanent. As the field intensity I is related to **E** by

$$I = 2\epsilon_0 c |\tilde{E}|^2, \tag{3.3}$$

equation 3.2 can be written as

$$U_{\text{Dipole}} = -\frac{1}{2\epsilon_0 c} \text{Re}(\alpha) I, \tag{3.4}$$

where $\text{Re}(\alpha)$ is the real component of the atomic polarizability. The dipole force is the gradient of this interaction potential and is hence proportional to the intensity gradient of the light field,

$$\mathbf{F}_{\text{Dipole}} = -\nabla U_{\text{Dipole}} = \frac{1}{2\epsilon_0 c} \text{Re}(\alpha) \nabla I. \tag{3.5}$$

An approximation of $\text{Re}(\alpha)$ can be calculated as a function of angular frequency ω by [159]

$$\text{Re}(\alpha) = 3\pi\epsilon_0 c^3 \sum_{f \neq i} \frac{A_{i,f}}{\omega_{0,f}^3} \left(\frac{1}{\omega_{0,f} - \omega} + \frac{1}{\omega_{0,f} + \omega} \right), \tag{3.6}$$

where $\omega_{0,f}$ and $A_{i,f}$ are the angular frequencies and Einstein A-coefficients of transitions from the atomic ground state i to an excited state f.

Inserting equation 3.6 into equation 3.4 gives the following expression for U_{Dipole},

$$U_{\text{Dipole}} = -\frac{3\pi c^2}{2} \sum_{f \neq i} \frac{A_{i,f}}{\omega_{0,f}^3} \left(\frac{1}{\omega_{0,f} - \omega} + \frac{1}{\omega_{0,f} + \omega} \right) I. \tag{3.7}$$

The dipole potential therefore is dependent on the proximity of the driving field to transition frequencies, with poles in U_{Dipole} at resonant frequencies $\omega_{0,f}$. The strength is characterised by $A_{i,f}$. The sign of the polarizability of $\text{Re}(\alpha)$ determines whether the potential is attractive or repulsive. At blue detunings from a transition $\omega > \omega_{0,f}$, U_{Dipole} has a positive value and is hence a repulsive potential. At red detunings from a transition $\omega < \omega_{0,f}$, U_{Dipole} has a negative value and is hence an attractive potential. For frequencies close to atomic transitions, the treatment of atomic transitions as two-level transitions is no longer valid, and the more complex structure has to be considered. This will be further discussed in later chapters. However, at frequencies far off-resonance from atomic transitions, the description of $\text{Re}(\alpha)$ given above is sufficient to model the dipole potential.

Optical dipole traps utilise the dipole potential and consist of coherent laser beams far off-resonance from any transition of the atom being trapped. Blue-detuned dipole traps can spatially confine atoms to regions of low light intensity. However, we consider red-detuned dipole traps, which attract atoms towards the region of highest beam intensity. Red-detuned dipole traps typically consist of laser beams with a Gaussian radial profile, focused to a beam waist ω_0, typically on the order of 10s to 100s of µm. Atoms confined by a single red-detuned beam typically form a cloud in a longitudinal 'cigar' shape along the beam axis, proportional to the intensity profile of the beam [159]:

$$I(r, z) = \frac{2P}{\pi \omega^2(z)} \exp\left(-\frac{2r^2}{\omega^2(z)} \right), \tag{3.8}$$

where the axially-dependent $1/e^2$ waist $\omega(z)$ is set by

$$\omega(z) = \omega_0 \sqrt{1 + \left(\frac{z}{z_{\text{R}}} \right)^2} \tag{3.9}$$

for a beam of wavelength λ, waist ω_0 at focus and Rayleigh range $z_\mathrm{R} = \pi\omega_0^2/\lambda$. If a pair of non-coherent, red-detuned beams are aligned to cross with the beam foci at the crossing point, a dipole potential with a magnitude of both potentials combined occurs. In this case, the atom cloud occupies a much smaller volume, referred to as a 'dimple', the size of which is governed by the waists of the two beams, and the crossing angle.

3.1.2 Trap frequency

In the case where the thermal energy of the trapped atoms are much lower than the magnitude of the dipole potential, $k_B T << U_\mathrm{Dipole}$, the potential experienced in a gaussian beam by the atoms is approximately harmonic, given by [159]

$$U(r,z) \simeq -U_0 \left[1 - 2\left(\frac{r}{\omega_0}\right)^2 - \left(\frac{z}{z_\mathrm{R}}\right)^2\right]. \tag{3.10}$$

The atoms undergo oscillations through the trap at associated harmonic trap frequencies with a radial trap frequency given by

$$\omega_r = \left(\frac{4U_0}{m\omega_0^2}\right)^{1/2}, \tag{3.11}$$

and an axial trap frequency of

$$\omega_z = \left(\frac{2U_0}{mz_\mathrm{R}^2}\right)^{1/2}. \tag{3.12}$$

3.1.3 Modifications to the trapping potential

The total potential U_tot experienced by atoms in an optical dipole trap can be modified by external potentials, including magnetic potentials U_mag and, in the vertical axis, the gravitational potential $U_\mathrm{grav} = mgz$, where m is the atom mass, z is vertical displacement, and g is acceleration due to gravity. Hence the full potential in the vertical axis may be written as

$$U_\mathrm{tot} = U_\mathrm{dipole} + U_\mathrm{mag} + mgz. \tag{3.13}$$

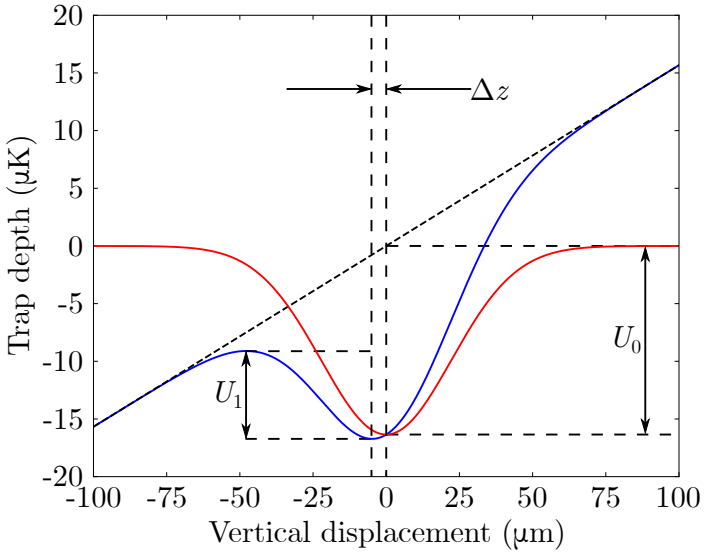

Figure 3.1: **Dipole trap profile and effect of gravitational potential.** Simulated profile of the dipole potential U_{dipole} (red curve) at the focus of the first 1070 nm dimple beam, with a vertical beam waist of 29 µm and a beam power of 200 mW. The depth of the trap is U_0. In the vertical axis we must consider the contribution of the gravitational potential $U_{\text{grav}} = mgz$ (black diagonal dashed line), giving a total potential U_{tot} (blue curve). This reduces the overall depth of the trap in this axis to U_1, and also causes a gravitational sag Δz of the trap centre.

If U_{mag} is assumed to be weak, U_{grav} has the significant effect of 'tilting' the trap and reducing U_{tot}. The vertical axis is therefore the axis through which atoms are typically lost from an optical dipole trap. U_{grav} also causes a displacement in the potential minimum in the vertical axis, referred to as the gravitational sag Δz of the trap. This is related to the trap frequency in the vertical axis by

$$\Delta z = -\frac{g}{\omega_z}. \tag{3.14}$$

For Cs, we also have the additional option of modifying U_{tot} in the vertical axis, with a magnetic potential $U_{\text{mag},z}$. This potential is made by using a magnetic field gradient $\frac{\partial B}{\partial z}$, generated by the quadrupole coils. This potential has the form

$$U_{\text{mag},z} = -m_F g_f \mu_{\text{B}} \frac{\partial B}{\partial z} z, \tag{3.15}$$

where g_f is the hyperfine Landé factor and μ_{B} is the Bohr magneton. For Cs atoms prepared in the high-field seeking $|F = 3, m_F = +3\rangle$ state, this is an upwards

potential counteracting gravity. During preparation of Cs in the reservoir trap, a field gradient of $31.3\,\mathrm{G\,cm^{-1}}$ is used to cancel out the gravitational potential. A magnetic field gradient can also be used to provide a vertical offset from centre of the dipole trap potential and induce centre-of-mass oscillations in the trap, as will be seen in chapter 4. Due to the lack of hyperfine splitting in the ground state of Yb, magnetic levitation is only possible with Cs in our experiment.

3.1.4 Atom heating and loss in a dipole trap

The frequency of optical dipole traps are typically far off-resonance from atomic transitions. This avoids heating effects due to near-resonant photon scattering. The photon scattering rate Γ_{sc} is given by

$$\Gamma_{\mathrm{sc}} = \frac{1}{\hbar\epsilon_0 c}\mathrm{Im}(\alpha)I = \sum_{f\neq i}\frac{3\pi c^2 A_{i,f}}{2\hbar\omega_{0,f}^3}\left(\frac{\omega}{\omega_{0,f}}\right)^2\left(\frac{1}{\omega_{0,f}-\omega}+\frac{1}{\omega_{0,f}+\omega}\right)^2 I. \tag{3.16}$$

The heating rate due to scattering, assuming a three-dimensional trap geometry, is then given by

$$\dot{T} = \frac{1}{3}T_{\mathrm{rec}}\Gamma_{\mathrm{sc}}, \tag{3.17}$$

where wavelength-dependent recoil velocity T_{rec} is given by

$$T_{\mathrm{rec}} = \frac{\hbar^2 k^2}{m}. \tag{3.18}$$

We must also consider losses from the dipole trap due to collisions. This decay of atom number N from the trap can be modelled by [159]

$$\dot{N}(t) = -\alpha N t - \beta\int_V n^2(\mathbf{r},t)d^3r - \gamma\int_V n^3(\mathbf{r},t)d^3r. \tag{3.19}$$

Single-particle loss is characterised by the loss coefficient α and is due to collisions between atoms in the trap and the background gas. This is typically suppressed for experiments under vacuum. Two- and three- body loss, characterised by the constants β and γ, are dependent on the in-trap density n, to the power of two and three respectively. Loss due to three-body recombination [149] is of particular concern to our experiment. In a collision of three atoms, two form a bound dimer

λ (nm)	α_{Cs} (a_0^3)	α_{Yb} (a_0^3)
532	-211	264
1070	1142	160

Table 3.1: The atomic polarizabilities of Cs and Yb at the bichromatic optical dipole trap (BODT) wavelengths.

state and a third absorbs the released energy, causing all three atoms to be lost. For Cs, this loss rate is $\sim 1 \times 10^{-27}\,\mathrm{cm}^6\,\mathrm{s}^{-1}$ [90; 150]. Therefore, it is important to manage the in-trap density of Cs.

3.2 Motivation for a bichromatic trap

The initial dipole trapping apparatus for the CsYb experiment consisted of two 1070 nm beams crossed at a 40° angle. The first beam of this crossed trap (dimple beam one, DB1) has a beam waist of 35(3) µm in the horizontal axis and 29(2) µm in the vertical axis. The second beam (dimple beam two, DB2), has a symmetrical beam waist of 70(4) µm. This crossed trap was sufficient to demonstrate quantum degeneracy in both species in single-species experimental runs, and indeed an atomic mixture of both species could be loaded into the trap for the purposes of interspecies thermalisation experiments [90], and photoassociation experiments [91; 92]. However, it was not possible to load both species into the crossed trap and evaporate to dual quantum degeneracy.

The first reason to consider for this is the mismatch in ground state polarizability of the two atomic species at the trapping wavelength of 1070 nm. Table 3.1 shows that, at this wavelength, while the polarizability is positive for both species and therefore both species are trapped at this wavelength, the magnitude of the polarizability for Cs is over seven times that for Yb. The resulting dipole trap is therefore deeper for Cs than for Yb by this factor. Therefore, the optimal traps for single-species evaporation to degeneracy are incompatible. The powers required for the final trap at the end of Yb evaporation are ∼4 times those required for initially loading Cs.

Similarly the powers required for the final trap at the end of Cs evaporation are ∼0.02 times those required for those required for the final trap at the end of Yb evaporation, and hence the trap is nonexistent for Yb.

The polarizability mismatch also means that there is a mismatch in the trapping frequencies for the two species. This leads to reduced overlap between the atomic clouds due to gravitational sag in the vertical direction. The other reason to consider, which follows on from the trapping mismatch, is that dual-species cooling relies on favourable conditions for sympathetic cooling, namely that elastic intraspecies collisions occur at a favourable rate compared to inelastic collisions which cause loss from the trap. Of particular concern in our system is loss due three-body recombination in Cs, which has a high three-body loss rate. Creating a sufficiently deep 1070 nm trap for Yb results in a much deeper and tighter trap for Cs, and as three-body loss is density-dependent, we observe loss of Cs and heating in this high-density dimple.

The solution for this problem has been to introduce a second wavelength to the dipole trap to alter the trapping potential – resulting in a dual-wavelength trap. We refer to this as the bichromatic optical dipole trap (BODT). BODTs were proposed in [163] have also been used in other groups working with alkali+alkaline-earth-like atomic mixtures [94; 29; 164]. Wavelengths such as 1070 nm and 1550 nm are commonly used for dipole trapping because they are far red-detuned from atomic transitions from the ground state and therefore result in an attractive optical potential. This is the case for both Cs and Yb, but it is the mismatch in detuning from the nearest transition which causes the mismatch in polarizability and trap depth.

Our additional trapping beam has a wavelength of 532 nm. As can be seen in figure 3.2(a), this wavelength lies between successive transitions for Cs and Yb but is sufficiently far-detuned for heating due to resonant scattering to be comparable to the case for 1070 nm. Crucially, the atomic polarizability of ground state Cs is negative at this wavelength, resulting in a repulsive optical potential, whereas for

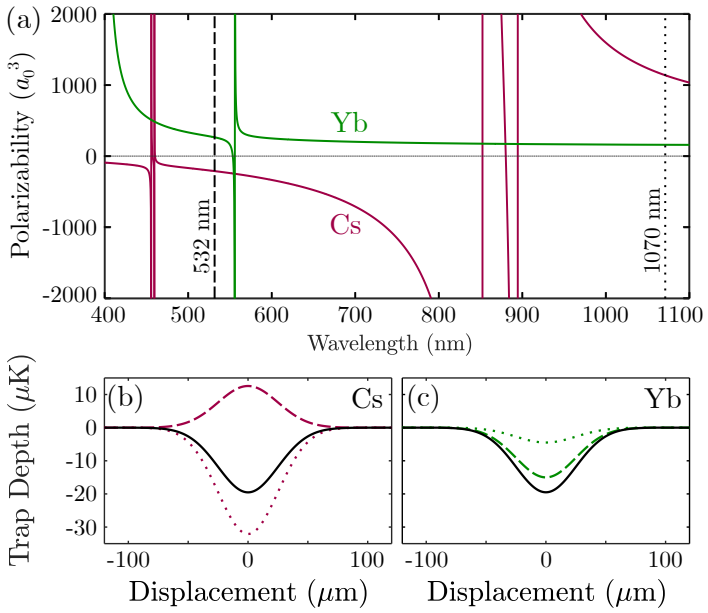

Figure 3.2: **Balanced trapping potentials for Cs and Yb.** (a): Atomic ground state polarizability as a function of wavelength, for Cs (red) and Yb (green). Vertical lines at 532 nm (dashed) and 1070 nm (dotted) are the bichromatic optical dipole trap (BODT) beam wavelengths. Polarizability here is converted from SI units (as stated in equation 3.6) to atomic units by a conversion factor of $\frac{1}{4\pi\epsilon_0}$ and displayed in units of a_0^3, where a_0 is the Bohr radius. The values of transition wavelengths and corresponding Einstein A-coefficients used in the calculation are listed in appendix A and are taken from [160] and [161]. (b) and (c): Cross-sections of a balanced trapping potential. The overall potential (solid black line) is the sum of contributing potentials from a 532 nm beam (dashed) and a 1070 nm beam (dotted), plotted for Cs(b) and Yb(c). Both beams have $1/e^2$ waists of $w_0 = 50\,\mu$m. The beam powers are $P_{532} = 1\,$W and $P_{1070} = 0.5\,$W. Figure reproduced from [162].

Yb the polarizability is positive. The values for polarizability of both species at both wavelengths of our BODT are given in table 3.1. The principle of our BODT is as follows: by increasing the intensity contribution of the 532 nm beam to the trap, we can reduce the effective trap depth for Cs while increasing it for Yb. We can ultimately use this to balance out the potentials for two species, making the trap conditions more favourable for sympathetic cooling. This is shown in figures 3.2(b) and 3.2(c). These are the trapping conditions which have ultimately allowed us to observe double-degenerate mixtures, as well as high-PSD mixtures for Feshbach spectroscopy, in our experiment.

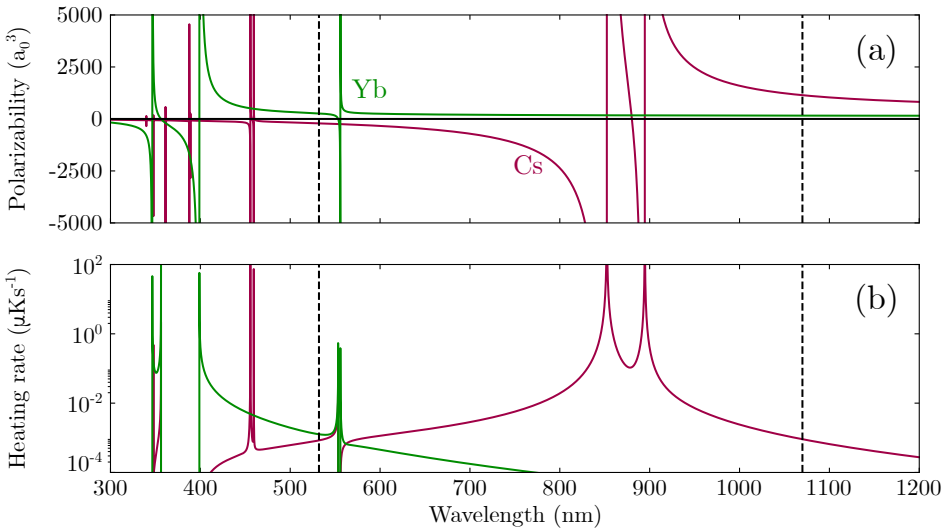

Figure 3.3: **Comparing polarizability and heating rate of Cs and Yb.** (a) : the polarizabilities of ground state Cs (red) and Yb (green) across a wavelength range 400 nm – 1200 nm, calculated using equation 3.6. (b): heating rates across the same wavelength range, using a laser intensity sufficient to trap Yb at a depth of 1 µK. The vertical lines in (a) and (b) show the two wavelengths of our BODT at 532 nm and 1070 nm.

We also consider the effect of heating of both species due to off-resonant photon scattering. The laser intensity I required for a Yb trap depth of 1 µK, which is representative for our purposes, was calculated across the wavelength range 300 nm – 1200 nm , and the resulting scattering and heating rates calculated. This is shown in figure 3.3(b). Contributions to the heating rate are comparable for both species at 532 nm, as well as being comparable to the heating rate for Cs at 1070 nm.

3.3 Experimental setup

The following section describes the setup of the 532 nm beam used in the BODT. This was performed with minimal changes to the existing 1070 nm setup, described in detail in [139; 140], with only the addition of dichroic mirrors to allow beams of both wavelengths to copropagate, and optics which are compatible with both wavelengths.

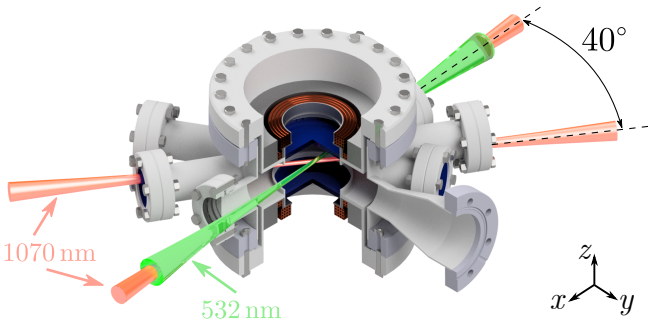

Figure 3.4: **The bichromatic trap in the CsYb experiment** 3-dimensional render of the science chamber, showing orientation of the three bichromatic optical dipole trap (BODT) trap lasers. The 532 nm beam and the first 1070 nm beam (dimple beam 1, DB1) copropagate through the chamber. The second 1070 nm beam (dimple beam 2, DB2) crosses the other beams at a 40° angle.

3.3.1 532 nm light source

The 532 nm laser light source (IPG GLR20, 20 W) is positioned on the main table of the laboratory near the atomic ovens. The laser replaced a previous laser of the same wavelength in the setup (Laser Quantum Finesse, 7 W). This laser was prone to loss in power due to overheating. In the worst cases power output was reduced from the specified 7 W to ~ 3 W. The GLR20 is able to operate at steady power and temperature with the output power set to 5 W. The full 20 W power output may be needed for future applications (see outlook), but 5 W output power is adequate for the BODT in its current configuration. We also do not wish to damage the photonic crystal fiber in the setup (see below) with high beam powers.

3.3.2 Optics at the laser output

We initially set up the beam to propagate from the laser light source to the chamber on a completely free-space path. However, it was found that vibrations due to the laser source were affecting the pointing stability of the beam at focus. In our initial attempts to cool Yb to quantum degeneracy, at the lower (≤ 0.5 W) powers at the final stages of evaporative cooling, this pointing instability caused

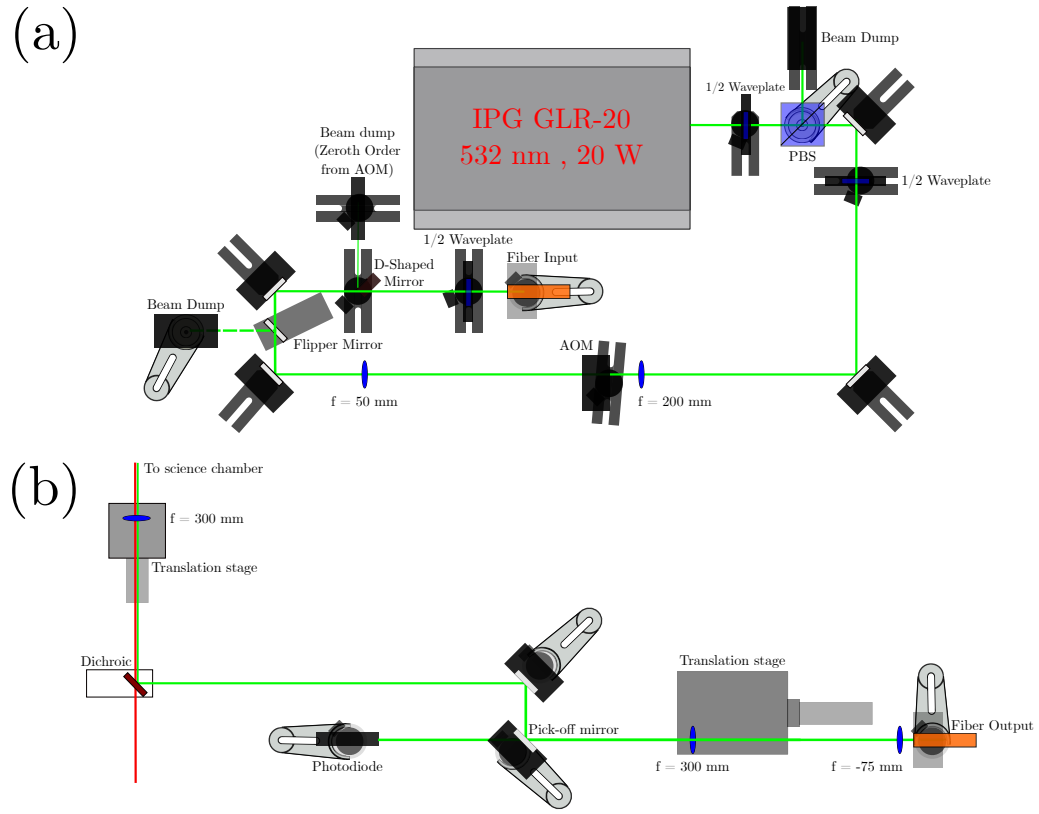

Figure 3.5: **Optical setup of the 532 nm beam.** a. Optics at the laser output. The beam is aligned through an Acoutso-optic modulator (AOM) for intensity stabilisation. The first diffracted order of the AOM output is coupled into a photonic crystal fiber. b. At the fiber output, the beam is expanded to be the correct size for focusing into the science chamber, before being combined with the existing 1070 nm dimple beam 1 using a dichroic.

atom heating and loss. The solution was to reconstruct the optical setup to incorporate a photonic crystal optical fiber into the beam path. This fiber is capable of transmitting up to 10 W of laser power. The spatial stability of the fiber output guarantees the pointing stability of the beam at focus. The power of the beam can be stabilised by monitoring the power of the fiber output (see below). Note this was originally motivated by pointing instability in the Finesse laser, but has been retained following installation of the GLR-20 laser.

The optics at the output of the laser is shown in figure 3.5a. The output is collimated with a beam waist of 486.3(18) µm in the x-axis and 557.8(15) µm in the y-axis. This gives a beam aspect ratio of 0.872(6). A half-waveplate and polarising

beam splitter (PBS) cube are used at the output the ensure linear polarisation of the light through the rest of the setup. For low-power alignment, waveplate can be adjusted to reflect and dump the majority of the laser power. A second-half wave is then used rotate the linear polarisation from horizontal to vertical. This orientation of the polarisation allows the most efficient propagation of the light through the mirrors and AOM (see below).

A 110 MHz AOM (Gooch and Housego 3110-120) is used for power stabilisation. The power in the BODT beam is stabilised and ramped using a feedback loop between this AOM and a monitor photodiode (see below). A custom-built 'servo box' compares the monitor signal to an external 'setpoint' analogue voltage, outputted from the main experimental control. A modulation voltage is outputted from the servo box to the AOM, controlling the amount of beam power the AOM diffracts into the first order.

The active aperture of the AOM crystal is 2.5(0.6) mm in the x(y) axis. We therefore use an $f = 200$ mm lens to focus the beam. The AOM is located approximately 50 mm after this lens along the beam path. This ensures the entirety of the beam fits within the active aperture, but is not too tightly focused, which may damage the AOM crystal. The AOM is aligned to optimise the power in the first diffracted order, with an efficiency of 75.25(17) %. A second lens with a focal length $f = 50$ mm recollimates the beam, with a beam waist of 119(3) µm in the x-axis and 125(2) µm in the y-axis. This gives a beam aspect ratio of 0.95(4). This is a suitable beam waist for coupling into the photonic crystal fiber. The first order of the AOM output is coupled into the fiber with a coupling efficiency of 70.70(12) %. A D-shaped mirror is used to deflect and dump the zeroth order of the AOM output. To avoid any stray light propagating through the fiber, a flipper mirror is also used to deflect and dump all of the AOM output. This is controlled by a digital TTL signal from the experimental control. The flipper mirror is set to be in the down position when the BODT is in use during the experimental sequence, and in the up position at all other times.

3.3.3 Beam path through the science chamber

The optics at the fiber output are shown in figure 3.5b. The output is on the same horizontal plane as the centre of the science chamber, and the existing 1070 nm optics. The beam output of the fiber is expanded by a 1:4 telescope consisting of an $f = -75$ mm planoconcave lens and $f = 300$ mm planoconvex lens. This second lens is mounted on a translation stage to fine-tune alignment. This collimates the beam to 1250(20) µm. After the telescope, approximately 0.1 % of the beam power is picked off and directed onto a photodiode. This is the monitor photodiode of the intensity stabilisation system. By positioning the photodiode after the fiber output, we ensure the stabilised power is constant at the fiber output, and not dependant on the coupling efficiency of the fiber.

Prior to setup of the 532 nm laser system, it was decided that the 532 nm dipole trap beam should be arranged either co- or counter-propagating the 1070 nm dimple beam 1, which passes through the chamber on the North-South axis. This is due firstly to the fact that the pairs of viewports on our experimental chamber have a range of anti-reflection coatings. The viewport pair for dimple beam 1 is also designed to have low reflectivity at 532 nm. Directing the new dipole trapping beam through this viewport pair was an obvious choice to minimise losses at the viewport surfaces. Setting up the beam to be colinear with one of the 1070 nm beams also allows the overlap of the two beams at the focus to be monitored and corrected more easily (see below). This also avoids unnecessary duplication of optics such as focusing and recollimation lenses.

The main beam is therefore combined with the 1070 nm dimple beam 1 using a long-pass dichroic (THORLABS DMLP900). This is shown in figure 3.5b. Both beams are focused into the science chamber by an $f = 300$ mm lens with an antireflection coating designed for high transmission at both laser frequencies (THORLABS LA4579-YAG-SP). This lens is mounted on a translation stage to fine-tune the axial alignment of both beams in the science chamber. An identical lens is used

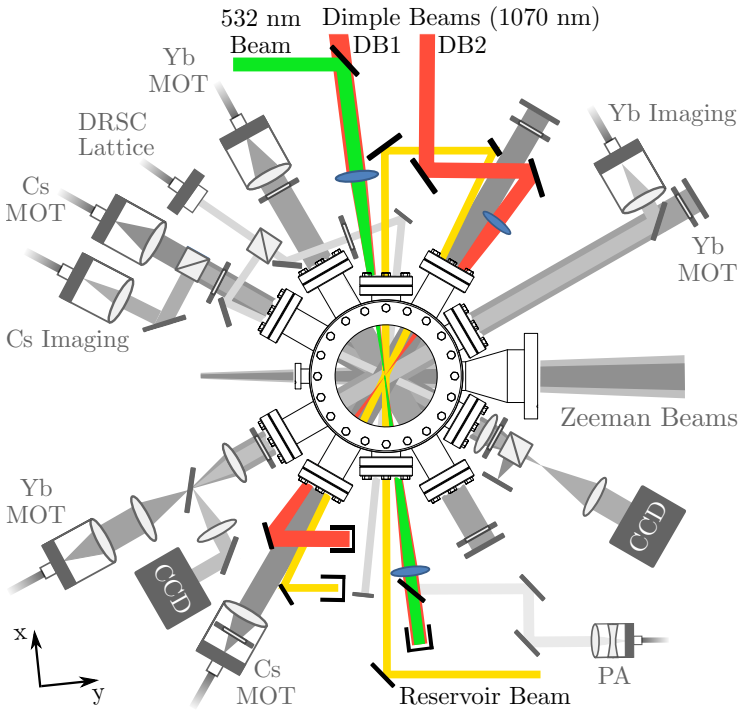

Figure 3.6: **Beam paths through the science chamber.** The beam layout for the BODT is shown in red, green and yellow. All other beam paths travelling through the science chamber in the horizontal plane are shown in grey. Here, we define a coordinate system (x, y, z). The x axis is parallel to DB1 and the 532 nm beam. The y axis is perpendicular to the x axis in the horizontal plane. The z axis is in the vertical direction. The axes for imaging Cs and Yb are rotated 35° and 25° from the y axis respectively. Figure reproduced from [162].

to recollimate both beams on the opposite side of the chamber. The geometry of the BODT beams, with respect to the other beams propagating through the science chamber, is illustrated in a top-down view in figure 3.6. Here, we define a coordinate system (x, y, z). The x axis is parallel to DB1 and the 532 nm beam. The y axis is perpendicular to the x axis in the horizontal plane. The z axis is in the vertical direction. The axes for imaging Cs and Yb are rotated 35° and 25° from the y axis respectively.

The 532 nm beam has a symmetric beam waist of 50(3) µm, and DB2 has a symmetric beam waist of 70(4) µm. DB1 has a horizontal beam waist of 29(2) µm, and a vertical beam waist of 35(3) µm. We can also modify DB1's horizontal waist by dithering the frequency of DB1's intensity stabilisation AOM, increasing the beam

waist to up to 72(4) µm.

3.3.4 Quadrant photodiode

The relative alignment of the copropagating BODT beams is critical to maintain both optimal trap depths and good overlap between the two atomic species. Due to the different polarizabilities, Cs is more strongly trapped by DB1, and Yb by the 532 nm beam. This can lead to strange trap potentials if the beams are not well aligned, for example a double well potential for Cs. If the 532 nm beam is misaligned relative to DB1, it can simultaneously pull Yb away from the trap centre and repel Cs, causing the two atom clouds to separate and reducing thermal contact. We therefore track the relative alignment of the beams with a quadrant photodiode (QPD). The QPD is a First Sensor Quadrant Photodiode, and is mounted in an evaluation board (QP50-6-18u SD2). It has an 18 µm gap between the photodiodes. The evaluation board provides voltage outputs for the beam positions in the horizontal and vertical axes. These voltages correspond to the difference between the left and right halves and the top and bottom halves of the photodetector respectively.

Figure 3.7 shows the optical setup for monitoring the relative positions of DB1 and the 532 nm beam. A small ($\leq 0.1\,\%$) amount of the power in both dipole trap beams is picked off from the main beam by a wedged blank. The beams (in the plane of the BEC) are then imaged onto the QPD using a pair of achromatic lenses. The lenses have focal lengths of 300 mm and 500 mm. The choice of focal lengths minimises the shift in the object plane between the two wavelengths. At the end of every experimental sequence, we image the beams, directing first DB1 and then the 532 nm beam onto the QPD. This tracks the relative position of the two beams over the course of multiple experimental sequences.

The QPD voltage signal in either axis has the form of an error function as a function of beam position, and is therefore approximately linear in the central region of the

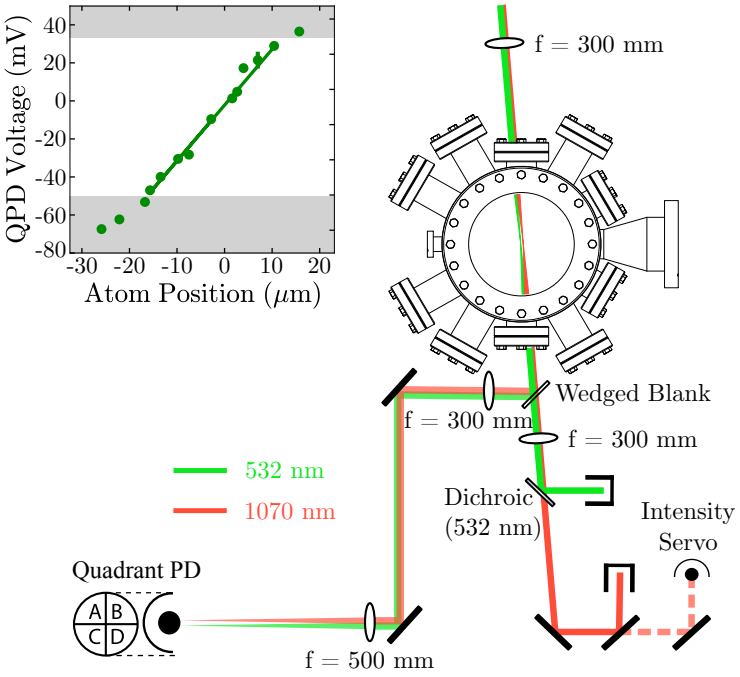

Figure 3.7: **Quadrant photodiode setup.** Optical setup to monitor the relative beam positions DB1 and the 532 nm beam. The positions of the beams in the plane of the BODT are imaged onto a quadrant photodiode (QPD). The imaging system uses a pair of achromatic lenses. The achromat focal lengths are 300 mm and 500 mm. Inset: calibration of the vertical QPD sensitivity for the 532 nm beam. Green circles are the measured vertical QPD voltages plotted against the vertical centre of mass (CoM) Yb atom position. The green line is a linear fit to the data, giving a sensitivity of 2.9(1) mV/µm. Measurements in the grey shaded areas are excluded from the linear fit. Figure reproduced from [162].

QPD (see inset of Figure 3.7). The sensitivity of the QPD was calibrated in this linear region for both DB1 and the 532 nm beam. In each case, the vertical QPD voltage signal was plotted against the vertical centre of mass (CoM) position of Yb atoms confined solely by the relevant beam. The vertical sensitivities were measured to be 2.3(1) mV/µm and 2.9(1) mV/µm for DB1 and the 532 nm beam respectively. The sensitivity calibration for the 532 nm beam is shown in the inset of Figure 3.7. Due to the non-orthogonal angles between the two beams and both the Cs and Yb imaging axes (see Figure 3.6), the same calibration cannot be made for the horizontal axis of the beams. The vertical sensitivity calibration is therefore also used as an estimate for the horizontal sensitivity calibration. The

QPD sensitivity allows us to measure the relative positions of both beams to within 3 µm in both axes.

3.4 Conclusion

We have discussed the experimental limitations of using the single-frequency 1070 nm dipole trapping beams for Cs+Yb mixtures and motivated the inclusion of an additional 532 nm beam to realise a bichromatic optical dipole trap (BODT). We have discussed the setup of the necessary optics for the 532 nm setup, and its integration into the existing apparatus. We have discussed issues related to the alignment stability of the BODT and introduced the use of a Quadrant photodiode (QPD) to monitor and correct the alignment. Chapter 4 discusses the experiments with ultracold gases of Cs and Yb which were subsequently made possible by these upgrades.

Chapter 4

Quantum degenerate mixtures of Cs and Yb

Following the setup of the BODT, we were able to improve our dual-species cooling routine to the point where evaporation to dual quantum degeneracy could be performed in two different mixtures. In this chapter, we give an overview of the changes to the experimental sequence to incorporate evaporative cooling in the BODT. We report dual degeneracy in both Cs+^{174}Yb and Cs+^{170}Yb. We utilise the attractive interspecies interactions of the Cs+^{174}Yb mixture to probe the dynamics of the mixture, including coupled centre-of-mass oscillations, and the collapse of the Cs BEC mediated by the presence of Yb. In contrast, we utilise the repulsive interspecies interactions of the Cs+^{170}Yb mixture to explore the atom number dependent immiscibility in this mixture.

4.1 Introduction: basics of a BEC experiment

A Bose-Einstein condensate (BEC) [165; 166; 167] is a phase of matter accessed by a bosonic gas. It occurs when the temperature of the gas T crosses below a critical temperature, T_c. The results of this chapter report on the creation of BECs in our BODT potential. Below T_c, a fraction of the atoms $\frac{N_0}{N}$ in the gas occupy the

ground state of the trapping potential, given by [165]

$$\frac{N_0}{N} = 1 - \left(\frac{T}{T_c}\right)^3. \tag{4.1}$$

The inter-atomic spacing in the gas becomes comparable to the atom de Broglie wavelength λ_{dB}, and the atoms form a coherent matter-wave across the trap.

4.1.1 Experimental signature of a BEC

The creation of a BEC within the experiment can be verified by analysing the density profile $n(\mathrm{r})$ of the atomic cloud through absorption imaging after time of flight. There is significant enhancement of the cloud's central density in comparison to that of a 'thermal' atom could with a temperature $T > T_c$. We consider the condensate in the Thomas-Fermi limit. This is appropriate for the range of magnitude of atomic interactions which are sufficiently strong for the system to be considered weakly correlated, but weak enough for condensation to occur, and neglects the kinetic energy of the condensate. In this limit, $n(\mathrm{r})$ is given by

$$n(\mathrm{r}) = \max\left(\frac{\mu - U_{\mathrm{trap}}(\mathrm{r})}{g'}, 0\right), \tag{4.2}$$

where $g' = 4\pi\hbar^2 a_s/m$, a_s is the s-wave scattering length (see section 4.1.2) and μ is the chemical potential. This can be thought of as the density distribution filling the trapping potential up to a 'height', given by μ [168]. Hence, in a harmonic trap, we can apply a parabolic fit to the density distribution of the cloud, as imaged after time of flight:

$$n(x,y) = n_0 \max\left(\left[1 - \frac{(x-x_0)^2}{R_{\mathrm{TF},x}^2} - \frac{(y-y_0)}{R_{\mathrm{TF},y}^2}\right], 0\right), \tag{4.3}$$

where $R_{\mathrm{TF},i}$ are the Thomas-Fermi radii of the atom cloud in each axis. It is possible that not all of the atoms in the trap cross the phase transition and become part of the BEC. In this case, a bimodal fit can be applied. This is a combination of the fit in equation 4.3 incorporating the atoms in the BEC, and a Gaussian fit to incorporate the thermal atoms. The ratio of amplitudes of these fits gives an

indication of the 'purity' of the BEC, with only the parabolic fit needed when every atom in the trap has condensed to become part of the BEC.

Another indicator of creation of a BEC is the aspect ratio inversion of the atom cloud under time of flight. This occurs because the time evolution of the Thomas-Fermi radius after a cigar-shaped trap is different in the radial r and axial z dimensions:

$$R_{\mathrm{TF},r}(t) = R_{\mathrm{TF},r}(0)\sqrt{1+\tau^2} \tag{4.4}$$

$$R_{\mathrm{TF},z}(t) = R_{\mathrm{TF},z}(0)\left(1+\left(\frac{\omega_z}{\omega_r}\right)^2\left[\tau\arctan\tau - \ln\left(\sqrt{1+\tau^2}\right)\right]\right), \tag{4.5}$$

where $\tau = \omega_r t$. Although we use a crossed dimple trap in our setup, the shallow crossing angle means the cloud can be regarded as cigar-shaped for the purposes of analysing the aspect ratio evolution. In the experiment, we therefore typically observe the aspect ratio inversion with the vertical size of the BEC increasing at a faster rate than the horizontal size [140].

4.1.2 Scattering properties of ultracold gases

Understanding the scattering and collisional properties of ultracold gases is important to be able to form gases of sufficient temperature and density to create stable degenerate gases such as BECs. It is also important in being able to identify experimental cooling routines to reach degeneracy by having favourable relative collision rates between elastic and inelastic collisions (see section 4.1.3).

The scattering properties of a colliding pair of ultracold atoms can be characterised by a parameter known as the scattering length, a_s. The colliding atoms experience a phase shift δ_0. The s-wave scattering length is defined as

$$a_s = -\lim_{k\to 0}\frac{\tan\delta_0(k)}{k}, \tag{4.6}$$

where k is the collision wavevector of the relative motion of the atoms. a_s can take positive or negative values, depending on the position of bound states within the

interatomic potential $V(R)$ relative to its threshold energy (see chapter 6). A positive scattering length gives rise to repulsive interactions and a negative scattering length gives rise to attractive interactions. The sign of the *intra*-species scattering length of a BEC is therefore important to classify its stability. Furthermore, in the case of degenerate mixtures, the sign of the *inter*-species scattering length is important to characterise the interspecies interaction, as will be seen in later sections of this chapter.

The scattering length is also important when considering evaporative cooling in single- and dual-species cold atom experiments. At ultracold temperatures below the p-wave centrifugal barrier of an interatomic collision, the elastic collision rate is dependent on the s-wave elastic scattering cross-section, σ. For identical bosons,

$$\sigma = 8\pi a_s^2. \tag{4.7}$$

The rate of elastic collisions is therefore greater for gases with a higher magnitude of a_s, which may assist in evaporative cooling techniques, although this has to be balanced against inelastic collision rates (see section 4.1.3). For interspecies collisions, the particles are non-identical, and σ becomes

$$\sigma = 4\pi a_s^2. \tag{4.8}$$

Similarly to the case of identical particles, the magnitude of a_s determines the efficacy of sympathetic cooling of one atomic gas by another through elastic collisions. The CsYb interspecies scattering length a_{CsYb} varies significantly in magnitude depending on the isotope of Yb used (see chapter 1). This affects to what extent sympathetic cooling can be used effectively in dual evaporation routines. However, the interspecies scattering lengths of the two degenerate mixtures discussed in this chapter are sufficient in magnitude to allow the sympathetic cooling of Cs by Yb to assist in cooling to dual degeneracy.

4.1.3 Principle of evaporative cooling

In the experiments described below we use the method of forced evaporative cooling, a method widely used in cold atom experiments [169]. By reducing the intensity of the dipole trap, the trap depth is lowered and the hottest atoms are lost from the trap. This truncates the Maxwell-Boltzmann distribution of the atoms in the trap, which then rethermalise through elastic collisions at an equilibrium temperature. The elastic collision rate Γ_{Elastic} is given by

$$\Gamma_{\text{Elastic}} = \frac{N m \sigma \bar{\omega}^3}{2\pi^2 k_{\text{B}} T}, \tag{4.9}$$

where σ is the scattering cross-section for an s-wave scattering length, a_s, given by equation 4.6, and $\bar{\omega}$ is the geometric mean trap frequency. For effective evaporative cooling, this collision rate has to be greater than the rate of inelastic collisions which cause losses from the trap. As discussed in chapter 3, three-body recombination is most significant loss mechanism for high-density optical traps. Loss due to three body combination scales as $\langle n^2 \rangle$ and therefore $\bar{\omega}^6$. Therefore, the trap density and trap frequency both have to be carefully managed throughout the evaporation sequence, to ensure the ratio of elastic to inelastic collisions is favourable.

The quantity used to evaluate the cooling of the atomic gas towards degeneracy is the phase-space density (PSD), given by

$$\text{PSD} = n_0 {\lambda_{\text{dB}}}^3, \tag{4.10}$$

where n_0 is the peak number density, and λ_{dB}, is the thermal de Broglie wavelength of the atoms, given by

$$\lambda_{\text{dB}} = \sqrt{\frac{2\pi\hbar^2}{m k_{\text{B}} T}}. \tag{4.11}$$

The requirement for Bose-Einstein condensation of a gas is [165; 167]

$$\text{PSD} \geq 2.612. \tag{4.12}$$

Experimentally, we wish to evaporate as high a number of atoms initially trapped in the BODT to degeneracy as possible, by increasing the PSD with minimal atom

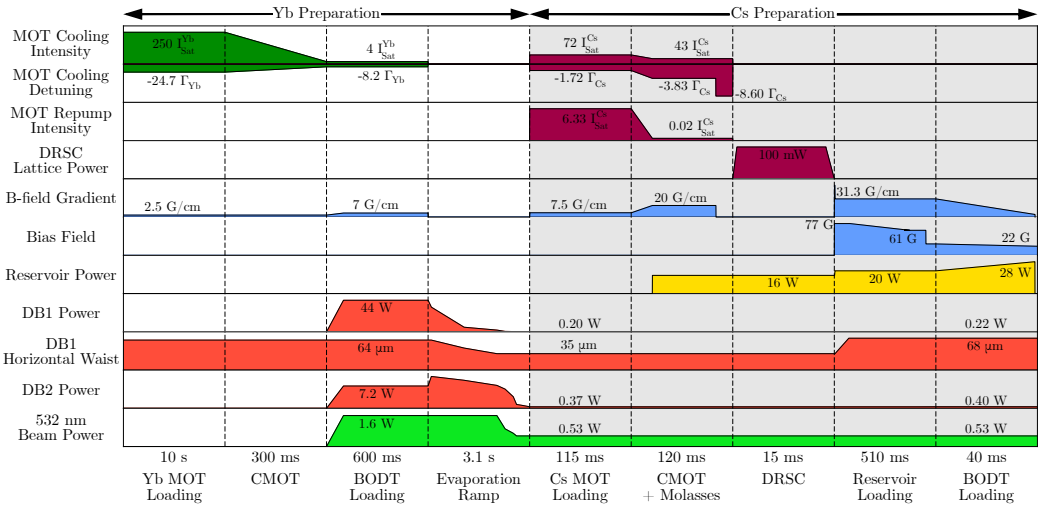

Figure 4.1: **Timing sequence for Cs and Yb preparation and BODT loading.** We load Yb in a magneto-optical trap (MOT) for 10 s, before compressing the MOT over 500 ms. We then load Yb atoms into the BODT directly from the compressed MOT (CMOT). Yb undergoes 3.1 s of forced evaporation prior to the start of Cs preparation. Cs is loaded in a MOT and then compressed. We then apply optical molasses, followed by degenerate Raman sideband cooling (DRSC). Cs is then loaded into the reservoir trap. From there, we load Cs atoms into the BODT. The horizontal waist of dimple beam 1 (DB1) can be modified by dithering the frequency of DB1's power stabilisation AOM. We reduce the powers of DB1 and Dimple beam 2 (DB2) slightly during the Cs preparation stages to reduce heating of Cs, before increasing them to the final powers for loading Cs into the BODT. Figure reproduced from [162].

loss. We therefore use the evaporation efficiency γ as a metric. This measures the relative increase in PSD, weighted against the corresponding loss in atom number N:

$$\gamma = -\frac{\ln(\mathrm{PSD}_f/\mathrm{PSD}_i)}{\ln(N_f/N_i)}. \tag{4.13}$$

In a typical evaporative cooling sequence, the dipole trap intensity will be lowered by a series of linear ramps. For each of these ramps, γ can be optimised by modifying the timing of the sequence, and plotting the PSD against number lost as the ramp progresses, see section 4.2.3.

4.2 Experimental sequence

In this upgraded experimental sequence, we load Yb and Cs into the BODT sequentially. The pre-cooling methods used to reach conditions for efficient trap loading are the same as those used in single-species cooling schemes outlined in chapter 2. Figure 4.1 shows the full timing sequence for dual-species preparation and BODT loading. Following loading of both species, forced evaporative cooling is used to reach dual degeneracy.

4.2.1 Preparation of Cs and Yb

We load ^{174}Yb into the BODT prior to loading Cs. This is for two reasons. Firstly, the Yb MOT load time is much longer than that required for Cs, typically taking $10 - 20\,\mathrm{s}$. Secondly, a tight trap with high beam powers is required for the initial stage of evaporative cooling in Yb. Loading Cs first would therefore cause heating and loss, and prevent the Cs from being cooled to degeneracy. Figure 4.1 shows how the 1070 nm trapping light dominates the BODT potential in the initial stages of the sequence. During these stages, the DB1 horizontal beam waist is set to 64 µm. This increases the volume of the BODT volume and improves loading of Yb. We then perform forced evaporative cooling of Yb by reducing BODT beam powers. This results in an approximately exponential ramp of the trap depth, taking place over 3.1 s. Over this time period, we also decrease the DB1 horizontal waist. This partially compensates for the decrease in trap frequency as the beam powers are decreased.

We then begin preparation of the Cs atoms, following the method summarised in chapter 2. The Cs MOT is loaded before being compressed by reducing the intensity and detuning of the MOT beams. The Cs atoms are then further cooled using optical molasses, followed by DRSC. This cools the atoms to $\sim 1\,\mu\mathrm{K}$ and optically pumps them into the $|F = 3, m_\mathrm{F} = +3\rangle$ hyperfine state. We then transfer

the remaining atoms into the reservoir trap. We apply a magnetic bias field to modify the elastic collision rate and improve the reservoir capture efficiency. We also briefly apply a magnetic field gradient of 55 G/cm. This applies a vertical force to the atoms. We then reduce the gradient to 31.3 G/cm, which levitates the atoms [170]. We also increase the DB1 horizontal beam waist to 68 µm. This reduces the Cs potential to 11 µK, which is a suitable trap depth for BODT loading and subsequent sympathetic cooling. At this stage, the Cs BODT mean trap frequency is reduced to 123 Hz. The Yb BODT potential is also slightly reduced to 3.1 µK. The Yb BODT mean trap frequency is reduced to 93 Hz.

We load the reservoir for 510 ms. We then ramp down the magnetic field gradient to 0 G/cm. Once the field gradient is removed, we extinguish the reservoir trapping light. This leaves a fraction of the Cs atoms from the reservoir confined in the BODT, co-trapped with the Yb atoms. Preparation of the Cs atoms with Yb atoms already loaded in the BODT takes ~ 1 s. This is between 5 and 10 times faster than the Cs single-species preparation time. This is largely due to the efficient sympathetic cooling of the Cs by the Yb, which reduces the number of Cs atoms we needed to initially load into the reservoir. Loading too many Cs atoms can in fact begin to heat the Yb atoms and have a detrimental effect on the rest of the evaporation sequence.

4.2.2 Dual-species overlap

The efficient sympathetic cooling of Cs by Yb requires the atomic samples to be in thermal contact and be well-overlapped throughout the evaporation sequence. To achieve this, the BODT beams must be carefully aligned. Figure 4.2 shows the Cs and Yb temperatures and atom numbers in the BODT midway through the dual-evaporation sequence, plotted against the 532 nm beam displacement. The QPD is used to track the vertical Δz and horizontal Δy displacement of the 532 nm beam. In each subplot, zero is defined as the position where the minimum Cs temperature is measured. This coincides with the highest measured Yb temperature. This

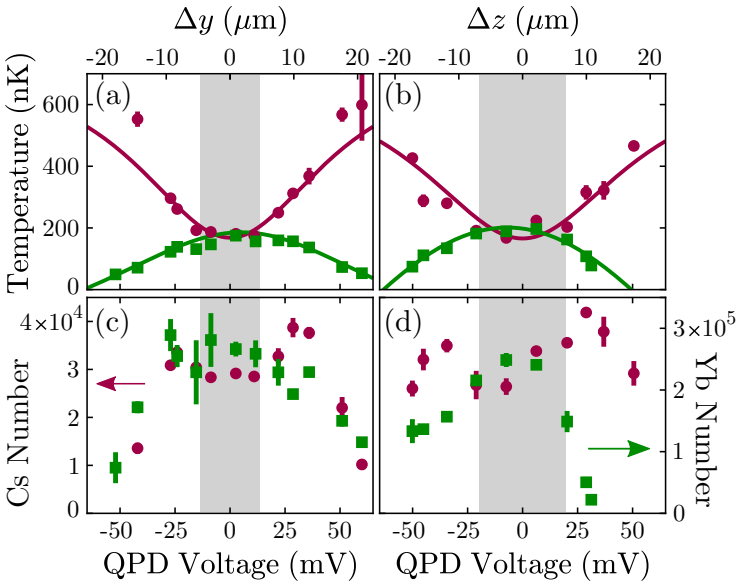

Figure 4.2: **Optimal atom cloud overlap** Atom temperature and number for both species is measured as a function of the displacement of the 532 nm beam. Improved thermalisation of the atom clouds indicates optimal overlap. The 532 nm beam displacement is measured using the QPD. (a) and (b) Cs (red circles) and Yb (green squares) temperature plotted against displacement of the 532 nm beam. (a) shows temperature versus horizontal displacement Δy. (b) shows temperature versus vertical displacement Δz. The solid lines are Lorentzian fits to the data. In both plots, zero is defined as the beam position of minimum Cs atom temperature according to the fits. (c) and (d) The atom numbers of Cs (red circles) and Yb (green squares), plotted against displacement of the 532 nm beam. The regions where the two atom clouds approximately thermalise, $T_{\mathrm{Cs}} \sim T_{\mathrm{Yb}}$, are shown by the grey shaded areas. Figure reproduced from [162].

is due to the optimal thermal contact between the cold Yb and the hotter Cs. Minimising the Cs temperature is therefore a signature of optimal overlap between the atomic clouds. This is demonstrated in figure 4.2(a) and figure 4.2(c), where the measured temperature minima/maxima and atom number maxima are both symmetric about $\Delta y = 0\,\mu\mathrm{m}$.

However, in the vertical axis, there is an asymmetry in the Yb atom number. This is shown in figure 4.2(d). In this axis, the alignment for optimal thermal contact does not correspond to perfect vertical overlap of DB1 and the 532 nm beam. This is due to the difference in gravitational sag in the BODT Δz_{grav} experienced by

the two species, given as

$$\Delta z_{\mathrm{grav}} = g\left(\frac{1}{\omega_{\mathrm{Cs},z}^2} - \frac{1}{\omega_{\mathrm{Yb},z}^2}\right). \tag{4.14}$$

The lower Yb vertical trap frequency $\omega_{\mathrm{Yb},z}$ causes the Yb atoms to undergo significant gravitational sag. In contrast, the trapping potential for the lighter Cs atoms is tighter. As a result, the Cs vertical trap frequency $\omega_{\mathrm{Cs},z}$ is greater, and the Cs atoms undergo a reduced amount of gravitational sag. Therefore, to ensure optimal thermal contact between Cs and Yb at the end of dual-evaporation, the 532 nm beam is required to be $5 - 10\,\mu$m above DB1. This shifts the minimum of the Yb trapping potential upwards towards that of the Cs. However, if the 532 nm beam is moved too far above DB1, the Yb trap depth will be further reduced, leading to loss of all Yb atoms.

4.2.3 Evaporation to dual degeneracy

We start dual evaporative cooling with 1.6×10^5 Cs atoms and 9.9×10^5 Yb atoms, simultaneously trapped in the BODT. At this point, the Cs atoms have a temperature of 2.6 µK, and the Yb atoms have a temperature of 240 nK. Figure 4.3(iii) shows the temperature evolution of the Cs atoms (red circles) and Yb atoms (filled green squares) during dual evaporative cooling. The single-species Yb evaporation ramp prior to the Cs loading is also shown in figure 4.3(i) (open green squares). The inset of figure 4.3 shows the PSD evolution during dual evaporation, plotted against atom number. The data points in the PSD subplot for Cs and Yb which correspond to $t = 0$ s in the main plot are indicated by arrows. At this point, the Yb sample has just crossed the phase transition to BEC, indicated by the horizontal dashed line corresponding to PSD = 2.61. The mixture, however, has not yet thermalised. For an initial thermalisation period of 200 ms, the BODT beam powers are held constant. During this thermalisation period, the Cs PSD increases by a factor of 20, whereas the Yb PSD decreases by a factor of 7. This demonstrates the favourable usage of the Cs–^{174}Yb mixture for both thermalisation and

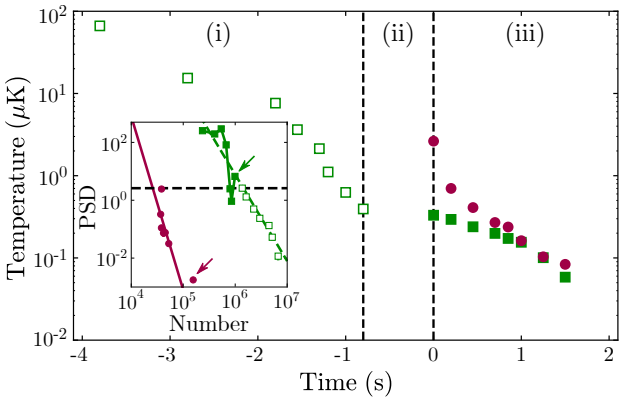

Figure 4.3: **Evaporative cooling of Cs and ^{174}Yb to dual quantum degeneracy.** Temperature evolution of the Yb and Cs samples. Region (i) corresponds to the initial single species evaporation of the Yb sample. Here open green squares denote the ^{174}Yb before the Cs is loaded into the BODT. Region (ii) corresponds to the preparation period of the Cs sample. Region (iii) correponds to the dual-species evaporation sequence. Here, filled green squares denote ^{174}Yb and red circles denote Cs, simultaneously trapped and cooled in the BODT. Inset: phase-space density (PSD) plotted against atom number. The dashed green line is a fit to the open green squares, giving an efficiency of $\gamma_{\mathrm{Yb}} = 3.0(6)$ for Yb in the absence of Cs. The solid red line with a value of $\gamma = 6$, and the solid green line which connects the Yb data points, are both guides to the eye. The arrows denote number/PSD measurements at the point of loading Cs into the BODT. This occurs before the two gases thermalise. Figure adapted from a figure in [162].

sympathetic cooling, due to its moderately large interspecies scattering length of $a_{\mathrm{CsYb}} = -75\,a_0$.

We then perform further forced evaporative cooling of the Yb atoms to begin cooling the mixture. This is achieved through the modification of the BODT beam powers shown in Figure 4.4(a). We apply a bias magnetic field of $B_0 = 22.2\,\mathrm{G}$ throughout this evaporation. This keeps Cs intraspecies scattering length at $a_{\mathrm{Cs}} = 275\,a_0$, close to the Efimov minimum in the three-body recombination rate [150]. Similar Cs evaporation efficiency can be found for bias magnetic fields between 17 G and 19.5 G, and between 20.5 G and 25 G. However, it is critical to avoid the Cs intraspecies Feshbach resonance at 19.9 G. The mean trap frequency and trap depth for both species during the evaporation are shown in figures 4.4(b) and 4.4(c)

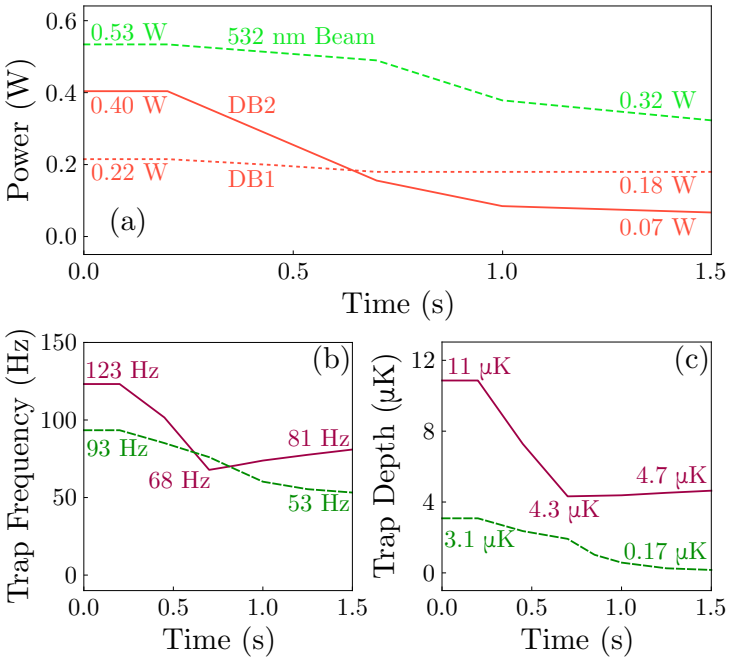

Figure 4.4: **Dual-species evaporative cooling in the BODT.** Yb is cooled by forced evaporation. In turn, the cooled Yb sympathetically cools Cs, resulting in dual-degeneracy. (a) The beam powers used during dual evaporation. The dotted red line is the DB1 power. The solid red line is the DB2 power. The dashed green line is the power of the 532 nm beam. (b) Geometric mean trap frequencies of both atomic species. (c) Trap depths for both atomic species, including 'tilting' of the trap potential due to gravity. In both (b) and (c) the parameters for Cs are shown in red, and those for Yb are shown in green. Figure reproduced from [162].

respectively. Following the evaporation, the trap frequencies in each trapping axis is $(\omega_x, \omega_y, \omega_z)/2\pi = (10, 120, 80)$ Hz for Yb and $(\omega_{\tilde{x}}, \omega_{\tilde{y}}, \omega_z)/2\pi = (40, 70, 260)$ Hz for Cs. The uncertainty on each value of trapping frequency is typically $\sim 10\%$. Note that the final Cs trap is rotated by 20° with respect to the Yb trap axes. We denote the rotated axes as $\tilde{x}$ and $\tilde{y}$.

The trajectories of the evaporation of both species can be seen in the PSD versus atom number plot in the inset of figure 4.3. Prior to the loading of the Cs atoms, the efficiency of the Yb evaporation is $\gamma_{\mathrm{Yb}} = 3.0(6)$. This is shown in the dashed green line of the plot, which is a fit to the open-square data points. Early in the dual-evaporation, Yb crosses back over the BEC transition. Following this, the sympathetic cooling of the Cs atoms continues and remains efficient. The solid red

line in the plot near the Cs data points is a guide to the eye and has an efficiency value of $\gamma = 6$.

4.3 Dual–BEC formation

Towards the end of the dual-species evaporation, Cs also crosses the BEC transition. We can thus produce dual-BECs with condensate atom numbers up to $N_{\mathrm{Yb}} \sim 1 \times 10^5$ for Yb and $N_{\mathrm{Cs}} \sim 2 \times 10^4$ for Cs. However, in this case the atom clouds are bimodal, with high thermal fractions. Figure 4.5 shows optical depth (OD) profiles of the Yb(a) and Cs(b) components of a dual-BEC. The OD profiles were measured by absorption imaging of the atom clouds after a 25 ms time of flight. Sympathetic cooling becomes less efficient after Cs crosses the BEC transition. We can however produce pure degenerate Bose-Bose mixtures by optimising the dual-evaporation parameters specifically for pure BECs. In this case, the pure condensate atom numbers are typically between 4×10^3 and 5×10^3 for Cs, and between 5×10^4 and 7×10^4 for ^{174}Yb. The BEC purity, and final BEC atom numbers, are both highly sensitive to the alignment of the BODT beams. The attractive interspecies interaction, however, helps ensure the BEC overlap. It is also balanced against the repulsive intraspecies interactions, which stabilises the mixture against collapse.

The atom number ratio of the mixture can be varied to some extent by altering the Cs MOT loading time. We are limited, however, to mixtures with a higher number of Yb atoms. The number of Cs atoms that reach low temperatures in any given trapping potential is limited by the Cs three-body recombination rate. Loading a higher number of Cs atoms into the dimple increases the heat load on the Yb atoms. This results in reduced Yb evaporation efficiency while not significantly increasing the final atom numbers in the Cs condensate. If more balanced atom numbers are required for experiment, Yb atoms could be selectively removed following the full evaporation sequence. This could be achieved using a pulse of appropriate time duration of the 399 nm imaging light.

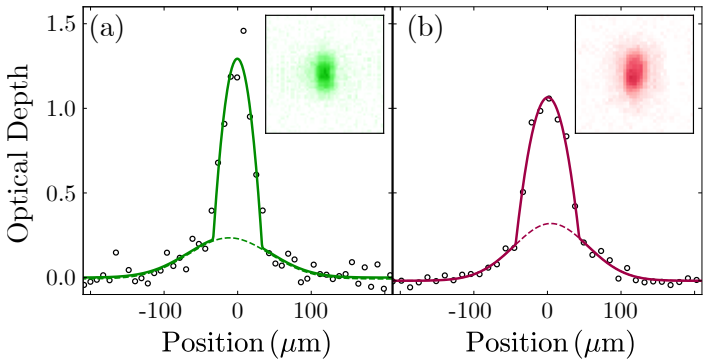

Figure 4.5: **Profiles of Cs and ^{174}Yb BECs.** Cross-sections through the centre of the full 2D optical depth (OD) images (insets) for the ^{174}Yb (a) and Cs (b) BECs. The solid lines are bimodal fits to the 1D OD profiles. Gaussian fits to the thermal contribution of each atom cloud are shown by the dashed lines. The atom numbers within each condensate are extracted from the fits, giving $N_{\mathrm{Yb}} = 6 \times 10^4$ and $N_{\mathrm{Cs}} = 1.6 \times 10^4$. The Yb (Cs) condensate fraction is 0.5 (0.4). Figure adapted from a figure in [162].

4.3.1 Mixture lifetime and losses

We perform lifetime measurements on the mixture by holding the gas in the BODT, with the final beam powers used at the end of evaporation. The decay of the atom number in both species is plotted against the hold time in figure 4.6. We observe double-exponential decay of the Cs atoms, shown by the solid red line in figure 4.6. The 1/e lifetimes from the fit are 0.5(1) s for the faster decay and 5(4) s for the slower decay. We only observe single exponential decay, however, of the Yb atoms, shown by the dashed green line figure 4.6. The lifetime from the fit the same as that of the slower Cs decay, at 5(1) s. The data points of Yb atom number below hold times of 1.2 s are excluded from the Yb single-exponential fit. The Yb atoms remain condensed throughout the lifetime plot. The Cs atoms, however, are no longer condensed after hold times exceeding 1 s.

Heating and loss in the BODT occurs due to three-body recombination and radiative heating caused by photon scattering. For hold times between 2 s and 8 s, we observe heating of the thermal Cs atoms, with a measured heating rate of 19(1) nK/s. The radiative heating rate we predict for Cs using the final BODT

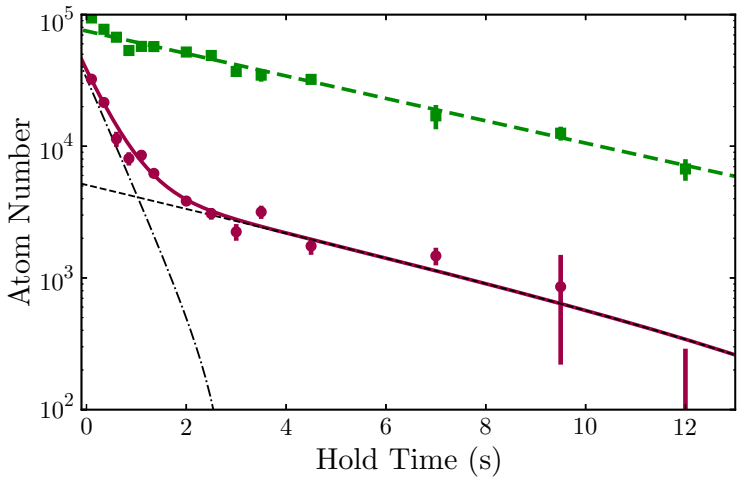

Figure 4.6: **Lifetimes of the dual-degenerate Cs–^{174}Yb mixture.** Cs atom number (red circles) and Yb atom number (green squares) plotted against hold time, following the end of dual-evaporation. The fit to the Cs data is shown by the solid red line, and is a double exponential. The short-term and long-term lifetimes form the fit are $\tau_{1,\mathrm{Cs}} = 0.5(1)\,\mathrm{s}$ and $\tau_{2,\mathrm{Cs}} = 5(4)\,\mathrm{s}$ respectively. The Cs atoms no longer form a BEC for hold times longer than 1 s. The fit to the Yb data is shown by the dashed green line and is a single exponential. The lifetime from the fit is $\tau_{\mathrm{Yb}} = 5(1)\,\mathrm{s}$. Yb lifetime data points at hold times less than 1.2 s are excluded from the exponential fit. Figure reproduced from [162].

beam powers is of the same order of magnitude, at 26 nK/s. Thermal contact between Cs and the Yb BEC should also partially mitigate the heating of Cs.

We calculate an upper bound on the Cs and Cs–Yb three-body loss rate $K_{3,\mathrm{Cs}}$ using the relations

$$K_{3,\mathrm{Cs}} = (\tau_{\mathrm{Cs},1}\langle n_{\mathrm{Cs}} n_{\mathrm{Cs}}\rangle_{\mathrm{sp}})^{-1}, \tag{4.15}$$

and

$$K_{3,\mathrm{CsYb}} = (\tau_{\mathrm{Cs},1}\langle n_{\mathrm{Cs}} n_{\mathrm{Yb}}\rangle_{\mathrm{sp}})^{-1}, \tag{4.16}$$

[24], where $\tau_{\mathrm{Cs},1} = 0.5\,\mathrm{s}$ is the Cs 1/e lifetime observed at shorter hold times, n_{Cs} and n_{Yb} are numerically calculated condensate densities [162], and $\langle\rangle_{\mathrm{sp}}$ denotes a 3D spatial average which is bounded by the spatial extent of the Cs cloud.

Assuming Cs three-body recombination is responsible for all atom loss in the first 1 s of hold time, we calculate a three-body loss rate of $\sim 1.3 \times 10^{-27}\mathrm{cm}^6/\mathrm{s}$ for the Cs condensate. This is a factor of 6 lower than the measured thermal three-body

loss rate of $K_{3,\mathrm{Cs}} \sim 8 \times 10^{-27}\mathrm{cm}^6/\mathrm{s}$, which is similar in magnitude to previous measurements [90; 150]. The factor of 6 is in agreement with the suppression of three-body recombination in a BEC due to the change in the three-body correlation function between a condensed and non-condensed gas, predicted in [171] and experimentally verified in [172]. This suggests Cs three-body recombination is the dominant loss mechanism in the mixture. Alternatively, we can assume that Cs–Yb three body recombination is wholly responsible for the loss. In this case, we can place an upper bound on the loss rate of $K_{3,\mathrm{CsYb}} \sim 2.4 \times 10^{-27}\mathrm{cm}^6/\mathrm{s}$. In practice, the overall loss in the mixture may be a combination of both intraspecies and interspecies processes. We have not been able to determine in our studies how much each process contributes to the overall loss.

4.4 Dynamics of a degenerate mixture of Cs and ^{174}Yb

We now discuss two experiments which utilise the attractive interspecies interactions of the Cs + ^{174}Yb mixture, with its negative scattering length of $-75\,a_0$. Firstly, we show the dynamics of the two condensates are coupled when inducing centre-of-mass oscillations in the Cs condensate. We then alter the scattering properties of the Cs condensate using a Feshbach resonance to investigate the collapse of the condensates of both species.

4.4.1 Centre-of-mass oscillations

In this first experiment, we excite vertical centre-of-mass (CoM) oscillations, and observe the resulting coupled dynamics of the degenerate mixture. A magnetic field gradient of 9.0 G/cm is ramped on adiabatically in the vertical direction at the end of the dual-species evaporation described in section 4.2. The field gradient

shifts the trap minimum position vertically by 0.96(7) µm for Cs, without directly affecting the trapping potential for Yb (recalling Yb has no magnetic moment).

We then rapidly switch off the magnetic field gradient. This excites a CoM dipole mode in the vertical direction. After a variable hold time, we extinguish the BODT beams. We then perform absorption imaging on the Cs BEC following a 40 ms period of levitated time of flight (ToF). During both the oscillation hold time and the following levitated ToF, a_{Cs} is held constant at $275\,a_0$. We also measure CoM oscillations of Cs in the absence of Yb as a reference. These measurements are taken in quick succession to the dual-species oscillation experiments. This ensures the vertical trap frequncies, which are highly sensitive to BODT alignment, are the same in both cases. For the Cs-only measurements, we perform dual-species evaporation as normal, before selectively removing Yb by applying a 5 ms pulse of resonant 399 nm light. We then excite the Cs CoM oscillations by applying the field gradient as before.

Figure 4.7a shows the Cs CoM oscillations in the presence of Yb, plotted as green circles. The Cs-only oscillations are plotted in figure 4.7b as green circles, the fit of which is also shown by the dashed green line in figure 4.7a. The Cs-only oscillations occur at a frequency of $2\pi \times 251(1)$ Hz. This is the Cs natural trap frequency according to our simulations of the BODT. There is also minimal damping in the Cs oscillations. In the presence of Yb, however, the Cs oscillation frequency is shifted upwards by 4(1) %. There is also significant damping in the oscillations. The frequency shift is in good agreement with predictions using first-order mean-field theory [173]. These predictions assume the Yb BEC has a Thomas-Fermi profile, and do not account for back-action on the Yb atoms by the Cs BEC, which may occur despite the large imbalance in atom number in our system. This model predicts an increase in frequency of 5 %. This is due to the Cs experiencing an additional attractive quadratic potential as a result of the interspecies interaction.

We find through further numerical simulations of the experiment [173] that, in the region of overlap between the two species, the attractive interspecies interaction

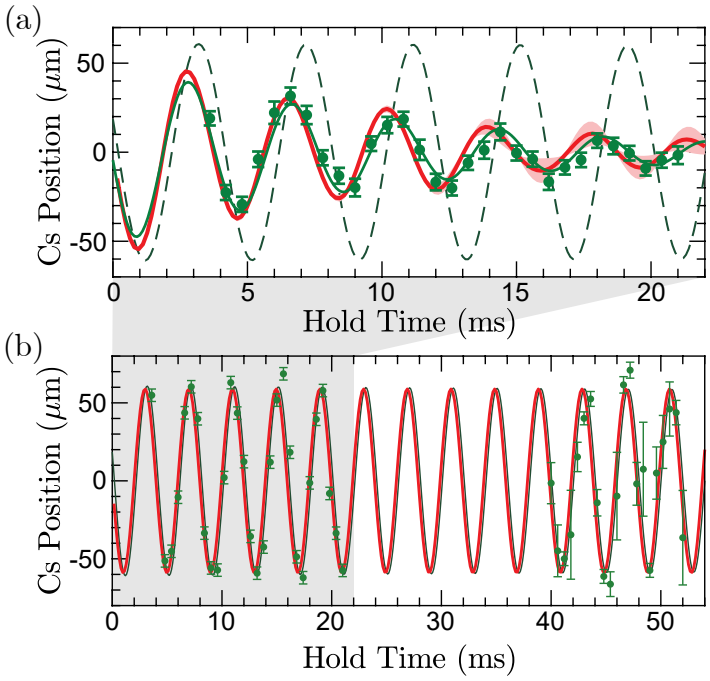

Figure 4.7: **Coupled dynamics of Cs and Yb.** (a) The vertical centre-of-mass position of the Cs BEC plotted against hold time in the BODT. The green points are experimental data points. We fit a sinusoidal function with an exponential decay term of the form $Ae^{-\beta t}\sin(\omega t + \phi_0)$ to the data. This is shown by the green line. The parameters of the fit are amplitude $A = 52(8)\,\mu\text{m}$, angular frequency $\omega = 2\pi \times 260(2)\,\text{Hz}$, and damping term $\beta = 0.10(2)\,\text{ms}^{-1}$. The red line is a numerical simulation [173]. The red band at longer hold times indicates the standard deviation of the simulation. (b) The centre-of-mass position of the Cs BEC in the absence of Yb. This yields an angular frequency of $\omega = 2\pi \times 251(1)\,\text{Hz}$. The fit to the measurement in (b) is re-plotted in (a) as the dashed green line. Figure adapted from a figure in [173].

causes a 'bulge' of density in the Yb BEC. This bulge is off-centre from the Yb trap centre. This shifts the Yb CoM upwards by $\Delta z_{\text{Yb}}^{\text{CoM}} = 0.1\,\mu\text{m}$. The interaction also reduces the shift of the Cs CoM shift to $\Delta z_{\text{Cs}}^{\text{CoM}} = 0.88\,\mu\text{m}$.

The red lines in figures 4.7a and 4.7b show the simulations of the Cs oscillations in the Cs+Yb case and the Cs-only case respectively. The simulations for the Cs+Yb mixture indicate that the relative atom numbers of the Cs and Yb BECs strongly affect the shifts in CoM and the ensuing coupled dynamics. In figure 4.7, ($N_{\text{Yb}}/N_{\text{Cs}} \approx 6$). Figure 4.8 shows representative plots where both the Cs and Yb atom numbers are varied over a wide range. Other factors affecting the

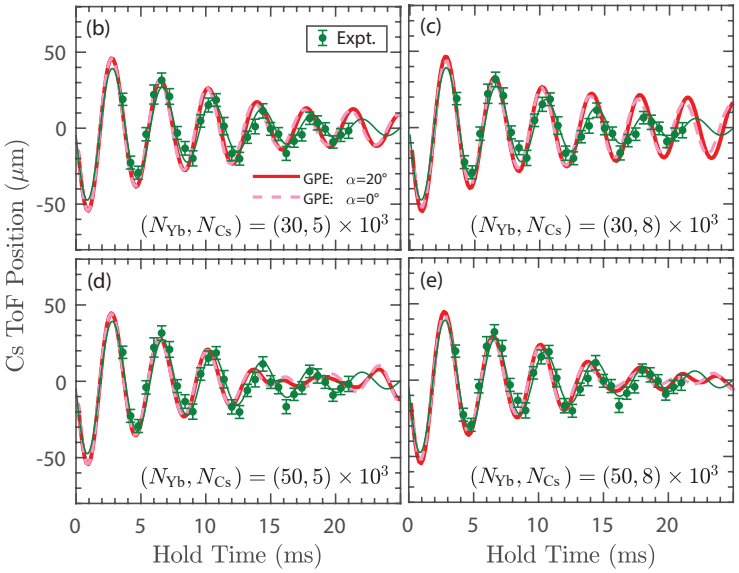

Figure 4.8: **Cs and Yb coupled dynamics for different atom numbers.** Cs vertical centre-of-mass positions in the presence of Yb. Green points are experimental data points. Green lines are a damped sinusoidal fit to the each set of experimental data. Red lines are numerical simulations [173] incorporating the physical geometry of the experiment $\alpha = 0°$, where α is the rotation angle of the long axis of the Cs BEC with respect to that of the Yb BEC. The dashed pink lines are numerical simulations using $\alpha = 0°$. Figure reproduced from [173].

dynamics are the difference in vertical trap frequencies of the two components ($\omega_{Cs,z} \approx 3\,\omega_{Yb,z}$), as well as the BODT geometry, with the Yb BEC having a broader spatial extent in the direction with weaker confinement. Therefore, the resulting dynamics is dominated by that of the central bulge within the Yb BEC, which interacts directly with the Cs BEC. Figures 4.7 and 4.8 also show significant damping as energy is transferred from the Cs to the Yb. Further theoretical studies in [173] give further insight into the damping and the complicated coupled dynamics during the energy transfer, as Cs pulls Yb along in the region of overlap. It is also predicted that, for longer hold times than those explored experimentally, there may be revivals in the amplitude of the Cs oscillations.

4.4.2 Dual-species collapse

In this experiment, we tune the relative mean-field contributions to the dynamics of the mixture by varying the scattering length of Cs. The attractive interspecies interaction causes the mean-field collapse of the Cs BEC in the presence of the Yb BEC. This is shown in figure 4.9.

In a BEC composed of a single component, collapse [174; 175; 176; 177; 178] occurs when an attractive intraspecies interaction is sufficient to overcome the zero-point kinetic energy related to the harmonic potential the BEC is trapped in. The experimental signature of the collapse is density-dependent atom loss. For a BEC of given atom number N, the onset of collapse is related to the critical scattering length $a^{(\mathrm{crit})}$, given by

$$|a^{(\mathrm{crit})}| = C\sqrt{\hbar/(m\bar{\omega})}/N. \tag{4.17}$$

Here, $\bar{\omega} = \sqrt[3]{\omega_x\omega_y\omega_z}$ is the geometric mean trap frequency. C is a numerical constant, which is weakly dependent on the geometry of the trap [176; 179; 180].

For a dual-species BEC, the threshold for collapse threshold depends primarily on the relative strengths of the inter- and intraspecies interactions. The critical point of collapse for a dual-species BEC is determined by the parameter δg, given by

$$\delta g = g_{12} + \sqrt{g_{11}g_{22}}. \tag{4.18}$$

This parameter describes the balance of the mean-field interactions in a two-component system. The interaction coupling constant g_{ij} is given by

$$g_{ij} = \frac{2\pi\hbar^2 a_{ij}(m_i + m_j)}{(m_i m_j)}, \tag{4.19}$$

for an atom pair i and j with masses m_i, m_j and scattering length a_ij. The onset of collapse occurs when $\delta g < 0$ [181; 13; 12].

We experimentally investigate dual-species collapse by varying a_{Cs}. This is performed in the magnetic bias field region of 16 G to 19.5 G, where a_{Cs} is highly tuneable due to the presence of Feshbach resonances at 14.4 G, 15.0 G and 19.9 G.

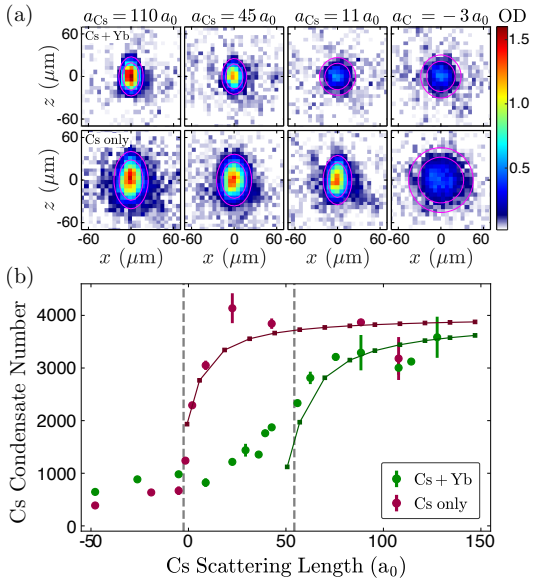

Figure 4.9: **Dual-species collapse.** (a) Optical depth (OD) profiles of the Cs BEC at varying values of a_{Cs}. Top row: The collapse of the Cs BEC mediated by the ^{174}Yb BEC. Bottom row: single-species collapse of the Cs BEC. The pink contours in each image show the radii at which OD is a factor of $1/e$ and $1/e^2$ of the peak value. (b) Cs condensate number as a function of a_{Cs}. Green circles correspond to Cs collapse mediated by ^{174}Yb. Red circles correspond to Cs single-species collapse. The single-species collapse threshold theoretically predicted for $N_{Cs} = 4 \times 10^3$ is at $a_{Cs} = -2.5\,a_0$ and is denoted by a dashed vertical line. The cancellation of the mean-field interactions $\delta g = 0$, occurs at $a_{Cs} = 54.3\,a_0$, also denoted by a dashed vertical line. The green and red squares are the results of the GPE simulations incorporating three-body loss [173], for the Cs-Yb mixutre and Cs only respectively. The solid green and red lines are guides to the eye. Figure reproduced from [173].

In this region, $a_{Cs} = 0$ at 17.0 G. The dual-species BEC is produced at a magnetic bias field of 19.4 G, corresponding $a_{Cs} = 147\,a_0$. The atom numbers of the dual BEC are $(N_{Yb}, N_{Cs}) = (50, 4) \times 10^3$. We first ramp a_{Cs} over 10 ms to the desired value of magnetic bias field. We then hold the mixture at this field for 30 ms, before applying a 10 ms ramp back to $a_{Cs} = 147\,a_0$. We then image the BECs after time of flight expansion. Figure 4.9 shows the onset of collapse, marked by a decrease in Cs atom number. This is due to 3-body losses ($K_{3,Cs} \sim 1 \times 10^{-27}$cm^{6}s^{-1} [90; 150; 162] in the magnetic field range of the experiment), enhanced by the increase in density. The profiles of the Cs BECs, for scattering lengths ranging from +110 a_0 to -3 a_0, are shown in the absorption images in figure 4.9(a). The top row shows Cs

in the presence of Yb, whereas the bottom row shows Cs in the absence of Yb. The collapse instability occurs at $a_{\mathrm{Cs}} > 0$ when Yb is present. At this point, we would expect single-component Cs BEC to be stable. We also observe that the aspect ratio of the Cs cloud changes. In figure 4.9(b), the Cs condensate number is plotted against the Cs scattering length. The red circles denote Cs condensate number in the absence of Yb. The predicted collapse point for $N_{\mathrm{Cs}} = 4 \times 10^3$ Cs atoms occurs at $a_{\mathrm{Cs}} = -2.5\,a_0$, marked by a vertical line. The collapse of Cs in the presence of Yb is marked by the green circles. The point for which $\delta g = 0$ in the Cs–Yb mixture occurs at $a_{\mathrm{Cs}} = 54.3\,a_0$, also marked by a vertical line.

The experimental protocol was modelled numerically by using 3D coupled Gross-Pitaevskii equations [173], which includes includes a density-dependent Cs 3-body loss term. A vertical trap frequency $\omega_{\mathrm{Cs,z}} = 2\pi \times 260\,\mathrm{Hz}$ is also used in the simulations. Figure 4.9(b) shows the results of the simulations, in the Cs+Yb case (green squares) and in the Cs-only case (red squares). The Yb-mediated collapse is experimentally observed to be broader than the simulations predict. However, this is not the case for the Cs-only collapse. Both the Cs+Yb and Cs-only collapse experiments were undertaken with similar atom temperatures. Therefore, the broadening of the Yb-mediated collapse cannot be explained by finite-temperature effects. It may be the possible that the broadening indicates the presence of beyond-mean-field effects. These could in future be utilised in the experimental formation of quantum droplets (see chapter 8).

4.5 A dual BEC of Cs and ^{170}Yb

We now discuss a dual-degenerate Bose-Bose mixture of Cs and ^{170}Yb. This was achieved using similar Cs and Yb preparation and dual-evaporation techniques as for Cs and ^{174}Yb, as discussed in section 4.2. In this mixture, the Cs–^{170}Yb interspecies scattering length is $96\,a_0$ and the ^{170}Yb intraspecies scattering length is $64\,a_0$. Although these scattering lengths are of the same order of magnitude

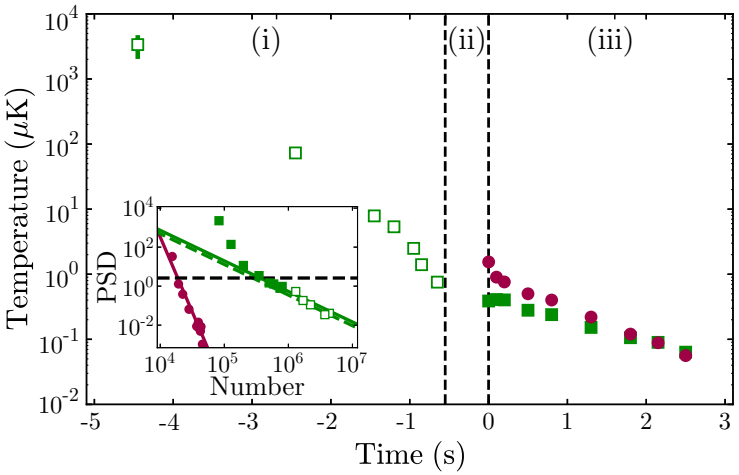

Figure 4.10: **Evaporative cooling of Cs and ^{170}Yb to dual-degeneracy.** (a) Temperature plotted against evaporation time. Region (i) shows the initial Yb evaporation. Here, open green squares denote the ^{170}Yb atom number. Region (ii) is the time period in which Cs is prepared for BODT loading. Region (iii) is the subsequent dual-species evaporation sequence. Here, the filled green squares denote the ^{170}Yb atom number. The red circles denote the Cs atom number. The inset shows the PSD plotted as a function of atom number. We calculate evaporation efficiencies from the fits to PSD data. The Cs evaporation efficiency is 7.7(6). The Yb evaporation efficiency is 1.6(2) with Cs present, and 1.6(5) with Cs absent. Figure reproduced from [162].

as the scattering lengths of Cs and ^{174}Yb, the critical difference in the Cs–^{170}Yb mixture is the positive interspecies scattering length. In contrast to the attractive interaction we have seen in the Cs–^{174}Yb mixture, this mixture therefore has a repulsive interspecies interaction.

4.5.1 Evaporation to dual degeneracy

This dual-evaporation routine is broadly similar to that of the Cs–^{174}Yb mixture. However, the initial preparation of ^{170}Yb takes longer. This is for two reasons. Firstly, our MOT loading times are longer. This is due to the low natural abundance of ^{170}Yb of 3 %, in comparison to that of ^{174}Yb, which is 32 %. Secondly, the lower intraspecies scattering length of ^{170}Yb means we require a longer single species evaporation stage. The temperature evolution of Cs and ^{170}Yb during Yb evaporation and dual evaporation is shown in figure 4.10. The inset of the figure

shows PSD plotted against atom number, with fits to the data, for both species. From the fits, we calculate a Cs evaporation efficiency of $\gamma_{\mathrm{Cs}} = 7.7(7)$. For Yb the efficiency is $\gamma_{\mathrm{Yb}} = 1.6(5)$ prior to loading the Cs, and $\gamma_{\mathrm{Yb}} = 1.6(2)$ for dual evaporation. We typically produce pure Cs–^{170}Yb dual-BECs, with atom numbers $N_{\mathrm{Yb}} \sim 4 \times 10^4$ and $N_{\mathrm{Cs}} \sim 1 \times 10^4$.

4.5.2 Immiscibility

Degenerate mixtures with repulsive interactions, such as Cs–^{170}Yb, possess a phase-instability. This is typically observable experimentally as the miscible-immiscible transition between the two BECs. Whether the mixture is miscible or immiscible depends on the balance of its interspecies and intraspecies interaction energies [182; 183]. In the limit where the density distributions of the gases are assumed to be homogeneous, the transition is characterised by

$$\Delta = \frac{g_{11}g_{22}}{g_{12}^2} - 1. \tag{4.20}$$

Phase separation of the gases occurs when $\Delta \leq 0$ [184]. Here, g_{ij} is the interaction coupling constant given by equation 4.19. In our BODT, the atoms are confined within a harmonic trap, and the density profile of our atomic gases is therefore inhomogenous. Nevertheless, Δ can still be used to quantify the miscibility of the mixture, provided the mixture's atom numbers are balanced, $N_1 \sim N_2$. Under this assumption, immiscibility would occur in our mixture for our mixture for $a_{\mathrm{Cs}} \leq 147\, a_0$. However, given the imbalance of atom number in our system, we must also consider the effects of our BODT trapping parameters, as well as the relative atom numbers of Cs and Yb [185].

The OD profiles of three different Cs–^{170}Yb mixtures, with a range of atom number ratios, are shown in figure 4.11. In each case, we use a fixed Cs atom number of $N_{\mathrm{Cs}} = 5.5 \times 10^3$, and varied the Yb atom number. This results in number ratios $N_{\mathrm{Cs}}/N_{\mathrm{Yb}}$ of 0.7, 1.9 and 4.7. Horizontal cross sections of the OD through the centre of each OD profile are shown on the bottom row of figure 4.11. The cross

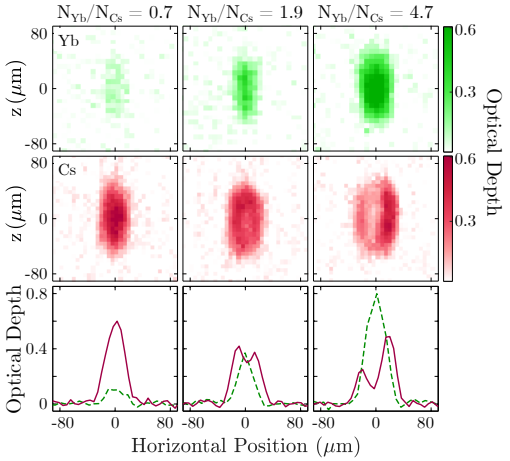

Figure 4.11: **Immiscibility in the Cs and ^{170}Yb dual-degenerate mixture.** Optical depth (OD) profiles of the ^{170}Yb BEC (top row) and the Cs BEC (middle row). The OD profiles are extracted from absorption images, which were taken after 20 ms time of flight expansion. Horizontal cross sections taken through the centre of the OD profiles are shown on the bottom row. The cross-sections show the average OD of the 6 pixels centred horizontally about $\Delta z = 0$. Cs OD cross-sections are shown by the solid red lines. Yb OD cross-sections are shown by the dashed green lines. A Gaussian fit to each atom cloud is used to independently centre each image. The atom number ratios are (L-R): $N_{\mathrm{Yb}}/N_{\mathrm{Cs}} = 0.7$, $N_{\mathrm{Yb}}/N_{\mathrm{Cs}} = 1.9$, and $N_{\mathrm{Yb}}/N_{\mathrm{Cs}} = 4.7$. For all three images, $N_{\mathrm{Cs}} = 5.5 \times 10^3$. The intraspecies scattering lengths are $a_{\mathrm{Yb}} = 64\,a_0$ and $a_{\mathrm{Cs}} = 440\,a_0$. The interspecies scattering length is $a_{\mathrm{CsYb}} = 96\,a_0$. The distortions in the Cs OD profiles in the two rightmost columns demonstrate partial immiscibility of the two BECs. A slight misalignment of the horizontal trap centres causes the asymmetry observed in the Cs 'lobes' in the rightmost Cs OD profile. Figure adapted from a figure in [162].

sections are an average of 6 pixels in the imaging system for each species, centred on $\Delta z = 0$. For these measurements, the dual-BECs were formed at the usual magnetic bias field of 22.2 G. We then ramped the magnetic bias field adiabatically to 26.0 G. The Cs intraspecies scattering length at this field is $a_{\mathrm{Cs}} = 440\,a_0$, and hence from equation 4.20, $\Delta = 2$. This places the system above the miscibility transition in the homogenous case by a comfortable margin. As we increase the Yb atom number, the mixture shifts towards the immiscible regime. This can be seen in both the OD profile and cross-section (bottom-centre and bottom-right panels of figure 4.11 respectively) for $N_{\mathrm{Yb}}/N_{\mathrm{Cs}} = 4.7$. Here, the number of Cs atoms in the centre of these images is reduced. This shift towards immiscibility may be due

to a combination of mis-matched trapping potentials between the two species in the BODT, and the imbalance in the two species' atom number [185].

Achieving and maintaining good BEC overlap is much more sensitive for the Cs–^{170}Yb mixture, with its repulsive interspecies interaction, than for the the Cs–^{174}Yb mixture. In that case, the attractive interspecies interaction assists in pulling the BECs towards each other and maintaining overlap. If the relative positions of the clouds are slightly offset, very different density profiles can be observed. This is demonstrated by the rightmost profile for the Cs atoms in figure 4.11, where asymmetry in the two lobes either side of the Yb cloud is observed. In the extreme case, all of the Cs atoms can be pushed into a single lobe on one side or the other. This motivates utilising a trapping geometry which does not have the trap alignment difficulties inherent in the BODT, and where the trap frequencies of the Cs and the Yb are better matched. One option to realise this could be use of an optical dipole trap tuned to a wavelength where the trap frequencies are equal for both species (see chapter 5).

4.6 Conclusion

In this chapter, the BODT was used to produce the first quantum mixtures of pure Cs–^{174}Yb BECs. The typical atom numbers of this mixture $N_{\mathrm{Yb}} \sim 5 \times 10^4$ and $N_{\mathrm{Cs}} \sim 5 \times 10^3$. We used similar methods to produce pure Cs–^{170}Yb BECs. The typical atom numbers in this mixture are $N_{\mathrm{Yb}} \sim 4 \times 10^4$ and $N_{\mathrm{Cs}} \sim 1 \times 10^4$. We utilise the favorable interspecies interactions during dual-species evaporative cooling, enabling efficient sympathetic cooling of Cs. This takes place in both Cs–^{174}Yb, where the interspecies scattering length of $a_{\mathrm{CsYb}} = -75\,a_0$ leads to attractive interspecies interactions, and Cs–^{170}Yb, where the interspecies scattering length of $a_{\mathrm{CsYb}} = 96\,a_0$ leads to repulsive interspecies interactions. The collective dynamics of the Cs+^{174}Yb mixture have been investigated. The dipole mode frequency of CoM oscillations of Cs have been observed to increase in the presence of Yb.

Significant damping of the oscillations is also observed, as energy is transferred from the Cs to the Yb. The stability of the degenerate mixture has also been investigated, by crossing the dual-species collapse transition. We find good agreement between experiment and coupled-GPE simulations which include a three-body loss term for Cs. We have also investigated the immiscibility of the Cs–^{170}Yb mixture, and its dependence on the relative atom numbers of each condensate.

Chapter 5

Measurement of atomic polarizability using a tuneable optical lattice

5.1 Introduction

Previous chapters have described our ability to realise, and conduct initial experiments with degenerate mixtures of Cs and Yb. These experiments to date have utilised three-dimensional bulk gas mixtures of Cs and Yb. We wish to extend our experimental capabilities by reducing the dimensionality of the system to two or one dimensions by introducing additional confining potentials. This would allow us to study the differing properties of degenerate mixtures in reduced dimensions. A three-dimensional optical lattice would also reduce losses due to collisions, which may be significantly enhance our ability to efficiently produce CsYb molecules. We would also like to exploit the differences in the atomic properties of Cs and Yb to create mixed-dimensional systems where the number of spatial dimensions the atoms are confined to is different for both species.

In this chapter, we report on the development of a tuneable, species selective optical

lattice in our experiment. We discuss how our choice of wavelength for the lattice allows us access multiple wavelengths of interest, including Cs-blind 'tune-out' wavelengths, where the real part of the atomic polarizability $\mathrm{Re}(\alpha)$ vanishes, and wavelengths where either the trapping potential or the trap frequency is equal for both species. We describe the experimental setup of a one-dimensional optical lattice and demonstrate Kapitza-Dirac diffraction of BECs of both Cs and ^{174}Yb. We describe the measurements undertaken to date of the atomic polarizability of Cs in the wavelength range accessible by the lattice. We discuss the limitations of these results, and possible improvements in order to take further measurements and implement the lattice into the experiment.

5.2 Atomic polarizability and tune-out wavelengths

As discussed in section 3.1.1, the potential due to the dipole force experienced by atom by light of intensity I is given by

$$U_{Edip} = -\frac{\mathrm{Re}(\alpha)I}{2\epsilon_0 c}. \tag{5.1}$$

An approximation of the real part of the atomic polarizability can be calculated as a function of angular frequency ω by [159]

$$\mathrm{Re}(\alpha) = 3\pi\epsilon_0 c^3 \sum_{f\neq i} \frac{A_{i,f}}{\omega_{0,f}^3}\left(\frac{1}{\omega_{0,f}-\omega} + \frac{1}{\omega_{0,f}+\omega}\right), \tag{5.2}$$

where $\omega_{0,f}$ and $A_{i,f}$ are the angular frequencies and Einstein A-coefficients of transitions from the atomic ground state i to an excited state f.

Figure 3.2 (shown in chapter 3) shows the polarizability of both Cs and Yb in the atomic ground state across a wavelength range 300–1200 nm. Equation 5.2 gives the primary contribution to the polarizability by the valence electrons of the atom. In figures 3.2 and 5.1, polarizability is converted from SI units (as stated in equation 5.2) to atomic units by a conversion factor of $\frac{1}{4\pi\epsilon_0}$ and displayed in units of a_0^3, where a_0 is the Bohr radius. A full model of the polarizability also incorporates

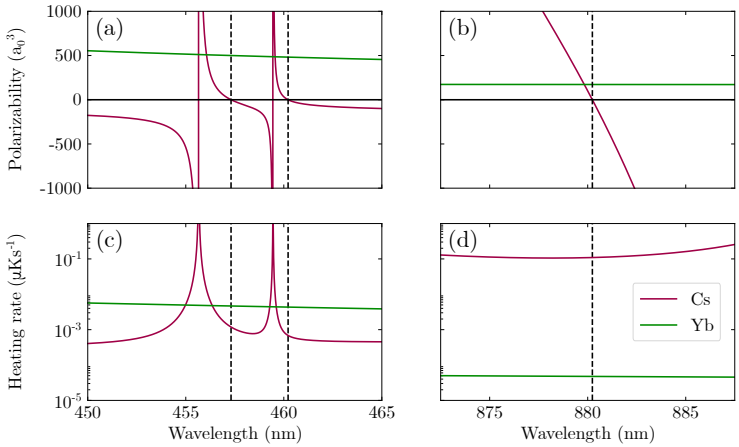

Figure 5.1: **Comparing tune-out wavelengths at 460 nm and 880 nm.** (a) and (b): the polarizabilities of ground state Cs (red) and Yb (green), calculated using equation 5.2. The values of transition wavelengths and corresponding Einstein A-coefficients used in the calculation are listed in appendix A and are taken from [160] and [161]. (a) polarizability near the Cs 6s→7p transitions around 460 nm. (b) The zero-crossing of polarizability in Cs between the D1 and D2 lines, at 880.24 nm. Vertical lines denote the position of the tune-out wavelengths. (c) and (d): the heating rates of Cs and Yb, (c) around 460 nm and (d) around 880 nm, using a laser intensity sufficient to trap Yb at a depth of 1 μK. The vertical dashed lines show the tune-out wavelengths summarised in table 5.1.

static contributions to the polarizability from the ionic core, and excitations to the occupied valence shell by the inner electrons (the valence-core or Pauli-blocking term) [186]. For Cs, a core polarizability contribution, calculated in [187] of 15.5 a_0^3 is added in our calculation. The valence-core contribution is assumed to be negligible and is not included in the calculation. There is no information for the core and valence core contributions for the polarizability of Yb, but in the discussion below we consider the far-detuned case where contributions of the order of those for Cs would make a negligible contribution to the overall polarizability.

This wavelength range encompasses multiple atomic transitions from the ground state. Between successive transitions, there are wavelengths for which the contributions to the polarizability from each transition cancel out, giving a net polarizability of zero. In turn, this means that the atoms experience no dipole potential at these wavelengths– the atoms are 'blind' to the trapping light used. We refer to these

wavelengths as 'tune-out' wavelengths [188; 189], although the term 'magic-zero' wavelength is also used in literature [164]. The values of tune-out wavelengths for a number of alkali atoms are given in [189].

The use of a tune-out wavelength enables creation of species selective potentials in our experiment [188; 189]. We are able to identify wavelengths which are a tune-out wavelength for one species, but have positive polarizability and hence an attractive potential for the other. This leads to a scenario where one species is trapped by an optical potential of that wavelength, but the other is not and will only be confined in the science chamber by additional potentials. This allows us to realise a mixed-dimension system. Such systems have previously been realised experimentally, allowing the measurement of properties such as scattering properties[190; 110], entropy exchange[191], and lattice band structure[110].

The measurement of tune-out wavelengths has gained specific interest within the wider field of precision measurements of atomic polarizability. Applications for these measurements include optical lattice clocks and quantifying lattice potentials. polarizability data of the alkali atoms can be used as benchmarks for testing theoretical methods of calculating polarizability for more complex atoms such as Er and Dy [164]. Measurements of tune-out wavelengths specifically can be used to determine atomic properties such as dipole matrix elements, oscillator strengths, and state lifetimes [164; 192]. Recently reported discrepancies between theory and experiment of such properties [193; 194; 195; 196] further highlight the importance of such measurements as a benchmark test.

Atomic polarizability can be measured directly using a number of experimental techniques, including atom diffraction [164], parametric heating [196], and atom interferometry [197]. Such measurements have been previously been made in alkali metal atoms including Li [198; 199], K[192; 200] and Rb [164; 191; 201], other atomic species including He [202], Sr [196] and Dy[203], and the ground state of the NaK molecule[204]. The polarizability of Cs has been the subject of much theoretical work [205; 206; 207; 208]. Recently, the tune-out wavelength between

λ (nm)	α_{Yb} (a_0^3)	$\delta(\alpha_{\mathrm{Cs}})$ ($a_0^3\mathrm{THz}^{-1}$)	$\delta(\alpha_{\mathrm{Yb}})$ ($a_0^3\mathrm{THz}^{-1}$)
457.31	499.9	80	4.60
460.22	481.7	80	4.24
880.24	172.4	1100	0.25

Table 5.1: The tune-out wavelengths where $\alpha_{\mathrm{Cs}} = 0$, with the corresponding values of polarizability in Yb. The tune-out wavelengths are calculated using equation 5.2 and the additional core contribution to the polarizability, and give 0.01 nm agreement to the values calculated in [189]. The values of polarizability in Yb values are positive, indicating that optical trapping of Yb is possible at these wavelengths. Also shown is the shift in polarizability per unit frequency for each species at these wavelengths.

the D1 and D2 lines at 880.24 nm has been measured experimentally [209]. In this chapter however, we consider tune-out wavelengths at higher frequencies.

For our purposes, we consider the 6s→7p transitions in Cs, at 455.66 nm and 459.45 nm. The polarisabilty of both atomic species around these transitions is shown in figure 5.1(a). We identify two tune-out wavelengths for Cs in this wavelength range. One is between the transitions to the $7P_{\frac{3}{2}}$ and $7P_{\frac{1}{2}}$ states at 457.31 nm. The other is red-detuned of the transition to the $7P_{\frac{1}{2}}$ state, at 460.22 nm. Crucially, at these wavelengths, the polarizability of Yb is positive and has a value of $\sim 500\, a_0^3$. This fulfils the criteria for a species-selective trap outlined above.

Alternatively, the tune-out wavelength at 880.24 nm (shown in figure 5.1(b)) can be used. One advantage of this wavelength is that more optical power may be available to create a deeper potential for Yb. However, it can be seen in table 5.1 that the polarizabilities of Yb at the tune-out wavelengths around 460 nm are approximately three times the magnitude of the polarizability at the 880.24 nm tune-out wavelength. Hence, at these wavelengths, less laser intensity is needed to create an optical trap of equivalent depth.

We also wish to avoid the scenario where drifts in the laser frequency change the polarizability of Cs to a value where an appreciable dipole potential is experienced.

	λ (nm)	α_{Cs} (a_0^3)	α_{Yb} (a_0^3)	$\delta(\alpha_{\mathrm{Cs}})$ ($a_0^3\mathrm{THz}^{-1}$)	$\delta(\alpha_{\mathrm{Yb}})$ ($a_0^3\mathrm{THz}^{-1}$)
$\alpha_{\mathrm{Cs}} = \alpha_{\mathrm{Yb}}$	456.06	508.2	508.2	1100	4.72
	459.56	485.7	485.7	3700	4.28
$\alpha_{\mathrm{Cs}}/\alpha_{\mathrm{Yb}} = \sqrt{m_{\mathrm{Cs}}/m_{\mathrm{Yb}}}$	456.10	445.6	507.9	900	4.72
	459.57	425.8	485.6	2900	4.27

Table 5.2: Upper two rows: wavelengths where $\alpha_{\mathrm{Cs}} = \alpha_{\mathrm{Yb}}$, resulting in equal trapping potential both species. Lower two rows: wavelengths where $\alpha_{\mathrm{Cs}}/\alpha_{\mathrm{Yb}} = \sqrt{m_{\mathrm{Cs}}/m_{\mathrm{Yb}}}$, resulting in equal trap frequencies for both species. Also shown is the shift in polarizability per unit frequency for each species at these wavelengths.

As the tune-out wavelengths are far-detuned from atomic transitions, spectroscopic techniques cannot be used to stabilise the trapping light wavelength. Our lattice light source is locked to a reference cavity (see section 5.4.1). However, this system is more susceptible to wavelength drifts than spectroscopic techniques. It can be seen in table 5.1 that, at 880.24 nm, while the polarizability of Yb is an order of magnitude less sensitive to frequency changes than at the wavelengths around 460 nm, the polarizability of Cs is an order of magnitude more sensitive. Therefore, in order to create a Cs-blind optical trap at 880.24 nm the wavelength of the light must be stabilised to within a smaller frequency range.

Another feature of the wavelength range around 460 nm is the ability to create more balanced traps for both species. This may, for example, assist in the later stages of evaporative cooling to double degeneracy. The wavelengths where polarizability are equal for both species correspond to equal *depths* of trap for the two species. These wavelengths are given in the upper section of table 5.2. However, creating a trap of equal *frequency* may prove more useful as this minimises differential gravitational sag and ensures optimal overlap of the two atomic species. Assuming a harmonic potential for the lattice both radially and axially, the criterion for this is simply that the ratio of trap depths for each species is equal to the square root of the mass ratio. In our case, $\sqrt{m_{\mathrm{Cs}}/m_{\mathrm{Yb}}} = 0.876$. The wavelengths where the ratio of the

λ (nm)	Intensity ($\mathrm{Wcm^{-2}}$)	Γ_{sc}(Yb) (Hz)	$\dot{T}$(Yb) ($\mathrm{nKs^{-1}}$)	Γ_{sc}(Cs) (Hz)	$\dot{T}$(Cs) ($\mathrm{nKs^{-1}}$)
457.31	880	26.4×10^{-3}	4.7	5×10^{-3}	1.2
460.22	924	24.9×10^{-3}	4.3	3×10^{-3}	0.7
880.24	2582	1.0×10^{-3}	0.048	1760×10^{-3}	109.3

Table 5.3: The laser intensity required to trap Yb with a depth of 1 µK at each wavelength, and corresponding scattering and heating rates for both atomic species at these intensities.

polarizability has this value are given in the lower part of table 5.2. We identify 456.10 nm as the more useful of these wavelengths, as it is further detuned from the transition to the $7P_{\frac{3}{2}}$ state than the equivalent wavelength near the transition to the $7P_{\frac{1}{2}}$ state, and will cause less heating of the Cs due to photon scattering.

We also consider the effect of heating of both species due to off-resonant photon scattering. The heating rate, assuming a three-dimensional trap geometry, is given by

$$\dot{T} = \frac{1}{3} T_{\mathrm{rec}} \Gamma_{\mathrm{sc}}, \tag{5.3}$$

where wavelength-dependent recoil velocity T_{rec} is given by

$$T_{\mathrm{rec}} = \frac{\hbar^2 k^2}{m}, \tag{5.4}$$

and photon scattering due to the dipole potential is given by [159]

$$\Gamma_{\mathrm{sc}} = \sum_{f \neq i} \frac{3\pi c^2 A_{i,f}}{2\hbar\omega_{0,f}^3} \left(\frac{\omega}{\omega_{0,f}}\right)^2 \left(\frac{1}{\omega_{0,f} - \omega} + \frac{1}{\omega_{0,f} + \omega}\right)^2 I. \tag{5.5}$$

The laser intensity I required at each tune-out wavelength for a Yb trap depth of 1 µK, which is representative for our purposes, was calculated using equation 5.1, and the resulting scattering and heating rates calculated. The heating rates for both atom species at a trap depth of 1 µK are shown in figure 5.1(c) an 5.1(d) around the tune-out wavelengths near 460 nm and 880 nm respectively. The parameters relevant to atom heating are summarised in table 5.3. While the Yb heating rate is two orders of magnitude lower at 880.24 nm compared to the wavelengths around

λ(nm)	Nearest transition	Δ/Γ
457.31	6s $^2S_{\frac{1}{2}} \rightarrow$ 7p $^2P_{\frac{3}{2}}$	1.3×10^6
460.22	6s $^2S_{\frac{1}{2}} \rightarrow$ 7p $^2P_{\frac{1}{2}}$	1.4×10^6
880.24	6s $^2S_{\frac{1}{2}} \rightarrow$ 6p $^2P_{\frac{1}{2}}$	190×10^3

Table 5.4: The tune-out wavelengths, with detuning expressed as number of linewidths away from the nearest atomic transition.

460 nm, the heating rate for Cs is two orders of magnitude higher at 109 nK s^{-1}. This can be understood by comparing the fine structure splitting of both the 6s $\rightarrow$ 6p and 6s $\rightarrow$ 7p transitions in Cs, measured as numbers of linewidths of the respective transitions. For the 6s $\rightarrow$ 6p transition, this figure of merit is $\sim 5 \times 10^5$ whereas for the 6s $\rightarrow$ 7p transition, it is $\sim 5 \times 10^6$. Therefore, as seen in table 5.3, when measured by number of linewidths, the tune-out wavelength at 880.24 nm is closer to the nearest transition than those near 460 nm. This, and the requirement for higher laser intensity to create a trap of equivalent depth due to the lower value of α_{Yb}, results in a higher heating rate at this wavelength.

5.3 Kapitza-Dirac diffraction using a optical lattice

5.3.1 Introduction to optical lattices

Optical lattices are a well-established technique of optical trapping of neutral atoms and molecules [210]. Two counterpropagating beams of coherent light of the same frequency will interfere, with intensity maxima at the electric field antinodes and minima at the nodes. The interference provides additional axial confinement on the scale of the radiation wavelength compared to single or crossed dipole trapping beams. As with dipole traps discussed previously, atoms which experience an attractive dipole potential will be attracted towards regions of high intensity. The antinodes of the lattice thus become a series of periodically spaced optical

microtraps.

The simplest experimental method of creating an optical lattice is to retroreflect a dipole trapping beam which is already focused at the position of the atoms to trap them. The beam must be recollimated prior to retroreflection so that the retroreflected beam waist approximately matches the waist of the first pass of the beam. In this case, the trap depth of each lattice site is four times that of the equivalent dipole trap generated by the single-pass beam. The lattice spacing is half that of the radiation wavelength.

5.3.2 Introduction to Kapitza-Dirac diffraction

The techniques used to characterise dipole traps, such as trap loading, lifetime and trap frequency measurements, are also applicable to optical lattices. However, the depth of the lattice potential can also be measured by probing the lattice's band structure properties [210]. The method of Kapitza-Dirac diffraction was employed, as will be seen in later sections, to perform characterisation of the lattice. It was then further used to probe the variation in the polarizability of Cs within the lattice wavelength range.

Kapitza-Dirac diffraction [211] employs pulses of the lattice on an ultracold gas, typically on the order of µs. A schematic of such an experiment can be seen in figure 5.2. The lattice transfers quanta of momentum $2\hbar kl$ to a population of the BEC along the axis of the lattice, where k is the lattice wavevector $k = \frac{2\pi}{\lambda}$ and l is an integer. Following the lattice pulse, the different momentum states can be resolved and imaged using absorption imaging after time of flight. The diffraction pattern produced depends on the depth of the lattice and the time duration of the pulse. A deeper lattice will result in higher orders of diffraction contributing to the overall diffraction pattern. The method is therefore routinely used to measure lattice depths [212; 213; 214], and has been further applied to make polarizability measurements near tune-out wavelengths [201; 203; 209]. The following sections

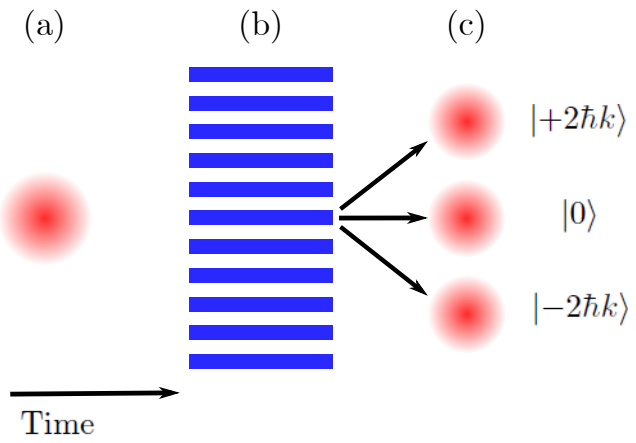

Figure 5.2: **Principle of Kapitza-Dirac diffraction.** A BEC at time (a) is subject to a pulsed lattice potential at time (b), during which quanta of momenta $\pm 2\hbar k$ is transferred to a population of the BEC along the lattice vector. For clarity, we assume a lattice depth where only the first diffracted orders are populated. Following the pulse, time of flight expansion (c) allows the different diffracted populations of the BEC to be resolved by absorption imaging.

describe how the evolution of the diffracted population of each order with time duration of pulse can be used to determine lattice depth.

5.3.3 Kapitza-Dirac Theory

The optical lattice potential is an example of a periodic potential $V(x)$ of the form

$$V(x) = V_0 \cos^2(kx), \tag{5.6}$$

Where V_0 is the lattice depth, lattice wavevector $k = \frac{2\pi}{\lambda}$ and lattice period $a = \frac{\lambda}{2}$. Here we assume the lattice is approximately a plane wave for the spatial extent of the BEC. The waist of the focused lattice beam must exceed the BEC size sufficiently for this potential to be valid across the BEC. This allows us to write a time-independent Schrödinger equation for the BEC in the lattice of the form

$$-\frac{1}{k^2}\frac{d^2\psi(x)}{dx^2} + s \cdot \cos^2(kx)\psi(x) = \epsilon\psi(x). \tag{5.7}$$

Here the lattice depth and energy eigenstate are given as dimensionless quantities, $V_0 = sE_\mathrm{R}$ and $E = \epsilon E_\mathrm{R}$, scaled by the lattice depth $E_\mathrm{R} = \frac{\hbar^2 k^2}{2m}$. To solve equation 5.7, we can invoke Bloch's theorem, which states that all solutions to a wavefunction in a periodic potential $V(x)$ can be written as a product of a plane wave $e^{\frac{iqx}{\hbar}}$ and a function $u_{n,q}(x)$ with the same periodicity as the potential:

$$\psi_{n,q}(x) = e^{iqx/\hbar} u_{n,q}(x). \tag{5.8}$$

Here, the index n is the lattice band, and q is the quasimomentum. Using this ansatz in equation 5.7 gives

$$-\frac{1}{k^2}\left(-\frac{q^2}{\hbar^2} + \frac{2iq}{\hbar}\frac{d}{dx} + \frac{d^2}{dx^2}\right) u_{n,q}(x) + s\cos^2(kx) u_{n,q}(x) = \epsilon_{n,q} u_{n,q}(x). \tag{5.9}$$

As $u_{n,q}(x)$ has the same periodicity as the lattice, it can be expanded as a Fourier series:

$$u_{n,q}(x) = \sum_{l=-\infty}^{\infty} c_{l,n,q} e^{i2klx} = \sum_{l=-\infty}^{\infty} c_{l,n,q} \left|\phi_{2\hbar kl}\right\rangle. \tag{5.10}$$

The Bloch wavefunctions can then be written as:

$$\psi_{n,q}(x) = \sum_{l=-\infty}^{\infty} c_{l,n,q} e^{ix(2kl+q/\hbar)} = \sum_{l=-\infty}^{\infty} c_{l,n,q} \left|\phi_{2\hbar kl+q}\right\rangle. \tag{5.11}$$

Note the momentum of these wavefunctions is $2\hbar kl + q$. By substituting equation 5.10 into equation 5.9 and comparing terms with the same factor of e^{i2klx}, an equation for the Hamiltonian can be written in matrix form:

$$\sum_{l=-\infty}^{\infty} H_{l,l'} . c_{l,n,q} = \epsilon_{n,q} c_{l,n,q}, \tag{5.12}$$

where

$$H_{l,l'} = \begin{cases} \left(2l + \frac{q}{\hbar k}\right)^2 + \frac{s}{2} & \text{if } l = l' \\ -\frac{s}{4} & \text{if } |l - l'| = 1 \\ 0 & \text{otherwise} \end{cases}. \tag{5.13}$$

This system of equations can be solved to find the eigenstates and eigenenergies of lattice. This is in general a linear combination of momentum states l, with energy $\epsilon_{n,q}$. A finite range of l must be chosen to solve equation 5.12. The resulting band

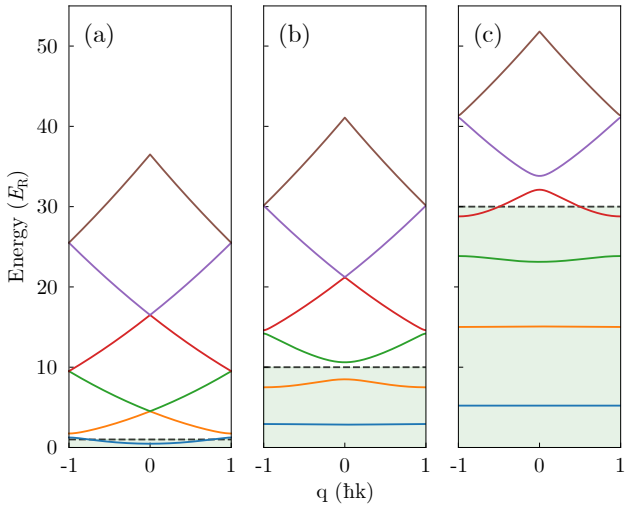

Figure 5.3: **The band structure of an optical lattice.** The energy eigenvalues $\epsilon_{n,q}$ of the six lowest lattice bands n, plotted against the quasimomentum q, for lattice depths of (a) $1\,E_\mathrm{R}$, (b) $10\,E_\mathrm{R}$, and (c) $30\,E_\mathrm{R}$. The eigenvalues were calculated by solving equation 5.7 numerically [215], for $l_\mathrm{min} = -20$ and $l_\mathrm{max} = 20$. The green shaded areas bounded by the dashed horizontal lines indicate lattice depth. Note that with increasing lattice depth, the energy variation of the lower bands with respect to q becomes flatter, and the energy spacing of the bands becomes greater.

structure of the lattice is shown in figure 5.3, where the eigenenergies of the first 6 bands of the lattice have been calculated. Further discussion of the minimum and maximum l to choose in the calculation to simulate the lattice dynamics is given in [215].

We now consider non-adiabatic loading of a BEC into the lattice, as in the case of suddenly switching on the lattice during a pulse sequence. We consider the BEC as a plane-wave, $|\phi_q\rangle = e^{iqx}$ with momentum q. When the lattice is switched on, the BEC state is projected onto the Bloch states $|n, q\rangle = \phi_{n,q}(x)$:

$$|\psi(t=0)\rangle = \sum_{n=0}^{\infty} |\psi_n(t=0)\rangle = \sum_{n=0}^{\infty} |n,q\rangle \langle n,q|\phi_q\rangle \,. \tag{5.14}$$

Using equation 5.11 to calculate $\langle n, q|\phi_q\rangle$ gives

$$\langle n,q|\phi_q\rangle = \sum_{l=-\infty}^{\infty} c^*_{l,n,q} \langle \phi_{2\hbar k l+q}|\phi_q\rangle = c^*_{0,n,q}. \tag{5.15}$$

We can substitute the solution of equation 5.15 into equation 5.14, and then allow each eigenstate to evolve for a time t, according to the lattice eigenenergies calculated in equation 5.12:

$$|\psi_n(t)\rangle = |\psi_n(t=0)\rangle\, e^{-i\epsilon_{n,q}\hbar k^2 t/2m} \tag{5.16}$$

$$|\psi_n(t)\rangle = c^*_{0,n,q}\,|n,q\rangle\, e^{-i\epsilon_{n,q}\hbar k^2 t/2m}. \tag{5.17}$$

At time t, the lattice is switched off and the states are projected back onto the plane-wave basis:

$$|\psi_n(t)\rangle = \sum_{n=0}^{\infty} c^*_{0,n,q} c_{l,n,q} e^{-i\epsilon_{n,q}\hbar k^2 t/2m}\,|\phi_{2\hbar k l+q}\rangle \tag{5.18}$$

$$|\psi_n(t)\rangle \equiv \sum_{n=0}^{\infty} b_{l,n,q}\,|\phi_{2\hbar k l+q}\rangle\,. \tag{5.19}$$

The $b_{l,n,q}$ coefficients give the fractional population in each band n and momentum state l. Our detection method of absorption imaging of the BEC after time of flight is able to resolve the l states. The population of the BEC with momentum $2\hbar l k$ is given by

$$P(l) = \left|\sum_{n=0}^{\infty} b_{l,n,q}\right|^2. \tag{5.20}$$

We are not, however, able to resolve the bands n. The time-dependence of the populations can be interpreted as interference between the bands n, whose phases evolve sinusoidally at different rates according to equation 5.17.

For our purposes of lattice calibration and polarizability measurement, we were able to utilise software previously developed by the RbCs group in Durham [215] in Python, with the SciPy package which has libraries for linear algebra and matrix manipulation. The program solves the model above and simulates the evolution of populations for a given lattice spacing and atomic mass. The simulations can be fit to data from Kapitza-Dirac experiments using a nonlinear least-spares fit. The total BEC number N and dimensionless lattice depth s are the fitting parameters, and statistical uncertainties of both variables are calculated from the covariance

matrix of the fit. Further details of how our experimental data is used in the program is given below. The program assumes $q = 0$, which is valid only if the lattice and BEC are static relative to each other. The outgoing and retroreflection beams of are lattice have no relative detuning, and we assume our BEC to have no initial momentum at the start of the lattice pulse, so we conclude this is a valid assumption for our system.

5.4 Experimental setup of the tuneable lattice

This section describes the experimental setup of a one-dimensional optical lattice beam oriented near to the vertical axis through the main experimental chamber. This orientation was chosen for ease of optical access, and so that a viewport pair with low reflectivity around 460 nm could be used. Ultimately, as will be seen in later sections, we would instead wish to switch to a horizontally orientated one-dimensional lattice. However, the setup described below has been used to demonstrate lattice diffraction of a Cs BEC. It has also been used to refine both the experimental setup of the lattice beam, and experimental process. These insights can be carried forward into a future horizontal lattice setup.

5.4.1 Lattice light source

The lattice light source is the frequency-doubled output of a Ti:Sapphire laser system. The Ti:Sapphire laser used in this setup is the SolsTiS system from MSquared. An etalon within the Ti:Sapphire cavity ensures a narrow linewidth output. Transmission on a single longitudinal etalon mode is achieved by locking the etalon to peak transmission on the nearest mode. Further frequency stabilisation and reduction in the linewidth to less than 50 kHz can be achieved by locking to the fringe of a reference cavity, also provided by MSquared, which some of the output of Ti:Sapphire is directed to.

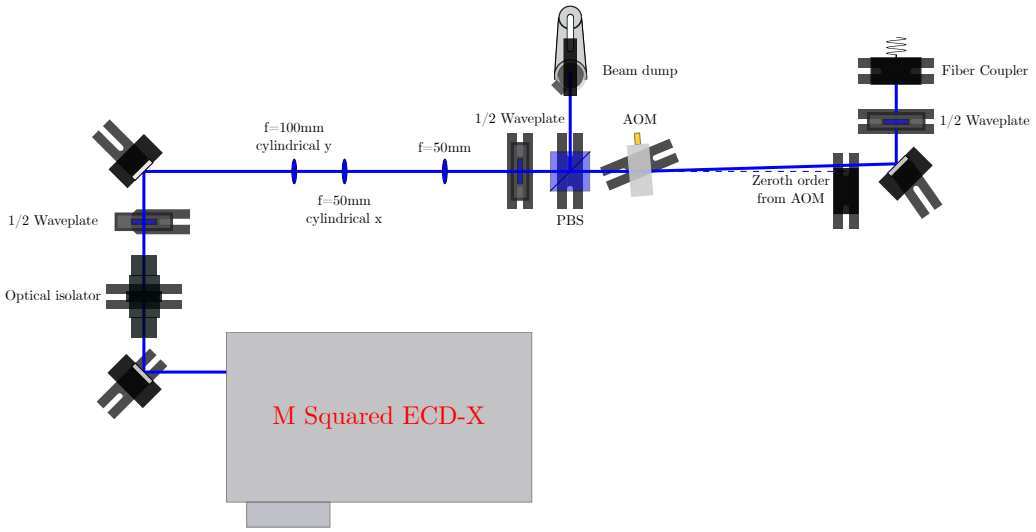

Figure 5.4: **Lattice laser table optics.** The output of the ECD-X doubling cavity is aligned through an optical isolator, beam reshaping telescope and AOM. The first diffracted order of the AOM is aligned into the optical fiber.

The output beam of the Ti:Sapphire is aligned into a doubling cavity. This an ECD-X cavity from MSquared. The doubling crystal in the cavity is efficient over the frequency range 457.5 nm to 461 nm. For a 1.6 W input of light from the SolsTiS tuned to 919.0 nm, we have been able to get a maximum output of 800 mW of light at 459.5 nm from the doubling cavity.

Further detail of the lattice light source is given in appendix B.

5.4.2 Lattice laser table optics

The optical setup on the optical table, from the doubling cavity output to the optical fiber input, is shown in figure 5.4. Retroreflections back into the cavity may result in cavity tuning issues. As the beam is ultimately retroreflected to form the optical lattice, an optical isolator (Thorlabs IO-5-440-HP) is used after the cavity output. The transmission efficiency of the isolator when aligned is 90.8(1.5) %.

The output of the ECD-X is collimated by a pair of cylindrical lenses within the ECD-X module. However, we found the output profile to be elliptical, with a

horizontal waist of 320 µm and a vertical waist of 680 µm. This corresponds to a horizontal to vertical aspect ratio of 0.47. To ensure good fiber coupling and AOM efficiency, we use a pair of cylindrical telescopes to reshape the beam to be circular. This consists of a 2:1 telescope in the y axis and a 1:1 telescope in the x axis. The y (x) axis of the beam is focused by a cylindrical lens of focal length 100 mm (50 mm). To save space on the optical table and to minimise optical components, the beam is collimated in both axes by a single spherical lens of focal length 50 mm. All three of the telescope lenses can be translated longitudinally to fine-tune the beam collimation and aspect ratio. This results in a collimated beam with a horizontal waist of 366(12) µm and a vertical waist of 373(6) µm. The beam aspect ratio is 0.98(5).

We use a fixed-frequency AOM (Isomet 1206-C, 833) in single-pass configuration for power stabilisation. Contrary to the dipole trapping beams, we align the beam as collimated by the telescope through the AOM. The collimated beam propagates fully through the active aperture of the AOM crystal (1 mm). We use the first diffracted order of the AOM as the fiber input. This allows us to switch the lattice beam on off at the experiment on the order of the AOM rise time (53 ns for a beam of 0.34 mm diameter). We can control the beam intensity using an analogue output from the experimental control. We can either stabilise the intensity using the analogue output and the same design of servo box used for the dipole trapping beams, or directly drive the analogue input of the AOM rf driver-amplifier (Isomet 533C–2). The latter is used for pulsed applications for two reasons. Firstly, the bandwidth of the servo box is not sufficient to produce an adequately square-wave pulse on the µs scale. The second reason is beam pointing through the AOM. The beam pointing drifts after a time period of the order of a few seconds. The difference in beam pointing between immediately after the AOM is switched on ('AOM cold'), and the steady state position after the beam has drifted ('AOM hot'), is sufficient to affect fiber coupling. Therefore, when using the lattice beam for continuous-wave applications, we align the setup with the AOM on continu-

ously, and use beam intensity stabilisation. For pulsed applications, we drive the amplitude modulation input of the driver-amplifier directly to produce the beam of desired power. In either 'hot' or 'cold' alignment configurations, the optimum AOM efficiency is 81.0 %.

The first diffracted order of the AOM is coupled into a high-power single-mode fiber (Ozoptics QPMJ-A3AHPCA3AHPC-488-3/125-3AS-9-1-AR2-SP) to couple the light over to the main experimental table. A 60FC-F-4-M5-33 collimator from Schäfter and Kirchoff is used to couple light into the fiber. The optimal fiber coupling efficiency achieved is 70 %, including losses in the fiber itself. The fiber was routed across the lab through a foam insulated pipe to minimise the effect of temperature drifts.

We have designed the optical setup with provision for splitting the collimated light on a PBS. This would create a second beam path, which would propagate through an additional AOM and fiber. The second fiber would be routed through the same insulated pipe as the first. This would allow us to set up a horizontal lattice path in the science chamber, resulting in a two-dimensional lattice. However, the power in each lattice beam would effectively be half of the power currently available in the one-dimensional lattice. To create a deep optical lattice for Cs, the lattice wavelength would have to be chosen carefully. The appropriate wavelength range for this is near-resonance red detunings from either transition.

5.4.3 Lattice beam optics

The vertical viewport pair was chosen for the one-dimensional lattice due to the favourable transmission of the viewport pairs. The transmission of the 460 nm beam through both vertical viewports is 80.5(1.7) %. The vertical viewports had only been previously used for the vertical MOT beams, vertical DRSC beam and the DRSC polariser beam. This axis allows for a greater angle of deviation between the beam and the viewport axis. This allowed us to devise a beam path at a greater

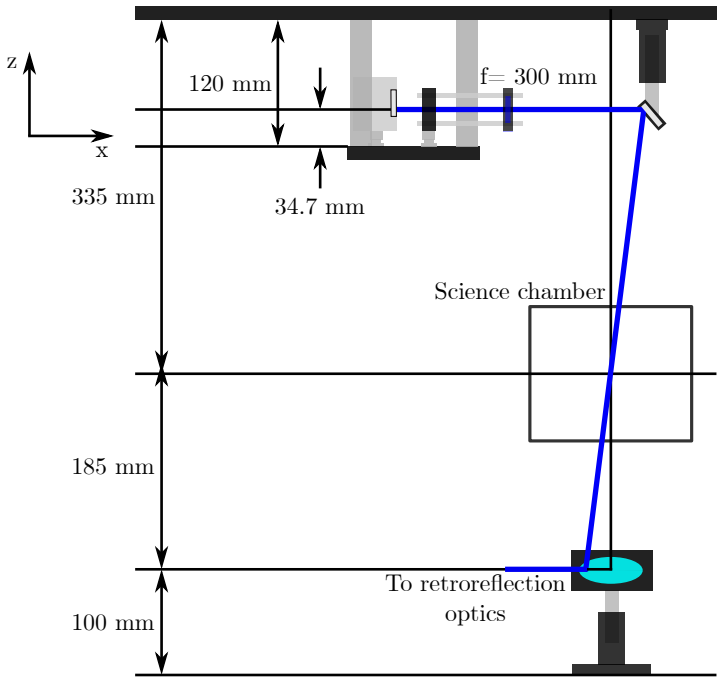

Figure 5.5: **The vertical lattice beam path.** The breadboard for the fiber output is suspended 120 mm below the upper breadboard. The fiber output is horizontal with a beam height of 34.7 mm above the breadboard. The focused lattice beam propagates from the breadboard optics (see figure 5.6a) to the deflection mirror. From this deflection mirror, the beam propagates through the science chamber at an angle of approximately 7 ° to the vertical. Beneath the chamber, the beam is propagates to the retroreflection optics via a 2 inch mirror already *in situ* for the vertical MOT beams.

angle of deviation from orthogonal to the viewport planes, allowing the existing beam paths to be avoided. A 2 inch diameter mirror underneath the chamber already *in situ* for the MOT beams is used to deflect the lattice beam.

The path of the lattice beam through the science chamber is shown in figure 5.5. The pre-existing breadboard above the main chamber contained the retroreflection optics for the MOT beams and fiber outputs for the DRSC beams. For the lattice beam fiber launch, we chose to use a second breadboard suspended 120 mm below the first breadboard by four posts. The optics contained on this breadboard is shown in figure 5.6a. The same type of collimator as the fiber input (Schäfter and Kirchoff 60FC-F-4-M5-33) is used to collimate the fiber output. This results in a horizontal beam waist of 346(11) µm and a vertical beam waist of 341(5) µm. The

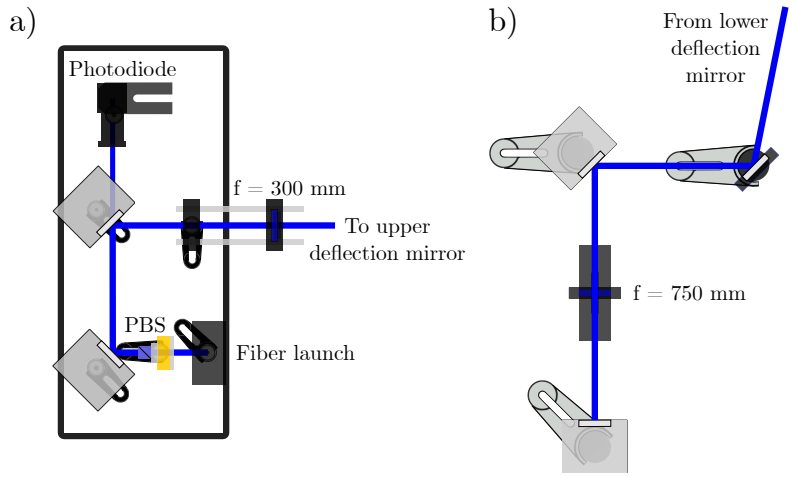

Figure 5.6: **Lattice beam optics - horizontal sections.** a) The upper breadboard. The beam is launched from the fiber and collimated, before passing through a PBS cube to ensure linear polarisation at the beam focus. The beam is aligned though a focusing lens of focal length 300 mm. There is also a beam pickoff to a photodiode, for beam monitoring and stabilisation. b) Beneath the chamber the lattice beam is recollimated by a lens of focal length 750 mm and retroreflected.

aspect ratio of the collimated beam is 1.01(5). The breadboard also contains a pickoff using a rear-polished mirror onto a photodiode. The type of photodiode used here again depends on the application of the beam. For monitoring a lattice pulse or pulses, a fast photodiode can be used. For using the beam in continuous-wave mode, a homebuilt photodiode designed to monitor continuous-wave light can be used with the photodiode signal connected to the sensor input of the servo box to allow intensity stabilisation. The breadboard also contains a 300 mm focal length lens to focus the beam in the centre of the science chamber. The optical design gives a beam waist of 126(6) µm. This lens is mounted in a cage mount. This allows axial adjustment of the lens to adjust the axial position of the beam focus.

The beam propagates through, and leaves, the breadboard optics in a horizontal orientation. To deflect the beam downward through the chamber, a mirror is suspended from the breadboard above the lattice breadboard. The positioning of this mirror is not in any conflict with other vertical beams. Care was taken to

mount the mirror in a mechanically robust way to prevent damage to the science chamber viewport directly beneath. The mirror mount is a Thorlabs KM100T mount, with the original screw adjusters replaced by higher-precision micrometer adjusters (Thorlabs DM22). This would give us more precise experimental control when aligning the beam.

The positioning of this deflection mirror means the beam propagates through the chamber at an angle of approximately 7 ° to the vertical, with this deflection being parallel to the Zeeman slower axis. This deflection means the beam is still reflected by the 2 inch mirror underneath the main chamber. This mirror deflects the beam into a horizontal plane approximately 100 mm above the surface of the main optical table. The optics to subsequently recollimate and retroreflect the beam are shown in figure 5.6b. A further two mirrors steer the beam to an axis where it can be recollimated. The recollimation lens has a focal length of 750 mm. The correct axial position of this lens to ensure collimation was determined using a shear plate interferometer. Behind this recollimation lens is positioned the retroreflection mirror. This mirror is located near the edge of the optical table, allowing ease of adjustment of the retroreflected beam. The mirror is mounted in a POLARIS-K1 mount, allowing higher precision adjustment of the retroreflected beam.

Provided the lattice beam is recollimated sufficiently well, the retroreflected beam should back-couple through the optical fiber with close to 100 % efficiency. Therefore, having first performed coarse alignment to ensure the retroreflection was incident on the fiber output, a non-polarising beam splitter cube was placed on the optical table in the beam path before the fiber input. The power measured here has components split off from the outgoing and retroreflected beams, so the outgoing component is subtracted to give the retroreflected component. This power was then optimised for the adjustment of the retroreflection mirror, and for fine-tuning the axial position of the recollimation lens. This method of lattice realignment was used regularly while taking measurements which required regular changes to the lattice frequency. We note that any changes to the alignment of the outgoing beam

will in turn require realignment of the retroreflected beam.

5.5 Characterisation of the tuneable lattice

5.5.1 Lattice characterisation using Kapitza-Dirac diffraction

Prior to using the lattice for polarizability measurements, we wished to know the range of lattice depths we could expect to measure, given the beam waist and available beam powers. We also wished to characterise the sensitivity of the alignment of the lattice and how this might affect measurements.

The intensity of the lattice is dependent on both the beam power and waist. The beam power cannot be measured directly within the science chamber, but can be inferred from measurements on either side, and the resulting transmission values from each viewport pair. We must also consider that the retroreflected beam has a lower power than the incoming beam due to power losses at the retroreflection optics. The effective beam power contributing to the lattice is therefore $2\sqrt{P_{in}P_{\mathrm{Retro}}}$. The excess contribution from the incoming beam $P_{\mathrm{Incoming}} - P_{\mathrm{Retro}}$ contributes as an effective additional dipole potential. Yb has a polarizability of $\sim 500\, a_0^3$ within the lattice tuning range, but in comparison to the dipole trapping beams, the available beam powers are low and the beam waist is of the order of three times the size. This makes exciting either centre-of-mass or breathing mode oscillations, in order to extract a trap frequency, difficult experimentally, although parametric heating could be used.

We instead consider Kapitza-Dirac diffraction of a BEC, using a single lattice pulse, for characterisation. As discussed in section 5.3.3, the time evolution of the diffracted orders can be used to extract a lattice depth. This value is obtained independently of prior knowledge of the beam waist or intensity. The wavelength-dependent lattice depth of Cs could then be compared to that of Yb at the same wavelength,

provided the pulse intensity was kept consistent, and beam waist and alignment was not altered.

5.5.2 Producing the lattice pulses

We found that producing the lattice pulse using intensity stabilisation through the servo box would be unfeasible for the required pulse duration (of the order 10s of µs). This is due to the low bandwidth of the servo box affecting the pulse shape. For the pulses of less than $\sim 20\,\mu s$, the beam did not reach full intensity within the pulse duration. We drive the driver-amplifier with a square-wave pulse generated by a function generator (SRS DS345). The function generator was set to operate in 'burst mode', where the function generator outputs a finite number of square waves. This mode is triggered by a digital output from the experimental control. The amplitude, offset, frequency, and phase of the burst is set so that the output is a top-hat pulse of the required pulse duration. The AOM driver receives a modulation voltage of between 0 and 1.0 V. We therefore send pulses of amplitude 0.8 V to the driver, resulting in a reproducible modulation signal sent to the AOM, and a reproducible value of power in the lattice beam. For the following measurements we set the function generator to output a single oscillation, resulting in a single square-wave pulse. However, we have the capability to output a train of multiple pulses, which may in future be useful in enhancing the diffraction signal at low magnitudes of polarizability (see section 5.9.3).

The amplitude and shape of the pulse was monitored on a fast photodiode (THORLABS PDA8A/M, bandwidth 50 MHz). This allowed us to monitor the lattice intensity in real-time while running the experiment. If a reduction in photodiode signal was detected, it could be improved by checking the fiber coupling or the status of the doubling cavity intensity stabilisation.

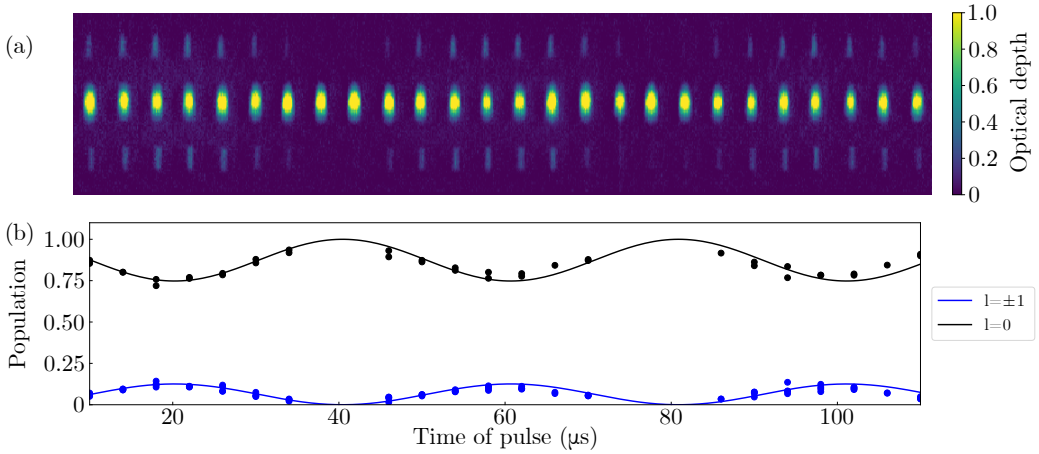

Figure 5.7: **Kapitza-Dirac diffraction of an Yb BEC.** Initial diffraction experiment with bosonic Yb, proving the efficacy of the lattice. Diffraction as a result of a pulsed lattice of depth 3.24(3) E_{R}. (a) Absorption images showing time dependence of the diffraction pattern. The undiffracted $l = 0$ order is visible in the centre row and the $|l = 1|$ diffraction orders (top and bottom rows) are visible. (b) Evolution of the populations of each momentum state. The solid lines are Kapitza-Dirac simulations fitted to the data. Data points where the atom number in the $|l = 1|$ orders were too low to be fitted by our image analysis software were omitted.

5.5.3 Experimental sequence

The typical experimental sequence closely resembles that for single-species evaporation of either Cs or a bosonic Yb isotope to degeneracy. The Cs evaporation sequence only requires the use of the 1070 nm beams. As the intensity of these beams is lower when Cs is loaded from the reservoir, the gravitational sag of the dimple trap is increased compared to the Yb or dual-species dimple trap. Therefore, the dimple beams must be carefully realigned to optimise the loading of Cs. Once a pure BEC has been produced, the BODT beams are extinguished and the function generator is simultaneously triggered to generate a pulse of the optical lattice. The lattice pulses are of the order 10s of μs and the free fall of the BEC under gravity is assumed to be negligible in this time period.

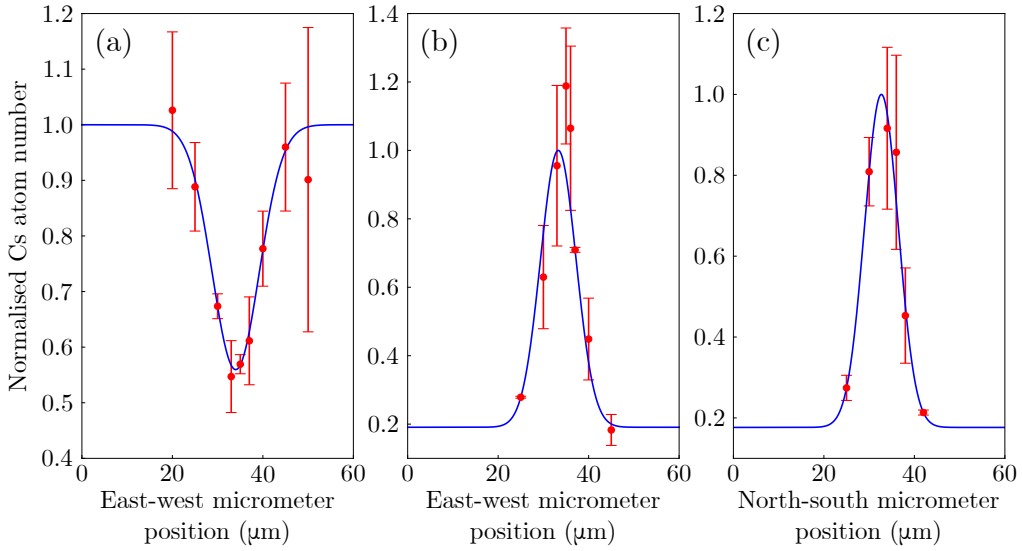

Figure 5.8: **Using Kapitza-Dirac diffraction to fine-tune alignment.** Having produced a three-component diffraction pattern of a Cs BEC, we set the lattice pulse time to 6 μs and measure the atom number in each component. (a) The atom number in the central $l = 0$ component is minimised by adjusting the east-west axis of the final alignment mirror. (b) and (c) the atom number in the $l = +1$ component is maximised by adjusting the east-west and north-south axes of the final alignment mirror respectively. Blue solid lines are Gaussian fits to the data used to find the centre of each alignment.

5.5.4 Using lattice diffraction to fine-tune alignment

After first verifying that Kapitza-Dirac diffraction could be observed, we would then measure the diffraction pattern for a range of pulse lengths. An example of this measurement for an Yb BEC is shown in figure 5.7. A characteristic signature of Kapitza-Dirac diffraction for all lattice depths is that, for pulse times immediately after zero, the $l = 0$ population reduces from 100 % and the $l = 1$ population increases. We initially map out this trend with our lattice measurements as in figure 5.7. By fixing the pulse time in this region, the alignment of the lattice (both alignment to the BEC and relative alignment of the lattice beams) can be optimised by minimising the $l = 0$ and maximising the $l = \pm 1$ populations. This process is shown in figure 5.8, where the lattice pulse time has been set to 6 μs. Initially the atom number in the $l = 0$ order is minimised by adjusting the alignment in the east-

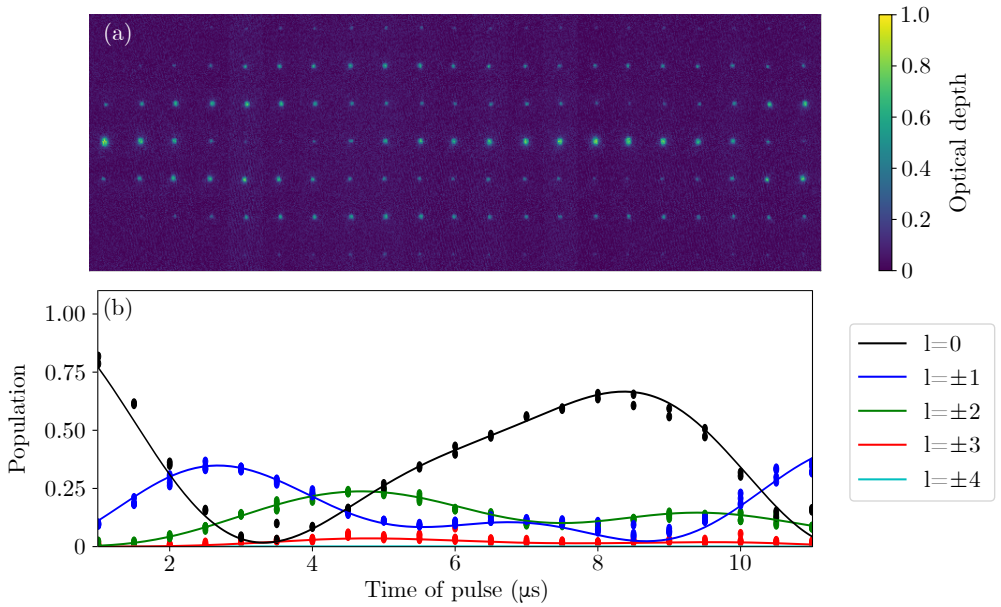

Figure 5.9: **Kapitza-Dirac diffraction of a Cs BEC.** Diffraction as a result of a pulsed lattice of depth 31.98(7) E_R. (a) Absorption images showing time dependence of the diffraction pattern. The undiffracted $l = 0$ order is visible in the centre row and diffraction orders up to $|l = 3|$ (top and bottom rows) are visible. (b) Evolution of the populations of each momentum state. The solid lines are Kapitza-Dirac simulations fitted to the data.

west axis. At this point there is a sufficient population in $l = 1$ to perform fitting on the order to measure the atom number in this order. This is then maximised by adjusting the alignment in both axes. Note that for every adjustment of the final alignment mirror, the retroreflected beam must be realigned. This is achieved by optimising the fiber back-coupling of the retroreflected beam.

5.6 Kapitza-Dirac diffraction of Cs

We then proceeded with Kapitza-Dirac diffraction experiments with a Cs BEC, across the wavelength range accessible by the laser system. A typical measurement would consist of between 15 and 20 different timings of lattice pulse. The range of pulse timings was chosen such that at least one 'oscillation' (reduction and recovery) of the undiffracted $l = 0$ order could be observed. Kapitza-Dirac simulations were

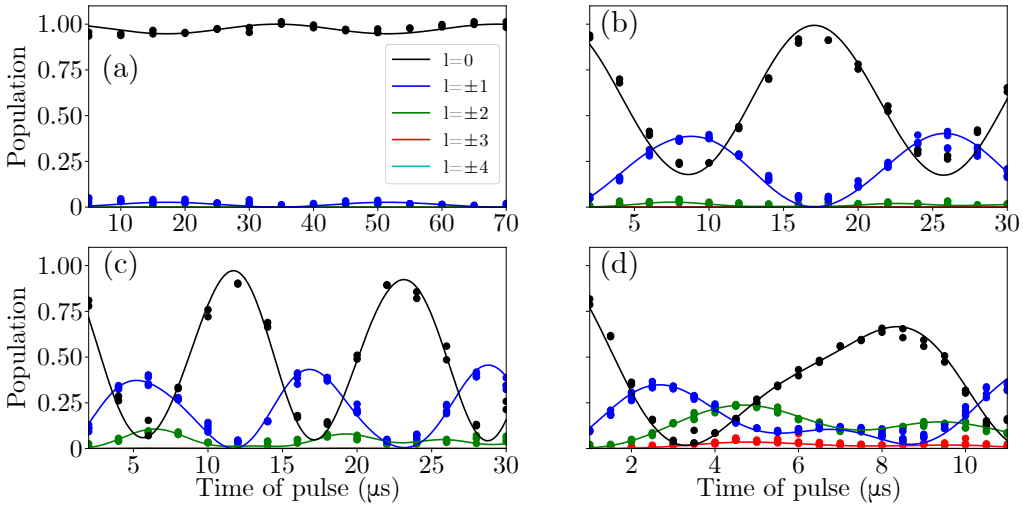

Figure 5.10: **Measuring lattice depths with Kapitza-Dirac diffraction.** The range of wavelengths, as well as beam intensities, accessible with the lattice beam, allowed us to measure lattice depths ranging from $\sim 1\,E_\mathrm{R}$ to $\sim 32\,E_\mathrm{R}$. The plots show the population evolution of momentum states for lattices with depths (a) $1.33(4)\,E_\mathrm{R}$ ($0.453(14)\,\mu\mathrm{K}$), (b) $10.81(3)\,E_\mathrm{R}$ ($3.684(9)\,\mu\mathrm{K}$), (c) $18.09(3)\,E_\mathrm{R}$ ($6.167(9)\,\mu\mathrm{K}$), and (d) $31.98(7)\,E_\mathrm{R}$ ($10.91(3)\,\mu\mathrm{K}$). The solid lines are Kapitza-Dirac simulations fitted to the data.

performed to determine the expected timescales of these oscillations. Two repeat measurements were taken at each value of pulse time and the ordering of pulse times during each measurement run was randomised. The trace of each pulse as recorded on the photodiode, as well as the wavelength of the (undoubled) Ti:Sapph output, was recorded. This provided a value of lattice wavelength and power for each set of measurements. All the data required at one particular wavelength would be taken before retuning and relocking the laser, as this process could take up to 5 minutes. The alignment of the lattice beam would also be checked approximately once every 5 data runs to mitigate any beam drifts.

Figure 5.9 shows results of a Kapitza-Dirac diffraction experiment for a lattice depth of $31.98\,E_\mathrm{R}$. Successive absorption images show the distribution of the diffracted orders parallel to the axis of the lattice beam. For short pulse times, the majority of the BEC population remains in $l = 0$, but as pulse time increases, higher orders become populated and the central order population is reduced. Dif-

fracted orders up to $|l = 3|$ can be observed in the absorption images. Furthermore, the population of the BEC diffracted into order $l = +n$ is the same as that in order $l = -n$. The fluctuation in the relative population in each order is plotted and a Kapitza-Dirac simulation is fit.

The depth of lattice depends on both the wavelength and intensity. It was found that the pulse power as measured by the photodiode could vary by up to 10 % as the laser was retuned and relocked. This reinforced the importance of constant monitoring of the power to be able to obtain a reliable measurement of polarizability. Figure 5.10 shows four different Kapitza-Dirac measurements, with lattice depths covering the range of those observed during the measurements. The plot in figure 5.9(b) is shown again in figure 5.10(d) and shows the deepest lattice measurement made. The lowest lattice depths measured were approximately $1\,E_R$ or $0.4\,\mu K$, where $> 10\,\%$ of the BEC was diffracted into $|l = 1|$. Methods which could in future be used to enhance the lattice diffraction and allow measurement of lower lattice depths are discussed in sections 5.9.2 and 5.9.3.

5.7 Results for polarizability

The lattice wavelengths investigated covered the range between the two transitions, as well as frequencies below the $6S_{\frac{1}{2}} \rightarrow 7P_{\frac{1}{2}}$ transition. This $\sim$5 nm range was the range accessible without requiring realignment of the doubling cavity.

Figure 5.11 shows the full set of polarizability results across the wavelength range. These results are shown with a fit of the polarizability. The fit allows us to determine some of the characteristics of the lattice beam. The lattice reflectivity is set as a fixed parameter, determined from measurements of the beam power transmission through the chamber viewports and retroreflection optics. The retroreflected lattice beam is 59(1) % of the power of the ingoing beam. The beam waist is determined from the fit to be 157(2) µm. This exceeds the 126(6) µm anticipated during the design of the optical setup. The size of the resonance features in the polarizability

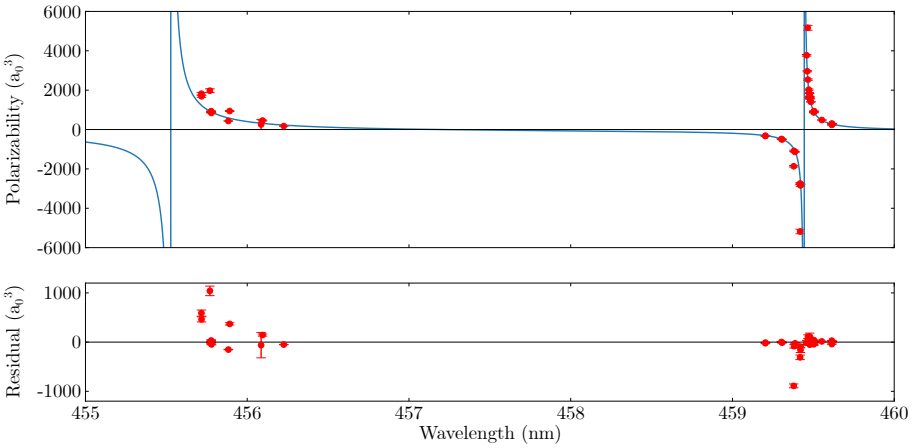

Figure 5.11: **Full results for polarizability.** Polarizability results (upper plot) from Kapitza-Dirac diffraction measurements. The polarizability theory plot is given by the blue solid line. The fit gives a lattice beam waist of 157(2) µm. Shift of the resonances from the expected values are also left as free parameters in the fit. The shifts in resonances are +3.9(1.2) GHz (+185(20) GHz) for the transition to the $7P_{\frac{1}{2}}$ ($7P_{\frac{3}{2}}$) state.

data show the relative strengths of the two transitions are as expected. However there are frequency shifts of +3.9(1.2) GHz and +185(20) GHz for the transition to the $7P_{\frac{1}{2}}$ and $7P_{\frac{3}{2}}$) states respectively. The fact that one of these shifts is two orders of magnitude larger than the other suggested that the shifts were not caused by a systematic error in the data taking. However, the residual plot of figure 5.11 shows that a greater proportion of the data points taken near the transition to the $7P_{\frac{3}{2}}$ state deviate from the fit. It should be noted that the error on the shift of this transition is also an order of magnitude larger than that on the shift of the transition to the $7P_{\frac{1}{2}}$ state. The position of the transition to the $7P_{\frac{3}{2}}$ state could be measured with less uncertainty by taking further polarizability measurements at blue detunings from the transition. The possible origins of the frequency shifts are discussed in section 5.8.

To be able to rule out wavelength drifts, measurements were taken across the accessible wavelength range in a single day. These results are shown in figure 5.12. Here the beam waist is determined to be a lower value of 111.9(7) µm, with

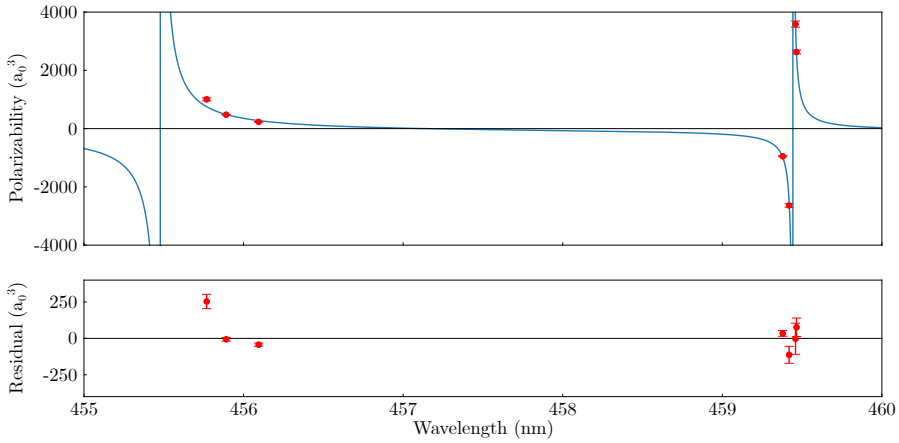

Figure 5.12: **Polarizability results taken in a single day.** Polarizability results (upper plot) from Kapitza-Dirac diffraction measurements, taken in a single day to rule out wavelength drift effects. The polarizability theory plot is given by the blue solid line. Shift of the resonances from the expected values are also left as free parameters in the fit. The fit gives a lattice beam waist of 111.9(7) µm. The shifts in resonances are +4.5(4) GHz (+255(11) GHz) for the transition to the $7P_{\frac{1}{2}}$ ($7P_{\frac{3}{2}}$) state.

the error determined from the fit. The discrepancy in the waist measurement is due to error in the power measurement and systematic errors due to the lattice alignment. The transition frequency shifts are +4.5(4) GHz and +255(11) GHz for the transition to the $7P_{\frac{1}{2}}$ and $7P_{\frac{3}{2}}$ states respectively. The result for the shift of the transition to the $7P_{\frac{1}{2}}$ state agrees with that of figure 5.11 to within error. However, the the result for the shift of the transition to the $7P_{\frac{3}{2}}$ state differs from that of 5.11 by 70 GHz, which is not accounted for by the errors from the fit in either result. This suggests the errors from the polarizability model do not reflect the error to which the frequency shift is actually known. This suggests further measurements, particularly at blue detunings from the transition, should help reduce the uncertainty in this measurement of frequency shift.

Figure 5.13 shows similar analysis to just the data around the $7P_{\frac{1}{2}}$ transition. In this case the only fit parameters are the beam waist and shift of this transition alone. These values respectively are 154.1(2) µm, and +4.77(12) GHz. This frequency shift

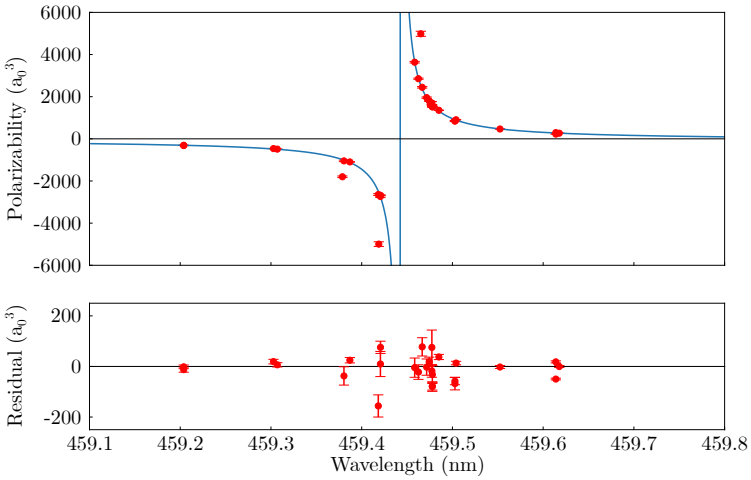

Figure 5.13: **Polarizability results around the $7P_{\frac{1}{2}}$ transition.** polarizability results (upper plot) from Kapitza-Dirac diffraction measurements. The polarizability theory plot is given by the blue solid line. Shift of the resonance from the expected values is also left as a free parameter in the fit. The fit gives a lattice beam waist of 154.1(2) µm. The shift of the transition to the $7P_{\frac{1}{2}}$ state. is +4.77(12) GHz. Some data points fall outside the range of the residual plot.

is in agreement with the results in 5.11 and 5.12 to within errors.

The shifts in the position of each transition in turn affect the position of the tune-out wavelengths. In the modified polarizability fit in figure 5.11, the higher tune-out wavelength is found to be 460.20(5) nm. As the $7P_{\frac{3}{2}}$ transition is shifted by a greater amount, the lower tune-out wavelength has a greater shift. We determine this wavelength to be 457.19(3) nm.

5.8 Investigating origin of the frequency shifts

The results for the atomic transitions and tune-out wavelengths from the Kapitza-Dirac diffraction differ from our expectations by the order of GHz. By looking at repeat measurements, we find that our uncertainty of shift of the transition to to the $7P_{\frac{3}{2}}$ state is greater than the error values obtained from fitting the polarizability model, and further measurements may be needed. However, across repeat

measurements we find agreements in the shift of the transition to the $7P_{\frac{3}{2}}$ state, of the order of 4 GHz. We attribute this to the simple model of atomic polarizability used in the fitting. This model does not consider the hyperfine structure of the Cs atom. This is of particular importance to our experiment, as the Cs atoms are pumped into the $|F = 3, m_F = +3\rangle$ ground state during DRSC prior to lattice diffraction. Other theoretical and experimental studies of atomic polarizability [208; 209] have used extended models of polarizability. We apply these here to discuss explanations to our discrepancies in the results. We also discuss how the geometry and polarisation of the lattice, and presence of a magnetic field, may have affected results.

5.8.1 Scalar polarizability incorporating fine structure

We first consider a model of dynamic (wavelength-dependent) polarizability $\alpha^{(0)}(\omega)$ incorporating only fine structure. This model is given in [208] as

$$\alpha^{(0)}(\omega) = \sum_n \frac{f_{0\to n}}{(\Delta E^2_{0\to n} - \omega^2)}, \tag{5.21}$$

Where $\Delta E^2_{0\to n}$ is the energy of the transition from the ground state to a state n and the oscillator strength $f_{0\to n}$ is given by

$$f_{0\to n} = \frac{2|\langle \gamma_n J_n||\mathbf{D}||\gamma_0 J_0\rangle|^2 \Delta E^2_{0\to n}}{3(2J_0+1)}. \tag{5.22}$$

Note the static polarizability can be calculated by setting ω to 0. For the calculation, energy levels up to $8\mathrm{P}_{\frac{3}{2}}$ are considered. The energy levels used to calculate $\Delta E^2_{0\to n}$ are taken from [161] and are tabulated in table 5.5. The (fine structure) matrix elements $\langle \gamma_n J_n||\mathbf{D}||\gamma_0 J_0\rangle$ are those used in the calculation in [208] and are tabulated in table 5.6. We also include the Cs core polarizability of 15.5 a_0^3. Table 5.7 shows the values of the tune-out wavelengths given in this model, and those calculated in [208] as a comparison. The static polarizability is also tabulated.

State	Energy (cm^{-1})
$6s_{\frac{1}{2}}$	-31406.5×10^2
$6p_{\frac{1}{2}}$	-20228.2×10^2
$6p_{\frac{3}{2}}$	-19674.2×10^2
$7p_{\frac{1}{2}}$	-9641.1×10^2
$7p_{\frac{3}{2}}$	-9460.1×10^2
$8p_{\frac{1}{2}}$	-5697.6×10^2
$8p_{\frac{3}{2}}$	-5615.0×10^2

Table 5.5: States and energy values of ^{133}Cs used in the calculation of the scalar polarizabliity $\alpha^{(0)}(\omega)$, taken from [161].

Transition	Matrix element (a.u.)
$6s_{\frac{1}{2}} \rightarrow 6p_{\frac{1}{2}}$	4.5057(16)[216]
$6s_{\frac{1}{2}} \rightarrow 6p_{\frac{3}{2}}$	6.3349(48)[217]
$6s_{\frac{1}{2}} \rightarrow 7p_{\frac{1}{2}}$	0.27810(45)[216]
$6s_{\frac{1}{2}} \rightarrow 7p_{\frac{3}{2}}$	0.57417(57)[216]
$6s_{\frac{1}{2}} \rightarrow 8p_{\frac{1}{2}}$	0.072(4)[161]
$6s_{\frac{1}{2}} \rightarrow 8p_{\frac{3}{2}}$	0.210(8)[161]

Table 5.6: Matrix elements of the transitions in ^{133}Cs used in the calculation of the scalar polarizabliity $\alpha^{(0)}(\omega)$. The references for each value are given in the table.

	Our calculation	[208]
Static polarizability (a_0^3)	400.23(10)	400.80(97)
$\sim$ 457.2 nm tune-out wavelength (nm)	457.239(4)	457.2504(171)
$\sim$ 460.2 nm tune-out wavelength (nm)	460.203(9)	460.2154(63)
$\sim$ 880.2 nm tune-out wavelength (nm)	880.211(15)	880.2144(158)

Table 5.7: Static polarizability and value of tune-out wavelengths calculated using equation 5.21 and constants tabulated in tables 5.5 and 5.6, compared with values given in [208].

State	J	A (MHz)	B (MHz)
6s	$\frac{1}{2}$	2298.157943[218; 219]	
6p	$\frac{1}{2}$	291.9309(12)[220]	
6p	$\frac{3}{2}$	50.28825(23)[221]	-0.4940(17)[219; 187]
7p	$\frac{1}{2}$	94.35(4)[222]	
7p	$\frac{3}{2}$	16.609(5)[223]	-0.15(3)[224]

Table 5.8: Hyperfine structure constants A and B used to calculate hyperfine energy levels E^{hf} according to equations 5.23, 5.24 and 5.25. Values of the constants are taken from the references given in the table.

5.8.2 Scalar polarizability incorporating hyperfine structure

We now consider the effect of hyperfine structure. The energy levels of each hyperfine state E^{hf} are modified from the fine structure energy levels E_J by

$$E^{\text{hf}} = E_J + W_F, \tag{5.23}$$

where

$$W_F = \frac{1}{2}AR + B\frac{\frac{3}{2}R(R+1) - 2I(I+1)J(J+1)}{2I(2I-1)2J(2J-1)}, \tag{5.24}$$

where A and B are hyperfine structure constants (used in the calculation in [208] and tabulated in table 5.8 with references), nuclear spin $I = \frac{7}{2}$ for Cs, and R is given by

$$R = F(F+1) - I(I+1) - J(J+1). \tag{5.25}$$

The transition matrix elements between hyperfine states T^{hf}_{ig} are given by

$$\begin{aligned} T^{\text{hf}}_{ig} &= \langle \gamma_i J_i I F_i || \mathbf{D} || \gamma_g J_g I F_g \rangle \\ &= (-1)^{I+J_g+F_i+1}\sqrt{2F_i+1}\sqrt{2F_g+1}\begin{Bmatrix} I & J_i & F_i \\ 1 & F_g & J_g \end{Bmatrix} T_{ig}. \end{aligned} \tag{5.26}$$

Figure 5.14 shows the how the polarizability of each hyperfine state is modified in the proximity of the tune-out wavelengths. Tables 5.9 and 5.10 give the calculated values of the frequency shifts of the hyperfine transitions and tune-out wavelengths respectively. For our experimental setup, the observed shifts should be 5.14727(8) GHz for the transition to the $7p_{\frac{1}{2}}$ state and 5.11411(3)) GHz for

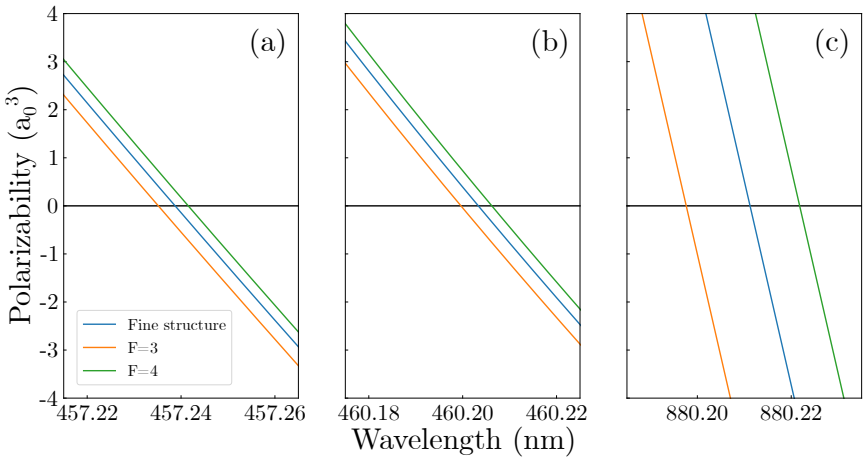

Figure 5.14: **Effect of hyperfine structure on predicted tune-out wavelengths.** The position of the tune-out wavelengths is shifted depending on whether the Cs atom is in the F=3 (orange) or F=4 (green) hyperfine state of $6s_{\frac{1}{2}}$. The tune-out wavelengths near 457.2 nm (a), 460.2 nm (a), and 880.2 nm (a) are shown. The polarizability calculation not considering hyperfine structure is shown in blue.

the transition to the $7p_{\frac{3}{2}}$ state. Our measured shift in the $7p_{\frac{1}{2}}$ transition is 4.59(12) GHz, which is below the theoretical prediction but of the same order of magnitude. This suggests that the hyperfine structure analysis of the polarizability explains the observed frequency shift for this transition. Our measured shift for the $7p_{\frac{3}{2}}$ transition, however, is two orders of magnitude greater, at 228(2) GHz. A more precise measurement of the shift of this transition could be made if polarizability measurements were made at blue-detuned frequencies from the transition.

5.8.3 Vector polarizability

We have so far only considered the scalar contribution $\alpha^{(0)}$ to the polarizability of Cs. The full equation for the dipole potential U, incorporating the vector ($\alpha^{(1)}$) and tensor ($\alpha^{(2)}$) contributions, can be written as

$$U = -\frac{\langle E^2 \rangle}{2}\left[\alpha^{(0)} - \xi \cos \hat{\mathbf{k}} \cdot \hat{\mathbf{B}} \frac{m_F}{F}\alpha^{(1)} + \left(\frac{3(\hat{\boldsymbol{\epsilon}} \cdot \hat{\mathbf{B}})^2 - 1}{2}\right)\frac{3m_F^2 - F(F+1)}{F(2F+1)}\alpha^{(2)}\right]. \tag{5.27}$$

Transition	Frequency shift (GHz)
$6s_{\frac{1}{2}}(F=3) \rightarrow 7p_{\frac{1}{2}}(F=3)$	4.95857(9)
$6s_{\frac{1}{2}}(F=3) \rightarrow 7p_{\frac{1}{2}}(F=4)$	5.33597(7)
$6s_{\frac{1}{2}}(F=3) \rightarrow 7p_{\frac{1}{2}}$(Average)	5.14727(8)
$6s_{\frac{1}{2}}(F=3) \rightarrow 7p_{\frac{3}{2}}(F=2)$	5.05866(5)
$6s_{\frac{1}{2}}(F=3) \rightarrow 7p_{\frac{3}{2}}(F=3)$	5.108598(14)
$6s_{\frac{1}{2}}(F=3) \rightarrow 7p_{\frac{3}{2}}(F=4)$	5.175077(15)
$6s_{\frac{1}{2}}(F=3) \rightarrow 7p_{\frac{3}{2}}$(Average)	5.11411(3)

Table 5.9: The frequency shift of the hyperfine transitions from $6s_{\frac{1}{2}}(F=3)$ to $7p_{\frac{1}{2}}$ and $7p_{\frac{3}{2}}$ around 460 nm, relative to the position of the transitions considering fine structure only.

tune-out wavelength (nearest 0.1 nm)	$F=3$ shift (GHz)	$F=4$ shift (GHz)
457.2 nm	4.3(1.4) 5.08(15)[208]	-4.3(1.5) -4.10(15)[208]
460.2 nm	5.7(1.5) 5.17(14)[208]	-4.2(1.4) -4.10(15)[208]
880.2 nm	5.4(3) 5.24(4)[208]	-3.9(4) -4.11(4)[208]

Table 5.10: The shift of the tune-out wavelengths for both $F=3$ and $F=4$ hyperfine states of $6s_{\frac{1}{2}}$. The results of our calculation, and those presented in [208] are shown.

The vector contribution to the polarizability is dependent on the angle between the lattice wavevector $\hat{\mathbf{k}}$ and any present magnetic bias field $\hat{\mathbf{B}}$. It can be eliminated if $\hat{\mathbf{k}}$ and $\hat{\mathbf{B}}$ are orthogonal. In the experimental setup described above, $\hat{\mathbf{k}}$ and $\hat{\mathbf{B}}$ are almost parallel. The experimental geometry therefore allows the vector polarizability to have almost its greatest possible contribution. Other geometries are discussed in section 5.9.1. The vector contribution is also, proportional to the polarisation ellipticity ξ, and can be minimised by using linear polarisation. Even with the use of polarisation optics such as Glan-Taylor polarisers, the lattice beam may contain small circular or elliptical polarisation components which may affect precision measurements. By taking polarizability measurements with two orthogonal linear polarisations and taking the average, the contribution of these components can be eliminated.

5.8.4 Tensor polarizability

Unlike the vector polarizability, there is always a contribution to the dipole potential from the tensor component of the polarizability $\alpha^{(2)}$. It can however be reduced by making the polarisation vector $\hat{\boldsymbol{\epsilon}}$ orthogonal to the bias field $\hat{\mathbf{B}}$. $\alpha^{(2)}$ is given, for an atom in ground state g with transitions to states i, by

$$\alpha^{(2)}(\omega) = 6\left(\frac{5F_g(2F_g-1)(2F_g+1)}{6(F_g+1)(2F_g+3)}\right)^{\frac{1}{2}} \sum_i (-1)^{F_g+F_i} \begin{Bmatrix} F_g & 1 & F_i \\ 1 & F_g & 2 \end{Bmatrix} \frac{f^{\mathrm{hf}}_{g\to i}}{\Delta E^2_{g\to i} - \omega^2}. \tag{5.28}$$

Through equation 5.28 it can also be seen that the tensor contribution to the polarizability is also dependent on the Zeeman sublevels m_F of the hyperfine state F. In [208], the shift of the tune-out wavelengths due to the mF state splitting is calculated and tabulated. It is assumed in these calculations that $\hat{\boldsymbol{\epsilon}} \cdot \hat{\mathbf{B}} = 0$ It is concluded that the resultant wavelength shifts are of the order of 10^{-5} or 10^{-6} nm. Therefore, for the experimental geometry, wavelength would have to be measured at fm precision for the Tensor contribution to the polarizability to be observed.

5.8.5 Zeeman shifts

We also consider shifts in transition frequency due to the Zeeman shifts of the upper and lower states. This shift in the presence of a magnetic field B is given by

$$\omega_{k,v} = \omega_{k,v}^{(0)} + \frac{1}{\hbar}(g'_F m'_F - g_F m_F)\mu_B B, \tag{5.29}$$

where the hyperfine Landé factor g_F is given by

$$\begin{aligned} g_F &= g_J \frac{F(F+1) + J(J+1) - I(I+1)}{2F(F+1)}, \\ g_J &= \frac{3}{2} + \frac{S(S+1) - L(L+1)}{2J(J+1)}, \end{aligned} \tag{5.30}$$

here assuming that the Landé factor $g_S = 2$. We assume that the lattice polarisation is sufficiently linear that only transitions with $m_F = 3 \to m'_F = 3$ contribute. We also assume that each hyperfine transition within the allowed transitions from the ground state to $7p_{\frac{1}{2}}$ and $7p_{\frac{3}{2}}$ have equal strengths.

For the transitions to $7s_{\frac{1}{2}}$, the Zeeman shifts of the hyperfine transitions are

$$\begin{aligned} 1.050\,\mathrm{MHz\,G^{-1}} \text{ for } |F=3, m_F=3\rangle \to |F'=3, m'_F=3\rangle\,, \\ -\,262\,\mathrm{kHz\,G^{-1}} \text{ for } |F=3, m_F=3\rangle \to |F'=4, m'_F=3\rangle\,. \end{aligned} \tag{5.31}$$

The average shift of the two transitions is $394\,\mathrm{kHz\,G^{-1}}$.

For the transitions to $7s_{\frac{3}{2}}$, the Zeeman shifts of the hyperfine transitions are

$$\begin{aligned} 919\,\mathrm{kHz\,G^{-1}} \text{ for } |F=3, m_F=3\rangle \to |F'=2, m'_F=3\rangle\,, \\ 394\,\mathrm{kHz\,G^{-1}} \text{ for } |F=3, m_F=3\rangle \to |F'=3, m'_F=3\rangle\,, \\ 184\,\mathrm{kHz\,G^{-1}} \text{ for } |F=3, m_F=3\rangle \to |F'=4, m'_F=3\rangle\,. \end{aligned} \tag{5.32}$$

Under our assumptions, the transitions combine to give an average shift of $499\,\mathrm{kHz\,G^{-1}}$. Both shifts are of the order of 4 to 5 orders of magnitude too small to explain the shift in the expected position of this state.

5.8.6 Summary

While our model for the polarizability was adequate in explaining the position of the atomic resonances and tune-out wavelengths at the fine structure level, frequency shifts of the order of 5 GHz are predicted when the hyperfine splitting of states is considered. This may partially account for the shift of similar magnitude in the transition to $7P_{\frac{1}{2}}$. It does not account for the shift of the transition to $7P_{\frac{3}{2}}$, which according to our fitting is some two orders of magnitude further from the initially predicted position. However, using the polarizability measurements taken to date, discrepancies between repeat measurements suggest our uncertainty on the shift of this transition is greater than the error from our fitting. Further polarizability measurements blue-detuned of this transition may give a result for the shift of this transition with similar uncertainty to that of the shift of the transition to $7P_{\frac{1}{2}}$.

It is possible that there is a vector contribution to the polarizability arising from the lattice geometry and possible elliptically polarised components in the lattice beam. This may further explain smaller deviations in the transition to $7P_{\frac{1}{2}}$ from the scalar polarizability model. It is however, difficult to quantify the magnitude of the circularly polarised component, and a more permanent solution would be to alter the lattice geometry and take averages of data with orthogonal linear polarisations. We have also considered the effect of the tensor contribution to the polarizability and the Zeeman shift to each transition, and have concluded that both of these effects give a negligible contribution to the shifts observed.

5.9 Summary and conclusion of measurements to date

We have incorporated a one-dimensional vertical lattice into the experimental setup. The light source of the lattice is tuneable in the wavelength range incorporating the 6s→7p transitions in Cs. This has allowed us to probe the dynamic polarizability of Cs in this range, and make measurements which will contribute

to measurements of the tune-out wavelengths in this range. There is also the scope to create Cs lattice potentials which are equal in trap depth or frequency to the strong attractive potential experienced by Yb in this range. We have demonstrated Kapitza-Dirac diffraction of BECs of both Cs and Yb using lattice pulses on the order of µs. We have demonstrated Kapitza-Dirac diffraction at multiple wavelengths can be used to measure the wavelength-dependent polarizability of Cs, and determine the positions of both atomic transitions and tune-out wavelengths. The positions of the transition wavelengths were shifted by the order of GHz from those predicted by models of the scalar polarizability. This led to further studies of the polarizability, and prompted improvements to the existing setup, which are discussed below.

5.9.1 A horizontally-oriented lattice

A significant simplification to the polarizability calculations to the system can be made if the vector contribution is eliminated. This is achieved if the lattice wavevector k is orthogonal to any bias magnetic field $\mathbf{B}$. We assume that the greatest contribution to any bias field will be in the vertical direction due to the experiment's bias coils. Therefore, the current beam, at 7 ° to the vertical, almost maximises the possible vector contribution to the polarizability. We therefore wish to move to a horizontal lattice beam for future measurements.

For the new beam, one of the horizontal viewport pairs can be used. The viewport pairs for the Yb MOT have the most favourable coatings for the lattice wavelength, with reflectivities of 96.2(1.6) %. We would use an angle as close as possible 90 ° between the lattice and Cs imaging axes, to allow resolution of the different diffracted orders in time-of-flight imaging. The Yb MOT viewport axes are, however, at angles of 30 ° and 120 ° to the Cs imaging axis. Therefore, for the former of these two options, the separation of orders in the plane of the imaging will be approximately half of that observed with the vertical lattice beam. For a 25 ms time of flight, we predict a separation in this geometry of 163.2(4) µm, giving a ratio

of separation to cloud width of 5.46(9). Therefore, the diffracted orders should be resolvable under this geometry.

The optical access incorporating the optical components described in section 5.4 will require careful design if the Yb MOT beams are not to be blocked and allow dual-species applications. However, for applications of the lattice which only require Cs, a simple lattice setup can be incorporated. A temporary setup has already been trialled through the Yb MOT horizontal axis which does not have the Yb imaging beam copropagating. The setup was removed before any lattice measurements could be taken to allow unrelated experiments to take place. It could however be reinstated quickly at any time. The optics for the vertical lattice have been retained. This keeps open the possibility of a two-dimensional lattice, with light for each axis of the lattice propagating through separate optical fibers.

5.9.2 Improving the lattice depth

Improving the intensity (and hence depth) of the optical lattice at the position of the atoms is desirable. With a deeper lattice higher, orders of diffraction would become visible and attain a greater population value. Simulations of higher lattice depths fit to such data would have less uncertainty. This would improve calibration and alignment of the lattice using an Yb or Cs BEC. It would also allow us to increase the range of polarizabilities we could probe with single-pulse diffraction measurements, and close the gaps (1.09 nm below and 1.90 nm above the predicted 457.31 nm tune-out wavelength and 0.60 nm below the predicted 460.22 nm tune-out wavelength) for which we have no data.

The simplest way to achieve this is to decrease the lattice beam waist. The current beam waist exceeds the spatial extent of the BEC by a factor of ~ 4. A reduced beam waist can increase lattice depth while still providing a uniform depth across the BEC. We have purchased a replacement collimator (Schäfter and Kirchoff 60FC-SF-4-M12-33), which has an increased focal length of 12 mm. This will collimate

the fiber output beam to 676(3) µm compared to the current 346.3(2) µm. The existing beam focusing and recollimating optics can be adjusted to give a predicted beam waist of 65.0(3) µm compared to the current 134 µm. This should increase lattice depth at a given wavelength by a factor of approximately 4. This should in turn increase the wavelength range accessible by single pulse measurements (to a minimum of ~ 0.6 nm from the predicted 457.31 nm tune-out wavelength and ~ 0.4 nm from the predicted 460.22 nm tune-out wavelength), assuming a minimum measurable lattice depth of $1\,E_{\mathrm{R}}$.

The fluctuation in output power of the doubling cavity has also affected the lattice depths we have been able to measure. It is hoped that inspection and repair or replacement of the doubling crystal by the manufacturer will improve the overall power output and will eliminate drifts in power. It may also increase the tuning range accessible without reoptimising the crystal angle or cavity alignment and eliminate the need to periodically clean the crystal surfaces. These two measures would considerably enhance the rate at which experimental data can be taken. It is also possible that the overall power output of the Ti:Sapph system, including the doubling cavity, could be improved with a higher power pump laser.

5.9.3 Measuring lower lattice depths with multi-pulse sequences

A high-precision measurement of the tune-out wavelengths will require direct polarizability measurements much closer to the predicted wavelengths than those currently made. Lattice depths lower than the $\sim 1\,E_{\mathrm{R}}$ minimum seen with single pulse measurements will have to be measured. A method using multiple pulses [164; 203] can be applied in our setup to enhance the population of the BEC diffracted into the $l = \pm 1$ orders. At low lattice depths, the Kapitza-Dirac diffraction pattern can be approximated as oscillations of part of the BEC population between $l = 0$ and $l = \pm 1$. The time period of the oscillations saturates to $\frac{h}{4E_{\mathrm{R}}}$, known as the Talbot time. For Cs in our lattice beam of approximately 460 nm, the Talbot time is 35.2 µs. The method described in [164] applies a sequence of multiple

pulses, alternating between lattice pulse and free evolution with duration of half the Talbot time ($\frac{h}{4E_{\mathrm{R}}}$, ∼17.6 µs for Cs in our lattice). The effect of each lattice pulse coherently adds to the overall diffraction pattern. This causes an enhancement of the $l = \pm 1$ population. The enhancement was found to be proportional to the square of both the lattice depth and the number of pulses n_{P} for $n_{\mathrm{P}} \leq 18$ and for lattice depths of less than $1\,E_{\mathrm{R}}$.

A simulation of a multi-pulse diffraction routine, which could be fit to experimental data, could be made by alternatingly operating on the BEC wavefunction with the lattice operator and with free-space evolution for the number of pulses applied. An analytic solution [225] has also been derived for a zero-temperature BEC in limit of a weakly-diffracting lattice. Experimental results from our lattice could test the validity of this model for BECs typically produced in experiments. Experimentally, implementation of the pulse is achievable with no modification to the experimental setup. The pulse sequence sent to the lattice AOM can be generated by a function generator set to output a train of square-wave pulses with time period of the Talbot time. This output can be triggered by a digital signal from the experimental control. The number of pulses in the pulse train can be varied to determine the efficacy of the multi-pulse method.

5.9.4 Further experiments

The polarizability measurements made to date indicate the wavelengths at which the Cs polarizability is negligible compared to that of Yb. Wavelengths where the lattice depths or trap frequencies are equal for both species can also be identified. We therefore have the capability in future to load Yb into a Cs-blind lattice or load both species into a balanced lattice. A significant limitation is the low lattice depth, which necessitates low temperatures of both species through evaporative cooling to allow successful lattice loading. This will be further exacerbated if the available lattice power used for the one-dimensional lattice is split to create a two-

dimensional lattice. Improvements to the lattice depth outlined above may improve the ability to load into the lattice.

Chapter 6

Interspecies Feshbach resonances in Cs-Yb mixtures

The identification and characterisation of interspecies magnetic Feshbach resonances is a critical step in identifying a pathway to the formation of CsYb molecules. In this chapter we build on previous experimental and theoretical work by performing Feshbach spectroscopy on the CsYb mixture for magnetic bias fields and isotopic combinations where resonances are predicted to occur. We discuss the physical origins of the resonances and which resonances are most promising to be observed experimentally. We describe the experimental upgrades relating to bias field generation and calibration necessary to perform Feshbach spectroscopy. We report on the observations of resonances at 622 G and 702 G in the Cs–^{173}Yb mixture.

6.1 Introduction to Feshbach Spectroscopy

Atomic Feshbach resonances have been an important and useful tool for cold atom experiments for several decades [69]. The ability to tune the intraspecies scattering length of a given atomic species near a Feshbach resonance has allowed a rich area of study on the behaviour of quantum degenerate gases with a range of scattering

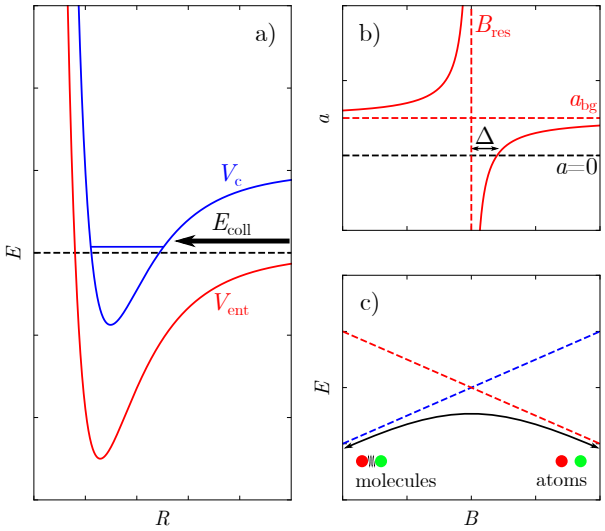

Figure 6.1: **The principle of magnetic Feshbach resonances.** a) Two ultracold ground state atoms approach each other with a collision energy E_{coll}, very close to the zero-energy threshold of a molecular potential, called the entrance channel V_{ent}. The energy approaches that of a bound state in an excited molecular potential, called the closed channel V_c. The energy of the bound state can be tuned relative to E_{coll} using an external bias magnetic field. b) Provided there is a coupling mechanism between the entrance and closed channels, at the field B_{res} where the two states cross, a pole in the scattering length a, described by equation 6.1, occurs. c) Provided there is a coupling mechanism between the entrance and closed channels, an avoided crossing between states can exist at B_{res}. Atoms can be associated to the molecular bound state (and molecules dissociated into constituent atoms) by performing an adiabatic ramp across this field.

properties and with dynamic scattering properties. This has been extended from bulk gases to a range of trapping geometries and dimensionalities, and as we have seen in previous chapters, can be extended to studying interspecies scattering properties between two different atomic species. In the context of ultracold molecules, identifying and utilising appropriate interspecies Feshbach resonances is often a key step in the route to creating molecules by indirect cooling and magnetoassociation [226; 227], by performing an adiabatic ramp in magnetic field across the resonance.

A magnetic Feshbach resonance is a physical property of the collision of two ultracold atoms. It can be described by a two-channel model, depicted in figure 6.1a.

At large internuclear separation R, the energy of the ground state molecular electronic potential of the atom pair asymptotically approaches the sum of the atomic state energies. This potential is referred to as the entrance channel, V_{ent}. The collision energy, E_{coll}, is in excess of the value of V_{ent} at large R. A higher molecular electronic potential may exist, which is not energetically accessible to the separated atom pair. This potential is referred to as a the closed channel, V_c. However, there may exist a bound state within V_c which has a value near to E_{coll}. The energy of this bound state can be tuned by applying a tuneable magnetic bias field, B. If there is a coupling mechanism between the entrance and closed channels, state mixing occurs. The scattering length of a colliding pair near the energy crossing, $a(B)$, depends on the position of the bound state relative to the threshold value of V_{ent}. If it is above the threshold (and hence is a virtual bound state), $a(B)$ is negative, causing attractive interactions. If it below the threshold, $a(B)$ is positive, causing attractive interactions. At the threshold, $a(B)$ diverges. The characteristic pole in $a(B)$ at the resonance position B_{res} is given by [228]

$$a(B) = a_{\text{bg}} \left(1 - \frac{\Delta}{B - B_{\text{res}}}\right), \tag{6.1}$$

where a_{bg} is the background scattering length of the mixture near the resonance and Δ is the width of the resonance, defined as the difference in field magnitude between the resonance pole and the zero crossing of the scattering length. This is shown in figure 6.1b. A figure of merit frequently used to quantify the strength of the resonance is the product $\bar{\Delta} = a_{\text{bg}}\Delta$. This quantity gives a measure of how observable the resonance is using three-body loss spectroscopy (see section 6.1.4), and is also proportional to the optimal rate of magnetic field sweep for magnetoassociation [229; 230] (see section 6.1.1).

6.1.1 Magnetoassociation using a Feshbach Resonance

The strength of a Feshbach resonance depends on the strength of the coupling between the state of the colliding atoms in the entrance channel, and the bound

molecular state in V_c. For sufficiently strong couplings, the avoided energy crossing between states at B_{res} can followed adiabatically by a ramp of the bias field. The atomic pair can be therefore associated into the molecular state. This process is shown in figure 6.1c. This is readily achievable experimentally if one can generate the magnetic fields required either side of the resonance and execute linear ramps between them. The molecules created in the magnetoassociation process are in weakly-bound states near the atomic threshold, and occupy a single rovibrational level. They are referred to in literature as 'Feshbach molecules'. These molecules retain the phase space density of the constituent atom pairs. The lifetimes of Feshbach molecules in these high-energy states are relatively short, with molecules undergoing vibrational relaxation due to atom-molecule and molecule-molecule collisions. The efficiency of the magnetoassociation process for a bulk gas in an optical dipole trap is limited by resonant loss due to these collisions, and, in two-species experiments, phase space density and spatial overlap of the two species. The best reported conversion efficiency in such systems is 40 % [231]. This however can be improved by performing magnetoassociation on atoms confined in an optical lattice [232], preventing collisions with other atoms or molecules and improving the lifetime. Provided one atom of each species is loaded per lattice site, near unity conversion efficiency by magnetoassociation is possible. This has been reported in experiments on KRb molecules [233].

To reach the rovibrational ground state of the molecule required for quantum simulation and computation applications requires a further rapid transfer of the population from this Feshbach state using techniques such as Stimulated Raman adiabatic passage (STIRAP) [70; 71]. The Feshbach molecules can also be dissociated into their constituent atoms by a reverse ramp across the avoided crossing at the Feshbach resonance. The magnetoassociation method therefore has an advantage over other molecular association methods such as photoassociation of being coherent and reversible. As experiments producing cold molecules by indirect cooling typically use imaging of the constituent atoms as the method of detecting molecules,

having such a reversible method is necessary in verifying the successful creation of molecules.

6.1.2 Interspecies Feshbach resonances in alkali + alkaline-earth-like mixtures

The method of magnetoassociation was first proposed in a number of publications [229; 234; 235]. It has since has been well-established experimentally, and is used routinely in the creation of homonuclear dimer molecules of alkali metal atoms such as Rb_2 [73] and Cs_2 [72], and heteronuclear bialkali molecules such as KRb [74], RbCs[75; 76], NaK[77; 236; 237], and NaRb[78]. These mixtures are well-suited to the method as their atomic structure gives rise to strong and wide Feshbach resonances at bias fields which are readily attainable experimentally. However, this is not the case in alkali + alkaline-earth-like mixtures owing to the closed shell structure of alkaline-earth-like atoms. Due to the absence of electronic spin in the ^{1}S ground state of these atoms, the strong couplings which provide the wide resonances found in bi-alkali systems are not present in alkali + alkaline-earth-like systems. However, narrow resonances are predicted to occur in such mixtures, either through modification of the hyperfine coupling of the alkali atom by the closed-shell atom at short range [85; 87], or by the interaction between electron spin of the alkali atom and the closed-shell atom [86]. Experimental observation of such narrow resonances has posed a significant challenge. However in recent years multiple interspecies Feshbach resonances have been observed in Rb–Sr[88] and Li–Yb [89] mixtures. This was a promising indicator that similar observations could be made in Cs-Yb mixtures.

6.1.3 Predicted Feshbach resonances in the Cs-Yb mixture

Predictions for Feshbach resonances are typically based on knowledge of the molecular ground state electronic potential. These were previously determined ex-

Yb Isotope	Mechanism	Cs hyperfine state (F, m_F)	Widest Yb state m_I	B_{res} (G)	Δ (mG)	$\bar{\Delta}$ (mG)
171	II	(3,3)	1/2	149	0.40	0.33
171	I + II	(3,3)	1/2	171	0.078	0.065
171	II	(3,2)	1/2	203	0.016	0.013
171	I + II	(3,1)	1/2	423	0.52	0.44
173	II	(3,3)	-1/2	167	0.677	0.011
173	III	(3,3)	-3/2	553	0.641	0.010
173	II	(3,3)	1/2	620	29.21	0.48
173	I + II	(3,3)	-5/2	700	20.99	0.32

Table 6.1: A selection of predicted interspecies resonances from [93], for mixtures of Cs and the two Fermionic Yb isotopes, ^{171}Yb and ^{173}Yb. These resonances are of a field magnitude and normalised width $\bar{\Delta} = (a_{bg}/\bar{a})\Delta$ hoped to be observable in our experimental setup. The position and width of the widest resonance in each set is given, with the corresponding value of the Yb nuclear spin substate $m_{I,\text{Yb}}$.

perimentally by measuring the binding energies of near-threshold molecular states, using two-photon photoassociation spectroscopy [92]. The improved knowledge of the ground state potentials allowed a theoretical study [93] to calculate predictions for the strength, width, and field position of each isotopolog. The resonances are caused by couplings between open and closed channels, in turn caused by the change in hyperfine interactions when the Cs and Yb atoms are in close proximity. The theoretical study in [93] identifies three specific coupling mechanisms referred to as mechanisms I, II and III. A brief summary of these mechanisms is given here. Mechanism I is due to the variation in hyperfine coupling on the Cs atom. It arises because the approaching Yb atom pulls electron spin density away from the Cs nucleus, reducing the strength of the hyperfine interaction. This coupling mechanism was first proposed in [85], and has been studied theoretically for multiple Yb+alkali-metal mixtures [87]. Mechanism II is due to the variation in hyperfine coupling on the Yb atom. As in mechanism I, electron-spin density is pulled away from the Cs nucleus, some of which comes into contact with the Yb nucleus, where it can interact with a nuclear spin. This mechanism was first proposed in [86]. Mechanism III is due to the tensor, or anisotropic, hyperfine coupling on the Yb

atom. The approach of the Cs atom breaks the spherical symmetry of the electron density around the Yb nucleus, allowing a dipolar coupling. This mechanism was considered in [86] and later observed experimentally in the Rb+Sr mixture [88]. Mechanism I relies on the Cs nuclear spin and therefore exists for all Cs+Yb isotopologs. As mechanisms II and III both rely on the Yb nuclear spin, they only exist for combinations of Cs and the Fermionic Yb isotopes, ^{171}Yb and ^{173}Yb. Further detail of the coupling mechanisms are given in [93].

Considering the predictions in [93], we decided to focus our efforts experimentally on searching for resonances in the mixtures involving the Fermionic Yb isotopes, ^{171}Yb and ^{173}Yb. Table 6.1 lists the resonances in these mixtures we hope to measure using the current experimental setup. Here the resonance widths given are normalised widths $\bar{\Delta}$ defined as [93]

$$\bar{\Delta} = \frac{a_{\mathrm{bg}}\Delta}{\bar{a}}, \tag{6.2}$$

where the mean scattering length $\bar{a}$ is given by [238]

$$\bar{a} = \left(\frac{2\mu C_6}{\hbar^2}\right)^{\frac{1}{4}} \times 0.4779888, \tag{6.3}$$

for atom-atom scattering of a system with reduced mass μ and molecular constant C_6. The value of $\bar{a}$ therefore varies for each isotopolog. $\bar{\Delta}$ gives an indication of the resonance strength through the product $a_{\mathrm{bg}}\Delta$ but is normalised to the mean scattering length $\bar{a}$ of Gribakin and Flambaum [238] to give a value in Gauss. There are also low-lying resonances predicted in the Cs + ^{174}Yb mixture at 66 G and 134 G. These resonances are weak in comparison to those listed in table 6.1. However they may be promising for observation, being in an isotope mixture where we have already demonstrated cooling to degeneracy.

6.1.4 Feshbach spectroscopy techniques

The high value of $|a|$ in the proximity of a Feshbach resonance results in an increase in atom loss due to inelastic collisions, namely two-body collisions and three-body

recombination. This atom loss is a readily observable feature in bulk cold atomic gases when a bias field near a resonance is applied. The collisional loss rate is proportional to a characteristic length b which can be modelled as [69]

$$b = \frac{1}{2} a_{\mathrm{res}} \frac{\gamma^2}{E_0^2 + (\gamma/2)^2}, \tag{6.4}$$

where

$$a_{\mathrm{res}} = a_{\mathrm{bg}} \Gamma_0 / \gamma \tag{6.5}$$

is the resonant length parameter, Γ_0 is the resonance strength, $\gamma/\hbar$ is the decay rate of the bound state, and E_0 is the energy at which the location is located. The inelastic loss feature, as a function of B and hence E, therefore typically has a lorentzian lineshape. We can, however, observe resonances where the scattering due to the bound state interferes with scattering with background states in the continuum. In this case, an asymmetric Fano lineshape can be observed.

The principle of a Feshbach spectroscopy experiment is straightforward. Firstly, the bias field experienced by an atomic mixture is ramped to near the predicted position of the resonance. The atoms are then held for a time period t to allow loss from the mixture. Finally, the field is ramped back to a lower value, in order to undertake absorption imaging of the remaining atoms after time of flight. The result is a field-dependent loss feature. The requirements for such an experiment are to start with a trapped mixture with sufficiently high phase-space density that loss due to scattering occurs at a fast rate compared to the trapping lifetime, and to be able to generate magnetic fields either side of the resonance. The magnetic fields must be known to a certainty sufficient to be able to map out the width of the resonance, and the experiment must be held at these fields for sufficient time for loss due to scattering to occur. The experimental challenges to meet these requirements in the CsYb experiment are discussed in the next section.

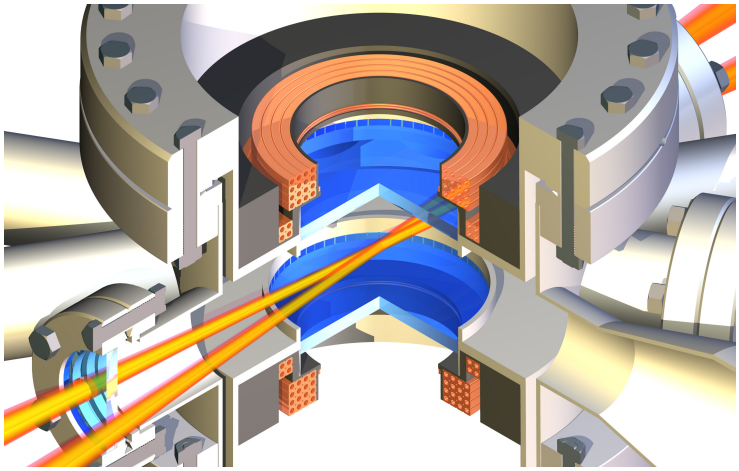

Figure 6.2: **Magnetic field generation coils for the science chamber.** Rendered cut-away section of the science chamber showing the MOT and bias coils located within the re-entrant flanges. The MOT coils are the outer set consisting of 16 turns of wire per coil. The bias coils are the inner set consisting of four turns of wire per coil. The reservoir trap beams are also shown to illustrate the horizontal trapping plane of the science chamber.

6.2 Experimental requirements for Feshbach spectroscopy

6.2.1 Magnetic field generation

A comprehensive study of Feshbach resonances of all isotopologs would require magnetic bias fields of up to 1500 G. To search for the most promising resonances involving the Fermionic isotopes of Yb requires fields of up to 700 G. Figure 6.2 shows the electrical coils present in the experiment for field generation within the science chamber. The smaller bias coil was designed primarily for the implementation of DRSC and the reservoir trap during our Cs cooling sequence. The critical bias fields for these and for evaporative cooling occur at a few tens of G. These include a zero crossing in the Cs scattering length at 17 G, and a minimum in the Cs three-body loss rate at 22 G. The maximum bias field this coil can produce is ∼200 G. This places a severe limit on the number of resonances we can hope to observe using this coil alone. A set of coils capable of reaching a bias field of ∼ 2000 G

have been designed and constructed [139]. However, they were not installed in the experiment at the time of construction, as it was unknown whether fields of this magnitude would be required for Feshbach spectroscopy. The installation of these or similar coils at present would be a lengthy process which would disrupt running of the experiment. It could also affect the optical access into the science chamber, leading to revisions of the optical setup. An alternative to this is to increase the bias fields attainable by repurposing other field generation coils already integrated into the setup. We therefore consider the coils which generate the quadrupole field used for our Cs and Yb MOTs. For this purpose, these coils are used in anti-Helmholtz configuration. However, reconfiguring them to Helmholtz configuration allows us to effectively consider the coil pair as a single coil generating a uniform bias field at the centre of the science chamber. We were able to achieve switching the coils' configuration during the experimental sequence through installation of a H-bridge, see section 6.2.2. With this coil pair used in bias configuration and in combination with the dedicated bias coil, we are able to generate magnetic bias fields up to approximately 700 G.

6.2.2 The H-bridge

To perform Feshbach spectroscopy of atomic mixtures at these fields, we must be capable of operating the quadrupole coils in anti-Helmholtz configuration in the earlier stages of the experimental sequence. They must then be switched to Helmholtz configuration to generate the necessary fields to observe the Feshbach resonances. The field generated by the bias field is directed in an upward direction, as is the upper quadrupole coil, whereas the lower quadrupole field is directed downward. The direction of the current in the lower coil must therefore be reversed during the experimental sequence, in a time interval that will not interrupt the rest of the sequence. The solution is the implementation of a 'H-bridge' circuit, see figure 6.3. Electrical current flowing from +V to the ground of the power supply always travels in the same direction through coil 1. However, the direction

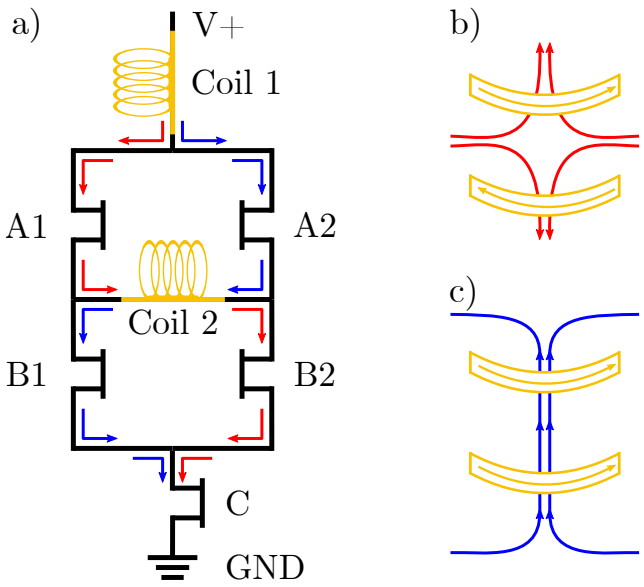

Figure 6.3: **The principle of the H-bridge.** a) Diagram of the quadrupole coil setup including the H-bridge. Current always through coil 1 in the same direction, but the direction of current flow through coil 2 depends on which pairs of H-bridge gates are closed: A1 and B2 (red arrows) or A2 and B1 (blue arrows). The ramping MOSFETs at C determine the magnitude of the current flow for both cases. b) When gate pair A1 + B2 is closed, the coils are in anti-Helmholtz configuration, and a quadrupole field is generated with the field minimum in the centre of the science chamber. c) When gate pair A2 + B1 is closed, the coils are in Helmholtz configuration, and a bias field is generated in the science chamber.

of current flow through coil 3, on the central bar of the H-bridge, is determined by the which pair of gates in the circuit (A1 + B2 or A2 + B1) is closed.

In practice, the gates are realised by sets of MOSFETs. The amplitude of the current in both coil configurations is governed by the 'ramping' MOSFETs, four MOSFETs in parallel which the current passes through after the H-bridge. The MOSFETs on the H-bridge itself are always either fully open or fully closed. Therefore, the power dissipation at these MOSFETs was not anticipated to be problematic. We have found that one MOSFET at gates A1 and B2 was adequate for running the currents for the MOTs in anti-Helmholtz configuration (up to ~ 60 A). However, running the higher (up to ~ 400 A) currents for Feshbach spectroscopy requires three MOSFETs in parallel at gates A2 and B1. The gate pairs A1/B1 and A2/B2 are each controlled by a driver PCB. The drivers work in a 'half-bridge'

configuration. A gate voltage of 3.3 V can only be sent to MOSFETs A or B. This ensures that the two A gates or the two B gates can never be closed simultaneously. A switching circuit controls which gate voltage the MOSFET drivers send. This consists of a logic PCB controlled from a TTL signal from our LabVIEW control. When this TTL is low, the logic circuit sends the correct signal for Helmholtz configuration, and when it is high, the correct signals for anti-Helmholtz configuration are sent. This configuration allows us to limit the current flowing through the single MOSFET gates. A comparator prevents the switching circuit from outputting in the anti-Helmholtz configuration if the analogue output to the coils' current servo circuit (which dictates the gate voltage sent to the ramping MOSFETs) is too high. In practice, we have restricted the current in anti-Helmholtz configuration to 160 A. A pair of level-shifter circuits are also required to convert the 5 V logic TTL signals to the 3.3 V driven by the MOSFET drivers' internal regulators. This avoids competition between regulators in the circuit. A digital reset signal must be applied to the drivers, also from the LabVIEW control via the logic circuit, to enable the switch to take place. This ensures no current can flow through the circuit while the switch is taking place. The driver also has a fault reset digital input signal, which we can also trigger from the LabVIEW control via the logic circuit. We execute the H-Bridge switch in 50 ms, incorporating wait time to ensure the digital reset signal is in place during the switch. We also need to reconfigure the power supply of the quadrupole fields to access the high bias fields. The maximum voltage and current the power supply can operate is set by the GPIB output of the experimental control software. For running the MOTs in anti-Helmholtz configuration this is usually set to 2.5 V, but for Feshbach spectroscopy this can be set to a maximum 10.5 V.

6.2.3 Preparation of Cs and Yb

The preparation of a Cs + Yb mixture for Feshbach spectroscopy largely follows the evaporative cooling process in the BODT described in previous chapters. However,

it should be noted that the aim of evaporative cooling in this experiment is to obtain an atomic mixture with high overlap between the two species, as opposed to creating quantum degenerate gases. Indeed, cooling to quantum degeneracy may in some cases affect the miscibility of the mixture. In the development of the BODT we have demonstrated effective sympathetic cooling of Cs by two bosonic Yb isotopes, ^{170}Yb and ^{174}Yb. However, our focus on Feshbach spectroscopy to date has been on the Cs + ^{173}Yb. This isotopolog has an interspecies scattering length of $1(1)\,a_0$ [92]. Therefore, when working with this mixture, we have effectively considered sympathetic cooling between the species to not be possible. Instead, the cooling processes for each species are used separately for preparation of the mixture. It is worth noting that we have previously been able to produce a degenerate Fermi gas (DFG) of ^{173}Yb in the experiment using a single-colour 1070 nm crossed ODT [140]. However, the experimental routines for a Cs BEC and a ^{173}Yb DFG are incompatible without introducing an additional sympathetic coolant for ^{173}Yb. A further challenge is anticipated when performing Feshbach spectroscopy on the Cs + ^{171}Yb mixture. The low intraspecies scattering length of -3 a_0[130] of ^{171}Yb limits the efficiency of loading this isotope into an optical dipole trap and performing evaporative cooling. In this case, Cs, or a second Yb isotope, will likely have to be used as a sympathetic coolant for ^{171}Yb.

We typically prepare a mixture of 3×10^5 Yb atoms at a temperature of 0.8 µK, and 2×10^5 Cs atoms in the $|F = 3, m_F = +3\rangle$ state, and at a temperature of 2.0 µK, for Feshbach spectroscopy. To make the experimental sequence more time effective, we have found that the Yb evaporative cooling stage and the Cs cooling stages prior to loading into the BODT can be performed simultaneously. This has no detrimental effect on the final conditions of either species.

Predicted B (G) [134]	Measured B (G)	Partial wave
47.79	47.97(3) [132]	g
53.79	53.50(3) [132]	g
112.41	112.78(3) [132]	g
130.52	131.06(3) [132]	d
226.73		d
554.06	554.06(2) [134]	g
555.39	557.45(3) [134]	i
559.18	562.17(3) [134]	i
565.00	565.48(3) [134]	g
601.28	602.54(3) [134]	g

Table 6.2: The Cs_2 intraspecies Feshbach resonances measured to calibrate our bias magnetic field. Fields theoretically predicted in [134] are given, as well as experimental results, with references given in the table. Note there is no published experimental result for the resonance predicted at 226.73 G.

6.3 Magnetic field calibration

A recalibration of the magnetic bias field was required following the upgrade of our field generation apparatus. It is important to consider here that any interspecies Feshbach resonances may deviate from the predicted positions and widths, and to be able to measure and characterise any discrepancies will be important in developing our understanding of the resonances. In the following sections we summarise two different methods used to calibrate our bias field.

6.3.1 Cs_2 Feshbach resonances

In this method we exploit the rich Feshbach structure of Cs across the range of fields we can access in our experiment. The intraspecies Feshbach resonances have been comprehensively studied and experimentally measured [131; 132; 133; 134] and any resonances we measure in the experiment can be easily calibrated against the well-known literature values. Additionally, the high three-body loss rates in trapped Cs discussed previously are advantageous in the measurement of such resonances, with comparatively weak (up to i-wave) resonances being detectable.

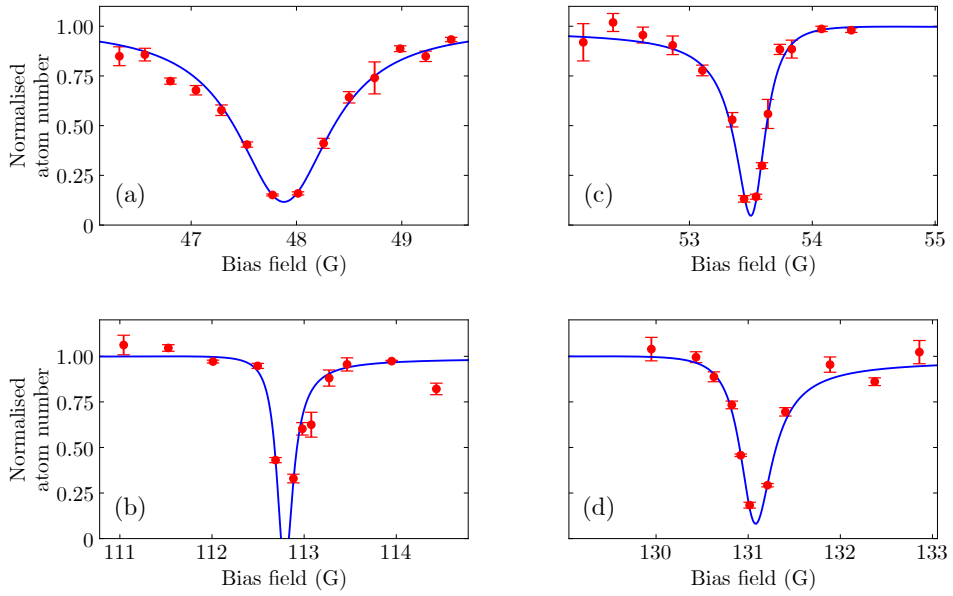

Figure 6.4: **Low-field Cs_2 Feshbach resonances.** Detection of Feshbach resonances by measuring resonant loss of Cs atoms after a 500 ms hold at the target field. Scans were performed across the resonant fields of (a) 47.97 G, (b) 53.50 G, (c) 112.78 G, and (d) 131.06 G. The blue curves are Fano lineshape fits to the data. The bias field, in this case generated by the quadrupole coils in Helmholtz configuration, is calibrated by the central position of the resonances.

To measure the Cs_2 Feshbach resonances, we prepare 1.0×10^5 Cs atoms at 2.1 µK in the absence of Yb, before switching the configuration of the quadrupole fields to Helmholtz using the H-bridge, and increasing the maximum permissible coil current, ramping to the desired field in 12 ms, holding for 500 ms, and ramping back to 22 G in 12 ms.

Our experimental emphasis was to measure Cs_2 resonances in the vicinity of the field of any predicted interspecies resonance, ideally with at least one Cs_2 resonance above and below the resonance, to improve the accuracy of our calibration in the region of the resonance. For a good calibration in the region of the predicted 167 G resonance, low-field Cs_2 resonances were measured at 47.97 G, 53.50 G, 112.78 G, 131.06 G, and 226.73 G, see figures 6.4 and 6.5. Using measurements of the first four resonances, we were able to perform a calibration of this configuration at low field.

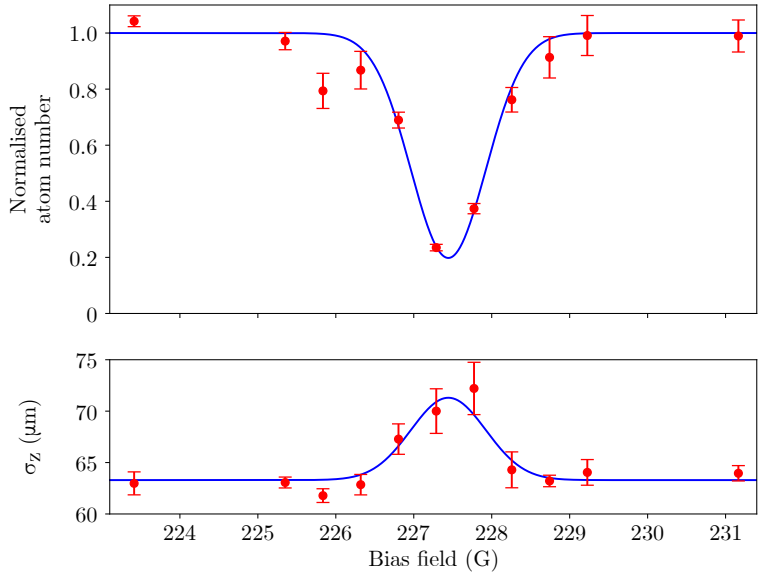

Figure 6.5: **The Cs_2 Feshbach resonance at 226 G.** The resonance which was predicted in [134] to occur at 226.73 G. Upper plot: atom-loss curve using the same methods as in figure 6.4. The blue curve is a Gaussian fit to the data. According to the field calibration from the resonances measured in figure 6.4, the resonance centre position is 227.444(14) G and the width is 1.13(5) G. Lower plot: demonstration that the atom cloud width can also be used as a diagnostic for Feshbach resonances, with a 13% increase in σ_z on resonance for this data. The blue curve is a Gaussian fit to the data with the central position and width of the curve constrained to be the same as the curve in the upper plot.

We performed Fano lineshape fits to the data of each resonance and calibrated the central analogue output to the coil servo V_{LV} to the known values of the resonance positions. The resulting calibration gives the field magnitude B of 48.48(5) G/V - 1.436(9) V.

The latter of these resonances is the only one lying above the position of the predicted interspecies resonance and to our knowledge had not been previously measured experimentally. Using the calibration from the other four resonances, we measure this resonance at a field of 227.444(14) G and a width of 1.13(5) G. For the predicted 553 G resonance, Cs_2 resonances were measured at 554.06 G, 557.45 G, 562.18 G, and 565.48 G, see figure 6.6. These four resonances lie close to a broad

Feshbach resonance predicted to be centred at 548.44 G, and are all above the predicted interspecies resonance, but give closely-spaced calibration points within $< 3\%$ of the resonance. For this resonance and the predicted 620 G resonance, the Cs_2 resonance at 602.54 G was measured. This, in combination with the multiple resonances around 550 G, should give an adequate calibration for this resonance. For higher fields near the predicted 700 G resonance, Cs_2 resonances within $< 5\%$ occur at 707.03 G and 729.03 G. A scan for the first of these two resonances was unsuccessful. We are confident that the second of the two resonances should be measurable in the experiment. However the field value required is beyond that which we are confident that the coils can generate safely, so measurement of the interspecies resonance was made our priority.

The resulting bias field was now a combination of contributions from the dedicated bias coil and the quadrupole coils in Helmholtz configuration. For repeated measurements around a resonance to determine the width and shape of the loss feature, the current of one of the coils was kept at a constant value. The current of the other was varied in small increments around the position of the resonance. In this way, Cs_2 resonances were measured by both keeping the bias current constant and varying the quadrupole (Helmholtz) current varied, and by keeping the quadrupole (Helmholtz) current constant and varying the bias current.

While both methods were effective in measuring these resonances, it was decided for future measurements to ramp the quadrupole (Helmholtz) current to a set a value and vary the bias current. This is due to higher values of bias fields being accessible with the quadrupole (Helmholtz) coils alone.

We now consider the second method of calibration, using microwave spectroscopy of Cs. This method has the advantage of being able to measure the field at any value within the accessible range, including at the predicted values for the interspecies resonances.

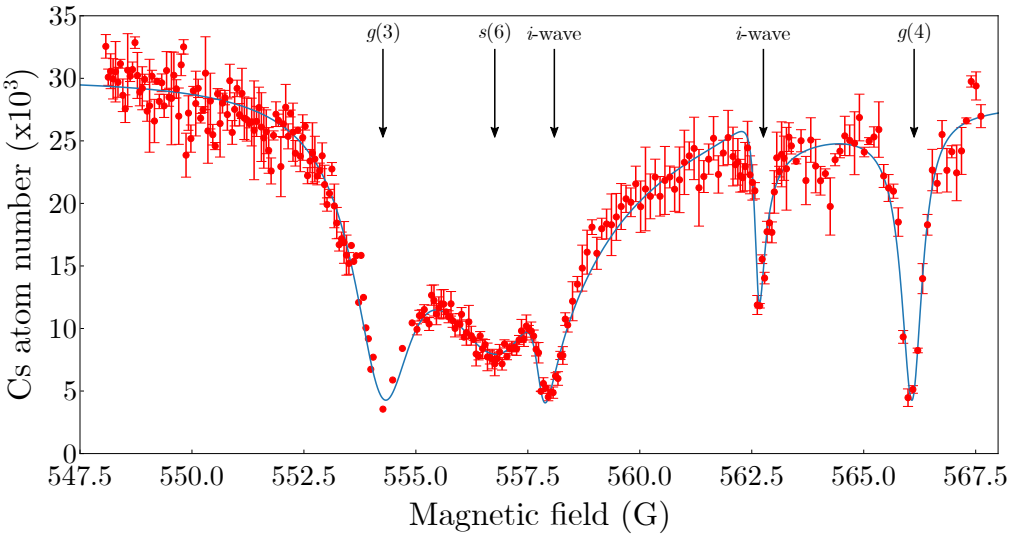

Figure 6.6: **Cs_2 Feshbach resonances around 553 G.** The Feshbach structure was probed in this field by measuring resonant loss of Cs atoms after a 500 ms hold at the target field. The scan range encompasses resonances at 554.06 G, 557.45 G, 562.18 G, and 565.48 G. Each resonance is labelled by its assigned molecular state given in [134]. The blue curve is a fit to the data which is a combination of Fano profiles for each resonance. There is also a predicted CsYb resonance in this region at 553 G, but this could not be detected when repeating the experiment with a Cs-Yb mixture.

6.3.2 Microwave spectroscopy of Cs

The principle of this method is to utilise the microwave transition in the Cs 6s ground state manifold from $|F = 3, m_F = +3\rangle$, the state into which the Cs is prepared by our cooling routine for absorption imaging, to $|F = 4, m_F = +4\rangle$. Both states experience a Zeeman shift, given by the Breit-Rabi formula [239]:

$$E_{4,4} = -\frac{E_{\text{hfs}}}{2(2I+1)} + g_I \mu_B 4B + \frac{E_{\text{hfs}}}{2}\sqrt{1 + 4\frac{4x}{2I+1} + x^2} \tag{6.6}$$

$$E_{3,3} = -\frac{E_{\text{hfs}}}{2(2I+1)} + g_I \mu_B 3B + \frac{E_{\text{hfs}}}{2}\sqrt{1 + 4\frac{3x}{2I+1} + x^2}, \tag{6.7}$$

where

$$x = (g_J - g_I)\mu_B \frac{B}{E_{\text{hfs}}}, \tag{6.8}$$

E_{hfs} is the hyperfine splitting between states $F = 3$ and $F = 4$ at zero field, the nuclear spin $I = 7/2$ for Cs g_I and g_J are the g-factors for nuclear and electron

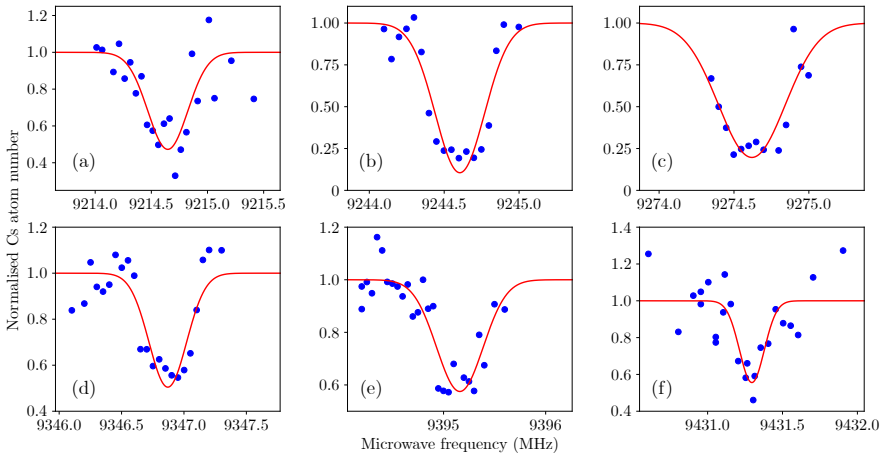

Figure 6.7: **Microwave calibration of the MOT coils in bias configuration.** Population of Cs atoms remaining in the $|F = 3, m_F = +3\rangle$ state after a 500 ms pulse of microwave radiation at 0 dBm output power. The MOT coils were switched to bias configuration, with an analogue output on the LabVIEW control of (a) 0.20 V, (b) 0.45 V, (c) 0.70 V, (d) 1.30 V, (e) 1.70 V, and (f) 2.00 V. The red curves are Gaussian fits to the data to determine the centre frequency of the transition. The Gaussian widths of the curves correspond to those expected due to power broadening.

spin respectively, and μ_B is the Bohr magneton. The measured resonant microwave frequency ν_a is thus

$$\nu_a = (E_{4,4} - E_{3,3} - E_{\text{hfs}})/h. \tag{6.9}$$

The transition frequency at zero magnetic field E_{hfs}/h is 9.192 631 770 GHz. At the bias field of 22 G typically used in our experimental routine, the transition frequency is expected to be 9.246 494 554 GHz. The microwave field was generated using a microwave horn directed at the science chamber.

A calibration curve for any of the field generation coils could then be generated by ramping the coil to a set value and performing a scan of the microwave field across the predicted value for the transition and measuring the loss of the population of Cs atoms in $|F = 3, m_F = +3\rangle$. Using a levitation gradient during time of flight makes the two states experience a different levitation potential and spatially separate. Alternately, the population in $|F = 4, m_F = +4\rangle$ could be measured by using no repump light during absorption imaging. Figure 6.7 shows the loss curves of

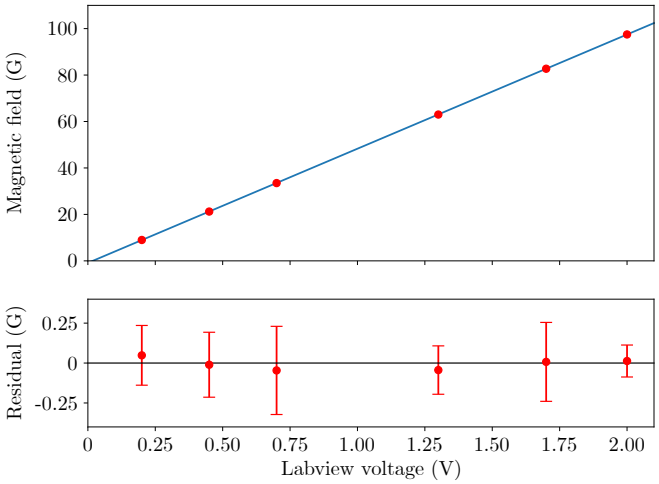

Figure 6.8: **Microwave calibration of the MOT coils in bias configuration.** Magnetic fields determined from the central frequency of the loss curves in figure 6.7 and the differential magnetic moment from the Zeeman shift of each state, plotted against the analogue output on the LabVIEW control. The straight line is a linear fit giving a calibration for the magnetic field of 49.19(2) G/V - 0.91(3) G.

Cs atoms remaining in the $|F = 3, m_F = +3\rangle$ after a pulse of resonant microwave radiation for a range of analogue output voltages for the MOT coils in bias configuration. Figure 6.8 then shows a linear calibration of the field using these results of 49.19(2) G/V - 0.91(3) G. The microwave calibration varies from that using the Cs_2 resonances, with the m value of the linear fit varying by 1.46(15) % and the c value by 58(6) %. Note that figures 6.7 and 6.8 only give a calibration for the field up to 100 G. For a full calibration across the field range of interest, further microwave spectroscopy experiments will have to be taken at higher fields.

6.4 Feshbach Spectroscopy of Cs + ^{173}Yb

6.4.1 Experimental procedure

A simplified diagram of the experimental sequence is shown in figure 6.9. Our starting point for performing Feshbach spectroscopy is 2×10^5 Cs atoms in the

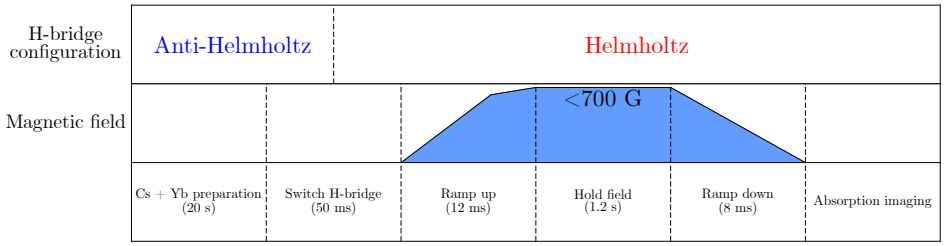

Figure 6.9: **Experimental sequence for Feshbach spectroscopy.** Following preparation of Cs and Yb atoms in the BODT, we switch the H-bridge to Helmholtz configuration and ramp the bias field to a target value. We hold the mixture at this value for a hold time, before ramping down and performing absorption imaging.

$|F = 3, m_F = +3\rangle$ state at a temperature of 2.0 µK, and $3{\times}10^5$ ^{173}Yb atoms at a temperature of 0.8 µK, optically trapped in the BODT. The cooling and evaporation techniques used to reach these conditions are outlined in previous sections. Once the atomic samples are prepared, the quadrupole coils are switched by the H-bridge from anti-Helmholtz to Helmholtz configuration. This is performed in 50 ms. The maximum permissible voltage and current of the coil power supplies is also increased. This takes $\sim$ 200 ms to take effect, so the voltages are changed a few steps in the experimental routine (using the experimental control Labview program) prior to the H-bridge switch. The bias and quadrupole currents are then ramped up in 12 ms. The ramp up is performed in two stages. The first stage ramps over 8 ms to a value near but below the field value of interest. A second stage ramps over 4 ms to the field value of interest. This is then varied over the course of the experimental run to scan for any potential resonances over a given region of bias field. The intermediate field value is unchanged.

The field ramp necessarily passes through the field value of many Cs intraspecies Feshbach resonances. However, a uniform field ramp across these resonances means the inevitable loss in Cs atoms is also uniform between experimental runs. A shorter second ramp over a smaller current range also prevents overshoot in the value of current. For many of the field values discussed below, the quadrupole coils are

ramped to their highest possible current, and the bias coil is ramped to a variable current depending on the field value of interest. We then hold the mixture at the set field value. We have found that a hold time of up to 1200 ms does not result in any significant heat dissipation in the circuit of the bias or quadrupole coils, and when monitoring the current of the coils found that this was stable over the duration of such a hold time to within $< 0.01\,\%$. We then ramp the fields down to 0 G in 8 ms, reset the maximum voltage of the power supplies, and image the remaining atoms after time-of-flight absorption imaging. The H-bridge is reset to anti-Helmholtz configuration at the start of each successive experimental sequence. In order to further mitigate heating of the coil circuits during an experimental run of 20 to 30 successive sequences, we implement a wait time of 10 s between sequences.

Atom loss due to three-body recombination is strongly enhanced for the large scattering lengths which occur near the pole of a Feshbach resonance. This is ultimately useful for our purposes in searching for interspecies resonances. However, the rich Feshbach structure of Cs-Cs [134] means the Cs intraspecies scattering length a_{Cs} is large at many magnetic fields, including those of interest to us experimentally. We therefore observe a large amount of background loss of Cs due to the high homonuclear three-body recombination rate, and through having to ramp across multiple resonances to reach the 'target' field. We observe that, for a hold time of $1\,s$ around a 'target' magnetic field near to, but off-resonant from, the predicted 622 G resonance, there is less than 5 % of the initial Cs atom number remaining, in the absence of Yb. Off-resonance around 553 G, there were typically 2.5×10^4 after the Feshbach ramp. The loss here can be attributed to being in proximity to a broad intraspecies resonance. Around the 167 G resonance and the 622 G resonances, the remaining number was 7.0×10^4 and 4.5×10^4. The Yb atoms, in contrast, have a much longer lifetime which is not noticeably affected by the Feshbach ramps. We typically have 1.2×10^5 Yb atoms remaining after the Feshbach ramp to any field. This large number imbalance in favour of Yb means the fractional change

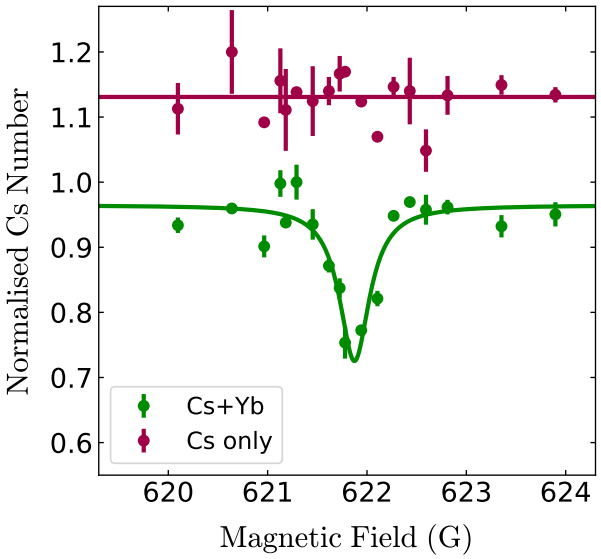

Figure 6.10: **The CsYb interspecies Feshbach resonance at 622 G.** Resonant loss (green) of Cs atoms in the Cs–^{173}Yb mixture after a 1200 ms hold time at the magnetic field of interest. The solid line is a lorentzian fit to the data giving a field centre of 621.8 $\pm$ 0.1_{stat} $\pm$ 1_{sys} G and a full width half maximum of 0.40 ± 0.08 G. A measurement using Cs atoms only (red) verifies the resonance is only seen in the dual-species mixture. This data and the straight-line fit are offset in the plot for clarity.

in Yb at an interspecies resonance is very small compared to that of Cs. This necessitates the use of remaining Cs atom number as the probe for the detection of an interspecies resonance.

6.4.2 622 G and 702 G resonances

Using the experimental procedure outlined above, we were able to reproducibly measure the predicted resonances at 622 G and 700 G. Figure 6.10 shows the loss feature of Cs atoms around the 622 G resonance, decreasing to $\sim$ 70% of the background Cs atom number measured at off-resonant fields near the resonance. The fit gives a central magnetic field of $621.8 \pm$ ś 0.1_{stat} $\pm$ 1_{sys} G and a resonance full width half maximum of 0.40 ± 0.08 G. The predicted value of this resonance of 619.54 G (for the widest m_F state in the set of resonances) falls outside the error margin of

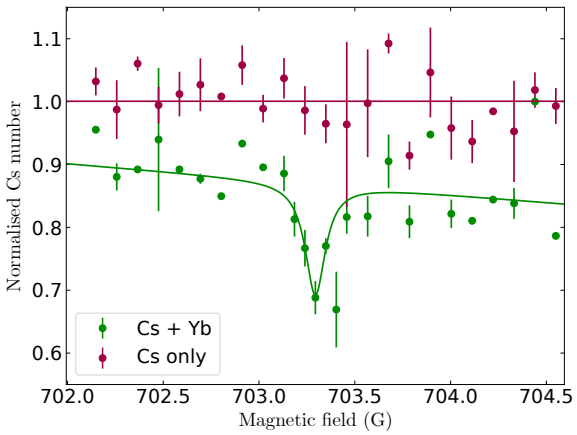

Figure 6.11: **The CsYb interspecies Feshbach resonance at 702 G.** Resonant loss (green) of Cs atoms in the Cs–^{173}Yb mixture after a 1200 ms hold time at the magnetic field of interest. The green line is a lorentzian fit to the data giving a field centre of $703.29 \pm 0.05_{\text{stat}} \pm 1_{\text{sys}}$ G and a full width half maximum of 0.13 ± 0.03 G. A measurement using Cs atoms only (red) verifies the resonance is only seen in the dual-species mixture.

our experimental result by over 1 G.

Figure 6.11 shows the loss feature of Cs atoms around the 702 G resonance. Again, the Cs number decreases to $\sim$ 70% of the background measured at off-resonant fields near the resonance. The fit gives a central magnetic field of $703.29 \pm 0.05_{\text{stat}} \pm 1_{\text{sys}}$ G and a resonance full width half maximum of 0.13 ± 0.03 G. The predicted value of this resonance of 699.76 G (for the widest m_F state in the set of resonances) falls outside the error margin of our experimental result by over 2 G. Note that the calibration of the bias field in this case is extrapolated from Cs_2 resonance measurements at lower fields. The absence of any nearby Cs_2 resonances indicates that another interspecies resonance is observed. A higher precision measurement can be made in concurrence with a microwave calibration around this field.

Repeat measurements of the 622 G and 702 G resonances were made following replacement of electrical components in the magnetic field stabilisation circuits with higher-precision equivalents, and optimisation of the feedback gain in the stabilisation circuits. These modifications improved the magnetic field stability at the

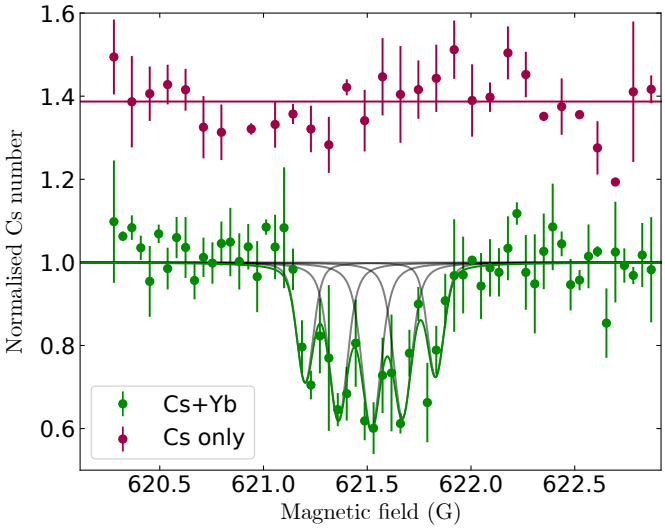

Figure 6.12: **Evidence of further structure in the 622 G resonance.** A scan across the same field as in figure 6.10 after improvements to the field stability. Multiple loss features can be observed, corresponding to the m_F nuclear spin substates in ^{173}Yb. The solid green line is a sum of 5 Voigt profiles. Each black line is a Voigt profile contributing to the full sum. The position of each resonance is shifted by $+1.98(3)$ G from the predicted value in table 6.3. The Gaussian and Lorentzian widths of each resonance are, respectively, 38 mG as determined from microwave spectroscopy, and the predicted width given in table 6.3 The depths of each resonance feature are scaled by the Lorentzian widths. The measurement with no Yb atoms present is offset for clarity.

currents corresponding to the resonances. The repeat measurements are shown in figures 6.12 and 6.13. Here, we see a number of smaller loss features. We attribute each of these smaller features to the resonances between Cs and each of the nuclear spin substates m_F of ^{173}Yb. At the 622 G resonance, these are predicted to occur in five of the six m_F states and are estimated to have a spacing of 0.16 G in the calculations of [93]. At the 702 G resonance, these are predicted to occur in all six m_F states, albeit with very different strengths, and are estimated to have a spacing of 0.15 G. The full list of resonances for every m_F state, with predicted position and width, at both regions of magnetic field, is shown in table 6.3.

However, the success in measuring these resonances is suggestive that we could indeed measure the resonance between Cs and each m_F state of ^{173}Yb in isolation

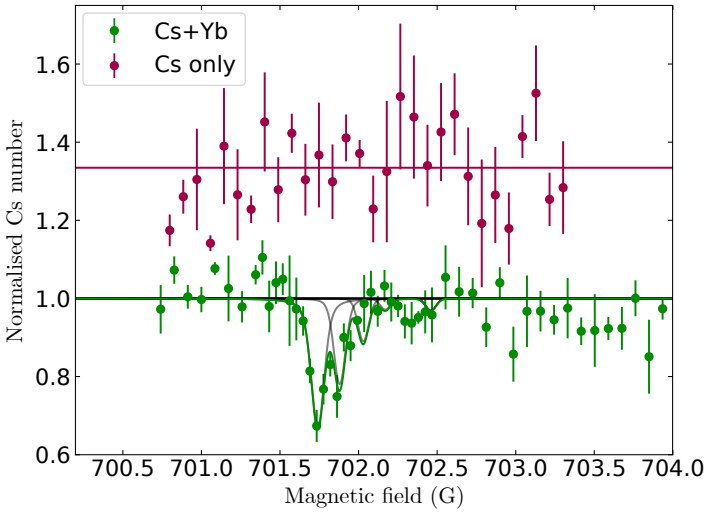

Figure 6.13: **Evidence of further structure in the 702 G resonance.** A scan across the same field as in figure 6.11 after improvements to the field stability. Multiple loss features can be observed, corresponding to the m_F nuclear spin substates in ^{173}Yb. The position of each resonance is shifted by +1.98(3) G from the predicted value in table 6.3. The gaussian and lorentzian widths of each resonance are, respectively, 38 mG as determined from microwave spectroscopy, and the predicted width given in table 6.3. The depths of each resonance feature are scaled by the Lorentzian widths. The measurement with no Yb atoms present is offset for clarity.

using our present methods of field generation, with an appropriate method of optical pumping to isolate the desired m_F state. As in initial attempt to prove this concept, we attempted to optically pump the trapped Yb to either spin-stretched state of $m_F = +\frac{3}{2}$ or $m_F = -\frac{3}{2}$. For this we exploited the use of circularly polarised beams already *in situ* in the experiment capable of optical pumping of Yb, namely the circularly polarised 399 nm imaging and Zeeman slower beams. We implemented 100 ms of optical pumping prior to loading the Cs, after having loaded the Yb from the CMOT to the dipole trap, and a 10 ms wait time for the MOT fields to fully switch off. This means we could perform the optical pumping with no vertical field from the MOT or Bias coils and could set the horizontal field using combinations of the horizontal shim coils. The target stretched state could be changed by reversing the current through the shim coils. To date, we have found

Yb m_F	B(G)	Δ(mG)
$-\frac{3}{2}$	619.22	16.831
$-\frac{1}{2}$	619.38	26.440
$\frac{1}{2}$	619.54	29.207
$\frac{3}{2}$	619.69	25.502
$\frac{5}{2}$	619.85	15.661
$-\frac{5}{2}$	699.76	20.993
$-\frac{3}{2}$	699.90	11.545
$-\frac{1}{2}$	700.05	4.9926
$\frac{1}{2}$	700.19	1.1901
$\frac{3}{2}$	700.33	1.1184×10^{-3}
$\frac{5}{2}$	700.48	1.2981

Table 6.3: Predicted positions and widths of interspecies Feshbach resonances between Cs and ^{173}Yb in the 620 G and 700 G regions of magnetic field, taken from [93].

no convincing experimental evidence using either beam that the distribution of m_F states had changed and therefore that optical pumping was taking place. We conclude that to perform full spin-resolved Feshbach spectroscopy, we will first need a method of measuring the spin distribution as a diagnostic of effective optical pumping, and possibly a new dedicated optical pumping setup. Both of these are further discussed in chapter 7.

6.4.3 Lower-field interspecies resonances

The resonances predicted at 167 G and 553 G have predicted normalised widths $\bar{\Delta}$ of 0.0110 mG and 0.0053 mG respectively (for the widest m_F state in each set of resonances), more than an order of magnitude lower than the resonance measured at 622 G. Scans of the bias field across these values following the methods described above produced no reproducible loss feature that could be attributed to these resonances. We conclude that we are unlikely to be able to successfully measure these resonances with the presently available magnetic field and atom trapping stability of the experiment.

6.5 Conclusion and outlook

We have performed Feshbach spectroscopy of the Cs + ^{173}Yb mixture and measured and characterised resonances at 622 G and 702 G. By developing a H-bridge configuration to switch our magnetic quadrupole coils between anti-Helmholtz and Helmholtz configurations, we were able to scan bias magnetic fields of up to approximately 700 G. We were able to show that both resonance features were a combination of resonances between Cs and the different nuclear spin substates m_F of ^{173}Yb.

6.5.1 Outlook: other Yb isotopes

Of the other experimentally accessible Yb isotopes, ^{171}Yb is the most promising for further observation of Feshbach resonances of a similar order of magnitude of width, and are predicted at field values comfortably within the accessible range of our setup. Table 6.4 lists the most promising resonances for experimental observation. The main experimental challenge for working with this isotope, however, will be efficient loading of ^{171}Yb into the BODT and subsequent evaporative cooling to reach phase-space densities of the mixture suitable for Feshbach spectroscopy. We must also consider broadening effects on the resonance due to thermal broadening and field instability. The Voigt profiles fit to the data in figures 6.12 and 6.13 use a width of the gaussian component of 38 mG, and a lorentzian component equal to the predicted widths. The gaussian width is on the order of the predicted widths of the resonances around 622 G and the widest of the resonances around 703 G. However the widths of the Cs–^{171}Yb resonances listed in table 6.4 are two orders of magnitude lower than the widths of the observed resonances. We should therefore aim to significantly reduce broadening effects when searching these resonances, either through making further improvements to the field stability, or reducing the temperature of the Cs–^{171}Yb mixture.

B (G)	Δ (mG)	Cs (F, m_F)	Yb m_F (Widest resonance)
149	0.40	(3,3)	$\frac{1}{2}$
171	0.078	(3,3)	$\frac{1}{2}$
203	0.41	(3,2)	$\frac{1}{2}$
423	0.53	(3,1)	$\frac{1}{2}$

Table 6.4: The most promising interspecies resonances between Cs and ^{171}Yb for experimental observation.

The experimental setup has previously been used to load ^{171}Yb into an optical dipole trap, however loading was inefficient compared to other isotopes. One solution may be to develop an experimental sequence where Cs is used as a sympathetic coolant. From our acquired knowledge of the molecular ground state potential, we predict an interspecies scattering length of $+70\,a_0$ for this isotoplog, which is promising for sympathetic cooling. Another option may be to sequentially load two isotopes of Yb, and use a second isotope such as ^{174}Yb to sympathetically cool ^{171}Yb. This would likely require additional laser power and upgrades to our 399 nm and 556 nm laser locking methods, see outlook. State transfer of Cs from the ground state to the target state, by a microwave Landau-Zener sweep or by optical pumping, will have to be considered for two of the resonances listed in table 6.4.

There are also a number of predicted resonances in the Cs+ ^{174}Yb at 66 G and 134 G, which are of a similar width to those lower-field resonances we were unable to measure in the Cs+ ^{173}Yb. One method we have considered in order to observe these weaker Feshbach resonances is the enhancement of loss rate due to photoassociation near a resonance. Narrow, low-field Cs_2 resonances have previously been observed in collisions of both $|F = 3, m_F = +3\rangle + |F = 3, m_F = +3\rangle$ mixtures and $|F = 3, m_F = +3\rangle + |F = 3, m_F = +2\rangle$ mixtures through the use of radiative Feshbach spectroscopy [240; 132], where light off-resonant from an atomic transition excites a one-photon transition from the bound state responsible for the resonance to the repulsive excited-state continuum, dissociating the atoms and promoting them with sufficient energy to leave the trapping potential without affecting

individual atoms not involved in the collision. This is a two-body process and therefore may be advantageous for narrow resonances compared to the three-body loss processes used for our measurements of wider resonances. In our experiment, we have the advantage of knowledge of the photoassociation spectrum of the experimentally accessible Cs-Yb isotopologs, and the experimental setup for one-photon photoassociation spectroscopy is still available for use with minimal modifications.

6.5.2 Outlook: resonances for magnetoassociation

There are still many questions that must be addressed prior to finding a Feshbach resonance suitable for magnetoassociation. The strength of the resonances must be considered. For the measured resonances, only $\sim 30\,\%$ of the Cs atoms in the mixture are lost during the hold time of 1200 ms. This value may be improved upon if the trapped Yb can be spin-polarised, so manipulation and detection of the Yb spin is an avenue we wish to consider. This explored in chapter 7. The practicality of routinely running the experiment at high fields and the dissipation of heat in the magnetic field coils to effectively perform a magnetoassociation ramp across a high-field resonance may have to be considered. We have found during the Feshbach spectroscopy measurements that there is significant Cs loss due to ramping through intraspecies resonances. For example, only $\sim 20\,\%$ of Cs atoms remain in the trap following a ramp to an off-resonant field near the 622 G resonance. This may place a limitation on number of CsYb Feshbach molecules produced in one magnetoassociation run.

The main challenges for efficient magnetoassociation will be retaining a high-PSD mixture, and applying a field ramp of an appropriate speed. The need for a high-PSD mixture arises from the need to keep the atoms in sufficiently close proximity during the Feshbach ramp. For our system, it may ultimately be required to create a Mott insulator of Cs and Yb for sufficiently high PSD for efficient magnetoassociation. The maximum efficiency is set by the PSD. The ability to reach this efficiency, however, depends the ramp speed $\frac{\mathrm{d}B}{\mathrm{d}t}$. The required ramp speed is in

turn dependent on the width Δ of the resonance, and the background scattering length a_{bg} of the mixture. For a field ramp of time t, the populations of the atomic and Feshbach states, $|C_0(t)|^2$ and $|C_1(t)|^2$ can be modelled by the Landau-Zener formulae [241]:

$$|C_0(t)|^2 = \mathrm{e}^{-2\pi\delta_{\mathrm{LZ}}}, \tag{6.10}$$

$$|C_1(t)|^2 = 1 - \mathrm{e}^{-2\pi\delta_{\mathrm{LZ}}}, \tag{6.11}$$

where δ_{LZ} is the Landau-Zener parameter for a two-body collision:

$$\delta_{\mathrm{LZ}} = \frac{4\pi\hbar|\mathrm{a_{bg}}||\Delta|}{\nu|\frac{\mathrm{d}B}{\mathrm{d}t}|} \tag{6.12}$$

where ν is a constant dependent on a_{bg}, the trapped atom number and the trap harmonic oscillator length [241]. For the widest individual resonance in the two sets of resonances we have measured, we estimate that using a field ramp of $\frac{\mathrm{d}B}{\mathrm{d}t} = 0.3\,\mathrm{G\,s^{-1}}$ results in a conversion efficiency of 3 %. We note that the conversion efficiency could be significantly enhanced to potentially $> 90\,\%$ in a lattice geometry where the trap frequency is increased and the harmonic oscillator length is reduced. This is further motivation for creation of Mott insulators of Cs and Yb for magnetoassociation.

We must also consider instabilities within the magnetic field, which are likely dominated by 50 Hz noise. We will have to consider whether our field is sufficiently stable to allow us realise the required value of $\frac{\mathrm{d}B}{\mathrm{d}t}$ across the resonance to within an appropriate margin. Indeed, it may be concluded that there is no convenient Feshbach resonance for efficient magnetoassociation. While we have identified resonances with widths on the order of 100s of mG, the low scattering length of $1\,a_0$ is a severe limitation for magnetoassociation using this isotopolog.

It may yet be proven that all-optical methods of molecular association, for example the method of free-bound STIRAP transfer from two free atoms as has been used to produce Sr_2 atoms [242; 243], are more appropriate for the Cs-Yb system. Alternatively, one-photon photoassociation could be used to produce molecules in an

excited electronic state, which then decay to a high-lying state within the electronic ground state. From there, STIRAP could be used to transfer molecules to the rovibrational ground state. Both methods rely on favourable wavefunction overlap between the scattering state, intermediate excited molecular states and the molecular ground state [244]. As photoassociation is an incoherent process, both efficiency of production and detection of ground state molecules may be limited by this method. Similarly to magnetoassociation, both methods may benefit from additional confinement of atoms in an optical lattice, to reduce unwanted collisions and allow more control over the initial spin state of the atoms, for example if utilising a resonance where Cs is in a state other than $|F = 3, m_F = +3\rangle$.

Chapter 7

Nuclear spin substate detection and manipulation in Fermionic Yb

7.1 Introduction: nuclear spin substates in Fermionic Yb

The atomic structure of alkaline-earth-like atoms such as Yb, in comparison to alkali-metals such as Cs, allow relative simplicity of laser trapping and cooling. Specifically, the lack of hyperfine splitting in the ground state means that cooling transitions are closed and repump beams are not required. However, while the spin and orbital angular momenta of the Yb ground state are zero, there can also be contributions to the atomic structure from the nuclear spin I. For all the bosonic isotopes which are experimentally accessible, $I = 0$. However, both Fermionic isotopes possess non-zero nuclear spin. For ^{171}Yb, $I = \frac{1}{2}$, and for ^{173}Yb $I = \frac{5}{2}$. This gives rise to nuclear spin substates m_I satisfying $-I \leq m_I \leq +I$. These substates are distinguishable in the presence of a magnetic field to provide a quantisation axis. For both isotopes, given $J = 0$, these nuclear spin substates are

the only contributions to the hyperfine structure substates, $m_F = m_I$. For ground state ^{171}Yb and ^{173}Yb, there are two and six m_F states respectively.

These nuclear spin substates have had numerous applications, including in quantum logic and in quantum simulation for realisations of systems with SU($N = 2I + 1$) symmetry [105; 245; 246]. For areas of research involving Yb as one component in a two-species mixture, and for various schemes involving molecular association, there is growing interest in the manipulation and isolation of these substates [89]. The Feshbach resonances discussed in chapter 6, involving Fermionic isotopologs, can vary on position and width according to the spin state, and indeed may not exist for certain spin states. It is therefore an important aim in our experiment to modify our fermionic Yb sample to isolate a single substate and perform Feshbach spectroscopy with each such isolated state. This would improve our spectroscopy signal and, in the instances where resonances between neighbouring states are closely spaced, remove the problem of overlap in the resonance data between neighbouring states. Suitable resonances for magnetoassociation could then be identified. A method of appropriately preparing the Yb sample for such resonances could then be applied.

To make such measurements effectively, we must implement a method of manipulating the spin substates to isolate Yb into a target spin state. It is also important to have a method of determining the spin composition, and to also use this to verify we can effectively isolate a target spin state. In this chapter, we review the challenges related to realising this in our experimental setup, and methods that can be readily employed in the experiment. We conclude that spin manipulation and detection can be implemented in the near future with minor modifications to the experiment and can be used to further our understanding of the Feshbach structure of the Cs-Yb mixture.

7.2 Near-resonant AC Stark shifts and the optical Stern-Gerlach effect

In the following section, we describe the variation of the AC Stark shift for different m_F states at low detunings from atomic transitions. For this, we consider the vector and tensor contributions to the AC Stark shift as well as the scalar contribution. We then discuss how this variation can be used to effectively resolve the m_F states. We then discuss practical considerations of implementing such a scheme into the experiment.

7.2.1 Separation and resolution of $\mathbf{m_F}$ states

The spin composition of the Fermionic Yb sample could be resolved by applying a state-dependent force. This force needs to be sufficiently large to spatially separate the m_F states to the extent where clouds of neighbouring states are resolvable upon absorption imaging. This is readily achievable for alkali-metal atoms such as Cs. The m_F states can be resolved using the Stern-Gerlach effect. The state-dependent force F_z on an atom in state m_F within a magnetic field gradient $\frac{\mathrm{d}B}{\mathrm{d}z}$ is given by

$$F_z = g_F m_F \mu_B \frac{\mathrm{d}B}{\mathrm{d}z}, \tag{7.1}$$

where μ_B is the Bohr magneton, and g_F is the hyperfine Landé factor, which is given by

$$\begin{aligned} g_F &= g_J \frac{F(F+1)+J(J+1)-I(I+1)}{2F(F+1)} - g_I \frac{F(F+1)+I(I+1)-J(J-1)}{2F(F+1)}, \\ g_J &= g_L \frac{J(J+1)+L(L+1)-S(S+1)}{2J(J+1)} + g_S \frac{J(J+1)+S(S+1)-L(L+1)}{2J(J+1)}, \end{aligned} \tag{7.2}$$

where $g_L = 1$ and $g_S \simeq 2$. This force exists at a practically useful magnitude for ground state alkali-metal atoms with electron spin $S = \frac{1}{2}$ due to the electronic magnetic moment $g_S \mu_B S \simeq 1\,\mu_B$. A practically achievable field gradient of the order of a few 10s of $\mathrm{G\,cm^{-1}}$ is sufficient to provide a force which can spatially separate m_F

states. For example, the Stern-Gerlach effect was previously used in our experiment to verify DRSC was effectively pumping Cs atoms into the $|F = 3, m_F = +3\rangle$ state [140]. However, for ground state Yb, $S = 0$ and there is no electronic magnetic moment. To apply the Stern-Gerlach effect in this case would rely on the much weaker nuclear magnetic moment $-g_I \mu_B I$ and would require impractically high magnetic field gradients (see below for further discussion of g_I). We therefore consider application of a near-resonant light field [105; 247]. In this case, the force each individual m_F state experiences depends on the strength of the coupling to the relevant excited state as opposed to the Zeeman splitting of the ground state, This may provide an adequate difference in force between neighbouring m_F states. The theory and practical application of such a field is further discussed in the following sections.

7.2.2 Near-resonant AC Stark shifts

We have seen in previous chapters that the scalar contribution to the AC Stark shift is adequate to describe the optical potential of far detuned dipole trapping beams. However, for low detunings from atomic transitions, the vector and tensor contributions, and their dependence on the hyperfine structure substates, must also be considered. In this case, we use these dependencies advantageously to create state-dependent attractive or repulsive potentials and hence state-dependent forces.

The AC Stark shift per unit intensity of light field, V_0, of an atom in state $|F, m_F\rangle$ is given by

$$V_0 = -\frac{1}{2\epsilon_0 c}\left(\alpha^{(0)} + q\frac{m_F}{F}\alpha^{(1)} + \frac{3|\hat{e}_z| - 1}{2}\frac{3{m_F}^2 - F(F+1)}{F(2F-1)}\alpha^{(2)}\right), \tag{7.3}$$

where $\alpha^{(0,1,2)}$ are the scalar, vector, and tensor polarizabilities respectively, q is determined by the polarisation of the light satisfying

$$\begin{aligned} q &= -1, \text{ for circular polarisation driving } \sigma^- \text{ transitions} \\ q &= 0, \text{ for linear polarisation} \\ q &= +1, \text{ for circular polarisation driving } \sigma^+ \text{ transitions} \end{aligned} \tag{7.4}$$

and $\hat{e}_z$ is the projection of the polarisation vector on the quantisation axis. The three polarizability components for an atom in state $|F\rangle$ with allowed transitions to state $|F'\rangle$ are given by [248]

$$\alpha^{(0)} = \sum_{F'} \frac{2}{3} \frac{\omega_{F'F}}{\hbar(\omega_{F'F}{}^2 - \omega^2)} |\langle F|\mathbf{d}|F'\rangle|^2$$

$$\alpha^{(1)} = \sum_{F'} (-1)^{F'+F+1} \sqrt{\frac{6F(2F+1)}{F+1}} \begin{Bmatrix} 1 & 1 & 1 \\ F & F & F' \end{Bmatrix} \frac{\omega_{F'F}}{\hbar(\omega_{F'F}{}^2 - \omega^2)} |\langle F|\mathbf{d}|F'\rangle|^2$$

$$\alpha^{(2)} = \sum_{F'} (-1)^{F'+F} \sqrt{\frac{40F(2F+1)(2F-1)}{3(F+1)(2F+3)}} \begin{Bmatrix} 1 & 1 & 2 \\ F & F & F' \end{Bmatrix} \frac{\omega_{F'F}}{\hbar(\omega_{F'F}{}^2 - \omega^2)} |\langle F|\mathbf{d}|F'\rangle|^2, \tag{7.5}$$

where $\omega_{F'F}$ is the transition angular frequency, ω is the angular frequency of the light field,$\{\cdot\}$ is the Wigner-6j symbol, and $\langle F|\mathbf{d}|F'\rangle$ is the reduced dipole matrix element of the transition.

From equation 7.3, it can be seen that V_0 is dependent on the m_F state at low detunings due to both the vector and the tensor polarizability. The vector contribution can be eliminated by choosing linearly polarised light (as with the tuneable lattice in section 5.8.3), but can be maximised by choosing a circular polarisation of either handedness. The tensor light shift also contributes, and can be maximised by choosing linearly polarised light with the axis of polarisation aligned parallel to the quantisation axis. Figure 7.1 shows the variation of V_0 for the different m_F states of ^{173}Yb, in the region of the $^1S_0 \rightarrow {}^3P_1(|F = \frac{5}{2}\rangle \rightarrow |F'\rangle)$ transition, using circularly polarised light driving σ^+ transitions ($q = 1$).

Table 7.1 shows the contribution from each polarizability component to the AC Stark shift experienced by each m_F state, at a detuning of $+0.9\,\mathrm{GHz}$ from the $(|F = \frac{5}{2}\rangle \rightarrow |F' = \frac{7}{2}\rangle)$ transition (the choice of detuning is further discussed in section 7.2.4). It can be seen that for all states, the vector contribution exceeds the tensor contribution for circularly polarised light.

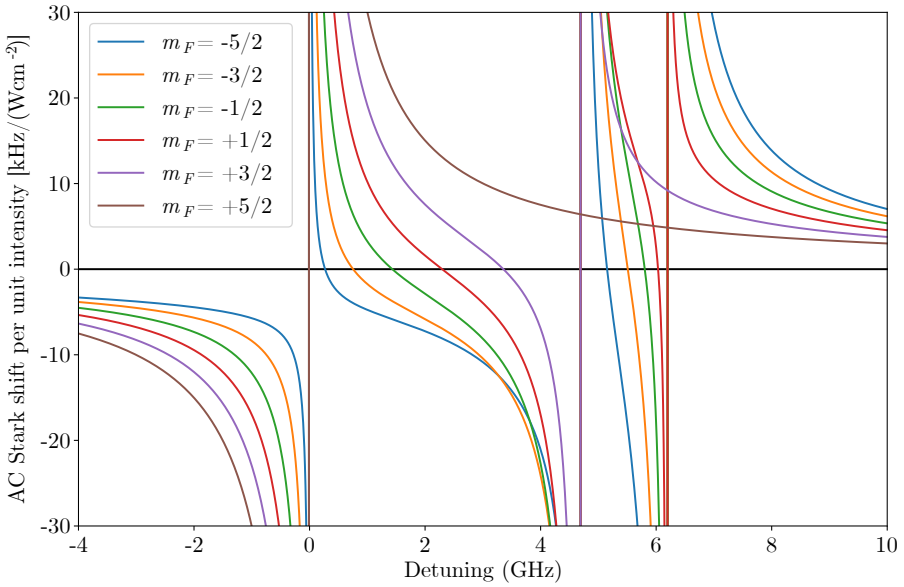

Figure 7.1: **Spin-dependent AC Stark shift in ^{173}Yb.** The AC Stark shift for all m_F states in ^{173}Yb, using circularly polarised light driving σ^+ transitions ($q = 1$), around the $^1S_0 \rightarrow {}^3P_1$ transition at 556 nm. The hyperfine transitions are located at the solid vertical lines and are (L–R): $|F = \frac{5}{2}\rangle \rightarrow |F' = \frac{7}{2}\rangle, |F = \frac{5}{2}\rangle \rightarrow |F' = \frac{5}{2}\rangle, |F = \frac{5}{2}\rangle \rightarrow |F' = \frac{3}{2}\rangle$. The detuning axis is relative to the $|F = \frac{5}{2}\rangle \rightarrow |F' = \frac{7}{2}\rangle$ transition.

m_F	-$\frac{5}{2}$	-$\frac{3}{2}$	-$\frac{1}{2}$	$\frac{1}{2}$	$\frac{3}{2}$	$\frac{5}{2}$
Scalar [kHz/(W cm^{-2})]	10.9	10.9	10.9	10.9	12.2	14.8
Vector [kHz/(W cm^{-2})]	-18.9	-11.4	-3.79	3.79	10.2	15.9
Tensor [kHz/(W cm^{-2})]	3.53	-0.71	-2.82	-2.82	-0.83	2.65
Total [kHz/(W cm^{-2})]	-4.46	-1.12	4.34	11.9	21.6	33.4

Table 7.1: The scalar, vector and tensor polarizabilty contributions to the AC Stark shift for each m_F state of ^{173}Yb, at a detuning of +0.9 GHz from the $^1S_0 \rightarrow {}^3P_1$ ($|F = \frac{5}{2}\rangle \rightarrow |F' = \frac{7}{2}\rangle$) transition, using circularly polarised light driving σ^+ transitions ($q = 1$).

7.2.3 The optical Stern-Gerlach effect

The optical Stern-Gerlach (OSG) effect takes advantage of the spin-dependent force of light blue detuned by the order of ∼100s of MHz from an atomic transition to separate and resolve the m_F states. It was first implemented in the group of Yoshiro Takahashi for both ^{171}Yb and ^{173}Yb [105], before subsequently being implemented in ^{87}Sr [247]. This Fermionic isotope of Sr has a nuclear spin $I = \frac{9}{2}$, and hence 10 m_F states, which were fully resolved. The method has subsequently been used in multiple Fermionic Yb experiments [89; 249; 250] using 556 nm light blue detuned from the $^1S_0 \rightarrow {}^3P_1$ transition. An OSG experiment typically consists of a circularly polarised, blue-detuned beam whose waist is chosen to be large compared to that of the atom cloud (typically, optically trapped Yb with an in-trap size of a few 10s of µm). The OSG beam is aligned off-centre such that the gradient of the intensity, and hence the spin-dependent force, is at its greatest at the position of the atoms in-trap. For a Gaussian beam of waist ω_0 and power P, the light shift $V_{\mathrm{AC}}(\mathbf{r})$ at radius $\mathbf{r}$ is given by

$$V_{\mathrm{AC}}(\mathbf{r}) = V_0 \frac{2P}{\pi\omega_0^2} e^{-\frac{2r^2}{\omega_0^2}}, \tag{7.6}$$

where V_0 is the AC Stark shift per unit intensity at the beam centre, given by equation (2). Hence, the radial dipole force $F(\mathbf{r})$ is given by

$$F(\mathbf{r}) = \frac{4r}{\omega_0^2} V_{\mathrm{AC}}(r). \tag{7.7}$$

The maximum force is therefore experienced by the atoms at

$$r = \pm\frac{\omega_0}{2}. \tag{7.8}$$

A small magnetic bias field, typically a few G, is applied parallel to the OSG beam, providing an axis of quantisation and ensuring the OSG beam couples to $\sigma^{\pm}$ transitions only.

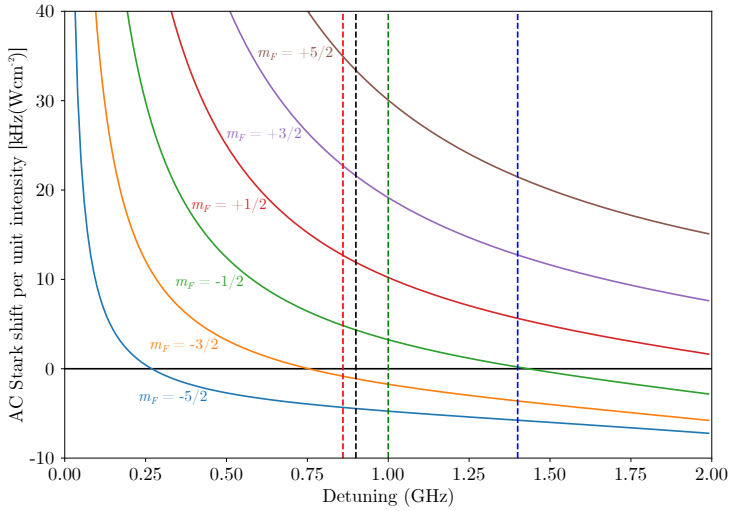

Figure 7.2: **Choice of detuning for the OSG beam.** The AC Stark shift for all m_F states in ^{173}Yb, using circularly polarised light driving σ^+ transitions ($q = 1$), for detunings up to 2 GHz from the $^1S_0 \rightarrow {}^3P_1(|F = \frac{5}{2}\rangle \rightarrow |F' = \frac{3}{2}\rangle)$ transition. Vertical dashed lines show the experimental detunings used for the OSG beam in references [89] (red), [250] (black), [105] (green) and [249] (blue). Note that for all of these examples, the OSG beam results in an attractive potential for the $m_F = -\frac{5}{2}$ and $m_F = -\frac{3}{2}$ states, and a repulsive potential for all other states.

7.2.4 Choice of OSG beam parameters

The OSG beam waist, power, and detuning must be chosen carefully to ensure the m_F states are separated sufficiently to be resolvable by absorption imaging after time of flight. Figure 7.2 shows V_0 for detunings above the $^1S_0 \rightarrow {}^3P_1(|F = \frac{5}{2}\rangle \rightarrow |F' = \frac{3}{2}\rangle)$ transition and compares the experimental detunings used by various Yb experimental groups [105; 249; 250; 89] which have employed an OSG beam. Table 7.2 further summarises the parameters chosen by the same groups [105; 247; 249; 250; 89].

At low detunings, there is high variation of V_0 for the different m_F states. However, the heating of the atoms due to near-resonant photon scattering must be considered. Figure 7.3a shows the photon scattering rate across the three hyperfine transitions, using an OSG beam with power 45 mW and waist 100 µm. Figure 7.3b shows the

Experiment	[105]	[247]	[249]	[250]	[89; 251]
Atom	^{171}Yb, ^{173}Yb	^{87}Sr	^{173}Yb	^{173}Yb	^{173}Yb
Number of beams	1	2	1	1	1
Beam waist (µm)	100	80, 60	100	100	100
Beam power (mW)	4	4, 0.5	45	40	-
Detuning (MHz)	+1000	+100, -100	+1400	+900	+860

Table 7.2: Comparison of OSG beam parameters used by other experimental groups.

region of detunings used by other experimental groups. Photon scattering prevents the effective use of an OSG beam for detunings less than ∼0.5 GHz. At these detunings, for a 45 mW beam with waist 100 µm, the scattering rate exceeds 10 kHz. This equates to 10 photon scattering events for a 1 ms OSG pulse. This precludes the use of the narrow region between the $|F = \frac{5}{2}\rangle \rightarrow |F' = \frac{5}{2}\rangle$ and $|F = \frac{5}{2}\rangle \rightarrow |F' = \frac{3}{2}\rangle$ transitions. The wider region of detuning between the $|F = \frac{5}{2}\rangle \rightarrow |F = \frac{7}{2}\rangle$ and $|F = \frac{5}{2}\rangle \rightarrow |F = \frac{5}{2}\rangle$ transitions is better suited to application of an OSG beam. Here, there is a high variation of V_0 for the different m_F states. The scattering rate, meanwhile, is low with less than 10 photon scattering events per OSG pulse for the beam parameters described above. This is sufficient for the heating of the atoms to not affect the OSG measurement.

Furthermore, a quantity which can be used for to interpret the efficiency of the OSG beam is the AC Stark shift between neighbouring m_F states, divided by the scattering rate. This is shown in figure 7.4 for an OSG beam of the same parameters as in figure 7.3. This quantity is reduced at low detunings due to the high scattering rate. It is optimised for various pairs of m_F states at various detunings between 1.5 GHz and 2.5 GHz. The ability to access these detunings is limited by the ability to efficiently shift the OSG beam frequency, see below.

7.2.5 Implementation of OSG

Typically, a horizontal OSG beam and bias field are used. The focus of the OSG beam is positioned above the position of the atoms by approximately $\frac{\omega_0}{2}$ to max-

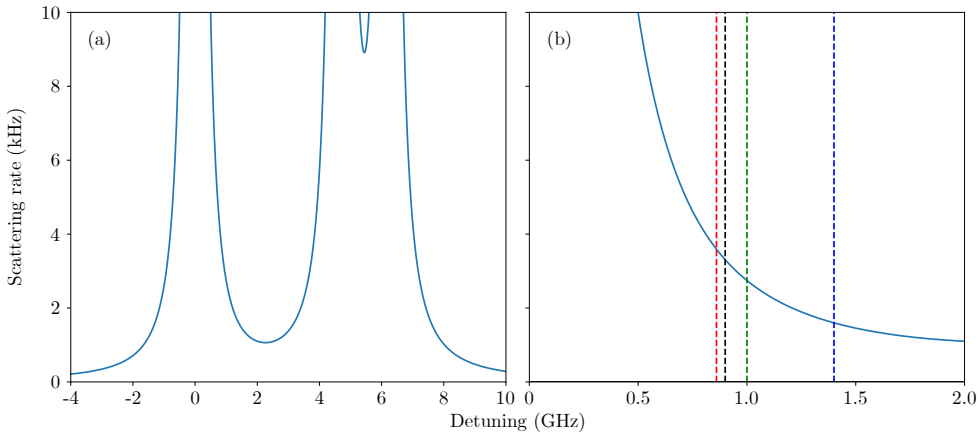

Figure 7.3: **Photon scattering in the OSG beam.** (a) The scattering rate for ^{173}Yb around the $^1S_0 \rightarrow {}^3P_1$ transition at 556 nm, using an OSG beam with power 45 mW and waist 100 µm. (b) The scattering rate at detunings up to 2 GHz from the $^1S_0 \rightarrow {}^3P_1(|F = \frac{5}{2}\rangle \rightarrow |F' = \frac{3}{2}\rangle)$ transition. Vertical dashed lines show the experimental detunings used for the OSG beam in references [89] (red), [250] (black), [105] (green) and [249] (blue).

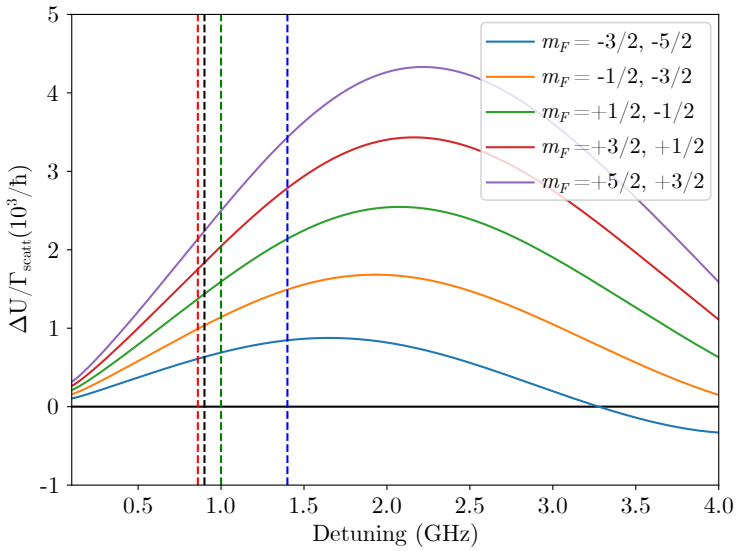

Figure 7.4: **'Efficiency' of the OSG beam.** The AC Stark shift between neighbouring m_F states in ^{173}Yb, divided by scattering rate, plotted for detunings up to 4 GHz from the $^1S_0 \rightarrow {}^3P_1(|F = \frac{5}{2}\rangle \rightarrow |F' = \frac{3}{2}\rangle)$ transition at 556 nm. The OSG beam parameters used are a power of 45 mW and a waist of 100 µm. Vertical dashed lines show the experimental detunings used for the OSG beam in references [89] (red), [250] (black), [105] (green) and [249] (blue).

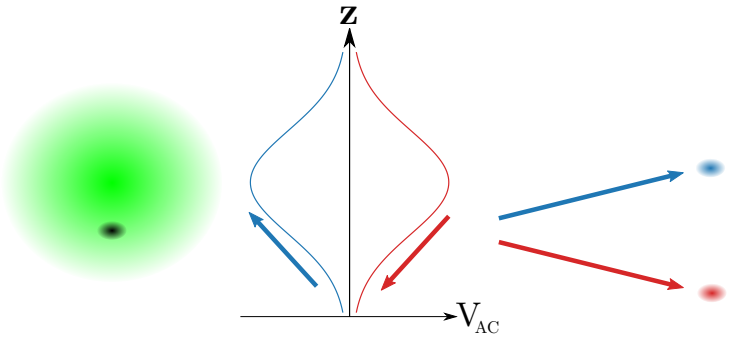

Figure 7.5: **Separation of nuclear spin substates using the optical Stern-Gerlach effect.** Schematic of an OSG setup: optically trapped Yb atoms (black) are exposed to a pulse of the OSG beam (green), which is aligned with the focus above the atoms. The magnitude and direction of the resulting potential V_{AC} depends on the nuclear spin substate m_F – depending on the detuning chosen, some states may be pulled upward towards the beam focus (blue arrows), whereas others may be pushed downward (red arrows). For sufficient OSG beam powers and pulse durations, the m_F states can be sufficiently spatially separated to resolve with absorption imaging after time of flight.

imise the force experienced by the atoms, in accordance with equation 7.7. The atoms thus experience an upward or downward force. All other optical traps are extinguished immediately prior to applying the OSG beam. The OSG beam is then usually applied for short pulse of a few ms with the atoms in free space. The pulse duration is limited therefore by the time in which the free-falling atoms are in the region where the gradient of the OSG beam intensity is high (recalling from section 7.2.1 that magnetic levitation of Yb is not practically achievable). We note from figure 7.2 that detunings are often used where V_{AC} is positive for some m_F states and negative for others; hence those states will be pushed towards and away from the focus of the OSG beam respectively, see figure 7.5. The positioning of the atoms above the focus means the states which are pushed away experience this force in the same direction as the force due to gravity. We also note that the difference in force between neighbouring states is reduced for lower m_F and indeed in most experiments those states could not be resolved. If the experimentalists wished to resolve these states, they could simply reverse the direction of circular polarisation of the OSG beam. This effectively 'flips' the vector polarizability contribution to

V_{AC}.

The success of the OSG method relies on being able to observe and resolve the m_F states after time of flight imaging. As a hard limit, the Yb falls out of our absorption imaging system's field of view after 25 ms of time of flight. However, we must also consider the spatial expansion and reduction in optical depth of the falling atoms. For the typical thermal Yb atom clouds used in our Feshbach spectroscopy measurements, the optical depth of the cloud is ∼0.7 for 10 ms time of flight. The width of the atom cloud is σ ∼600 µm in the vertical direction for this time of flight. This therefore is the lower limit for the splitting of neighbouring m_F states we consider in subsequent calculations. Improving the Yb evaporative cooling process can further lower this constraint. Considering our previous studies of Fermi degenerate gases of ^{173}Yb [140], a cloud width of 200 µm is achievable for a similar time of flight.

The choice of OSG beam waist determines the uniformity of the force experienced by the atoms in each m_F state across the atom cloud. Figures 7.6a and 7.6b show the radial dependence of the combined potential from the OSG beam V_{OSG} and the gravitational potential V_{grav}, and the resulting force, using an OSG beam with power 45 mW, waist 100 µm and detuning 0.9 GHz. For this choice of beam waist, there is a 32 µm region around the initial position of the atoms where the force is uniform to within 10 % (17 µm below the initial position and 15 µm above). As this region is of the order of the bichromatic trap beam waist, initially the atom cloud should experience a sufficiently uniform force. Atoms free-falling under gravity will fall out of this region after 1.9 ms. Therefore applying OSG pulses longer than this time duration may affect the uniformity of the force experienced by each state. The uniformity may also be affected by thermal expansion of the cloud. The temperature of the cloud should therefore be sufficiently low that expansion over the 1.9 ms time period keeps the spatial extent of the cloud within the region of uniformity.

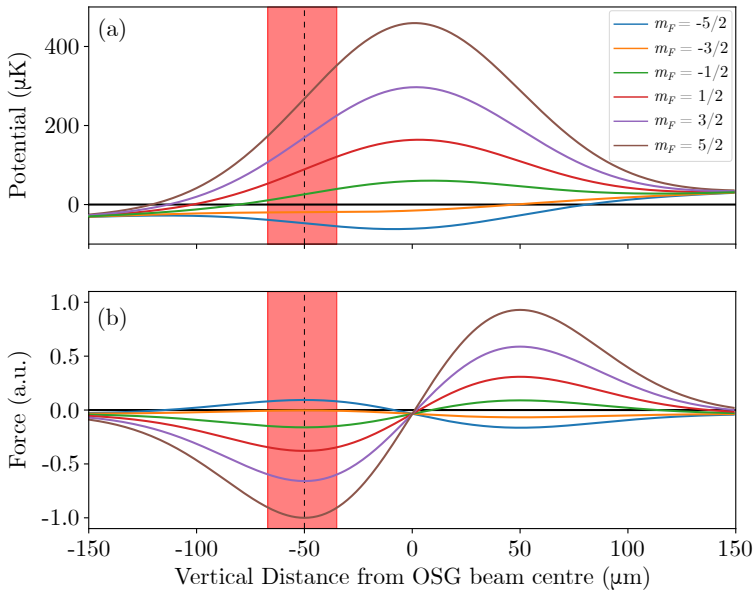

Figure 7.6: **The radial dependence on the OSG potential and force.** (a) The combined potential from the OSG beam V_{OSG} and the gravitational potential V_{grav} for all m_F states in ^{173}Yb, using an OSG beam with power 45 mW, waist $\omega_0 = 100\,\mu\mathrm{m}$ and detuning 0.9 GHz from the $^1S_0 \rightarrow {}^3P_1(|F = \frac{5}{2}\rangle \rightarrow |F' = \frac{3}{2}\rangle)$ transition at 556 nm. (b) The resulting force on each m_F state. The magnitude of the force is normalised to the minimum force experienced by the $|m_F = -\frac{5}{2}\rangle$ state. The OSG beam should be aligned such that the centre of the Yb atom cloud is initially $0.5\,\omega_0$ below the beam focus (dashed vertical line). The red shaded region shows the region in which the force on each state varies by less than 10 % from the maximum/minimum at $-50\,\mu\mathrm{m}$.

7.2.6 Predicted m_F state splitting in ^{173}Yb

A critical quantity is the expected spatial separation of neighbouring m_F states after both the pulse and the time of flight. The OSG pulse will be performed while the atoms are falling in free space, immediately after release from the bichromatic trap. We must therefore consider the effect of the OSG potential V_{OSG}, and also the gravitational potential V_{grav}, on each m_F state during the pulse. As atoms move away from the area of the OSG beam where the intensity gradient is highest, the effect of V_{OSG} is reduced. For states initially pushed downwards by the beam, this would result in V_{grav} eventually becoming the only significant potential. States

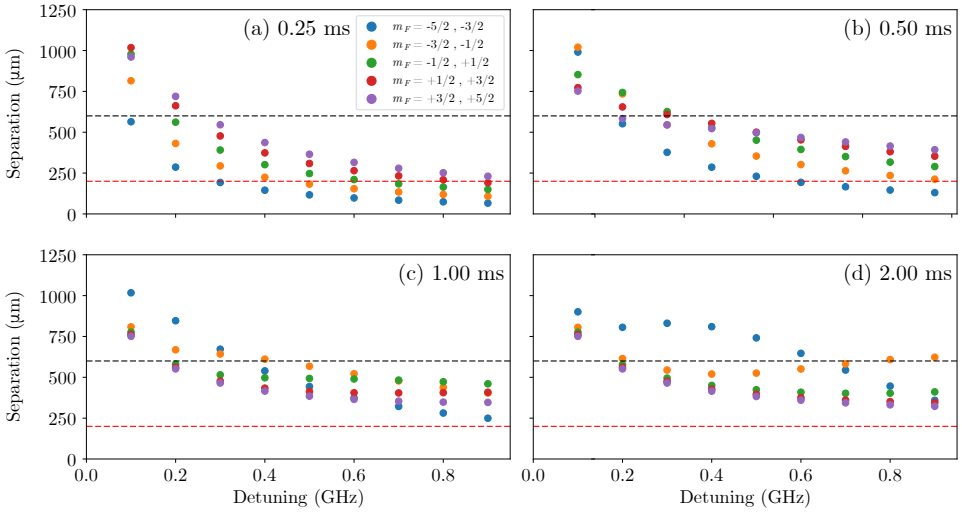

Figure 7.7: **Dependence of the OSG effect on detuning and pulse duration.** Calculation of the separation of neighbouring m_F states in ^{173}Yb for detunings of up to +9 GHz from the $^1S_0 \rightarrow {}^3P_1(|F = \frac{5}{2}\rangle \rightarrow |F' = \frac{3}{2}\rangle)$ transition, for pulse durations of (a) 0.25 ms, (b) 0.50 ms, (c) 1.00 ms, and (d) 2.00 ms, and 10 ms of time of flight. The calculation is for an OSG beam with power 45 mW and waist $\omega_0 = 100\,\mu$m, focused 50 µm above the atom cloud. Horizontal dashed lines show the approximate widths of the ^{173}Yb atom cloud at 0.8 µK (600 µm, black) and of a degenerate Fermi gas of ^{173}Yb (200 µm, red), in our optical dipole trap.

pulled towards the beam focus may eventually perform dipole oscillations around the position of the focus. After the pulse V_{grav} is the sole potential.

Figure 7.7 shows calculated spatial separations between neighbouring m_F states for OSG pulses of up to 2 ms and 10 ms time of flight, for an OSG beam with power 45 mW and waist $\omega_0 = 100\,\mu$m. The separations are calculated by calculating the displacement and velocity of atoms in each state during the pulse, in time increments of 10 µs. The displacement in each increment is due to the potentials $V_{\text{OSG}}(\mathbf{r})$ and V_{grav}, and the velocity at the beginning of the time increment. Following the end of the pulse, the subsequent displacement during time of flight is calculated. This displacement is due to V_{grav}, and the velocity at the end of the OSG pulse.

The effect of the pulse duration can be interpreted differently for the different m_F states. We first consider spacings between states for which V_{OSG} is always

repulsive in this detuning range (green, red and purple circles). For short pulses (figures 7.7a and 7.7b), as the pulse length increases the difference in V_{OSG} for neighbouring states allows them to spatially separate. However, for longer pulses (figures 7.7c and 7.7d), states which initially experienced a greater force are now further from the centre of the OSG beam, and V_{OSG} is reduced. Other states which are closer to the beam centre now experience a greater force and the separation is reduced. There is hence an optimal pulse duration for maximising each value of separation. For example, the separation between $|m_F = \frac{3}{2}\rangle$ and $|m_F = \frac{5}{2}\rangle$ (purple circles) appears to be optimised for a 0.5 ms pulse (figure 7.7b).

There is a different interpretation for separations between m_F states which experience a crossing in V_{OSG} from a repulsive to an attractive potential in this detuning range (blue and orange circles). For short pulse times, separation is low as $|V_{\mathrm{OSG}}|$ is comparatively low for these states. However, a 2 ms pulse (figure 7.7d) is sufficiently long for states which experience an attractive force to be pulled towards the OSG beam focus. In the detuning range up to ~ 0.75 GHz, the separation between $|m_F = -\frac{5}{2}\rangle$ and $|m_F = -\frac{3}{2}\rangle$ (blue circles) is the greatest out of any separation between states, as the former state is attracted to the beam focus while the latter is repelled. At ~ 0.75 GHz, V_{OSG} becomes attractive for $|m_F = -\frac{3}{2}\rangle$, so the separation between $|m_F = -\frac{3}{2}\rangle$ and $|m_F = -\frac{1}{2}\rangle$ (orange circles) is the greatest for detunings above this value.

For a 1 ms pulse (figure 7.7b), we predict that at higher detunings, all states except $m_F = -\frac{5}{2}$ and $m_F = -\frac{3}{2}$ would be resolvable. This is on the condition, however, that the atom cloud size is $> 200\,\mu$m after time of flight expansion. This would be in agreement with the typical distributions seen after OSG pulses in other Yb experiments. We cannot expect the states to be resolvable if the atom cloud size is $\sim 200\,\mu$m. Hence, we may have to develop a more effective evaporative cooling routine for ^{173}Yb for the OSG pulse to be an effective means of measuring its spin distribution.

7.2.7 Other experimental considerations

The 556 nm light for the OSG beam can be derived from the current 1112 nm + SHG setup used for the Yb MOT. When accounting for efficiencies of all optical components in this system, the full 200 mW output of the SHG is required for generation of the three MOT beams, as well as the beam for frequency stabilisation by fluorescence spectroscopy. We therefore cannot split off any of the output power for a dedicated OSG setup. However, the Yb MOT and OSG beam will not be on simultaneously during any experimental routine. We can therefore use the zeroth order of the Yb MOT AOM (AOM 12 on spectroscopy table) as our input beam for the OSG setup. The zeroth order can be split from the MOT beam setup using a D-shaped mirror. With AOM 12 off and maximum power in the zeroth order, and accounting for expected efficiency of the AOM in double-pass configuration and fiber coupling, we predict the available power for the OSG beam in the science chamber to be 45 mW. We also note that as we will upgrade to a different 556 nm source in the near future, see chapter 8. This would give us scope to develop a dedicated OSG setup independent of the MOT setup, and to increase the beam power if necessary.

For the OSG setup a frequency shifter will be needed to generate the blue detunings of up to 1 GHz required. This is achievable with an AOM in double-pass configuration, although for higher detunings a quadruple-pass configuration [252] may be considered. This would also allow us to pulse on and off the OSG beam on the ms timescale. There is space on the spectroscopy table adjacent to the other Yb spectroscopy setups to implement this. The OSG beam light would then be coupled to the main experimental table using polarisation-maintaining fibers similar to those used for the Yb MOT beams. On the experimental chamber, the beam will need to be collimated and then focused through the centre of the chamber, with the beam waist aligned above the centre of the Yb dimple trap. The beam would propagate through one of the horizontal Yb MOT beam viewport pairs, as these have

most appropriate antireflection coating for 556 nm light. A beam waist of ∼100 µm should be an appropriate size in relation to the in-trap atom cloud size of ∼ 20 µm. A quarter-wave plate will be required to modify the light polarisation to the correct circular polarisation; it may be advantageous to mount this waveplate in a motorised rotation mount so the direction of the circular polarisation can be reversed automatically if required. The shim coils can be used to generate a horizontal bias field sufficient to define the quantisation axis.

7.3 Optical pumping of Fermionic Yb

Once we have developed and tested an optical Stern-Gerlach setup to measure the spin distribution of Fermionic Yb, we will be able to manipulate the spin distribution and subsequently quantify its efficacy. For Alkali atoms such as Cs, different m_F states can be selected and prepared using the hyperfine coupling within the ground state manifold and driving transitions with rf or microwave radiation. However, this is not possible in ground state Yb, as $J = 0$ and there is no hyperfine splitting. We instead propose to use the method of optical pumping, using the $^1S_0 \rightarrow {}^3P_1$ transition as other experimental groups using Yb have [105; 253; 254; 89] (we note the $^1S_0 \rightarrow {}^1P_1$ transition has also been used [105; 251])). The following sections describe the potential options for implementation in our experimental setup.

7.3.1 Optical pumping with degenerate and non-degenerate excited states

Here, we discuss two distinct scenarios for optical pumping. The first, shown in figure 7.8(a), involves optical pumping on a transition where the m_F states of the excited states are degenerate [105; 247]. Circularly polarised light driving σ^+ or σ^- transitions pump atoms towards either $|F, m_F = +F\rangle$ or $|F, m_F = -F\rangle$ state (the 'spin-stretched' states). An advantage of using this method of pumping is that only

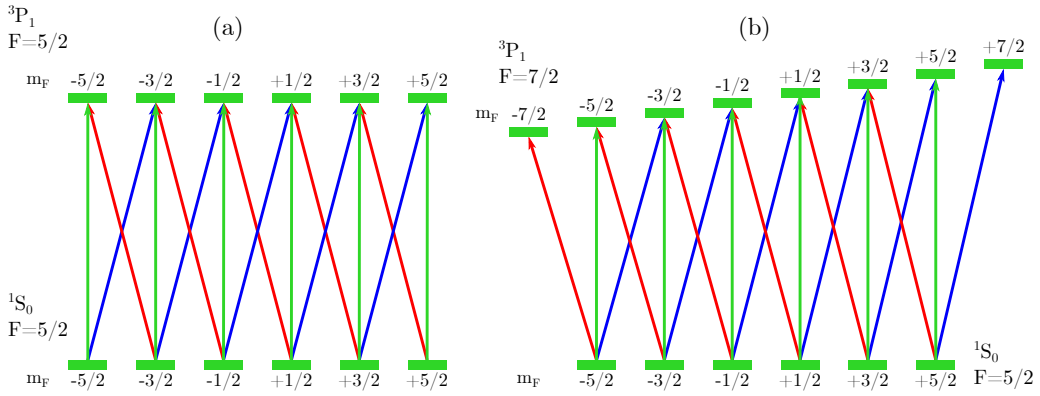

Figure 7.8: **Hyperfine transitions in ^{173}Yb for optical pumping** The spin distribution of Fermionic Yb atoms can be manipulated by driving transitions between m_F states, namely σ^+ transitions (blue) and σ^- transitions (red). π transitions are also shown in green. (a) Hyperfine pumping transitions on the $^1S_0 \rightarrow {}^3P_1(F = \frac{5}{2} \rightarrow \frac{5}{2})$ transition at 556 nm, with degenerate excited m'_F states can spin-polarise a sample to $m_F = \pm\frac{5}{2}$. (b) Hyperfine pumping transitions on the $^1S_0 \rightarrow {}^3P_1(F = \frac{5}{2} \rightarrow \frac{7}{2})$ transition with an applied bias field to lift the degeneracy in the excited m'_F states. The transition to each m'_F state hence has a unique resolvable frequency. A sequence of optical pumping pulses on σ transitions, driving atoms from unwanted m_F states, can hence be used to prepare Fermionic Yb in one or more chosen m_F states.

modest magnetic bias fields of a few G are required to define the quantisation axis. Additionally, the pumping can be performed with single-frequency light source tuned to the relevant atomic transition. The σ transitions driven can be changed by changing the direction of polarsiation of the light or reversing the direction of the magnetic field. The disadvantage, however, is the control over which desired m_F states the atoms are distributed into following pumping. For a sufficiently long time period of optical pumping, all atoms will end up in either stretched state, depending on whether σ^+ or σ^- transitions are being driven. Shorter pumping times can also result in a modified distribution of m_F states if the original distribution is well-known.

The second method, shown in figure 7.8(b), uses a larger bias magnetic field to lift the degeneracy of the m_F substates of the excited state manifold using the Zeeman effect, see section 7.3.2. With such a bias field applied, the allowed $\sigma^\pm$ and π transitions from each m_F state in the ground state manifold occur at different

frequencies that can be addressed separately. This allows the implementation of optical pumping routines where any m_F state in the ground state manifold can be isolated as the target for optical pumping. Alternately, routines can be devised to pump to a mixture of two or more m_F states. One potential application of this is to prepare the majority of the atoms in the state desired at the end of the evaporative cooling process, with the addition of a small fraction of another state. This 'sacrificial' state can act as a sympathetic coolant to the other state. It is subsequently either heated out of the trap during evaporative cooling, or removed by a resonant, state-selective pulse of light after evaporative cooling[89]. Many experiments employ this method of pumping on the ${}^1S_0 \rightarrow {}^3P_1(F = \frac{5}{2} \rightarrow F = \frac{7}{2})$ transition in ^{173}Yb [253; 254; 89]. The m_F state splitting must be sufficient to resolve the different transitions and avoid excitation to multiple states. However, the narrow linewidth of this transition means that bias fields of < 100G is sufficient to achieve this. The method requires a light source capable of tuning to the multiple frequencies necessary to address all transitions, as well as the ability to change the σ transitions driven, again by changing the light polarisation or bias field direction.

7.3.2 The Zeeman shift of the excited state

This second method uses magnetic fields up to $\sim$100 G, where the Zeeman shift can be approximated as linear and m_F is the relevant quantum number. The linear Zeeman shift $\Delta_z^{(1)}$ in a bias field $\mathbf{B}$ is given by

$$\Delta_z^{(1)} = \frac{\mu_B}{h} g_F m_F \mathbf{B}, \tag{7.9}$$

where μ_B is the Bohr magneton, h is Planck's constant, and g_F is the Landé factor for an atom in state ${}^{2S+1}L_J$ and with nuclear spin F, given by

$$\begin{aligned} g_F &= g_J \frac{F(F+1) + J(J+1) - I(I+1)}{2F(F+1)} - g_I \frac{F(F+1) + I(I+1) - J(J-1)}{2F(F+1)}, \\ g_J &= g_L \frac{J(J+1) + L(L+1) - S(S+1)}{2J(J+1)} + g_S \frac{J(J+1) + S(S+1) - L(L+1)}{2J(J+1)}. \end{aligned} \tag{7.10}$$

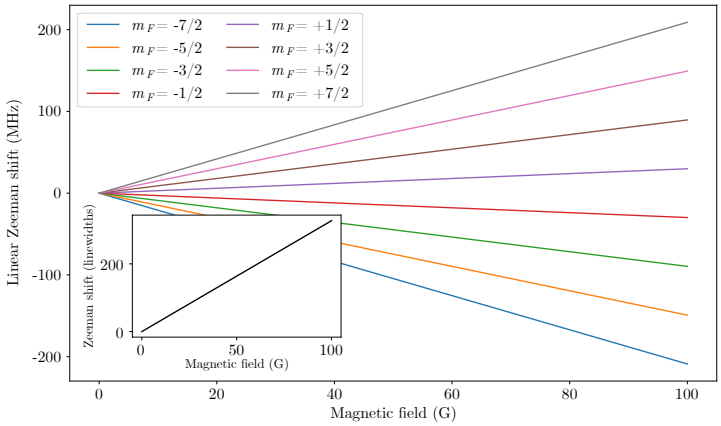

Figure 7.9: **Zeeman splitting of the $^3\mathbf{P_1}(\mathbf{F} = \frac{7}{2})$ state of ^{173}Yb.** The Zeeman shift for all m_F states for bias fields of up to 100 G. The inset shows the splitting between neighbouring m_F states over the same range, given in units of the $^1S_0 \rightarrow {}^3P_1$ transition linewidth (182.2 KHz).

Due to state mixing between the $^1P_1$, and $^3P_1$ states, we use a modified orbital Landé factor $g_J^{'}$ for the $^3P_1$ state, given by

$$g_J^{'} = \alpha^2 g_J(^3P_1^0) + \beta^2 g_J(^1P_1^0), \tag{7.11}$$

where $^3P_1^0$, $^1P_1^0$ are the bare (unmixed) states and the mixing angles β and α are given by

$$\frac{\beta^2}{\alpha^2} = \frac{\Gamma_{^3P_1}}{\Gamma_{^1P_1}} \frac{\nu^3(^1S_0 \rightarrow {}^1P_1)}{\nu^3(^1S_0 \rightarrow {}^3P_1)}, \tag{7.12}$$

using experimentally determined values for the transitions' frequencies and linewidths [255; 256] gives

$$\begin{aligned} \beta &= -0.1295(6), \\ \alpha &= \sqrt{1-\beta^2} = 0.99157(8). \end{aligned} \tag{7.13}$$

For ^{173}Yb in the $^3P_1^0$ $(F = \frac{7}{2})$ state, this results in a linear shift between neighbouring m_F states of 597.1 kHzG^{-1}. Figure 7.9 shows this linear shift for all m_F states, with the inset showing the shift magnitude between neighbouring states in units of the $^1S_0 \rightarrow {}^3P_1$ transition linewidth (182.2 kHz). We expect the limitation on the resolution of the states to be greater than the natural linewidth due to

power broadening, although by how much depends on the intensity of pumping beam used. For the ground state, $J = 0, F = I$ and equation 7.10 reduces to

$$g_F = -g_I = +207.30(1)\frac{h}{\mu_B}\,\mathrm{HzG}^{-1}, \tag{7.14}$$

the nuclear Landé factor g_I having been experimentally determined through m_F state-resolved optical pumping experiments [257]. Hence, the linear Zeeman shift of the ground state is three orders of magnitude weaker than that of the $^3P_1^0$ state. For higher magnetic fields >100 G, we would also have to consider the effect of hyperfine coupling, but the linear Zeeman shift gives a good enough approximation at fields where the m_F states can be resolved.

7.3.3 Implementation of optical pumping into the experiment

Optical pumping may be, in the degenerate case, feasible with one of the existing beams. The Zeeman slower beam or the probe beam could be used for the $^1S_0 \rightarrow {}^1P_1$ transition. Alternatively, one of the MOT beams could be used for the $^1S_0 \rightarrow {}^3P_1$ transition. The problems associated with use of these beams include that their circular polarisations are fixed, meaning the transitions to be driven must be determined by the orientation of the magnetic field. During our Feshbach spectroscopy measurements, we attempted to implement optical pumping using some of these beams tuned to resonance. However, without any diagnostic measurements of the spin composition, we could not prove the efficacy of this pumping. It may prove beneficial, therefore, to implement a separate optical pumping beam setup. This would be particularly true for the non-degenerate case, as an optical setup with a variable-frequency AOM could be used to provide the frequency shifts to the resolved hyperfine transitions, and to switch the beam on and off at the science chamber. In terms of available laser power, we again may be limited by the current 556 nm output from the SHG. However, the addition of a new laser may provide sufficient power for a dedicated optical pumping setup at this wavelength, see chapter 8. Light for the optical pumping beam will again have to be coupled

over to the main experimental table, and an optical setup devised to allow the beam to propagate through the chamber. A beam size must be chosen such that laser intensity is approximately uniform across the Yb atom cloud. As with the OSG beam, the pumping beam should propagate through the chamber using one of the same viewport pairs as the Yb MOT beams, for the most efficient transmission. In terms of the experimental routine, optical pumping should be implemented after atoms have loaded into the bichromatic trap, and while the trap is still sufficiently deep that atoms will not be lost from the trap due to resonant scattering. The bichromatic trap will induce a light shift on the transition, although that will not affect the relative splitting of the m_F states. Trap-loss experiments can be used to effectively determine the AOM detunings required for each pumping transition. The duration of the optical pumping pulse depends on both the intensity in the optical pumping beam available, and in the non-degenerate case, the relative line strengths of the transitions, but would be no more than the order of $\sim$100s of ms. In the non-degenerate case, multiple pulses can be implemented to polarise the sample in the desired m_F state.

7.4 Conclusion

In this chapter we have discussed the applications of measuring and manipulating the nuclear spin state distribution of the Fermionic isotopes of Yb, with particular emphasis on application to our ongoing Feshbach spectroscopy experiments. We have described the application of an OSG beam in the experiment to measure the spin distribution. We have discussed methods of optical pumping in order to prepare the Yb into the desired m_F state or states, which could then be verified with the OSG beam. We conclude that both experimental methods can be feasibly added to our experimental setup and carried out with minimal modifications and in conjunction with planned experimental upgrades.

Chapter 8

Conclusion and outlook

8.1 Summary

In this thesis, we have developed new methods of control of ultracold and quantum degenerate gases of Cs and Yb. This has enabled us to produce the first dual degenerate mixtures of Cs and Yb, and to detect interspecies Feshbach resonances in mixtures of Cs and Yb for the first time.

We have realised a bichromatic optical dipole trap (BODT) by the addition of a 532 nm dipole trapping beam to our existing 1070 nm dipole trapping apparatus. This experimental upgrade has allowed us to produce dual-degenerate mixtures in the experiment for the first time.

We have produced dual BECs of Cs and ^{174}Yb with typical atom numbers $N_{\mathrm{Yb}} \sim 5 \times 10^4$ and $N_{\mathrm{Cs}} \sim 5 \times 10^3$. We have investigated the attractive interspecies interactions in this degenerate mixture by exciting centre-of-mass oscillations and, by mediating dual-species collapse by changing the balance between the interspecies and intraspecies interactions. We have also produced dual BECs of Cs and ^{170}Yb with typical atom numbers $N_{\mathrm{Yb}} \sim 4 \times 10^4$ and $N_{\mathrm{Cs}} \sim 1 \times 10^4$. We have investigated the immiscibility of this degenerate mixture and its dependence on the relative atom numbers of the Cs and Yb gases.

To extend our study of degenerate gases into reduced and mixed dimensions, we have developed a tuneable optical lattice with $\lambda \sim 460\,\text{nm}$. The lattice can access 'tuneout' wavelengths, where Cs experiences no optical potential, as well as wavelengths where both species experience either equal trap depth or trap frequency. To better quantify the tuneability of the lattice, we have performed measurements of the Cs polarizability using Kapitza-Dirac diffraction. Our measurements indicated that our simple theoretical model of the atomic polarizablity, incorporating only scalar polarizability, was not sufficiently accurate for our choice of experimental geometry. We further investigated by using an extended model of polarizability and by considering the full hyperfine structure of Cs. We conclude that changing the geometry of our lattice beam to be perpendicular to our bias magnetic field, will be necessary to make a precision measurement of the tuneout wavelengths of Cs.

We have identified two sets of interspecies Feshbach resonances in an ultracold mixture of Cs and ^{173}Yb at 622 G and 702 G, which gives a promise of the possibility of formation of CsYb molecules using magnetoassociation. Our Feshbach spectroscopy measurements were able to resolve resonances between Cs and individual nuclear spin substates of Yb. The ability to measure and manipulate the spin composition of fermionic Yb will further extend our Feshbach spectroscopy studies, and we present a detailed plan for the future application of an optical Stern-Gerlach (OSG) beam and optical pumping techniques.

8.2 Outlook

Here we give a brief summary of other short and medium-term upgrades to the experimental apparatus. We discuss future research directions both in terms of the study of degenerate mixtures, Feshbach spectroscopy and molecule formation. We discuss some of the planned and possible upgrades specific to reaching these research goals.

8.2.1 New 556 nm light source

In recent years, the Menlo Orange One 1112 nm fiber laser system, which is frequency doubled to generate the 556 nm Yb MOT beams, has become increasingly unreliable, with the power amplifier stage of the laser sporadically shutting off while the laser is operational. Although in the last year we have been supplied with a replacement for a faulty power supply unit for the power amplifier, the cause of this issue remains unknown. The laser is operated at its maximum power output, which provides adequate power for the MOT beams and frequency stabilisation. However there is no surplus laser power for further applications. For the potential OSG and optical pumping applications discussed in chapter 7, the necessary laser power could be redirected from the MOT beams when needed. However, the potential plan to cool multiple isotopes of Yb in one experimental sequence (in order to, for example, facilitate sympathetic cooling between isotopes), poses an experimental challenge. Re-stabilising the laser to a second isotope's transition mid-sequence is not possible with the current frequency stabilisation hardware and would be challenging to implement.

Fortunately, we are at the time of writing awaiting delivery of a new 556 nm light source. This is a DLC TA-SHG pro system from Toptica, consisting of 1111.6 nm DL pro diode laser, tapered amplifier, and second harmonic generation cavity in a single module, generating 2 W of 556 nm output power. This significant enhancement in the available power means we could potentially have independent optical setups for each of the applications described above. Upon delivery, we will likely install the new system on the same laser table as that of the Ti:Sapphire laser, and fiber-couple the majority of the output to the existing 556 nm optics adjacent to the Yb beam machine. This will allow us to continue this optical setup with minimal modifications. We intend to retain the Menlo laser system in parallel for as long as it remains operational. One example of a new purpose for the Menlo system is to use it as the MOT beam for a second isotope, by stabilising its frequency to that

of the Toptica system and applying the necessary frequency shift.

8.2.2 Dual-degenerate mixtures

Our realisation of dual-degenerate mixtures opens up the possibility of many different areas of research. The experimental focus in the immediate future will be the formation and observation of quantum droplets (see below). However, the versatility of the system may allow studies of a range of research areas including impurity physics, collective dynamics, binary fluid dynamics, and two-component quantum turbulence. As well as the droplet-BEC phase transition discussed below, the miscible-immiscible phase transition [182; 183] could be studied in the Cs–^{170}Yb mixture.

As discussed in chapter 5, a Cs-blind lattice can be used to create a mixed-dimension system [110]. It could also be used for investigations of how the dynamics and temperature of Cs are affected by transport through Yb confined by a lattice. A Cs-blind lattice may also have applications in impurity physics [258], where the lattice-confined Yb atoms take on the role of impurity particles immersed within a Cs BEC. Lattice cooling schemes [259], where the lattice-confined Yb is cooled through collisions with the Cs superfluid, could be investigated. This could be a useful method for reducing the accessible temperature of Yb isotopes such as ^{171}Yb. Even if full lattice loading is not achieved, the lattice beam may be useful for modifying the relative densities of the atom clouds of the two species. This could prove to be particularly useful in quantum droplet formation.

We have also considered development of an accordion lattice [260]. This would require development of an optical lattice setup where the angle between the interfering light beams can be varied. This would enable a continuous variation of the lattice spacing, allowing efficient loading of two-dimensional samples in the optical lattice [261]. It would also allow us to explore the transition from a three-dimensional gas to a two-dimensional gas as the lattice spacing is changed. It is

likely that the lattice wavelength would be that of a far off-resonance dipole trap, making an attractive potential for both species. However, a Cs-blind accordion lattice, or a balanced-potential accordion lattice, could be realised by using the 460 nm tuneable lattice light source.

8.2.3 Formation of quantum droplets

In the experiments using the Cs–^{174}Yb degenerate mixture, we have seen the combined effects of the attractive interspecies interaction and the tuneable intraspecies interaction in Cs. It is therefore possible to tune the mixture to a magnetic field where the interactions are balanced. Here, the mean field effects generally used to describe quantum degenerate gases are cancelled out, and beyond-mean-field effects, described by the Lee-Huang-Yang (LHY) correction to the Gross-Pitaevskii equation, become detectable. Attractive interspecies interactions are balanced by quantum fluctuations described by the LHY model. This leads to the formation of atoms in a self-bound droplet phase within the gas, known as quantum droplets [8]. This phase of matter has previously been observed in dipolar BECs [262; 263], K spin mixtures [9; 264] and Rb–K mixtures [10]. For Cs–^{174}Yb, the weak and attractive net mean-field interaction δg required to support the droplet phase arises for Cs scattering lengths below and in the vicinity of $a_{\mathrm{Cs}} = 54.3\,a_0$. Observation of a quantum droplet–BEC phase transition in our experiment would be the first such observation in an alkali+alkaline-earth-like mixture.

8.2.4 Quantum droplets: relevant experimental upgrades

The current absorption imaging techniques will be insufficient to observe and resolve the formation of quantum droplets. We therefore aim to move to a new imaging system arranged in the vertical axis. This will be a dual-wavelength imaging system, which will give effective imaging of Cs and Yb on the transitions currently used at 852 nm and 399 nm respectively. Observation of quantum droplets will

require $\sim 1-2\,\mu$m resolution of both wavelengths, which will require an imaging objective with a numerical aperture of approximately 0.43. Integrating an imaging objective system into the apparatus will be an experimental challenge given the existing optical access constraints. However, at the time of writing, progress has been made on developing an effective design of objective for the setup.

We also wish to improve the BODT apparatus. Of particular concern is the spatial stability of the trap and variations in beam pointing towards the end of evaporative cooling sequences. This limits the temperature and stability of the ultracold gases at the low temperatures required to observe droplet formation. We will therefore complement the existing setup with vertically-oriented dipole trapping beams, which will spatially stabilise the trapping potential at lower powers. Light for these beams will be provided by an additional 20 W laser operating at 1064 nm, and the surplus of power available from the 20 W 532 nm IPG laser, which at present is only operated at 5 W.

8.2.5 Feshbach resonances and molecules

A longer-term overview of our future Feshbach resonance studies, and various options for formation of molecules using these resonances and other methods, is given in the outlook of chapter 6. To summarise, in the short-term, work is ongoing to experimentally prepare a sufficiently cold Cs–^{171}Yb mixture to search for promising interspecies Feshbach resonances in this mixture. Various methods, such as conventional sympathetic cooling and in-trap laser cooling, are being trialled, but it may be concluded that experimental upgrades may be required before such a mixture can be realised. Moving to the longer-term, in order to utilise Feshbach resonances already observed for magnetoassociation, we will have to predict and achieve the necessary PSD, and apply the necessary magnetic field ramps, for efficient production of Feshbach molecules. It may yet be concluded that production of the mixture in a Mott insulator state will first be required to achieve this long-standing goal

of the experiment. This would tie in well with our planned development of optical lattices to study degenerate gas mixtures.

8.3 Concluding remarks

The work in this thesis has demonstrated observation of the first dual-degenerate mixtures of Cs and Yb. This provides scope for further studies, including realisation of novel degenerate mixtures, exotic phases of matter, and studies of mixtures in reduced and mixed dimensions. The improvements in the phase space density of the mixtures are also promising for efficient loading of atoms into optical lattices, for further such studies, including potential molecular association routes. The work in this thesis has also demonstrated the first observation of interspecies Feshbach resonances between Cs and Yb atoms, realising one of the key initial goals of the experiment. These results are complimentary to the theoretical predictions of the resonances, and are an important step towards the production of paramagnetic CsYb molecules.

Appendix A

Atomic transition data used in the polarizability calculations

Transition	λ (nm)	A s^{-1}
6s $^2S_{1/2} \rightarrow$ 6p $^2P_{1/2}$	894.59296	28.62×10^6
6s $^2S_{1/2} \rightarrow$ 6p $^2P_{3/2}$	852.3472759	32.79×10^6
6s $^2S_{1/2} \rightarrow$ 7p $^2P_{1/2}$	459.4459	793×10^3
6s $^2S_{1/2} \rightarrow$ 7p $^2P_{3/2}$	455.6557	1.84×10^6
6s $^2S_{1/2} \rightarrow$ 8p $^2P_{1/2}$	388.9710415	89.9×10^3
6s $^2S_{1/2} \rightarrow$ 8p $^2P_{3/2}$	387.72473	386×10^3
6s $^2S_{1/2} \rightarrow$ 9p $^2P_{1/2}$	361.834	22.3×10^3
6s $^2S_{1/2} \rightarrow$ 9p $^2P_{3/2}$	361.25014	143×10^3
6s $^2S_{1/2} \rightarrow$ 10p $^2P_{1/2}$	348.1057	6.33×10^3
6s $^2S_{1/2} \rightarrow$ 10p $^2P_{3/2}$	347.7805	62.7×10^3
6s $^2S_{1/2} \rightarrow$ 11p $^2P_{1/2}$	340.0955	2.36×10^3
6s $^2S_{1/2} \rightarrow$ 11p $^2P_{3/2}$	339.8941	36.1×10^3

Table A.1: Cs transitions, wavelengths and Einstein A-coefficients used in the calculation of the Cs ground state scalar polarizability, shown in figures 3.2 and 5.1. Wavelengths and A-coefficients are taken from references [160]. Vacuum wavelengths are calculated from the differences in energy level given in the reference, given to within the uncertainty of the measured wavelengths for the same lines in the reference.

Transition	λ (nm)	A s^{-1}
4f14 6s2 $^1S_0 \rightarrow$ 4f14 6s6p $^3P_1$	555.80236	1.15×10^6
4f14 6s2 $^1S_0 \rightarrow$ 4f14 6s6p $^1P_1$	398.91142	192×10^6
4f14 6s2 $^1S_0 \rightarrow$ 4f14 5d 6s2 (7/2,5/2)1	346.5362	68.3×10^6
4f14 6s2 $^1S_0 \rightarrow$ 4f14 5d2 6s	267.2754	14.3×10^6
4f14 6s2 $^1S_0 \rightarrow$ 4f14 6s7p $^1P_1$	246.5242	100×10^6

Table A.2: Yb transitions, wavelengths and Einstein A-coefficients used in the calculation of the Yb ground state scalar polarizability, shown in figures 3.2 and 5.1. Wavelengths and A-coefficients are taken from references [161]. Vacuum wavelengths are calculated from the differences in energy level given in the reference, given to within the uncertainty of the measured wavelengths for the same lines in the reference.

Appendix B

Tuneable lattice light source

The lattice light source is the frequency-doubled output of a Ti:Sapphire laser system. The Ti:Sapphire laser used in this setup is the SolsTiS system from MSquared. The Ti:Sapphire laser had been previously used in the lab in CsYb photoassociation spectroscopy experiments. It consists of a Ti:Sapphire crystal within a bowtie cavity configuration. The cavity is pumped by a 532 nm pump laser (Lighthouse Sprout), operating at 10 W. One of the cavity mirrors is mounted on fast and slow piezo actuators. Coarse tuning of the output frequency is achieved by rotating the orientation of a birefringent filter within the cavity. An etalon within the cavity ensures a narrow linewidth output. Fine tuning of the output wavelength is achieved by adjusting the etalon spacing. Transmission on a single longitudinal etalon mode is achieved by locking the etalon to peak transmission on the nearest mode. The slow piezo actuator allows the cavity length to be adjusted to match the longitudinal mode. Further frequency stabilisation and reduction in the linewidth to less than 50 kHz can be achieved using a reference cavity, also provided by MSquared, which some of the output of Ti:Sapphire is directed to. The SolsTiS output frequency is locked to a cavity fringe, using the fast piezo actuator. The frequency can then be scanned or offset by adjusting the cavity length. Control of the birefringent filter angle, and monitoring, scanning, and locking of the etalon, Ti:Sapphire cavity piezo mirrors and reference cavity, is performed using MSquared control software

through the MSquared ICE-Bloc interface.

The SolsTiS in its current configuration has two free-space outputs. These outputs are split off at right angles from a polarising beam splitting cube (PBS) and have orthogonal linear polarisations. The relative power in each output can be controlled by a half waveplate before the PBS. The horizontally polarised component is used for frequency doubling. We therefore usually maximise the power in this output. Typically, when operating the Ti:Sapphire around 920 nm we have 1.7 W of power in the output for doubling, and 60 mW in the vertically polarised output. This output is normally dumped at the shutter on the SolsTiS module. We note however that this output could be used for future applications involving the tuneable fundamental output of the SolsTiS, without having to make any changes to the tuneable lattice setup described below. There is also an output on the SolsTiS of approximately 10 mW power designed for coupling to an FC–PC fiber. We use this output to monitor the SolsTiS frequency by fiber coupling to a wavemeter.

The horizontally polarised free-space output is realigned and focused into a doubling cavity. This an ECD-X cavity from MSquared, and is shown in figure B.1. It consists of an LBO doubling crystal within a bowtie cavity configuration. The doubling crystal is efficient over the frequency range 457.5 nm to 461 nm. The angle at which the crystal is most efficient is sensitive to wavelength of the input light. The crystal angle therefore can be controlled by a micrometer screw. This screw can only be accessed by opening the lid of the cavity. The frequency of the lattice should therefore be changed as infrequently as possible to avoid contamination of the cavity optics. The output of the cavity is optimised by an error signal generated from a pickoff from one of the cavity mirrors which feeds back to a piezoelectric transducer crystal mounted to one of the cavity mirrors (mirror M2 in figure B.1), which controls the cavity alignment. If the cavity output is not optimised, the crystal angle can be adjusted manually, as well as the alignment of the two mirrors either side of the crystal in the bowtie (mirrors M3 and M4 in figure B.1). Scanning and stabilisation of the cavity, as well as monitoring of the error signal and output

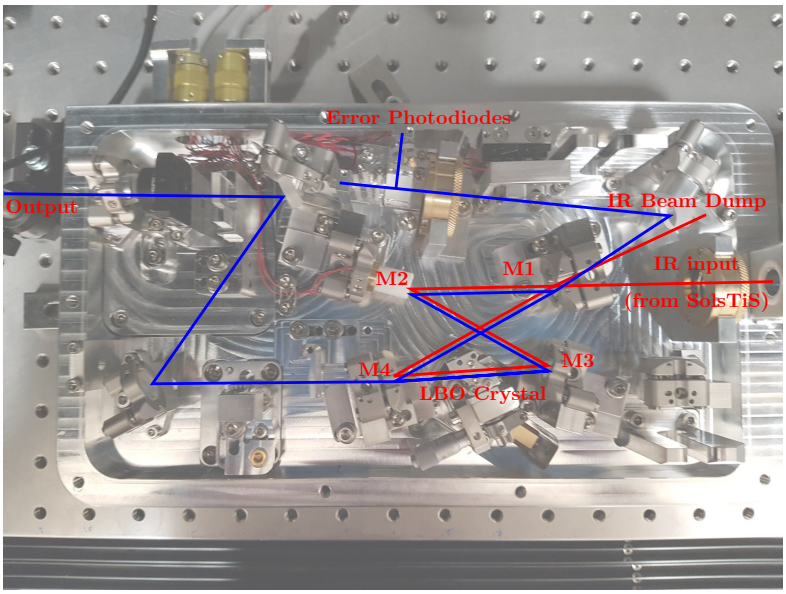

Figure B.1: **The ECD-X doubling cavity.** Input light from the SolsTis is aligned in a four-mirror bowtie cavity. The LBO frequency doubling crystal is situated on the beam path between mirrors M3 and M4. The angle of the crystal relative to the beam can be adjusted by the micrometer screw. The M3 and M4 mirror pair can also be adjusted to optimise the frequency-doubled output.

(through a pickoff onto a photodiode) is also performed using MSquared control software through the MSquared ICE-Bloc interface.

For a 1.6 W input of light from the SolsTiS tuned to 919.0 nm, we have been able to get a maximum output of 800 mW of light at 459.5 nm from the doubling cavity. We have found, however, that output power reduces by the order of 100 mW to 200 mW per month. Once the output power decreases below $\sim$ 350 mW, we can no longer stabilise the doubling cavity and produce a stable output. We have found the power loss is due to degradation on the surfaces on the LBO crystal. This is despite the cavity being housed in a sealed module and with laminar flow present above the optical table. In the short term, the surfaces of the crystal can be cleaned with high purity ($>$ 99.9 %) methanol, which restores the output to full power. We typically find this needs to be performed approximately every 3 months when the system is in regular use. Regular optimisation of the crystal

angle and the manually controlled cavity mirrors can also help maintain output power. However, a permanent solution to the output problem may be to return the ECD-X to MSquared to either repair or replace the crystal.

Appendix C

Tuneable lattice alignment

C.1 Coarse alignment to Cs MOT

For initial alignment of the lattice beam, we blocked the retroreflection beam and only considered the alignment of the beam in single-pass configuration. We took advantage of the Cs transitions within our laser tuning range to use loss of Cs due to resonant heating as our signal to optimise. We tuned the beam wavelength to 459.57 nm, as close as possible to the $6S_{\frac{1}{2}} \rightarrow 7P_{\frac{1}{2}}$ transition 459.45 nm where the cavity could be continuously locked. The beam power was set to 174 mW. We then ran the Cs MOT continuously with the beam on. The shim coils were set so that the Cs MOT was centred at the approximate position of the Cs DRSC beams (and hence the BODT beams). The fluorescence of the MOT was monitored in real-time on the usual monitoring photodiode. Figure C.1 shows the reduction of the MOT fluorescence with respect to the beam position, as controlled by the mirror above the chamber. For optimal alignment, the MOT fluorescence is reduced by approximately 50 %. The full width half maximum of the loss curves is 0.6(1.3) mm in the east-west (north-south) axis. This implies the Cs MOT has an asymmetric shape. We attribute this to imperfect alignment or imbalance of powers in the MOT beams. We left the mirror at the position where the fluorescence was minimised.

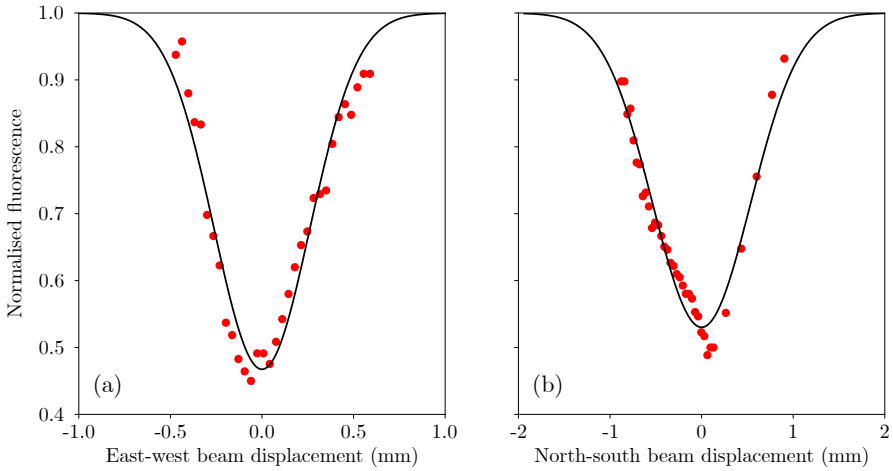

Figure C.1: **Aligning the lattice beam to the Cs MOT.** Reduction in the Cs MOT fluorescence with adjustment of the beam focus in the (a) east-west and (b) north-south axis. The beam was tuned near to the $6S_{\frac{1}{2}} \rightarrow 7P_{\frac{1}{2}}$ Cs resonance. The black line in each plot is a Gaussian fit to the data, used to find the centre of the alignment.

C.2 Alignment to optically trapped atoms

A more precise alignment can be performed by turning the lattice beam (with retroreflection blocked) on incident to either Cs or Yb atoms in the BODT. This is the exact location in the science chamber where the BECs are produced. We started this alignment procedure by observing transfer of ^{174}Yb atoms from the dimple trap to the beam. This was performed at the end of a Yb-only evaporative cooling routine. The beam was ramped on in 300 ms to a power of 174 mW, and held for 1650 ms during the Yb evaporation. In the final 1 s of evaporation, dimple beam 2 was ramped off to allow atoms to expand along the dimple beam 1 axis. Figure C.2 shows absorption images of the Yb atom cloud along this axis without (a) and with (b) the beam intersecting and providing additional confinement.

The two adjusters on the deflector mirror adjust the beam parallel and perpendicular to this axis. Therefore, we were first able to align the beam to this axis by optimising the atom number in the crossing, while adjusting the position of the

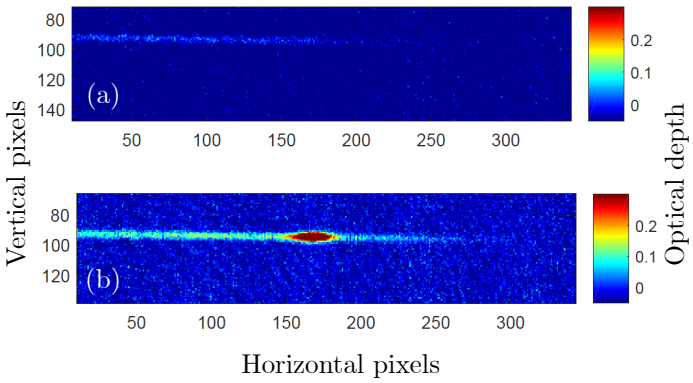

Figure C.2: **Trapping ^{174}Yb in the lattice beam.** ^{174}Yb trapped and allowed to expand along the axis of dimple beam 1, without (a) and with (b) the vertically intersecting lattice beam providing additional confinement.

'perpendicular' adjuster. This is shown in figure C.3(a). Once this was optimised, we could use the 'parallel' adjuster to 'track' the position of the intersection along the dimple beam 1 axis, as shown in figure C.3(b). In this way, the atom cloud was shifted to the axial position where the atoms in the BODT were observed if dimple beam 2 was not ramped off.

Final fine-tuning of the beam was performed by returning to near resonant heating of Cs in the BODT. The beam was left on throughout a sequence loading Cs only into the BODT. The beam power was 2.36 mW, with a dithered detuning of $+1.000 \pm 0.375$ GHz from the $6S_{\frac{1}{2}} \rightarrow 7P_{\frac{1}{2}}$ transition, dithered at a rate of 5 Hz. This detuning required re-locking of the reference cavity at regular intervals, but the cavity could stay locked over the course of several experimental runs (each run taking approximately 20 seconds). A lower detuning is used here compared to the MOT alignment. Figure C.4 shows Cs loss curves when adjusting either deflector mirror axis. The $\frac{1}{e^2}$ width of the fits to the data in figure C.4 are 91(3) µm in the east-west axis and 155(4) µm in the north-south axis. These equate to -27(3) % and +23(3) % deviations from our predicted waist of 125.92(17) µm. This implies that the beam focus at the atoms is elliptical or astigmatic. This could be due to imperfect alignment through the focusing lens, or the propagation through the

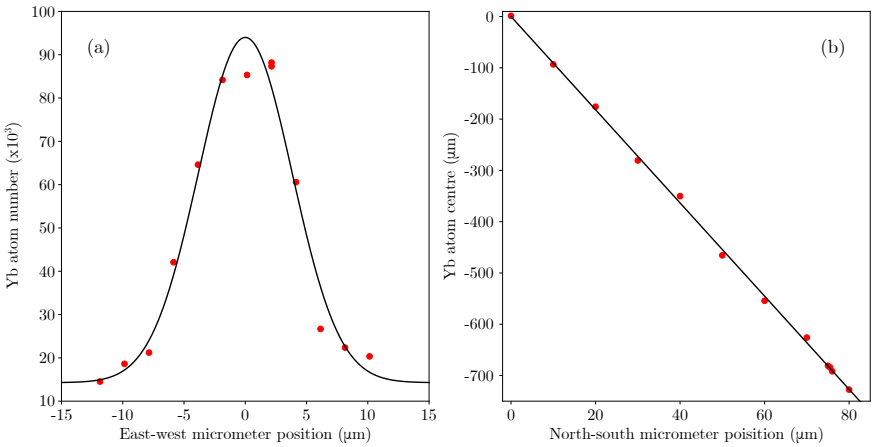

Figure C.3: **Aligning the lattice beam to optically trapped ^{174}Yb.** (a) Optimisation of the ^{174}Yb atom number trapped in the intersection of the lattice beam and dimple beam 1, with adjustment of the beam focus in the east-west axis. The black line is a Gaussian fit to the data, used to find the centre of the alignment. (b) Moving the focus position of the lattice beam along the dimple beam 1 axis. Position of ^{174}Yb trapped in the intersection of the lattice beam and dimple beam 1, with adjustment of the beam focus in the north-south axis. The black line is a linear fit to the data.

chamber viewports.

C.3 Alignment of retroreflected beam

Provided the lattice beam is recollimated sufficiently well, the back-coupling of the retroreflected beam through the optical fiber should be as efficient as the initial pass through the fiber. Therefore, having first performed coarse alignment to ensure the retroreflection was incident on the fiber output, a non-polarising beam splitter cube was placed on the optical table in the beam path before the fiber input. The power of the component of the retroreflected beam split from the main beam was subtracted from that split from the first pass of the beam. This power was then optimised for the adjustment of the retroreflection mirror, and for fine-tuning the axial position of the recollimation lens. This method of lattice realignment was used regularly while taking measurements which required regular changes to the

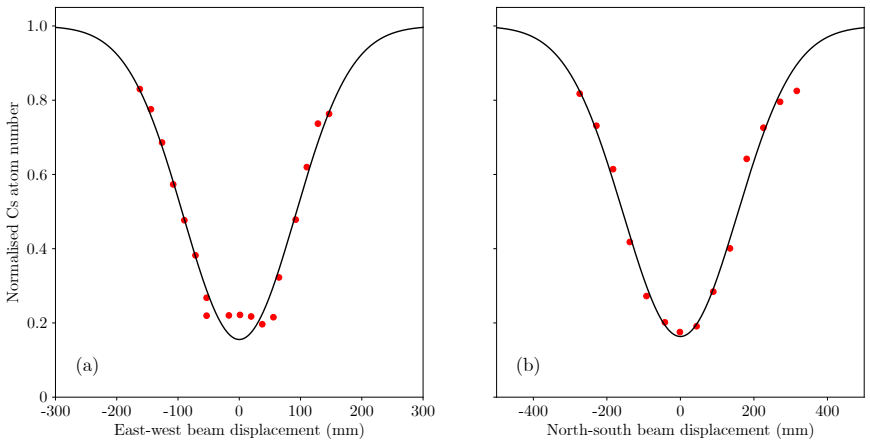

Figure C.4: **Aligning the lattice beam to Cs in the BODT.** Reduction in the Cs atom number with adjustment of the beam focus in the (a) east-west and (b) north-south axis. The beam was tuned near to the $6S_{\frac{1}{2}} \rightarrow 7P_{\frac{1}{2}}$ Cs resonance. The beam displacement is calculated using the calibration in figure C.3b and re-centred at zero. The black lines are Gaussian fits to the data, used to find the centre of the alignment.

lattice frequency. We note that any changes to the alignment of the outgoing beam will in turn require realignment of the retroreflected beam.

Appendix D

Analysing data from Kapitza-Dirac diffraction experiments

In experiments involving a single atom cloud, image analysis software is used in parallel to absorption imaging for fitting and analysis of the cloud. Kapitza-Dirac diffraction, however, inherently requires the simultaneous analysis of multiple diffracted orders of a BEC. Therefore, a process for analysing the data to quickly determine quantities such as lattice depth was developed. This would allow us to analyse Cs diffraction data and measure the Cs polarizability in parallel to further data being taken. A schematic of the process is shown in figure D.1.

D.1 Absorption imaging

All information regarding the atom cloud is derived from absorption images captured on the camera, with a fluorescence count per pixel of the camera plane. The absorption imaging light is resonant to a closed transition of frequency λ and has an intensity profile $I_0(x, y)$ which is low relative to the saturation intensity, $I_0 \ll I_{\text{sat}}$. In this case, the absorption cross section is given by $\sigma_{Total} = \frac{3\lambda^2}{2\pi}$ [265]. The reduc-

tion in intensity through an atom cloud of density profile $n(x, y)$ is described by the Beer-Lambert law [265]:

$$I(x, y) = I_0(x, y)e^{-n(x,y)\sigma_{\text{Total}}}. \tag{D.1}$$

Hence, the density profile can be calculated as

$$n(x, y) = -\frac{1}{\sigma_{\text{Total}}}\ln\left(\frac{I(x, y)}{I_0(x, y)}\right) = -\frac{1}{\sigma_{\text{Total}}}\text{OD}(x, y), \tag{D.2}$$

Where $\text{OD}(x, y)$ is the optical depth profile of the atom cloud.

An optical depth per pixel is calculated using the method of background subtraction. In practice, three camera images are captured per experimental run:

$$\begin{aligned} A_{\text{Cam}} &= \text{Imaging light and atoms,} \\ B_{\text{Cam}} &= \text{`Light background'; Imaging light and no atoms,} \\ C_{\text{Cam}} &= \text{`Dark background'; No imaging light or atoms.} \end{aligned} \tag{D.3}$$

The A_{Cam}, B_{Cam} and C_{Cam} images are captured by the imaging camera at the end of each experimental sequence. The A_{Cam} image is captured after time of flight expansion of the atoms, and the B_{Cam} and C_{Cam} images are subsequently taken after the atom cloud has fallen from the camera's field of view. The same camera exposure time of 100 µs is used for each image exposure. From these images a single image A_{OD} can be calculated pixel-by-pixel using

$$A_{\text{OD}} = \ln\left(\frac{A - C}{B - C}\right). \tag{D.4}$$

The numerical value of each entry of the array A_{OD} is the value of optical depth of the corresponding pixel in the camera field of view.

D.2 Extracting diffracted orders

The resulting absorption image contains all the diffracted orders (provided an appropriate time of flight was chosen) as well a large 'dark' region of no experimental interest. Further .csv files are created which cover smaller regions of interest within

the original absorption image. There are $2n + 1$ files, where n is the highest order of diffraction observed in the experiment. If the range of pixels each diffracted order falls within is known for one absorption image, the regions of interest for all subsequent images in a data set can be unambiguously defined as the same, provided the time of flight is not changed during the experiment. For our size of BEC and choice of lattice spacing and time of flight, the spatial separation between neighbouring orders of diffraction is sufficient to unambiguously define a boundary between the two. For the purposes of fitting the diffracted orders, the regions of interest must be defined with a sufficient area of dark background surrounding the atom cloud itself.

D.3 Calculating atom number

We then calculate atom number in each diffracted order using the method of one-dimensional integration. The two-dimensional array of optical density values is converted into a one-dimensional array by summing the optical density values in one dimension. Either each row can be summed to give an integrated one-dimensional column, or each column sum to give one integrated row. If an appropriate region of interest has been chosen, this one-dimensional array gives the density distribution of the atom cloud. Atom number can be calculated from fitting a function to this distribution and calculating the area under the fitted function.

We perform a Gaussian fit $f(x)$ to the density distribution of the form

$$f(x) = A_0 e^{\frac{-(x-x_0)^2}{2\sigma^2}} + y_0. \tag{D.5}$$

The atom number N is then calculated as

$$N = \frac{\sqrt{2\pi} A_0 p^2 \sigma}{\sigma_{\text{Total}}}, \tag{D.6}$$

where A_0 is the magnitude of the Gaussian curve, p is the pixel size, σ is the $\frac{1}{e^2}$ width of the atom cloud, and σ_{Total} is the total absorption cross-section. As the

Cs gas is quantum degenerate in this experiment, a Thomas-Fermi fit would be a more appropriate choice to determine atom number in each order more precisely. However, it was decided a Gaussian fit was sufficient for determining the relative populations of each order in the diffraction pattern. The atom number calculated should be the same if either the integrated row or integrated column is calculated. Whether the fitting from these two permutations agree to within error is a good method of determining the goodness of fit, and how appropriate the fitting function is. Initial fitting parameters had to be chosen carefully to ensure a good fit of the data.

An alternative method is to calculate the number from the optical depth of each individual pixel, and sum over the entire region of interest. In this case, the number N_{px} is given by

$$N_{\mathrm{px}} = \sum_{\mathrm{Pixels}} \frac{Ap^2}{\sigma_{\mathrm{Total}}}, \tag{D.7}$$

where A is the optical depth per pixel, p is the pixel size and σ_{Total} is the total absorption cross-section. Although this method is a useful alternative if no function can adequately be fitted to the density distribution, it is prone to overcounting the atom number if the region of interest incorporates a large area of background noise outside the atom cloud itself. In this case, a dark region equivalent to the background noise area can be analysed, and the calculated atom number can be subtracted from the number calculated from the image of the atoms.

D.4 Fitting a simulation to the data

The atom number for each diffracted order is calculated for every absorption image in a data run. The pulse duration, atom number of each order, and relative population percentage of each order, is tabulated and outputted in the appropriate format for inputting into the Kapitza-Dirac simulation code.

The code [215] has been used effectively to fit Kapitza-Dirac simulations to the data with very little modifications. The lattice spacing must be specified in µm. This is

one half of the lattice wavelength, and therefore one quarter of the undoubled light which is monitored and logged by the wavemeter for each experimental run. The maximum and minimum values for l in the simulation was found to not significantly affect the fitting result for $|l| > 10$, however $l = \pm 30$ was used in each simulation for consistency. To provide an 'initial guess' simulation, the lattice depth could be estimated using the pulse power (monitored on the photodiode), the estimate of the beam waist from the optical design, and the expected polarizability of the lattice wavelength based on the atomic data. As the normalised data set was used, the 'initial guess' for atom number was 1.

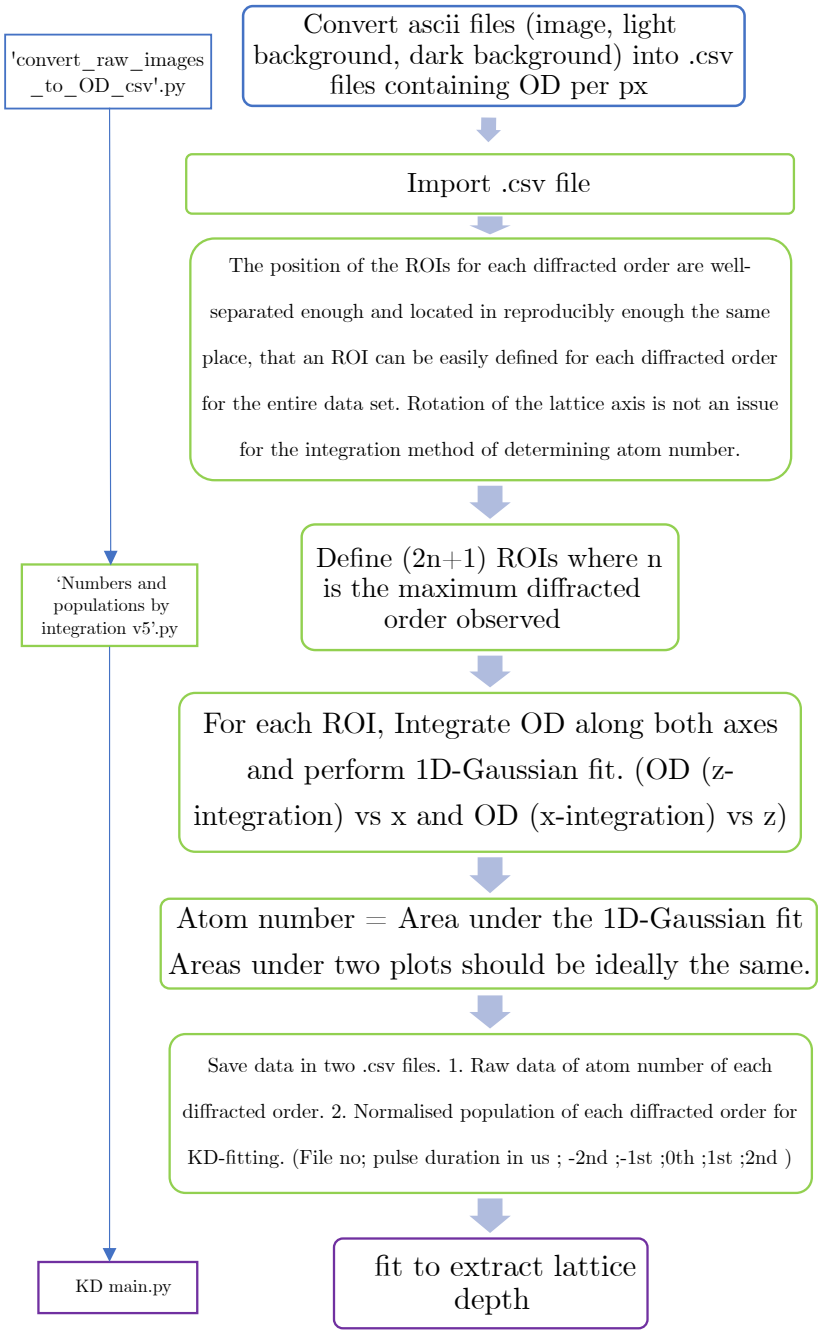

Figure D.1: **Schematic of the data analysis process for Kapitza-Dirac diffraction experiments.**

Bibliography

[1] K. Mølmer, "Bose condensates and Fermi gases at zero temperature," Phys. Rev. Lett. **80**, 1804 (1998).

[2] M. Lewenstein, L. Santos, M. A. Baranov, and H. Fehrmann, "Atomic Bose-Fermi mixtures in an optical lattice," Phys. Rev. Lett. **92**, 050401 (2004).

[3] M. Zaccanti, C. D'Errico, F. Ferlaino, G. Roati, M. Inguscio, and G. Modugno, "Control of the interaction in a Fermi-Bose mixture," Phys. Rev. A **74**, 041605 (2006).

[4] S. Ospelkaus, C. Ospelkaus, O. Wille, M. Succo, P. Ernst, K. Sengstock, and K. Bongs, "Localization of Bosonic atoms by Fermionic impurities in a three-dimensional optical lattice," Phys. Rev. Lett. **96**, 180403 (2006).

[5] K. Günter, T. Stöferle, H. Moritz, M. Köhl, and T. Esslinger, "Bose-Fermi mixtures in a three-dimensional optical lattice," Phys. Rev. Lett. **96**, 180402 (2006).

[6] K. Sengupta, N. Dupuis, and P. Majumdar, "Bose-Fermi mixtures in an optical lattice," Phys. Rev. A **75**, 063625 (2007).

[7] F. M. Marchetti, C. J. M. Mathy, D. A. Huse, and M. M. Parish, "Phase separation and collapse in Bose-Fermi mixtures with a Feshbach resonance," Phys. Rev. B **78**, 134517 (2008).

[8] D. S. Petrov, "Quantum mechanical stabilization of a collapsing Bose-Bose mixture," Phys. Rev. Lett. **115**, 155302 (2015).

[9] C. R. Cabrera, L. Tanzi, J. Sanz, B. Naylor, P. Thomas, P. Cheiney, and L. Tarruell, "Quantum liquid droplets in a mixture of Bose-Einstein condensates," Science **359**, 301 (2018).

[10] C. D'Errico, A. Burchianti, M. Prevedelli, L. Salasnich, F. Ancilotto, M. Modugno, F. Minardi, and C. Fort, "Observation of quantum droplets in a heteronuclear bosonic mixture," Phys. Rev. Research **1**, 033155 (2019).

[11] C. Hamner, J. J. Chang, P. Engels, and M. A. Hoefer, "Generation of dark-bright soliton trains in superfluid-superfluid counterflow," Phys. Rev. Lett. **106**, 065302 (2011).

[12] B. J. DeSalvo, K. Patel, G. Cai, and C. Chin, "Observation of fermion-mediated interactions between bosonic atoms," Nature **568**, 61 (2019).

[13] G. Modugno, G. Roati, F. Riboli, F. Ferlaino, R. J. Brecha, and M. Inguscio, "Collapse of a degenerate Fermi gas," Science **297**, 2240 (2002).

[14] I. Ferrier-Barbut, M. Delehaye, S. Laurent, A. T. Grier, M. Pierce, B. S. Rem, F. Chevy, and C. Salomon, "A mixture of Bose and Fermi superfluids," Science **345**, 1035 (2014).

[15] R. Roy, A. Green, R. Bowler, and S. Gupta, "Two-element mixture of Bose and Fermi superfluids," Phys. Rev. Lett. **118**, 055301 (2017).

[16] S.-K. Tung, K. Jiménez-García, J. Johansen, C. V. Parker, and C. Chin, "Geometric scaling of Efimov states in a ^{6}Li-^{133}Cs mixture," Phys. Rev. Lett. **113**, 240402 (2014).

[17] R. Pires, J. Ulmanis, S. Häfner, M. Repp, A. Arias, E. D. Kuhnle, and M. Weidemüller, "Observation of Efimov resonances in a mixture with extreme mass imbalance," Phys. Rev. Lett. **112**, 250404 (2014).

[18] R. A. W. Maier, M. Eisele, E. Tiemann, and C. Zimmermann, "Efimov resonance and three-body parameter in a Lithium-Rubidium mixture," Phys. Rev. Lett. **115**, 043201 (2015).

[19] J. Ulmanis, S. Häfner, R. Pires, E. D. Kuhnle, Y. Wang, C. H. Greene, and M. Weidemüller, "Heteronuclear Efimov scenario with positive intraspecies scattering length," Phys. Rev. Lett. **117**, 153201 (2016).

[20] G. Modugno, G. Ferrari, G. Roati, R. J. Brecha, A. Simoni, and M. Inguscio, "Bose-Einstein condensation of Potassium atoms by sympathetic cooling," Science **294**, 1320 (2001).

[21] M. Mudrich, S. Kraft, K. Singer, R. Grimm, A. Mosk, and M. Weidemüller, "Sympathetic cooling with two atomic species in an optical trap," Phys. Rev. Lett. **88**, 253001 (2002).

[22] Z. Hadzibabic, C. A. Stan, K. Dieckmann, S. Gupta, M. W. Zwierlein, A. Görlitz, and W. Ketterle, "Two-species mixture of quantum degenerate Bose and Fermi gases," Phys. Rev. Lett. **88**, 160401 (2002).

[23] F. M. Spiegelhalder, A. Trenkwalder, D. Naik, G. Hendl, F. Schreck, and R. Grimm, "Collisional stability of ^{40}K immersed in a strongly interacting Fermi gas of ^{6}Li," Phys. Rev. Lett. **103**, 223203 (2009).

[24] H. W. Cho, D. J. McCarron, D. L. Jenkin, M. P. Köppinger, and S. L. Cornish, "A high phase-space density mixture of ^{87}Rb and ^{133}Cs: towards ultracold heteronuclear molecules," Eur. Phys. J. D **65**, 125 (2011).

[25] D. J. McCarron, H. W. Cho, D. L. Jenkin, M. P. Köppinger, and S. L. Cornish, "Dual-species Bose-Einstein condensate of ^{87}Rb and ^{133}Cs," Phys. Rev. A **84**, 011603 (2011).

[26] L. Wacker, N. B. Jørgensen, D. Birkmose, R. Horchani, W. Ertmer, C. Klempt, N. Winter, J. Sherson, and J. J. Arlt, "Tunable dual-species Bose-Einstein condensates of ^{39}K and ^{87}Rb," Phys. Rev. A **92**, 053602 (2015).

[27] M. Gröbner, P. Weinmann, F. Meinert, K. Lauber, E. Kirilov, and H.-C. Nägerl, "A new quantum gas apparatus for ultracold mixtures of K and Cs and KCs ground-state molecules," J. Mod. Opt. **63**, 1829 (2016).

[28] B. Pasquiou, A. Bayerle, S. M. Tzanova, S. Stellmer, J. Szczepkowski, M. Parigger, R. Grimm, and F. Schreck, "Quantum degenerate mixtures of strontium and rubidium atoms," Phys. Rev. A **88**, 023601 (2013).

[29] V. D. Vaidya, J. Tiamsuphat, S. L. Rolston, and J. V. Porto, "Degenerate Bose-Fermi mixtures of rubidium and ytterbium," Phys. Rev. A **92**, 043604 (2015).

[30] Z.-X. Ye, L.-Y. Xie, Z. Guo, X.-B. Ma, G.-R. Wang, L. You, and M. K. Tey, "Double-degenerate Bose-Fermi mixture of strontium and lithium," Phys. Rev. A **102**, 033307 (2020).

[31] C. Ravensbergen, V. Corre, E. Soave, M. Kreyer, E. Kirilov, and R. Grimm, "Production of a degenerate Fermi-Fermi mixture of dysprosium and potassium atoms," Phys. Rev. A **98**, 063624 (2018).

[32] A. Trautmann, P. Ilzhöfer, G. Durastante, C. Politi, M. Sohmen, M. J. Mark, and F. Ferlaino, "Dipolar quantum mixtures of Erbium and Dysprosium atoms," Phys. Rev. Lett. **121**, 213601 (2018).

[33] M. D. Frye, S. L. Cornish, and J. M. Hutson, "Prospects of forming high-spin polar molecules from ultracold atoms," Phys. Rev. X **10**, 041005 (2020).

[34] L. Carr, D. DeMille, R. Krems, and J. Ye, "Cold and ultracold molecules: science, technology and applications," New J. Phys. **11**, 055049 (2009).

[35] C. Chin, V. V. Flambaum, and M. G. Kozlov, "Ultracold molecules: new probes on the variation of fundamental constants," New J. Phys. **11**, 055048 (2009).

[36] S. A. Moses, J. P. Covey, M. T. Miecnikowski, D. S. Jin, and J. Ye, "New frontiers for quantum gases of polar molecules," Nat. Phys. **13**, 13 (2017).

[37] J. L. Bohn, A. M. Rey, and J. Ye, "Cold molecules: Progress in quantum engineering of chemistry and quantum matter," Science **357**, 1002 (2017).

[38] D. DeMille, "Quantum computation with trapped polar molecules," Phys. Rev. Lett. **88**, 067901 (2002).

[39] S. F. Yelin, K. Kirby, and R. Côté, "Schemes for robust quantum computation with polar molecules," Phys. Rev. A **74**, 050301(R) (2006).

[40] M. Safronova, D. Budker, D. DeMille, D. F. J. Kimball, A. Derevianko, and C. W. Clark, "Search for new physics with atoms and molecules," Rev. Mod. Phys **90**, 025008 (2018).

[41] J. J. Hudson, D. M. Kara, I. J. Smallman, B. E. Sauer, M. R. Tarbutt, and E. A. Hinds, "Improved measurement of the shape of the electron," Nature **473**, 493 (2011).

[42] J. B. et al., "Order of magnitude smaller limit on the electric dipole moment of the electron," Science **343**, 269 (2014).

[43] W. B. Cairncross, D. N. Gresh, M. Grau, K. Cossel, T. S. Roussy, Y. Ni, Y. Zhou, J. Ye, and E. A. Cornell, "Precision measurement of the electron's electric dipole moment using trapped molecular ions," Phys. Rev. Lett. **119**, 153001 (2017).

[44] A. Micheli, G. Brennen, and P. Zoller, "A toolbox for lattice-spin models with polar molecules," Nat. Phys. **2**, 341 (2006).

[45] R. V. Krems, "Cold controlled chemistry," Phys. Chem. Chem. Phys. **10**, 4079 (2008).

[46] G. Quéméner and P. S. Julienne, "Ultracold molecules under control!" Chem. Rev **112**, 4949 (2012).

[47] K.-K. Ni, S. Ospelkaus, D. Wang, G. Quéméner, B. Neyenhuis, M. H. G. de Miranda, J. L. Bohn, J. Ye, and D. S. Jin, "Dipolar collisions of polar molecules in the quantum regime," Nature **464**, 1324 (2010).

[48] S. Ospelkaus, K.-K. Ni, D. Wang, M. De Miranda, B. Neyenhuis, G. Quéméner, P. Julienne, J. Bohn, D. Jin, and J. Ye, "Quantum-state controlled chemical reactions of ultracold potassium-rubidium molecules," Science **327**, 853 (2010).

[49] M. A. Nichols, Y.-X. Liu, L. Zhu, M.-G. Hu, Y. Liu, and K.-K. Ni, "Detection of long-lived complexes in ultracold atom-molecule collisions," Phys. Rev. X **12**, 011049 (2022).

[50] S. E. Maxwell, R. Brahms, N. and. deCarvalho, D. R. Glenn, J. S. Helton, S. V. Nguyen, D. Patterson, J. Petricka, D. DeMille, and J. M. Doyle, "High-flux beam source for cold, slow atoms or molecules," Phys. Rev. Lett. **95**, 173201 (2005).

[51] N. R. Hutzler, I. Lu, H, and J. M. Doyle, "The buffer gas beam: An intense, cold, and slow source for atoms and molecules," Chem. Rev. **112**, 4803 (2012).

[52] S. Truppe, M. Hambach, S. M. Skoff, N. E. Bulleid, J. S. Bumby, R. J. Hendricks, E. A. Hinds, B. E. Sauer, and M. R. Tarbutt, "A buffer gas beam source for short, intense and slow molecular pulses," J. Mod. Opt. **65**, 648 (2017).

[53] H. L. Bethlem and G. Berden, G. and. Meijer, "Decelerating neutral dipolar molecules," Phys. Rev. Lett. **83**, 1558 (1999).

[54] M. R. Tarbutt, H. L. Bethlem, J. J. Hudson, V. L. Ryabov, V. A. Ryzhov, B. E. Sauer, G. Meijer, and E. A. Hinds, "Slowing heavy, ground-state molecules using an alternating gradient decelerator," Phys. Rev. Lett. **92**, 173002 (2004).

[55] S. Y. van de Meerakker, P. H. Smeets, N. Vanhaecke, R. T. Jongma, and G. Meijer, "Deceleration and electrostatic trapping of OH radicals," Phys. Rev. Lett. **94**, 023004 (2005).

[56] S. Hoekstra, M. Metsälä, P. C. Zieger, L. Scharfenberg, J. J. Gilijamse, G. Meijer, and S. Y. T. van de Meerakker, "Electrostatic trapping of metastable NH molecules," Phys. Rev. A **76**, 063408 (2007).

[57] S. Y. T. van de Meerakker, H. L. Bethlem, N. Vanhaecke, and G. Meijer, "Manipulation and control of molecular beams," Chem. Rev. **112**, 4828 (2012).

[58] V. Zhelyazkova, A. Cournol, T. E. Wall, A. Matsushima, J. J. Hudson, E. A. Hinds, M. R. Tarbutt, and B. E. Sauer, "Laser cooling and slowing of CaF molecules," Phys. Rev. A **89**, 053416 (2014).

[59] N. J. Fitch and M. R. Tarbutt, "Principles and design of a Zeeman–Sisyphus decelerator for molecular beams," ChemPhysChem **17**, 3609 (2016).

[60] J. F. Barry, D. J. McCarron, E. B. Norrgard, M. H. Steinecker, and D. DeMille, "Magneto-optical trapping of a diatomic molecule," Nature **512**, 286–289 (2014).

[61] M. H. Steinecker, D. J. McCarron, Y. Zhu, and D. DeMille, "Improved radio-frequency magneto-optical trap of SrF molecules," Chem. Phys. Chem. **17**, 3664 (2016).

[62] L. Anderegg, B. L. Augenbraun, E. Chae, B. Hemmerling, N. R. Hutzler, A. Ravi, A. Collopy, J. Ye, W. Ketterle, and J. M. Doyle, "Radio frequency magneto-optical trapping of CaF with high density," Phys. Rev. Lett. **119**, 103201 (2017).

[63] A. L. Collopy, S. Ding, Y. Wu, I. A. Finneran, L. Anderegg, B. L. Augenbraun, J. M. Doyle, and J. Ye, "3D magneto-optical trap of Yttrium Monoxide," Phys. Rev. Lett. **121**, 213201 (2018).

[64] K. M. Jones, E. Tiesinga, P. D. Lett, and P. S. Julienne, "Ultracold photoassociation spectroscopy: Long-range molecules and atomic scattering," Rev. Mod. Phys. **78**, 483 (2006).

[65] M. Viteau, A. Chotia, M. Allegrini, N. Bouloufa, O. Dulieu, D. Comparat, and P. Pillet, "Optical pumping and vibrational cooling of molecules," Science **321**, 232 (2008).

[66] J. Deiglmayr, A. Grochola, M. Repp, K. Mörtlbauer, C. Glück, J. Lange, O. Dulieu, R. Wester, and M. Weidemüller, "Formation of ultracold polar molecules in the rovibrational ground state," Phys. Rev. Lett. **101**, 133004 (2008).

[67] P. Zabawa, A. Wakim, M. Haruza, and N. P. Bigelow, "Formation of ultracold $X^1\Sigma^+(v'' = 0)$ NaCs molecules via coupled photoassociation channels," Phys. Rev. A **84**, 061401 (2011).

[68] J. Deiglmayr, P. Pellegrini, A. Grochola, M. Repp, R. Côté, O. Dulieu, R. Wester, and M. Weidemüller, "Influence of a Feshbach resonance on the photoassociation of LiCs," New J. Phys. **11**, 055034 (2009).

[69] C. Chin, R. Grimm, P. Julienne, and E. Tiesinga, "Feshbach resonances in ultracold gases," Rev. Mod. Phys. **82**, 1225 (2010).

[70] K. Bergmann, H. Theuer, and B. Shore, "Coherent population transfer among quantum states of atoms and molecules," Rev. Mod. Phys. **70**, 1003 (1998).

[71] N. V. Vitanov, A. A. Rangelov, B. W. Shore, and K. Bergmann, "Stimulated Raman adiabatic passage in physics, chemistry, and beyond," Rev. Mod. Phys. **89**, 015006 (2017).

[72] J. G. Danzl, E. Haller, M. Gustavsson, M. J. Mark, R. Hart, N. Bouloufa, O. Dulieu, H. Ritsch, and H.-C. Nägerl, "Quantum gas of deeply bound ground state molecules," Science **321**, 1062 (2008).

[73] F. Lang, K. Winkler, C. Strauss, R. Grimm, and J. Hecker Denschlag, "Ultracold triplet molecules in the rovibrational ground state," Phys. Rev. Lett. **101**, 133005 (2008).

[74] K.-K. Ni, S. Ospelkaus, M. H. G. de Miranda, A. Pe'er, B. Neyenhuis, J. J. Zirbel, S. Kotochigova, P. S. Julienne, D. S. Jin, and J. Ye, "A high phase-space-density gas of polar molecules," Science **322**, 231 (2008).

[75] T. Takekoshi, L. Reichsöllner, A. Schindewolf, J. M. Hutson, C. R. Le Sueur, O. Dulieu, F. Ferlaino, R. Grimm, and H.-C. Nägerl, "Ultracold dense samples of dipolar RbCs molecules in the rovibrational and hyperfine ground state," Phys. Rev. Lett. **113**, 205301 (2014).

[76] P. K. Molony, P. D. Gregory, Z. Ji, B. Lu, M. P. Köppinger, C. R. Le Sueur, C. L. Blackley, J. M. Hutson, and S. L. Cornish, "Creation of ultracold ^{87}Rb ^{133}Cs molecules in the rovibrational ground state," Phys. Rev. Lett. **113**, 255301 (2014).

[77] J. W. Park, S. A. Will, and M. W. Zwierlein, "Ultracold dipolar gas of Fermionic ^{23}Na^{40}K molecules in their absolute ground state," Phys. Rev. Lett. **114**, 205302 (2015).

[78] M. Guo, B. Zhu, B. Lu, X. Ye, F. Wang, R. Vexiau, N. Bouloufa-Maafa, G. Quéméner, O. Dulieu, and D. Wang, "Creation of an ultracold gas of ground-state dipolar ^{23}Na^{87}Rb molecules," Phys. Rev. Lett. **116**, 205303 (2016).

[79] T. M. Rvachov, H. Son, A. T. Sommer, S. Ebadi, J. J. Park, M. W. Zwierlein, W. Ketterle, and A. O. Jamison, "Long-lived ultracold molecules with electric and magnetic dipole moments," Phys. Rev. Lett. **119**, 143001 (2017).

[80] J. Pérez-Ríos, F. Herrera, and R. V. Krems, "External field control of collective spin excitations in an optical lattice of $^2\Sigma$ molecules," New J. Phys. **12**, 103007 (2010).

[81] E. Abrahamsson, T. V. Tscherbul, and R. V. Krems, "Inelastic collisions of cold polar molecules in nonparallel electric and magnetic fields," J. Chem. Phys. **127**, 044302 (2007).

[82] G. Quéméner and J. L. Bohn, "Shielding $^2\Sigma$ ultracold dipolar molecular collisions with electric fields," Phys. Rev. A **93**, 012704 (2016).

[83] F. Herrera, Y. Cao, S. Kais, and K. B. Whaley, "Infrared-dressed entanglement of cold open-shell polar molecules for universal matchgate quantum computing," New J. Phys. **16**, 075001 (2014).

[84] M. Karra, K. Sharma, B. Friedrich, S. Kais, and D. Herschbach, "Prospects for quantum computing with an array of ultracold polar paramagnetic molecules," J. Chem. Phys. **144**, 094301 (2016).

[85] P. S. Żuchowski, J. Aldegunde, and J. M. Hutson, "Ultracold RbSr molecules can be formed by magnetoassociation," Phys. Rev. Lett. **105**, 153201 (2010).

[86] D. A. Brue and J. M. Hutson, "Magnetically tunable Feshbach resonances in ultracold Li-Yb mixtures," Phys. Rev. Lett. **108**, 043201 (2012).

[87] D. A. Brue and J. M. Hutson, "Prospects of forming ultracold molecules in $^2\Sigma$ states by magnetoassociation of alkali-metal atoms with Yb," Phys. Rev. A **87**, 052709 (2013).

[88] V. Barbé, A. Ciamei, B. Pasquiou, L. Reichsöllner, F. Schreck, P. S. Żuchowski, and J. M. Hutson, "Observation of Feshbach resonances between alkali and closed-shell atoms," Nat. Phys. **14**, 881 (2018).

[89] A. Green, H. Li, J. H. See Toh, X. Tang, K. C. McCormick, M. Li, E. Tiesinga, S. Kotochigova, and S. Gupta, "Feshbach resonances in p-wave three-body recombination within Fermi-Fermi mixtures of open-shell ^{6}Li and closed-shell ^{173}Yb atoms," Phys. Rev. X **10**, 031037 (2020).

[90] A. Guttridge, S. A. Hopkins, S. L. Kemp, M. D. Frye, J. M. Hutson, and S. L. Cornish, "Interspecies thermalization in an ultracold mixture of Cs and Yb in an optical trap," Phys. Rev. A **96**, 012704 (2017).

[91] A. Guttridge, S. A. Hopkins, M. D. Frye, J. J. McFerran, J. M. Hutson, and S. L. Cornish, "Production of ultracold Cs*Yb molecules by photoassociation," Phys. Rev. A **97**, 063414 (2018).

[92] A. Guttridge, M. D. Frye, B. C. Yang, J. M. Hutson, and S. L. Cornish, "Two-photon photoassociation spectroscopy of CsYb: Ground-state interaction potential and interspecies scattering lengths," Phys. Rev. A **98**, 022707 (2018).

[93] B. C. Yang, M. D. Frye, A. Guttridge, J. Aldegunde, P. S. Żuchowski, S. L. Cornish, and J. M. Hutson, "Magnetic Feshbach resonances in ultracold collisions between Cs and Yb atoms," Phys. Rev. A **100**, 022704 (2019).

[94] S. Tassy, N. Nemitz, F. Baumer, C. Höhl, A. Batär, and A. Görlitz, "Sympathetic cooling in a mixture of diamagnetic and paramagnetic atoms," J. Phys. B: At., Mol. Opt. Phys. **43**, 205309 (2010).

[95] N. Nemitz, F. Baumer, F. Münchow, S. Tassy, and A. Görlitz, "Production of heteronuclear molecules in an electronically excited state by photoassociation in a mixture of ultracold Yb and Rb," Phys. Rev. A **79**, 061403 (2009).

[96] F. Münchow, C. Bruni, M. Madalinski, and A. Gorlitz, "Two-photon photoassociation spectroscopy of heteronuclear YbRb," Phys. Chem. Chem. Phys. **13**, 18734 (2011).

[97] M. Borkowski, P. S. Żuchowski, R. Ciuryło, P. S. Julienne, D. Kedziera, Ł. Mentel, P. Tecmer, F. Münchow, C. Bruni, and A. Görlitz, "Scattering lengths in isotopologues of the RbYb system," Phys. Rev. A **88**, 052708 (2013).

[98] C. Bruni and A. Görlitz, "Observation of hyperfine interaction in photoassociation spectra of ultracold RbYb," Phys. Rev. A **94**, 022503 (2016).

[99] C. Bruni, F. Münchow, and A. Görlitz, "Optical Autler–Townes spectroscopy in a heteronuclear mixture of laser-cooled atoms," App. Phys. B **123**, 6 (2017).

[100] F. Baumer, F. Münchow, A. Görlitz, S. E. Maxwell, P. S. Julienne, and E. Tiesinga, "Spatial separation in a thermal mixture of ultracold ^{174}Yb and ^{87}Rb atoms," Phys. Rev. A **83**, 040702 (2011).

[101] Y. Takasu, K. Maki, K. Komori, T. Takano, K. Honda, M. Kumakura, T. Yabuzaki, and Y. Takahashi, "Spin-singlet Bose-Einstein condensation of two-electron atoms," Phys. Rev. Lett. **91**, 040404 (2003).

[102] T. Fukuhara, Y. Takasu, M. Kumakura, and Y. Takahashi, "Degenerate Fermi gases of Ytterbium," Phys. Rev. Lett. **98**, 030401 (2007).

[103] T. Fukuhara, S. Sugawa, and Y. Takahashi, "Bose-Einstein condensation of an ytterbium isotope," Phys. Rev. A **76**, 051604 (2007).

[104] Y. Takasu and Y. Takahashi, "Quantum degenerate gases of Ytterbium atoms," J. Phys. Soc. Jpn. **78**, 012001 (2009).

[105] S. Taie, Y. Takasu, S. Sugawa, R. Yamazaki, T. Tsujimoto, R. Murakami, and Y. Takahashi, "Realization of a SU(2) × SU(6) system of Fermions in a cold atomic gas," Phys. Rev. Lett. **105**, 190401 (2010).

[106] S. Sugawa, R. Yamazaki, S. Taie, and Y. Takahashi, "Bose-Einstein condensate in gases of rare atomic species," Phys. Rev. A **84**, 011610 (2011).

[107] M. Okano, H. Hara, M. Muramatsu, K. Doi, S. Uetake, Y. Takasu, and Y. Takahashi, "Simultaneous magneto-optical trapping of lithium and ytterbium atoms towards production of ultracold polar molecules," Appl. Phys. B **98**, 691–696 (2010).

[108] H. Hara, Y. Takasu, Y. Yamaoka, J. M. Doyle, and Y. Takahashi, "Quantum degenerate mixtures of alkali and alkaline-earth-like atoms," Phys. Rev. Lett. **106**, 205304 (2011).

[109] H. Hara, H. Konishi, S. Nakajima, Y. Takasu, and Y. Takahashi, "A three-dimensional optical lattice of Ytterbium and Lithium atomic gas mixture," J. Phys. Soc. Jpn. **83**, 014003 (2014).

[110] F. Schäfer, N. Mizukami, P. Yu, S. Koibuchi, A. Bouscal, and Y. Takahashi, "Experimental realization of ultracold Yb-^{7}Li mixtures in mixed dimensions," Phys. Rev. A **98**, 051602 (2018).

[111] H. Konishi, F. Schäfer, S. Ueda, and Y. Takahashi, "Collisional stability of localized Yb(^{3}P$_2$) atoms immersed in a Fermi sea of Li," New J. Phys. **18**, 103009 (2016).

[112] F. Schäfer, H. Konishi, A. Bouscal, T. Yagami, and Y. Takahashi, "Spectroscopic determination of magnetic-field-dependent interactions in an ultracold Yb(^{3}P$_2$) – Li mixture," Phys. Rev. A **96**, 032711 (2017).

[113] F. Schäfer, H. Konishi, A. Bouscal, T. Yagami, and Y. Takahashi, "Spin dependent inelastic collisions between metastable state two-electron atoms and ground state alkali-atoms," New J. Phys. **19**, 103039 (2017).

[114] F. Schäfer, H. Konishi, A. Bouscal, T. Yagami, M. D. Frye, J. M. Hutson, and Y. Takahashi, "Ultracold collisions in the Yb – Li mixture system," J. Phys.: Conf. Ser **1412**, 062005 (2020).

[115] F. Schäfer, N. Mizukami, and Y. Takahashi, "Feshbach resonances of large-mass-imbalance Er – Li mixtures," Phys. Rev. A **105**, 012816 (2022).

[116] A. Ciamei, J. Szczepkowski, A. Bayerle, V. Barbé, L. Reichsöllner, S. M. Tzanova, C.-C. Chen, B. Pasquiou, A. Grochola, P. Kowalczyk, W. Jastrzebski, and F. Schreck, "The RbSr $^2\Sigma^+$ ground state investigated

via spectroscopy of hot and ultracold molecules," Phys. Chem. Chem. Phys. **20**, 26221 (2018).

[117] V. V. Ivanov, A. Khramov, A. H. Hansen, W. H. Dowd, F. Münchow, A. O. Jamison, and S. Gupta, "Sympathetic cooling in an optically trapped mixture of alkali and spin-singlet atoms," Phys. Rev. Lett. **106**, 153201 (2011).

[118] A. H. Hansen, A. Khramov, W. H. Dowd, A. O. Jamison, V. V. Ivanov, and S. Gupta, "Quantum degenerate mixture of ytterbium and lithium atoms," Phys. Rev. A **84**, 011606 (2011).

[119] A. Hansen, A. Khramov, W. Dowd, A. Jamison, B. Plotkin-Swing, R. Roy, and S. Gupta, "Production of quantum degenerate mixtures of ytterbium and lithium with controllable inter-species overlap," Phys. Rev. A. **87**, 013615 (2013).

[120] A. Khramov, A. Hansen, W. Dowd, R. J. Roy, C. Makrides, A. Petrov, S. Kotochigova, and S. Gupta, "Ultracold heteronuclear mixture of ground and excited state atoms," Phys. Rev. Lett. **112**, 033201 (2014).

[121] R. Roy, R. Shrestha, A. Green, S. Gupta, M. Li, S. Kotochigova, A. Petrov, and C. H. Yuen, "Photoassociative production of ultracold heteronuclear YbLi$*$ molecules," Phys. Rev. A **94**, 033413 (2016).

[122] A. Green, J. H. S. Toh, R. Roy, M. Li, S. Kotochigova, and S. Gupta, "Two-photon photoassociation spectroscopy of the doublet-sigma YbLi molecular ground state," Phys Rev A. **99**, 063416 (2019).

[123] A. S. Flores, H. P. Mishra, W. Vassen, and S. Knoop, "An ultracold, optically trapped mixture of ^{87}Rb and metastable ^{4}He atoms," Eur. Phys. J. D **71**, 49 (2017).

[124] M. Witkowski, B. Nagórny, R. Munoz-Rodriguez, R. Ciuryło, P. S. Żuchowski, S. Bilicki, M. Piotrowski, P. Morzyński, and M. Zawada, "Dual Hg – Rb magneto-optical trap," Opt. Express **25**, 3165 (2017).

[125] F. Lackner, G. Krois, T. Buchsteiner, J. V. Pototschnig, and W. E. Ernst, "Helium-droplet-assisted preparation of cold RbSr molecules," Phys. Rev. Lett. **113**, 153001 (2014).

[126] J. V. Pototschnig, G. Krois, F. Lackner, and W. E. Ernst, "Investigation of the RbCa molecule: Experiment and theory," J. Mol. Spectroscopy **310**, 126 (2015).

[127] A. Stein, M. Ivanova, A. Pashov, H. Knöckel, and E. Tiemann, "Spectroscopic study of the $2^2\Sigma^+$ and the $4^2\Sigma^+$ excited states of LiCa," J. Chem. Phys. **138**, 114306 (2013).

[128] E. Schwanke, J. Gerschmann, H. Knöckel, S. Ospelkaus, and E. Tiemann, "The coupled system $2^2\Sigma^+$ and $(1)^2\,\Pi$ of $^7Li^{88}Sr$," J. Phys. B: At. Mol. Opt. Phys. **53**, 065102 (2020).

[129] J. R. De Laeter, J. K. Böhlke, P. De Bièvre, H. Hidaka, H. S. Peiser, K. J. R. Rosman, and P. D. P. Taylor, "Atomic weights of the elements. review 2000 (iupac technical report)," *Pure and Applied Chemistry*, Pure Appl. Chem. **75**, 683 (2009).

[130] M. Kitagawa, K. Enomoto, K. Kasa, Y. Takahashi, R. Ciuryło, P. Naidon, and P. S. Julienne, "Two-color photoassociation spectroscopy of ytterbium atoms and the precise determinations of s-wave scattering lengths," Phys. Rev. A **77**, 012719 (2008).

[131] C. Chin, V. Vuletić, A. J. Kerman, and S. Chu, "High resolution Feshbach spectroscopy of Cesium," Phys. Rev. Lett. **85**, 2717 (2000).

[132] C. Chin, V. Vuletić, A. J. Kerman, S. Chu, E. Tiesinga, P. J. Leo, and C. J. Williams, "Precision Feshbach spectroscopy of ultracold Cs_2," Phys. Rev. A **70**, 032701 (2004).

[133] A. D. Lange, K. Pilch, A. Prantner, F. Ferlaino, B. Engeser, H.-C. Nägerl, R. Grimm, and C. Chin, "Determination of atomic scattering lengths

from measurements of molecular binding energies near Feshbach resonances," Phys. Rev. A. **79**, 013622 (2009).

[134] M. Berninger, A. Zenesini, B. Huang, W. Harm, H.-C. Nägerl, F. Ferlaino, R. Grimm, P. S. Julienne, and J. M. Hutson, "Feshbach resonances, weakly bound molecular states, and coupled-channel potentials for cesium at high magnetic fields," Phys. Rev. A **87**, 032517 (2013).

[135] S. L. Kemp, K. L. Butler, R. Freytag, S. A. Hopkins, E. A. Hinds, M. R. Tarbutt, and S. L. Cornish, "Production and characterization of a dual species magneto-optical trap of cesium and ytterbium," Rev. Sci. Instrum. **87**, 023105 (2016).

[136] S. A. Hopkins, K. Butler, A. Guttridge, S. Kemp, R. Freytag, E. A. Hinds, M. R. Tarbutt, and S. L. Cornish, "A versatile dual-species Zeeman slower for caesium and ytterbium," Rev. Sci. Instrum. **87**, 043109 (2016).

[137] A. Guttridge, S. A. Hopkins, S. L. Kemp, D. Boddy, R. Freytag, M. P. A. Jones, M. R. Tarbutt, E. A. Hinds, and S. L. Cornish, "Direct loading of a large Yb MOT on the $^1S_0 \rightarrow {}^3P_1$ transition," J. Phys. B: At., Mol. Opt. Phys. **49**, 145006 (2016).

[138] K. L. Butler, *A dual species MOT of Yb and Cs* (PhD thesis, Durham University, 2014).

[139] S. L. Kemp, *Laser cooling and optical trapping of Ytterbium* (PhD thesis, Durham University, 2017).

[140] A. Guttridge, *Photoassociation of Ultracold CsYb Molecules and Determination of Interspecies Scattering Lengths* (PhD thesis, Durham University, 2018).

[141] W. Markowitz, R. G. Hall, L. Essen, and J. V. L. Parry, "Frequency of Cesium in terms of ephemeris time," Phys. Rev. Lett. **1**, 105 (1958).

[142] T. Weber, J. Herbig, M. Mark, H.-C. Nägerl, and R. Grimm, "Bose-Einstein condensation of Cesium," Science **299**, 232 (2003).

[143] D. A. Steck, *Cesium D Line Data*, available online at http://steck.us/alkalidata (revision 2.1.4), 2019.

[144] C. Alcock, V. Itkin, and M. Horrigan, "Vapour pressure equations for the metallic elements: 298–2500K," Can. Metall. Q. **23**, 309 (1984).

[145] J. H. Shirley, "Modulation transfer processes in optical heterodyne saturation spectroscopy," Opt. Lett. **7**, 537 (1982).

[146] D. J. McCarron, S. A. King, and S. L. Cornish, "Modulation transfer spectroscopy in atomic rubidium," Meas. Sci. Technol. **19**, 105601 (2008).

[147] G. C. Bjorklund, "Frequency-modulation spectroscopy: a new method for measuring weak absorptions and dispersions," Opt. Lett. **5**, 15 (1980).

[148] M. Gehrtz, G. C. Bjorklund, and E. A. Whittaker, "Quantum-limited laser frequency-modulation spectroscopy," J. Opt. Soc. Am. B **2**, 1510 (1985).

[149] T. Weber, J. Herbig, M. Mark, H.-C. Nägerl, and R. Grimm, "Three-body recombination at large scattering lengths in an ultracold atomic gas," Phys. Rev. Lett. **91**, 123201 (2003).

[150] T. Kraemer, M. Mark, P. Waldburger, J. G. Danzl, C. Chin, B. Engeser, A. D. Lange, K. Pilch, A. Jaakkola, H.-C. Nägerl, and R. Grimm, "Evidence for Efimov quantum states in an ultracold gas of caesium atoms," Nature **440**, 315 (2006).

[151] T. Kraemer, J. Herbig, M. Mark, T. Weber, C. Chin, H.-C. Nägerl, and R. Grimm, "Optimized production of a cesium Bose–Einstein condensate," Appl. Phys. B **79**, 1013 (2004).

[152] P. W. H. Pinkse, A. Mosk, M. Weidemüller, M. W. Reynolds, T. W. Hijmans, and J. T. M. Walraven, "Adiabatically changing the phase-space density of a trapped Bose gas," Phys. Rev. Lett. **78**, 990 (1997).

[153] D. M. Stamper-Kurn, H.-J. Miesner, A. P. Chikkatur, S. Inouye, J. Stenger, and W. Ketterle, "Reversible formation of a Bose-Einstein condensate," Phys. Rev. Lett. **81**, 2194 (1998).

[154] T. Weber, *Bose-Einstein Condensation of Optically Trapped Cesium* (PhD thesis, Leopold-Franzens-Universität Innsbruck, 2003).

[155] P. Ahmadi, B. P. Timmons, and G. S. Summy, "Geometrical effects in the loading of an optical atom trap," Phys. Rev. A **72**, 023411 (2005).

[156] S. Baier, *An optical dipole trap for Erbium with tunable geometry* (Master's thesis, University of Innsbruck, 2012).

[157] Y. Tang, N. Q. Burdick, K. Baumann, and B. L. Lev, "Bose–Einstein condensation of ^{162}Dy and ^{160}Dy," New J. of Phys. **17**, 045006 (2015).

[158] R. Roy, A. Green, R. Bowler, and S. Gupta, "Rapid cooling to quantum degeneracy in dynamically shaped atom traps," Phys. Rev. A **93**, 043403 (2016).

[159] R. Grimm, M. Weidemüuller, and Y. B. Ovchinnikov, "Optical dipole traps for neutral atoms," Adv. At., Mol., Opt. Phys. **42**, 95 (2000).

[160] J. Sansonetti, "Wavelengths, transition probabilities, and energy levels for the spectra of Cesium (Cs I-Cs LV)," J. Phys. Chem. Ref. Data **38**, 761 (2009).

[161] *NIST Basic Atomic Spectroscopic Data.*

[162] K. E. Wilson, A. Guttridge, J. Segal, and S. L. Cornish, "Quantum degenerate mixtures of Cs and Yb," Phys. Rev. A **103**, 033306 (2021).

[163] R. Onofrio and C. Presilla, "Reaching Fermi degeneracy in two-species optical dipole traps," Phys. Rev. Lett. **89**, 100401 (2002).

[164] C. D. Herold, V. D. Vaidya, X. Li, S. L. Rolston, J. V. Porto, and M. S. Safronova, "Precision measurement of transition matrix elements via light shift cancellation," Phys. Rev. Lett. **109**, 243003 (2012).

[165] F. Dalfovo, S. Giorgini, L. P. Pitaevskii, and S. Stringari, "Theory of Bose-Einstein condensation in trapped gases," Rev. Mod. Phys. **71**, 463 (1999).

[166] A. J. Leggett, "Bose-Einstein condensation in the alkali gases: Some fundamental concepts," Rev. Mod. Phys. **73**, 307 (2001).

[167] W. Ketterle, "Nobel lecture: When atoms behave as waves: Bose-Einstein condensation and the atom laser," Rev. Mod. Phys. **74**, 1131 (2002).

[168] W. Ketterle, D. Durfee, and D. Stamper-Kurn, "Making, probing and understanding Bose-Einstein condensates," Proceedings of the International School of Physics "Enrico Fermi" **140**, 67–176 (1999).

[169] W. Ketterle and N. V. Druten, "Evaporative cooling of trapped atoms," Adv. At., Mol., Opt. Phys. **37**, 181 (1996).

[170] Y. Li, G. Feng, R. Xu, X. Wang, J. Wu, G. Chen, X. Dai, J. Ma, L. Xiao, and S. Jia, "Magnetic levitation for effective loading of cold cesium atoms in a crossed dipole trap," Phys. Rev. A **91**, 053604 (2015).

[171] Y. Kagan, B. V. Svistunov, and G. V. Shlyapnikov, "Effect of bose condensation on inelastic processes in gases," JETP Lett. **42**, 205 (1985).

[172] E. A. Burt, R. W. Ghrist, C. J. Myatt, M. J. Holland, E. A. Cornell, and C. E. Wieman, "Coherence, correlations, and collisions: What one learns about Bose-Einstein condensates from their decay," Phys. Rev. Lett. **79**, 337 (1997).

[173] K. E. Wilson, A. Guttridge, I.-K. Liu, J. Segal, T. P. Billam, N. G. Parker, N. P. Proukakis, and S. L. Cornish, "Dynamics of a degenerate Cs-Yb mixture with attractive interspecies interactions," Phys. Rev. Research **3**, 033096 (2021).

[174] C. A. Sackett, J. M. Gerton, M. Welling, and R. G. Hulet, "Measurements of collective collapse in a Bose-Einstein condensate with attractive interactions," Phys. Rev. Lett. **82**, 876 (1999).

[175] J. M. Gerton, D. Strekalov, I. Prodan, and R. G. Hulet, "Direct observation of growth and collapse of a Bose–Einstein condensate with attractive interactions," Nature **408**, 692 (2000).

[176] J. L. Roberts, N. R. Claussen, S. L. Cornish, E. A. Donley, E. A. Cornell, and C. E. Wieman, "Controlled collapse of a Bose-Einstein condensate," Phys. Rev. Lett. **86**, 4211 (2001).

[177] E. A. Donley, N. R. Claussen, S. L. Cornish, J. L. Roberts, E. A. Cornell, and C. E. Wieman, "Dynamics of collapsing and exploding Bose-Einstein condensates," Nature (London) **412**, 295 (2001).

[178] S. L. Cornish, S. T. Thompson, and C. E. Wieman, "Formation of bright matter-wave solitons during the collapse of attractive Bose-Einstein condensates," Phys. Rev. Lett. **96**, 170401 (2006).

[179] P. A. Ruprecht, M. J. Holland, K. Burnett, and M. Edwards, "Time-dependent solution of the nonlinear Schrödinger equation for Bose-condensed trapped neutral atoms," Phys. Rev. A **51**, 4704 (1995).

[180] A. Gammal, T. Frederico, and L. Tomio, "Critical number of atoms for attractive Bose-Einstein condensates with cylindrically symmetrical traps," Phys. Rev. A **64**, 055602 (2001).

[181] C. Ospelkaus, S. Ospelkaus, K. Sengstock, and K. Bongs, "Interaction-driven dynamics of ^{40}K−^{87}Rb Fermion-Boson gas mixtures in the large-particle-number limit," Phys. Rev. Lett. **96**, 020401 (2006).

[182] S. B. Papp, J. M. Pino, and C. E. Wieman, "Tunable miscibility in a dual-species Bose-Einstein condensate," Phys. Rev. Lett. **101**, 040402 (2008).

[183] F. Wang, X. Li, D. Xiong, and D. Wang, "A double species ^{23}Na and ^{87}Rb Bose–Einstein condensate with tunable miscibility via an interspecies Feshbach resonance," Journal of Physics B: Atomic, Molecular and Optical Physics **49**, 015302 (2015).

[184] C. Pethick and H. Smith, *Bose-Einstein condensation in dilute gases* (Cambridge University Press, 2002).

[185] K. L. Lee, N. B. Jørgensen, I.-K. Liu, L. Wacker, J. J. Arlt, and N. P. Proukakis, "Phase separation and dynamics of two-component Bose-Einstein condensates," Phys. Rev. A **94**, 013602 (2016).

[186] M. S. Safronova, B. Arora, and C. W. Clark, "Frequency-dependent polarizabilities of alkali-metal atoms from ultraviolet through infrared spectral regions," Phys. Rev. A **73**, 022505 (2006).

[187] W. R. Johnson, D. Kolb, and K.-N. Huang, "Electric-dipole, quadrupole, and magnetic-dipole susceptibilities and shielding factors for closed-shell ions of the He, Ne, Ar, Ni (Cu+), Kr, Pb, and Xe isoelectronic sequences," At. Data Nucl. Data Tables **28**, 334 (1983).

[188] L. J. LeBlanc and J. H. Thywissen, "Species-specific optical lattices," Phys. Rev. A **75**, 053612 (2007).

[189] B. Arora, M. S. Safronova, and C. W. Clark, "Tune-out wavelengths of alkali-metal atoms and their applications," Phys. Rev. A **84**, 043401 (2011).

[190] G. Lamporesi, J. Catani, G. Barontini, Y. Nishida, M. Inguscio, and F. Minardi, "Scattering in mixed dimensions with ultracold gases," Phys. Rev. Lett. **104**, 153202 (2010).

[191] J. Catani, G. Barontini, G. Lamporesi, F. Rabatti, G. Thalhammer, F. Minardi, S. Stringari, and M. Inguscio, "Entropy exchange in a mixture of ultracold atoms," Phys. Rev. Lett. **103**, 140401 (2009).

[192] R. Trubko, M. D. Gregoire, W. F. Holmgren, and A. D. Cronin, "Potassium tune-out-wavelength measurement using atom interferometry and a multipass optical cavity," Phys. Rev. A **95**, 052507 (2017).

[193] Z. Meir, M. Sinhal, M. S. Safronova, and S.Willitsch, "Combining experiments and relativistic theory for establishing accurate radiative quantities in atoms: The lifetime of the $^2P_{\frac{3}{2}}$ state in $^{+40}$Ca," Phys. Rev. A **101**, 012509 (2020).

[194] K. J. Arnold, S. R. Chanu, R. Kaewuam, T. R. Tan, L. Yeo, Z. Zhang, M. S. Safronova, and M. D. Barrett, "Measurements of the branching ratios for $^6P_{\frac{1}{2}}$ decays in $^{+138}$Ba," Phys. Rev. A **100**, 032503 (2019).

[195] Z. Zhang, K. J. Arnold, S. R. Chanu, R. Kaewuam, M. S. Safronova, and M. D. Barrett, "Branching fractions for $P_{\frac{3}{2}}$ decays in Ba^+," Phys. Rev. A **101**, 062515 (2020).

[196] A. Heinz, A. J. Park, N. Šantić, J. Trautmann, S. G. Porsev, M. S. Safronova, I. Bloch, and S. Blatt, "State-dependent optical lattices for the Strontium optical qubit," Phys. Rev. Lett. **124**, 203201 (2020).

[197] R. H. Leonard, A. J. Fallon, C. A. Sackett, and M. S. Safronova, "High-precision measurements of the ^{87}Rb D-line tune-out wavelength," Phys. Rev. A **92**, 052501 (2015).

[198] E. Copenhaver, K. Cassella, R. Berghaus, and H. Müller, "Measurement of a ^{7}Li tune-out wavelength by phase patterned atom interferometry," Phys. Rev. A **100**, 063603 (2019).

[199] B. Décamps, J. Vigué, A. Gauguet, , and M. Büchner, "Measurement of the 671-nm tune-out wavelength of ^{7}Li by atom interferometry," Phys. Rev. A **101**, 033614 (2020).

[200] W. F. Holmgren, R. Trubko, I. Hromada, and A. D. Cronin, "Measurement of a wavelength of light for which the energy shift for an atom vanishes," Phys. Rev. Lett. **109**, 243004 (2012).

[201] F. Schmidt, D.Mayer, M. Hohmann, T. Lausch, F. Kindermann, and A. Widera, "Precision measurement of the ^{87}Rb tune-out wavelength in the hyperfine ground state f=1 at 790 nm," Phys. Rev. A **93**, 022507 (2016).

[202] B. M. Henson, R. I. Khakimov, R. G. Dall, K. G. H. Baldwin, L. Y. Tang, and A. G. Truscott, "Precision measurement for metastable Helium atoms of the 413 nm tune-out wavelength at which the atomic polarizability vanishes," Phys. Rev. Lett. **115**, 043004 (2015).

[203] W. Kao, Y. Tang, N. Q. Burdick, and B. L. Lev, "Anisotropic dependence of tune-out wavelength near Dy 741-nm transition," Opt. Express **25**, 3411 (2017).

[204] R. Bause, M. Li, A. Schindewolf, X. Y. Chen, M. Duda, S. Kotochigova, I. Bloch, and X. Y. Luo, "Tune-out and magic wavelengths for ground-state ^{23}Na^{40}K molecules," Phys. Rev. Lett. **125**, 023201 (2020).

[205] F. L. Kien, P. Schneeweiss, and A. Rauschenbeutel, "Dynamical polarizability of atoms in arbitrary light fields: General theory and application to cesium," Eur. Phys. J. D **67**, 92 (2013).

[206] W. W. Yu, R. M. Yu, Y. J. Cheng, and Y. J. Zhou, "Tune-out wavelengths for the alkaline-metal atoms," Chin. Phys. B **25**, 023101 (2016).

[207] M. S. Safronova, U. I. Safronova, and C. W. Clark, "Magic wavelengths, matrix elements, polarizabilities, and lifetimes of Cs," Phys. Rev. A **94**, 012505 (2016).

[208] J. Jiang, X.-J. Li, X. Wang, C.-Z. Dong, and Z. W. Wu, "Tune-out wavelengths of the hyperfine components of the ground level of ^{133}Cs atoms," Phys. Rev. A. **102**, 042823 (2020).

[209] A. Ratkata, P. D. Gregory, A. D. Innes, J. A. Matthies, L. A. McArd, J. M. Mortlock, M. S. Safronova, S. L. Bromley, and S. L. Cornish, "Measurement of the tune-out wavelength for ^{133}Cs at 880 nm," Phys. Rev. A. **104**, 052813 (2021).

[210] I. Bloch, "Ultracold quantum gases in optical lattices," Nat. Phys. **1**, 25 (2005).

[211] P. L. Kapitza and P. A. M. Dirac, "The reflection of electrons from standing light waves," Proc. Cambridge Phil. Soc. **29**, 297 (1933).

[212] J. H. Denschlag, J. E. Simsarian, H. Häffner, C.McKenzie, A. Browaeys, D. Cho, K. Helmerson, S. L. Rolston, and W. D. Phillips, "A Bose-Einstein condensate in an optical lattice," J. Phys. B: At. Mol. Opt. Phys. **35**, 3095 (2002).

[213] K. Viebahn, M. Sbroscia, E. Carter, J. C. Yu, and U. Schneider, "Matter-wave diffraction from a quasicrystalline optical lattice," Phys. Rev. Lett. **122**, 110404 (2019).

[214] B. Gadway, D. Pertot, R. Reimann, M. G. Cohen, and D. Schneble, "Analysis of Kapitza-Dirac diffraction patterns beyond the Raman-Nath regime," Opt. Express **17**, 19173 (2009).

[215] P. K. Molony, *Creation of ultracold polar ground-state RbCs molecules* (PhD Thesis, Durham University, 2016).

[216] A. Damitz, G. Toh, E. Putney, C. E. Tanner, and D. S. Elliott, "Measurement of the radial matrix elements for the $6s^2S_{1/2} \rightarrow 7p^2P_J$ transitions in cesium," Phys. Rev. A **99**, 062510 (2019).

[217] B. M. P. nad J. F. Sell, T. Ehrenreich, M. A. Gearba, G. M. Brooke, J. Scoville, and R. J. Knize, "Lifetime measurement of the cesium $6P_{3/2}$ level using ultrafast pump-probe laser pulses," Phys. Rev. A **91**, 012506 (2015).

[218] W. D. Williams, M. T. Herd, and W. B. Hawkins, "Spectroscopic study of the $7p_{1/2}$ and $7p_{3/2}$ states in cesium-133," Laser. Phys. Lett. **15**, 095702 (2018).

[219] A. W. Carr and M. Saffman, "Doubly magic optical trapping for Cs atom hyperfine clock transitions," Phys. Rev. Lett. **117**, 150801 (2016).

[220] V. Gerginov, K. Calkins, C. E. Tanner, J. J. McFerran, S. Diddams, A. Bartels, and L. Hollberg, "Optical frequency measurements of $6s^2S_{1/2} - 6p^2P_{1/2}$ (D_1) transitions in ^{133}Cs and their impact on the fine-structure constant," Phys. Rev. A **73**, 032504 (2006).

[221] W. R. Johnson, H. C. Ho, C. E. Tanner, and A. Derevianko, "Off-diagonal hyperfine interaction between the $6p_{1/2}$ and $6p_{3/2}$ levels in ^{133}Cs," Phys. Rev. A **70**, 014501 (2004).

[222] D. Feiertag, A. Sahm, and G. Z. Putlitz, "Core polarization of the ^{133}Cs atom by the 7p electron," Z. Phys. A **255**, 93 (1972).

[223] G. Belin, L. Holmgren, and S. Svanberg, "Hyperfine interaction, Zeeman and Stark effects for excited states in Cesium," Phys. Scr. **14**, 39 (1976).

[224] S. Svanberg and S. Rydberg, "Level crossing investigation of the 6p $^2P_{3/2}$ and 7p $^2P_{3/2}$ levels of Cs^{133}, Cs^{135}, and Cs^{137}," Z. Phys. A **227**, 216 (1969).

[225] B. T. Beswick, I. G. Hughes, and S. A. Gardiner, "Lattice-depth measurement using multipulse atom diffraction in and beyond the weakly diffracting limit," Phys. Rev. Lett. **99**, 013614 (2019).

[226] T. Köhler, K. Góral, and P. S. Julienne, "Production of cold molecules via magnetically tunable Feshbach resonances," Rev. Mod. Phys. **78**, 1311 (2006).

[227] J. M. Hutson and P. Soldán, "Molecule formation in ultracold atomic gases," Int. Rev. Phys. Chem. **25**, 497 (2006).

[228] A. J. Moerdijk, B. J. Verhaar, and A. Axelsson, "Resonances in ultracold collisions of ^{6}Li, ^{7}Li, and ^{23}Na," Phys. Rev. A **51**, 4852 (1995).

[229] F. H. Mies, E. Tiesinga, and P. S. Julienne, "Manipulation of Feshbach resonances in ultracold atomic collisions using time-dependent magnetic fields," Phys. Rev. A **61**, 022721 (2000).

[230] P. S. Julienne, E. Tiesinga, and T. Köhler, "Making cold molecules by time-dependent feshbach resonances," J. Mod. Opt. **51**, 1787 (2004).

[231] R. Bause, A. Kamijo, X.-Y. Chen, M. Duda, A. Schindewolf, I. Bloch, and X.-Y. Luo, "Efficient conversion of closed-channel-dominated Feshbach molecules of ^{23}Na^{40}K to their absolute ground state," Phys. Rev. A **104**, 043321 (2021).

[232] G. Thalhammer, K. Winkler, F. Lang, S. Schmid, R. Grimm, and J. H. Denschlag, "Long-lived Feshbach molecules in a three-dimensional optical lattice," Phys. Rev. Lett. **96**, 050402 (2006).

[233] A. Chotia, B. Neyenhuis, S. A. Moses, B. Yan, J. P. Covey, M. Foss-Feig, A. M. Rey, D. S. Jin, and J. Ye, "Long-lived dipolar molecules and Feshbach molecules in a 3D optical lattice," Phys. Rev. Lett. **108**, 199 (2012).

[234] E. Timmermans, P. Tommasini, M. Hussein, and A. Kerman, "Feshbach resonances in atomic Bose-Einstein condensates," Phys. Rep. **315**, 199 (1999).

[235] F. A. van Abeelen and B. J. Verhaar, "Time-dependent Feshbach resonance scattering and anomalous decay of a Na Bose-Einstein condensate," Phys. Rev. Lett. **83**, 1550 (1999).

[236] F. Seesselberg, N. Buchheim, Z.-K. Lu, T. Schneider, X.-Y. Luo, E. Tiemann, I. Bloch, and C. Gohle, "Modeling the adiabatic creation of ultracold polar ^{23}Na^{40}K molecules," Phys. Rev. A **97**, 013405 (2018).

[237] K. K. Voges, P. Gersema, M. Meyer zum Alten Borgloh, T. A. Schulze, T. Hartmann, A. Zenesini, and S. Ospelkaus, "Ultracold gas of Bosonic ^{23}Na^{39}K ground-state molecules," Phys. Rev. Lett. **125**, 083401 (2020).

[238] G. F. Gribakin and V. V. Flambaum, "Calculation of the scattering length in atomic collisions using the semiclassical approximation," Phys. Rev. A **48**, 546 (1993).

[239] M. Mark, *Exploring ultracold trapped cesium Feshbach molecules* (PhD Thesis, Universität Innsbruck, 2008).

[240] V. Vuletić, C. Chin, A. J. Kerman, and S. Chu, "Suppression of atomic radiative collisions by tuning the ground state scattering length," Phys. Rev. Lett. **83**, 943 (1999).

[241] K. Góral, T. Köhler, S. A. Gardiner, E. Tiesinga, and P. S. Julienne, "Adiabatic association of ultracold molecules via magnetic-field tunable interactions," J. Phys. B: At. Mol. Opt. Phys. **37**, 3457 (2004).

[242] S. Stellmer, B. Pasquiou, R. Grimm, and F. Schreck, "Creation of ultracold Sr_2 molecules in the electronic ground state," Phys. Rev. Lett. **109**, 115302 (2012).

[243] A. Ciamei, A. Bayerle, C.-C. Chen, B. Pasquiou, and F. Schreck, "Efficient production of long-lived ultracold Sr_2 molecules," Phys. Rev. A **96**, 013406 (2017).

[244] G. Reinaudi, C. B. Osborn, M. McDonald, S. Kotochigova, and T. Zelevinsky, "Optical production of stable ultracold $^{88}Sr_2$ molecules," Phys. Rev. Lett. **109**, 115303 (2012).

[245] S. Taie, R. Yamazaki, S. Sugawa, and Y. Takahashi, "An SU(6) Mott insulator of an atomic Fermi gas realized by large-spin Pomeranchuk cooling," Nat. Phys. **8**, 825–830 (2012).

[246] H. Ozawa, S. Taie, Y. Takasu, and Y. Takahashi, "Antiferromagnetic spin correlation of SU($\mathcal{N}$) Fermi gas in an optical superlattice," Phys. Rev. Lett. **121**, 225303 (2018).

[247] S. Stellmer, R. Grimm, and F. Schreck, "Detection and manipulation of nuclear spin states in fermionic strontium," Phys. Rev. A **84**, 043611 (2011).

[248] D. A. Steck, *Quantum and Atom Optics*, available online at http://steck.us/teaching (revision 0.13.10, 22 September 2021).

[249] A. Kochanke, *Towards Quantum Simulation of the Kondo-Lattice-Model* (PhD Thesis, University of Hamburg, 2017).

[250] L. Riegger, *Interorbital spin exchange in a state-dependent optical lattice* (PhD Thesis, LMU Munich, 2019).

[251] A. Green, *Heteronuclear Feshbach Resonances in Ultracold Mixtures of Ytterbium and Lithium* (PhD Thesis, University of Washington, 2019).

[252] B. Lu and D. Wang, "Note: A four-pass acousto-optic modulator system for laser cooling of sodium atoms," Rev. Sci. Instrum. **88**, 076105 (2017).

[253] A. Thobe, *Ultracold Yb Gases with Control over Spin and Orbital Degrees of Freedom* (PhD Thesis, University of Hamburg, 2014).

[254] F. Scazza, *Probing SU(N)-symmetric orbital interactions with ytterbium Fermi gases in optical lattices* (PhD Thesis, LMU Munich, 2015).

[255] Y. Takasu, K. Komori, K. Honda, M. Kumakura, T. Yabuzaki, and Y. Takahashi, "Photoassociation spectroscopy of laser-cooled Ytterbium atoms," Phys. Rev. Lett. **93**, 123202 (2004).

[256] K. Pandey, A. K. Singh, P. V. K. Kumar, M. V. Suryanarayana, and V. Natarajа, "Isotope shifts and hyperfine structure in the 555.8-nm $^1S_0 \rightarrow {}^3P_1$ line of Yb," Phys. Rev. A **80**, 022518 (2009).

[257] L. Olschewski, "Determination of the nuclear magnetic moments on free ^{43}Ca-, ^{87}Sr-, ^{135}Ba-, ^{137}Ba-, ^{171}Yb- and ^{173}Yb-atoms by means of optical pumping," Z. Physik **249**, 205–227 (1972).

[258] M. Bruderer, A. Klein, S. R. Clark, and D. Jaksch, "Transport of strong-coupling polarons in optical lattices," New J. Phys. **10**, 033015 (2008).

[259] A. Griessner, A. J. Daley, S. R. Clark, D. Jaksch, and P. Zoller, "Dark-state cooling of atoms by superfluid immersion," Phys. Rev. Lett. **97**, 220403 (2006).

[260] T. C. Li, H. Kelkar, D. Medellin, and M. G. Raizen, "Real-time control of the periodicity of a standing wave: an optical accordion," Optics Express **16**, 5465 (2008).

[261] J. L. Ville, T. Bienaimé, R. Saint-Jalm, L. Corman, M. Aidelsburger, L. Chomaz, K. Kleinlein, D. Perconte, S. Nascimbène, J. Dalibard, and J. Beugnon, "Loading and compression of a single two-dimensional Bose gas in an optical accordion," Phys. Rev. A **95**, 013632 (2017).

[262] M. Schmitt, M. Wenzel, F. Böttcher, I. Ferrier-Barbut, and T. Pfau, "Self-bound droplets of a dilute magnetic quantum liquid," Nature **539**, 259–262 (2016).

[263] L. Chomaz, S. Baier, D. Petter, M. J. Mark, F. Wächtler, L. Santos, and F. Ferlaino, "Quantum-fluctuation-driven crossover from a dilute Bose-Einstein condensate to a macrodroplet in a dipolar quantum fluid," Phys. Rev. X **6**, 041039 (2016).

[264] G. Semeghini, G. Ferioli, L. Masi, C. Mazzinghi, L. Wolswijk, F. Minardi, M. Modugno, G. Modugno, M. Inguscio, and M. Fattori, "Self-bound quantum droplets of atomic mixtures in free space," Phys. Rev. Lett. **120**, 235301 (2018).

[265] C. J. Foot, *Atomic physics* (Oxford University Press, 2004).